OSU

The Ohio State University

SIMULATION AND ANALYSIS OF

AIRBORNE ANTENNA RADIATION PATTERNS

J.J. Kim and W.D. Burnside

The Ohio State University

ElectroScience Laboratory

Department of Electrical Engineering
Columbus, Ohio 43212

NOTICES

When Government drawings, specifications, or other data are used for any purpose other than in connection with a definitely related Government procurement operation, the United States Government thereby incurs no responsibility nor any obligation whatsoever, and the fact that the Government may have formulated, furnished, or in any way supplied the said drawings, specifications, or other data, is not to be regarded by implication or otherwise as in any manner licensing the holder or any other person or corporation, or conveying any rights or permission to manufacture, use, or sell any patented invention that may in any way be related thereto.

50272-101

REPORT DOCUMENTATION PAGE	1. REPORT NO.	2.	3. Recipient's Accession No.
4. Title and Subtitle SIMULATION AND ANALYSIS OF AIRBORNE ANTENNA RADIATION PATTERNS			**5. Report Date** December 1984
			6.
7. Author(s) J.J. Kim and W.D. Burnside			**8. Performing Organization Rept. No.** 716199-1
9. Performing Organization Name and Address The Ohio State University ElectroScience Laboratory Department of Electrical Engineering 1320 Kinnear Road Columbus, Ohio 43212			**10. Project/Task/Work Unit No.**
			11. Contract(C) or Grant(G) No. (C) (G) NSG 1498
12. Sponsoring Organization Name and Address National Aeronautics and Space Administration Langley Research Center Hampton, Virginia 23665			**13. Type of Report & Period Covered** Technical
			14.

15. Supplementary Notes

16. Abstract (Limit: 200 words)

The object of this research is to develop an accurate and efficient analytic solution for predicting high frequency radiation patterns of fuselage-mounted airborne antennas. This is an analytic study of airborne antenna patterns using the Uniform Geometrical Theory of Diffraction (UTD). The aircraft is modelled in its most basic form so that the solution is applicable to general-type aircraft. The fuselage is modelled as a perfectly conducting composite ellipsoid; whereas, the wings, stabilizers, nose, fuel tanks, and engines, etc., are simulated as perfectly conducting flat plates that can be attached to the fuselage and/or to each other. The composite-ellipsoid fuselage model is necessary to successfully simulate the wide variety of real world fuselage shapes. Since the antenna is mounted on the fuselage, it has a dominant effect on the resulting radiation pattern so it must be simulated accurately, especially near the antenna. Various radiation patterns are calculated for commercial, private, and military aircraft, and the Space Shuttle Orbiter. The application of this solution to numerous practical airborne antenna problems illustrates its versatility and design capability. In most cases, the solution accuracy is verified by the comparisons between the calculated and measured data.

17. Document Analysis   a. Descriptors

Uniform Geometrical Theory of Diffraction (UTD)
Ray optical technique
Electromagnetic radiation and scattering
Airborne antenna radiation pattern

High frequency analysis
Elliptic cone perturbation method
Elliptic cylinder perturbation method
Exact geodesic paths
Efficient analytic solution
Composite ellipsoid fuselage model
Experimental verification

b. Identifiers/Open-Ended Terms

c. COSATI Field/Group

18. Availability Statement	**19. Security Class (This Report)** UNCLASSIFIED	**21. No. of Pages** 328
	20. Security Class (This Page) UNCLASSIFIED	**22. Price**

(See ANSI–Z39.18)   See Instructions on Reverse

OPTIONAL FORM 272 (4–77)
(Formerly NTIS–35)
Department of Commerce

TABLE OF CONTENTS

Page

LIST OF TABLES

LIST OF FIGURES

ix

xii

CHAPTER I

INTRODUCTION

Computer simulation and radiation pattern analysis of
fuselage-mounted airborne antennas at high frequencies are the object of
this research. The primary goal of this investigation is to develop an
analytic solution for predicting radiation patterns of airborne antennas
in a more accurate and efficient manner. The radiation pattern analysis
is based on the uniform geometrical theory of diffraction (UTD) which is
a uniform extension of Keller's geometrical theory of diffraction (GTD)
[1]. The UTD solution [2] for the radiation from sources on a convex
surface is employed to compute the radiated field from the antenna
mounted on an aircraft fuselage. The aircraft scattering analysis is
based on the UTD solutions for wedge [3,4] and corner diffraction
[6,21,29]. The theoretical formulation of UTD is discussed in some
detail in Chapter II.

One of the principle problems in the design of a reliable airborne antenna system is the location of the antennas on the aircraft structure in order to achieve the desired radiation coverage. If modern systems are to function properly, the antenna pattern must meet certain specifications. In fact, the antenna system performance is very much dependent upon the resulting antenna radiation patterns. Until recently, airborne antennas were located by simply choosing among those locations allowed by the aerodynamacist which met the required specifications and scale model measurements then were used to evaluate the performance of the antennas in terms of its desired pattern. This approach of airborne antenna design requires a lot of engineering time and is also very expensive; furthermore, there are many antennas mounted on a single aircraft. Therefore, the need for an efficient analytic solution to compute airborne antenna radiation patterns is quite apparent. If these antennas can be located on the aircraft at the design stage using an analytic solution, then one can expect better performance in that more optimum locations and necessary structural changes can be anticipated. In addition, a future relocation or addition of antennas on an aircraft within its useful lifetime can also be easily accomplished through this approach. Once an optimum region is determined, the antenna can simply be flight tested to ascertain its actual performance. Not only can these analytic solutions be used to determine the best location, but they can, also, determine a more optimum antenna design for a given application.

2

Since it is a study of general-type aircraft, the aircraft is modelled in its most basic form. Previously the aircraft fuselage was simulated by an elliptic cylinder and the rest of the aircraft appendages were modelled by finite flat plates [7,8,9]. However, the elliptic cylinder model could not predict the pattern close to the nose or tail sectors, where the deviation from the physical situation becomes very prominent. In fact, the fuselage has a dominant effect on the resulting radiation pattern of a flush-mounted airborne antenna. In order to overcome this deficiency, a composite prolate spheroid model was introduced [10,11]. The significance of this solution is that the spheroid model provides the proper polarization and curvature effects as opposed to the cylinder which models only one curvature. Note that the surface geometry dictates the polarization of the radiated field [2]. However, the prolate spheroid representation of the fuselage is not general enough to satisfactorily approximate the wide variety of aircraft. The inadequacy asociated with the prolate spheroid results from its circular cross-section. It has been shown in [8] that an elliptic cross-section is necessary to successfully simulate the wide variety of aircraft fuselage shapes. Therefore, the composite ellipsoid fuselage model used here becomes necessary. The development of the composite ellipsoid fuselage model should provide as much generality as needed to simulate the wide variety of aircraft found in practice.

In applying the UTD to antenna radiation problems involving curved surfaces, a major task is to determine the geodesic paths on the curved surface. An efficient numerical technique to find the creeping wave geodesic paths on an ellipsoid [13,14] and the computer simulation technique of the whole aircraft structures are discussed in some detail in Chapter III.

Based on these techniques, one applies a ray optics technique to determine the fields incident on the various scatterers. The fields diffracted are found using the UTD solutions in terms of rays which are summed with the geometrical optics terms. The rays from a given scatterer tend to interact with the other structures causing various higher-order terms. In this way one can trace out the various possible combinations of rays that interact between scatterers. Thus, one need only be concerned with the important structural scattering components which have dominant effects on the radiation pattern calculation, and neglect all other higher-order terms. The algorithms for the actual calculation of various UTD terms are discussed in Chapter IV.

Using these algorithms, the Ellipsoid-Model Aircraft Code [15] has been developed to compute and superimpose the various UTD terms for the near or far field calculation. The validity of this analytic solution is verified in terms of comparisons with measured data for the wide variety of aircraft. The radiation pattern analysis is presented in Chapter V.

Since UTD is essentially a high frequency solution, the source and various scattering centers should be separated by at least a wavelength. In terms of the ellipsoid structure its semi-minor axes should be at least a wavelength in extent. In terms of the scattering from a plate this means that each plate should have edges at least a wavelength long. In addition, each antenna element should be at least a wavelength from all edges. In some cases even this requirement can be relaxed. The upper frequency limit is dependent on how well the theoretical model simulates the important details of the actual structure.

CHAPTER II

THEORETICAL BACKGROUND

A. INTRODUCTION

The principal analytical tool employed in this report is the
uniform geometrical theory of diffraction (UTD). The UTD is basically a
uniform extension of Keller's geometrical theory of diffraction (GTD)
[1] but is valid within transition regions adjacent to shadow and
reflection boundaries. The radiation from sources on convex surfaces
and scattering from flat plates are analyzed using UTD in this
chapter. The surface parameters of an ellipsoid which is used to
simulate the aircraft fuselage are also introduced here. The curved
surface and plates are assumed to be perfectly conducting, and the
surrounding medium of the structure is free space. An exp $(j\omega t)$ time
dependence is assumed and suppressed throughout this chapter. One
is referred to references [16,34] for a more extensive treatment on the
theory and application of UTD.

B. RADIATION FROM A CONVEX SURFACE

The development of a uniform GTD (UTD) solution is presented in this section for the electromagnetic field radiated by an aperture in or a short monopole on a smooth perfectly conducting convex surface. For an aperture in a convex surface it is convenient to define an infinitesimal magnetic current moment $d\bar{P}_m(Q')$ at any point Q' in the aperture as

$$d\bar{P}_m(Q') = \bar{E}(Q') \times \hat{n}' da' \tag{2.1}$$

where

$\bar{E}(Q')$ is the electric field,

$\hat{n}'$ is the outward unit normal vector to the surface, and

da' is an incremental area at Q'.

The tangential electric field in the aperture is assumed to be known. The $d\bar{P}_m(Q')$ radiating in the presence of the perfectly conducting convex surface, which now covers the aperture as well, constitutes the equivalent source of the electric field $d\bar{E}_m(P/Q')$ produced at any point P exterior to the surface. The total radiated electric field $\bar{E}_m(P)$ is then found by integrating the incremental field $d\bar{E}_m(P/Q')$ over the total area A of the aperture. Thus, the radiated electric field is given by

$$\bar{E}_m(P) = \iint_A d\bar{E}_m(P/Q') \quad . \tag{2.2}$$

7

Following the above development for the equivalent sources in the aperture radiation problem one may similarly define an infinitesimal electric current moment $d\bar{P}_e(\ell')$ in dealing with the radiation by a monopole on a convex surface as

$$d\bar{P}_e(Q') = I(\ell')d\ell'\hat{n}' \quad , \tag{2.3}$$

where

$I(\ell')$ denotes the electric current distribution on the monopole and is assumed to be be known, and

ℓ' is the distance along its length measured from the base at Q'.

It is also assumed that the monopole is a short thin wire whose total length h is much smaller than the principal surface radii of curvatures at Q'. The current moment $d\bar{P}_e(\ell')$ radiating in the presence of the perfectly conducting surface constitutes the equivalent source of the electric field $d\bar{E}_e(P/\ell')$ produced at P exterior to the surface. The total radiated electric field $\bar{E}_e(P)$ then can be approximately calculated from a knowledge of only the field $d\bar{E}_e(P/Q')$, which is produced by the $d\bar{P}_e(Q')$ in the presence of the perfectly conducting convex surface, by simply replacing $d\bar{P}_e(Q')$ by $\int_0^h d\bar{P}_e(\ell') \cos(k\ell'\cos\theta^i)$ if P is in the lit region, or by $\int_0^h d\bar{P}_e(\ell')$ if P is in the shadow region. It is noted that the $\cos\theta^i$ inside the integral is defined by $\cos\theta^i = \hat{n}' \cdot \hat{s}$, where $\hat{s}$ is the radiation direction in the lit zone from any point on the monopole, with $0 < \ell' < h$.

According to geometrical optics, the space surrounding the source is divided into an illuminated and shadow regions by a plane tangent to the surface at Q'. This plane is referred to as a shadow boundary. The present formulation or ansatz of the uniform GTD solution leads to separate representations for the radiated field $d\bar{E}_m(P/Q')$ in the shadow and lit regions, respectively. However, these different representations will be shown to match exactly in polarization, amplitude, and phase at the shadow boundary.

1. Shadow Region

According to the generalized Fermat's principle, a ray emanating from a source, which is located on the surface, follows a geodesic path on the surface and continually sheds energy into the shadow region. Such a creeping wave mechanism is illustrated in Figure 2.1(a), from which it can be seen that a surface ray traverses from the source point at Q', follows a geodesic path $\overline{Q'Q}$ to the diffraction point Q and then propagates along the geodesic tangent at Q toward the observation point P_s which is located in the shadow region of the curved surface. As shown in Figures 2.1(b) and (c), $\hat{n}'$ is the unit surface normal vector, $\hat{t}'$ is the unit tangent vector of the geodesic path and the binormal unit vector is given by $\hat{b}' = \hat{t}' \times \hat{n}'$ at the source point Q'. Similar unit vectors are introduced along the geodesic path. Thus at the diffraction point Q, $\hat{n}$ is the unit surface normal vector, $\hat{t}$ is the unit
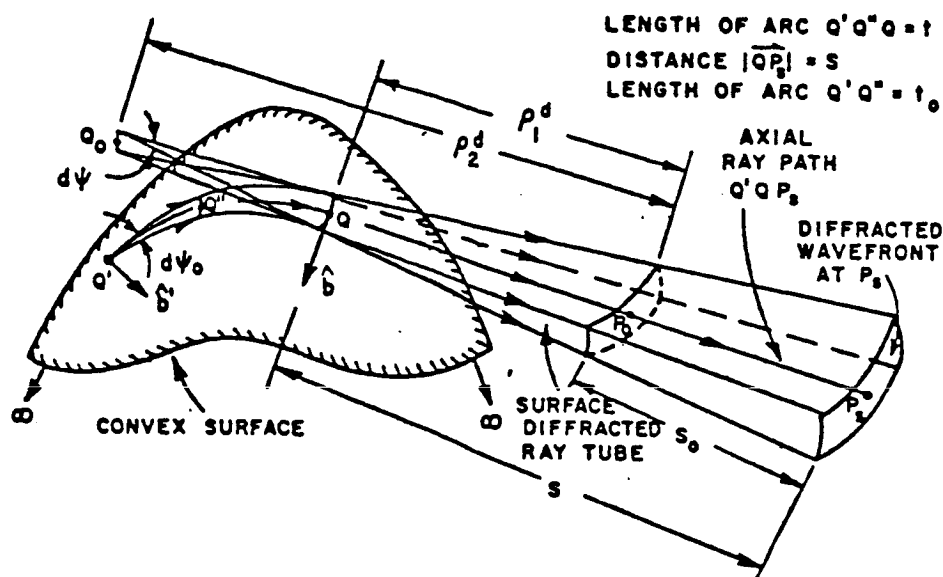
(a). Perspective view of a surface diffracted ray tube (enlarged view).

$$\hat{t} \times \hat{n} = \hat{b}$$
$$\hat{t}' \times \hat{n}' = \hat{b}'$$
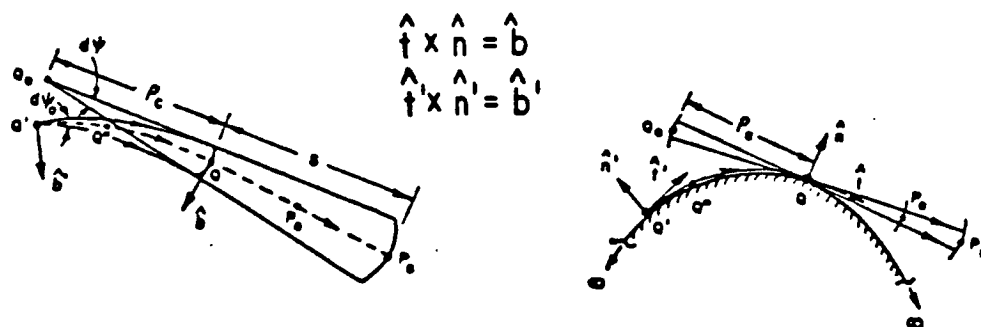
(b). Top view of diffracted ray
tube indicating the
divergence of the rays and
the unit binormal vectors
at Q' and Q.

(c). Side view of surface
diffracted ray tube and
the unit normal and
tangent vectors at Q'
and Q.

Figure 2.1. Surface diffracted ray tube and ray coordinates for the
shadow region.

10

tangent vector of the geodesic and the binormal unit vector is given by $\hat{b}=\hat{t}\times\hat{n}$. The following solution is valid for torsional geodesic paths, where $\hat{b}'\neq\hat{b}$.

The incremental field $d\bar{E}_{m_e}$ at P_s can be expressed in terms of the field at a reference point P_0 by [2]

$$d\bar{E}_{m_e}(P_s) \sim d\bar{E}_{m_e}(P_0) \sqrt{\frac{\rho_1^d \rho_2^d}{(\rho_1^d+s_0)(\rho_2^d+s_0)}}\ e^{-jks_0} + 0[m^{-2}, m^{-3}] \quad ,$$

(2.4)

where ρ_1^d and ρ_2^d are the principal radii of curvatures of the wavefront and $0[m^{-2}, m^{-3}, ...]$ are the higher order terms.

It is seen that if the reference point P_0 is moved to the curved surface diffraction point Q, then $\rho_1^d \to 0$, $\rho_2^d \to \rho_c$, and $s_0 \to s$. Note that ρ_c is the surface diffracted ray caustic distance which can be found via differential geometry [17]. Since $d\bar{E}_{m_e}(P_s)$ is independent of the reference point P_0, such that

$$\lim_{\substack{P_0 \to Q \\ \rho_1^d \to 0}} \sqrt{\rho_1^d}\ d\bar{E}_{m_e}(P_0) = \bar{L}_{m_e}(Q',Q)\ ;$$

(2.5)

then,

11

$$d\bar{E}_m(P_s) \sim \bar{L}_m(Q',Q) \sqrt{\frac{\rho_c}{s(\rho_c+s)}}\ e^{-jks} \quad . \tag{2.6}$$

Furthermore, $\bar{L}_m(Q',Q)$ can be related to the source strength $d\bar{P}_m$ at Q' by

$$\bar{L}_m(Q',Q) = d\bar{P}_m(Q')\cdot\bar{\bar{T}}_m(Q',Q) \tag{2.7}$$

where $\bar{\bar{T}}_m(Q',Q)$ is given by [2]

$$\bar{\bar{T}}_m(Q',Q) = \frac{-jk}{4\pi}\ \lfloor \hat{b}'\hat{n}T_1(Q')H + \hat{t}'\hat{b}T_2(Q')S + \hat{b}'\hat{b}T_3(Q')S + \hat{t}'\hat{n}T_4(Q')H\rfloor$$

$$e^{-jkt} \sqrt{\frac{d\psi_0}{d\eta(Q)}}\ \left[\frac{\rho_g(Q)}{\rho_g(Q')}\right]^{1/6} \quad . \tag{2.8}$$

$$\bar{\bar{T}}_e(Q',Q) = \frac{-jkZ_0}{4\pi}\ \lfloor \hat{n}'\hat{n}T_5(Q')H + \hat{n}'\hat{b}T_6(Q')S\rfloor$$

$$e^{-jkt} \sqrt{\frac{d\psi_0}{d\eta(Q)}}\ \left[\frac{\rho_g(Q)}{\rho_g(Q')}\right]^{1/6} \tag{2.9}$$

12

The quantities $T_1(Q')$, ... , $T_6(Q')$ are the torsion factors at Q' and are given in Table 2.1. It is noted that the effect of torsion is confined to the source location and depends on the direction of the surface ray with respect to the principal directions of the surface at the source point. In other words, it does not depend on the surface ray path away from the source. The uniform Fock functions are expressed as

$$H = g(\xi) \tag{2.10}$$

and

$$S = \frac{-j}{m(Q')} \tilde{g}(\xi) \tag{2.11}$$

with

$$g(\xi) = \frac{1}{\sqrt{\pi}} \int_{\infty\exp(-j2\pi/3)}^{\infty} d\tau \frac{\exp(-j\tau\xi)}{w_2'(\tau)} \tag{2.12}$$

and

$$\tilde{g}(\xi) = \frac{1}{\sqrt{\pi}} \int_{\infty\exp(-j2\pi/3)}^{\infty} d\tau \frac{\exp(-j\tau\xi)}{w_2'(\tau)} \tag{2.13}$$

which are known as the acoustic hard and soft Fock functions, respectively. The Fock type Airy function is given by

TABLE 2.1

SHADOW REGION

TYPE OF CONVEX SURFACE	SLOT OR $\delta\bar{P}_m$ CASE				MONOPOLE OR $\delta\bar{P}_e$ CASE		SURFACE RAY TORSION $T(Q')$	SURFACE RADIUS OF CURVATURE IN $\hat{n}$ DIRECTION $\rho_g(Q')$	SURFACE DIFFRACTED RAY CAUSTIC DISTANCE ρ_c
	$T_1(Q')$	$T_2(Q')$	$T_3(Q')$	$T_4(Q')$	$T_5(Q')$	$T_6(Q')$			
SPHERE	—	—	0	0	—	0	0	a	$a\tan\left(\frac{t}{a}\right)$
CIRCULAR CYLINDER	—	—	$\frac{\sin 2\alpha'}{2a}\cdot\frac{a}{\sin^2\alpha'}$	0	—	$\frac{\sin 2\alpha'}{2a}\cdot\frac{a}{\sin^2\alpha'}$	$\frac{\sin 2\alpha'}{2a}$	$\frac{a}{\sin^2\alpha'}$	—
ARBITRARY CONVEX SURFACE	—	—	$T(Q')\rho_g(Q')$	0	—	$T(Q')\rho_g(Q')$	$\frac{\sin 2\alpha'}{2}\left(\frac{1}{R_2(Q')}-\frac{1}{R_1(Q')}\right)$ WITH $R_1(Q') \geq R_2(Q')$	$\left(\frac{\cos^2\alpha'}{R_1(Q')}+\frac{\sin^2\alpha'}{R_2(Q')}\right)^{-1}$	$\frac{3}{2}\frac{\sqrt{3}}{\partial\theta/\partial t}$

Note: (1) α' is defined by $\hat{\tau}_1'\cdot\hat{t}'=\cos\alpha'$ where $\hat{\tau}_1'$ is the principal direction unit vector associated with $R_1(Q')$.

$$\hat{\tau}_1' = \hat{\tau}_2' \times \hat{n}$$
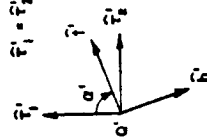
(2) The quantities E and G denote two of the three coefficients E, F, G that appear in the "first fundamental form" of Differential Geometry [17].

14

$$w_2(\tau) = \frac{1}{\sqrt{\pi}} \int_{\infty \exp(j2\pi/3)}^{\infty} dt \cdot \exp(\tau t - t^3/3) \tag{2.14}$$

and $w_2'(\tau)$ is the derivative of $w_2(\tau)$ with respect to τ. The Fock parameter ξ for the shadow region is given by [2]

$$\xi = \int_{Q'}^{Q} dt' \ \frac{m(t')}{\rho_g(t')} \tag{2.15}$$

with

$$m(t') = \left[\frac{k\rho_g(t')}{2} \right]^{1/3} \cdot \tag{2.16}$$

Here $\rho_g(\tau')$ is the surface radius of curvature along the ray path at t'. The wavenumber (k) is taken to be that of free space. The width of the surface ray tube at Q, $d\eta(Q)$, is given by

$$d\eta(Q) = \rho_c d\Psi \cdot \tag{2.17}$$

Note the parameters Z_0 and t are defined as the free space wave impedance and geodesic arc length from Q' to Q, respectively.

Combining Equations (2.6) - (2.17), the $\hat{n}$ and $\hat{b}$ directed components of $dE_m^e(P_s)$ are given by

(a) $d\bar{P}_m(Q')$ case:

$$dE_m^n(P_s) = \frac{-jk}{4\pi}(d\bar{P}_m \cdot \hat{b}')He^{-jkt} \left[\frac{\rho_g(Q')}{\rho_g(Q)}\right]^{-1/6} \sqrt{\frac{d\psi_0}{d\psi}} \sqrt{\frac{1}{s(\rho_c+s)}}$$

$$e^{-jks} + O[m^{-2}] \qquad\qquad (2.18)$$

and

$$dE_m^b(P_s) = \frac{-jk}{4\pi}[(d\bar{P}_m \cdot \hat{b}')T_0 S + (d\bar{P}_m \cdot \hat{t}')S]e^{-jkt} \left[\frac{\rho_g(Q')}{\rho_g(Q)}\right]^{-1/6}$$

$$\sqrt{\frac{d\psi_0}{d\psi}} \sqrt{\frac{1}{s(\rho_c+s)}} e^{-jks} + O[m^{-2}, m^{-3}] \qquad (2.19)$$

(b) $d\bar{P}_e(Q')$ case:

$$dE_e^n(P_s) = \frac{-jkZ_0}{4\pi} dP_e(Q')He^{-jkt} \left[\frac{\rho_g(Q')}{\rho_g(Q)}\right]^{-1/6} \sqrt{\frac{d\psi_0}{d\psi}} \sqrt{\frac{1}{s(\rho_c+s)}}$$

$$e^{-jks} + O[m^{-2}] \qquad\qquad (2.20)$$

16

and

$$dE_e^b(P_s) = \frac{-jkZ_0}{4\pi} dP_e(Q')T_0Se^{-jkt} \left[\frac{\rho_g(Q')}{\rho_g(Q)}\right]^{-1/6} \sqrt{\frac{d\psi_0}{d\psi}} \sqrt{\frac{1}{s(\rho_c+s)}}$$

$$e^{-jks} + O[m^{-2}] \tag{2.21}$$

where $T_0 = T(Q')\rho_g(Q')$ with $T(Q')$ being the surface torsion at the source location (refer to Table 2.1). The ray divergence factor $\sqrt{d\psi_0/d\psi}$ is used to describe the amount of separation between adjacent geodesic paths as surface rays propagate around the surface as shown in Figure 2.1(b), in which $d\psi_0$ and $d\psi$ are the angles subtended by the surface ray tube at the launching Q' and diffraction Q points, respectively.

2. Lit Region

In the lit region, the radiated energy propagates directly from the source Q' to the field point P_L along the incident ray of geometrical optics as shown in Figure 2.2(a). For convenience, a ray-fixed coordinate system is used to describe the polarization properties. The unit vector $\hat{s}$ is in the direction from Q' to P, and $\hat{n}'$ is again the unit surface normal vector at Q'. The incident plane is defined as the plane containing the unit vectors $\hat{s}$ and $\hat{n}'$. The unit tangent vector $\hat{t}'$ is the projection of the unit vector $\hat{s}$ in the tangent plane such that $\hat{s} = \hat{n}'\cos\theta^i + \hat{t}_\ell'\sin\theta^i$. The tangent plane is defined as the plane

17

(a)

$$\hat{n}' \cdot \hat{s} = \cos \theta^i$$

$$\hat{s} = \hat{n}' \cos \theta^i + \hat{t}'_i \sin \theta^i$$
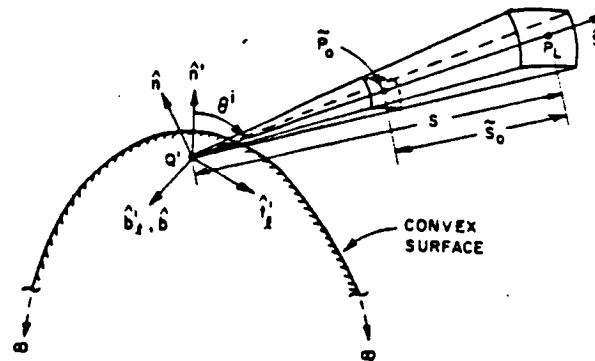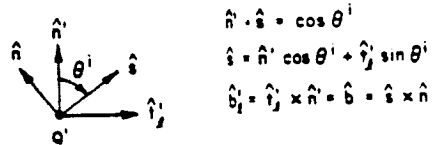
$$\hat{b}'_i = \hat{t}'_i \times \hat{n}' = \hat{b} = \hat{s} \times \hat{n}$$

(b)

Figure 2.2. Ray tube and ray coordinates for the lit region.

18

tangent to the curved surface at Q'. Hence, $\hat{t}'_\ell$ is tangent to the
curved surface at Q'. The binormal unit vector at Q' is defined by
$\hat{b}'_\ell = \hat{t}'_\ell \times \hat{n}'$. The unit vector $\hat{n}$ is in the incident plane, perpendicular
to $\hat{s}$ and directed outward from the curved surface. The binormal unit
vector at P_L is given by $\hat{b} = \hat{s} \times \hat{n}$.

In the ray optical approximation, the field $d\bar{E}_m^e(P_L)$ at the field
point P_L may be expressed by

$$d\bar{E}_m^e(P_L) \sim d\bar{E}_m^e(P_0) \sqrt{\frac{\rho_1^i \rho_2^i}{(\rho_1^i + \tilde{s}_0)(\rho_2^i + \tilde{s}_0)}} \; e^{-jk\tilde{s}_0} + O[m_\ell^{-2}, m_\ell^{-3}] \; . \tag{2.22}$$

Since Q' is the only caustic of the incident rays, the principal radii
of curvature ρ_1^i and ρ_2^i associated with the incident wavefront at $\tilde{P}_0$ are
identical, i.e., $\rho_1^i = \rho_2^i = \rho^i$. Furthermore, $d\bar{E}_m^e(P_L)$ is independent of
the reference point $\tilde{P}_0$. If $\tilde{P}_0$ is chosen to be at Q', it follows that

$$\lim_{\substack{\tilde{P}_0 \to Q' \\ \rho^i \to 0 \\ \tilde{s}_0 \to s}} \rho^i d\bar{E}_m^e(P_0) = \bar{L}_m^{e\,\ell}$$

$$\tag{2.23}$$

should exist. Thus, $\bar{L}_m^{e\,\ell}$ can be related to $d\bar{P}_m^e(Q')$ by [2]

19

$$\bar{L}_m^{\ell} = d\bar{P}_m(Q') \cdot \bar{\bar{T}}_m^{\ell} \qquad \qquad (2.24)$$

Equations (2.22) - (2.24) are, then, combined to yield

$$d\bar{E}_m(P_L) \sim d\bar{P}_m(Q') \cdot \bar{\bar{T}}_m^{\ell} \cdot \frac{e^{-jks}}{s} + O[m_\ell^{-2}, m_\ell^{-3}, \ldots] \qquad (2.25)$$

where

$$\bar{\bar{T}}_m^{\ell} = \frac{-jk}{4\pi} [\hat{b}_\ell'\hat{n}A + \hat{t}_\ell'\hat{b}B + \hat{b}_\ell'\hat{b}C + \hat{t}_\ell'\hat{n}D] \qquad (2.26)$$

and

$$\bar{\bar{T}}_e^{\ell} = \frac{-jkZ_0}{4\pi} [\hat{n}'\hat{n}M + \hat{n}'\hat{b}N] \qquad (2.27)$$

where A, B, C, D, M, and N are defined in Table 2.2. Note that $d\bar{E}_m(P_L)$ is decoupled into $\hat{n}$ and $\hat{b}$ components as follows:

(a) $d\bar{P}_m(Q')$ case:

$$dE_m^n(P_L) = \frac{-jk}{4\pi} [(d\bar{P}_m \cdot \hat{b}')(H^{\ell} + T_0^2 F\cos\theta^i) + (d\bar{P}_m \cdot \hat{t}')T_0 F\cos\theta^i]$$

$$\frac{e^{-jks}}{s} + O[m_\ell^{-2}] \qquad (2.28)$$

and

20

TABLE 2.2

FOR LIT REGION

SLOT OR $d\bar{P}_m$ CASE				MONOPOLE OR $d\bar{P}_e$ CASE		T_0	F
A	B	C	D	M	N		
$H' + T_0^2 F\cos\theta'$	$S' - T_0^2 F\cos^2\theta'$	$T_0 F$	$T_0 F\cos\theta'$	$\sin\theta'[H' + T_0^2 F\cos\theta']$	$\sin\theta' T_0 F$	$T(\theta')\,\rho_s(\theta')$	$\dfrac{S' - H'\cos\theta'}{1 + T_0^2\cos\theta'}$

$$dE_m^b(P_L) = \frac{-jk}{4\pi}\left[(d\bar{P}_m\cdot\hat{b}')T_0 F + (d\bar{P}_m\cdot\hat{t}')(S^\ell - T_0^2 F\cos^2\theta^i)\right]$$

$$\frac{e^{-jks}}{s} + O[m_\ell^{-2},\ m_\ell^{-3}] \tag{2.29}$$

(b) $d\bar{P}_e(Q')$ case:

$$dE_e^n(P_L) = \frac{-jkZ_0}{4\pi}\,dP_e(Q')\sin\theta^i\left[H^\ell + T_0^2 F\cos\theta^i\right]\frac{e^{-jks}}{s} + O[m_\ell^{-2}] \tag{2.30}$$

21

and

$$dE_e^b(P_L) = \frac{-jkZ_0}{4\pi} \, dP_e(Q') \sin\theta^i T_0 F \, \frac{e^{-jks}}{s} + O[m_\ell^{-2}] \quad .$$ (2.31)

The functions H^ℓ and S^ℓ are defined by

$$H^\ell = g(\xi_\ell) \, e^{-j\xi_\ell^3/3}$$ (2.32)

and

$$S^\ell = \frac{-j}{m_\ell(Q')} \, \tilde{g}(\xi_\ell) \, e^{-j\xi_\ell^3/3}$$ (2.33)

in which the hard and soft Fock function g and $\tilde{g}$ have been defined previously in (2.12) and (2.13), respectively. The Fock parameter ξ_ℓ for the lit region is given by

$$\xi_\ell = -m_\ell(Q')\cos\theta^i$$ (2.34)

where

$$m_\ell(Q') = \frac{m(Q')}{(1+T_0^2\cos^2\theta^i)^{1/3}} \quad .$$ (2.35)

Here the angle θ^i is defined by $\hat{n}'\cdot\hat{s} = \cos\theta^i$ as shown in Figure 2.2. Also,

$$F = \frac{S^\ell - H^\ell\cos\theta^i}{1+T_0^2\cos^2\theta^i}$$ (2.36)

as defined in Table 2.2. The other parameters are the same as before.

3. Pattern Factor

The solutions for short magnetic or electric dipoles have been given in Sections 1 and 2. One approach to analyze an extended aperture or linear antenna problem is to integrate the above solutions over the source distribution as discussed previously. This is an application of the superposition theorem, and one approximates the source distribution by an array of short magnetic (or electric) dipoles on the conducting surface. This is an accurate solution, however, it is rather tedious. A more efficient approach has been introduced in reference [18]. It is assumed that the dominant waveguide mode exists across the aperture (i.e., a cosine distribution along the B dimension and uniform along the A dimension). The slot can be axially oriented or circumferentially oriented as shown in Figure 2.3. Notice that any slot with arbitrary orientation can be resolved into these two orthogonal components. For the monopole case, a sinusoidal distribution with unit amplitude is assumed for the current density over the monopole of length L. This approach is to modify $d\bar{P}_{m_e}(Q')$ such that

(a) in the shadow region:

$$\bar{P}_m = \hat{P}_m \frac{2B}{\pi} \left[\frac{\cos\left(\frac{kB}{2}(\hat{P}_m \cdot \hat{t}')\right)}{1-\left(\frac{kB}{\pi}(\hat{P}_m \cdot \hat{t}')\right)^2} \right] \left[\frac{\sin\left(\frac{kA}{2}\hat{P}_m \cdot \hat{b}'\right)}{\frac{kA}{2}\hat{P}_m \cdot \hat{b}'} \right] \qquad (2.37)$$

23
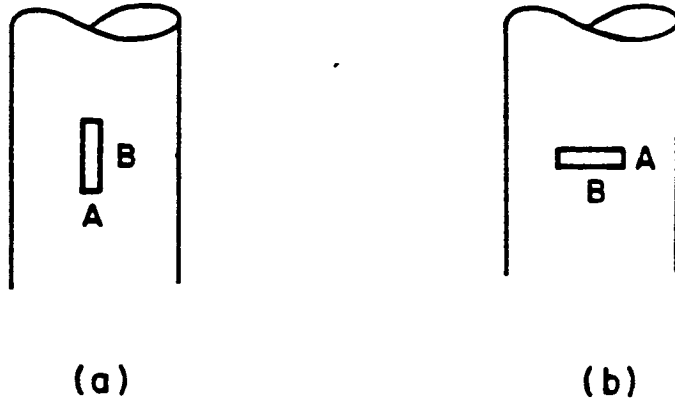
Figure 2.3. A conducting cylinder upon which (a) an axial slot or (b) a circumferential slot is mounted.

and

$$\bar{P}_e = \hat{n}'[1-\cos(kL)]$$

(2.38)

(b) in the lit region:

$$\bar{P}_m = \hat{P}_m \frac{2B}{\pi} \left[\frac{\cos\left(\frac{kB}{2}\sin\theta^i\,(\hat{P}_m\cdot\hat{t}')\right)}{1-\left(\frac{kB}{\pi}\sin\theta^i\,(\hat{P}_m\cdot\hat{t}')\right)^2} \right] \left[\frac{\sin\left(\frac{kA}{2}\sin\theta^i(\hat{P}_m\cdot\hat{b}')\right)}{\frac{kA}{2}\sin\theta^i(\hat{P}_m\cdot\hat{b}')} \right]$$

(2.39)

and

$$\bar{P}_e = \hat{n}'\, \frac{\cos(kL\hat{n}'\cdot\hat{s})-\cos(kL)}{1-(\hat{n}'\cdot\hat{s})^2} \quad .$$

(2.40)

24

Here, $\hat{P}_m$ = unit vector in the direction of magnetic current moment, A,B are dimensions of the slot, and L is the length of the monopole. It is noted that L is not to exceed a quarter wavelength for the solutions to be valid.

C. SCATTERING FROM FLAT PLATES

1. Diffraction by a Wedge

The Uniform Geometrical Theory of Diffraction (UTD) developed by Kouyoumjian and Pathak [3,4] is sufficiently general to handle the three dimensional wedge structures. The UTD wedge diffraction formulations are based on the fundamental Geometrical Theory of Diffraction (GTD) which was originally developed by Keller and his associates at the Courant Institute of Mathematical Sciences [1]. The GTD is a ray optical technique and, therefore, it allows one to gain substantial physical insight into the significant physical mechanisms involved in the scattering of flat plates. Accordingly, one is able to determine the dominant diffraction mechanisms for a given geometry.

The field radiated from a source at O and observed at P in the presence of a perfectly conducting wedge is shown in Figure 2.4. It is assumed that the source and observation points are sufficiently removed from the wedge surface so that the contributions from the surface ray

OBSERVATION
POINT
$\bullet$ P

z

$\hat{D}$

β_0

$\hat{\beta}_0$

$(2-n)\pi$

S

CONE OF
DIFFRACTED RAYS

Q_E

$\hat{\beta}_0'$

β'

y

x

s'

$\hat{I}$

$\bullet$ O

SOURCE POINT

y

ρ'

$\hat{\phi}'$

$\hat{\phi}$

ϕ'

ρ

ϕ

$\rho' = s' \sin\beta_0$

$\rho = s \sin\beta$

x

$(2-n)\pi$

SIDE VIEW
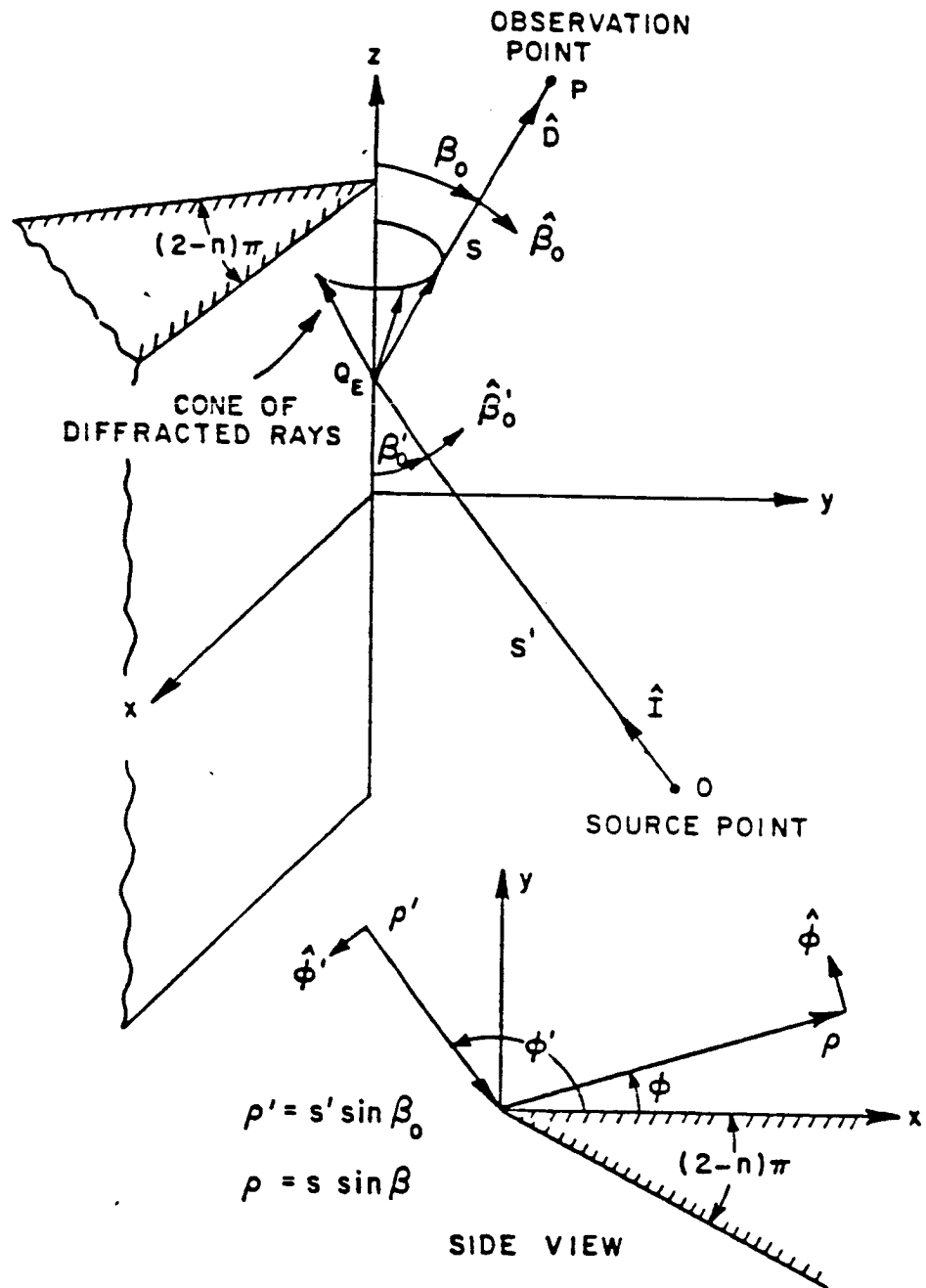
Figure 2.4. Geometry for three-dimensional wedge diffraction problem.

field can be neglected. Applying the generalized Fermat's principle, the distance along the ray path $\overline{OQ_EP}$ is a minimum which in terms of edge diffraction this leads to $\hat{s}'\cdot\hat{e} = \hat{s}\cdot\hat{e}$.

Kouyoumjian and Pathak have shown that the diffracted fields can be written in a compact way if these fields are written in terms of an edge-fixed coordinate system [19,20]. This coordinate system is centered at the diffraction point Q_E, and this point is unique for a given source and observation points. The incident ray diffracts as a cone of rays such that $\beta_0 = \beta_0'$. The orthogonal unit vectors associated with the edge-fixed coordinate system are defined as $\hat{\beta}_0' = \hat{\phi}' \times \hat{s}'$ and $\hat{\beta}_0 = \hat{\phi} \times \hat{s}$, where $\hat{s}'$ is the unit vector in the direction of incidence, and $\hat{s}$ is the unit vector in the direction of diffraction.

The diffracted field $\bar{E}_d$ can be asymptotically expressed by [3]

$$\bar{E}^d(s) \sim \bar{E}^i(Q_E) \cdot \bar{\bar{D}}(\hat{s},\hat{s}')A(s)e^{-jks} \qquad (2.41)$$

in which $\bar{\bar{D}}(s,s')$ is the dyadic edge-diffraction coefficient as given by

$$\bar{\bar{D}} = -\hat{\beta}_0'\hat{\beta}_0 D_s - \hat{\phi}'\hat{\phi}D_h \qquad . \qquad (2.42)$$

The diffraction fields can also be written in a matrix form as

$$\begin{bmatrix} E_{\parallel}^d(s) \\ \\ E_{\perp}^d(s) \end{bmatrix} = \begin{bmatrix} -D_s & 0 \\ \\ 0 & -D_h \end{bmatrix} \begin{bmatrix} E_{\parallel}^i(Q_E) \\ \\ E_{\perp}^i(Q_E) \end{bmatrix} A(s)e^{-jks} \qquad . \qquad (2.43)$$

Expressions for the scalar diffraction coefficients which are valid at all points away from the edge (again excluding $\phi' = 0$ or $n\pi$) are [3]

$$D_{s,h}(L,\phi,\phi',\beta_0) = \frac{-e^{-j\pi/4}}{2n\sqrt{2\pi k}\,\sin\beta_0} \left[\cot\left(\frac{\pi+\beta^-}{2n}\right)F(kLa^+(\beta^-)) \right.$$

$$\left. + \cot\left(\frac{\pi-\beta^-}{2n}\right)F(kLa^-(\beta^-)) \mp \left[\cot\left(\frac{\pi+\beta^+}{2n}\right)F(kLa^+(\beta^+)) \right.\right.$$

$$\left.\left. + \cot\left(\frac{\pi-\beta^+}{2n}\right)F(kLa^-(\beta^+)) \right] \right] \tag{2.44}$$

where the minus $(-)$ sign applies to D_s and the plus $(+)$ sign for D_h. Note that D_s is referred to as the soft scalar diffraction coefficient for the acoustically soft (Dirichlet) boundary condition at the surface of the wedge, i.e.,

$$\left(\bar{E} \Big|_{\text{Wedge}} \right) = 0 \tag{2.45}$$

D_h is referred to as the hard scalar diffraction coefficient for the acoustically hard (Neumann) boundary condition at the surface of the wedge, i.e.,

$$\left(\frac{\partial \bar{E}}{\partial n} \Big|_{\text{Wedge}} \right) = 0 \tag{2.46}$$

28

where the $\partial/\partial n$ is the derivative along the normal direction to the boundary surface. The angle parameter β is given by

$$\beta^{\mp} = \phi \mp \phi' \tag{2.47}$$

and

$$a^{\pm}(\beta^{\pm}) = 2\cos^2\left(\frac{2\pi n N^{\pm} - \beta^{\pm}}{2}\right) \tag{2.48}$$

where $N^{\pm}$ are the integers which most nearly satisfy the following equations:

$$2\pi n N^{+} - \beta^{\pm} = \pi \tag{2.49}$$

and

$$2\pi n N^{-} - \beta^{\pm} = -\pi \quad . \tag{2.50}$$

Note that the β^{-} terms are associated with the incident field and the β^{+} terms are associated with the reflected field as shown in Table 2.3. The wedge angle number (n) is given by

$$n = 2 - \frac{WA}{\pi} , \tag{2.51}$$

where WA is the wedge angle in radians. The wedge transition function which is basically a Fresnel integral is given by

29

TABLE 2.3

COTANGENT FUNCTIONS FOR THE DYADIC DIFFRACTION COEFFICIENT

	The cotangent is singular when	value of N at the boundary
$\cot\left(\dfrac{\pi+(\phi-\phi')}{2n}\right)$	$\phi = \phi' - \pi$, a SB surface $\phi = 0$ is shadowed	$N^+ = 0$
$\cot\left(\dfrac{\pi-(\phi-\phi')}{2n}\right)$	$\phi = \phi' + \pi$, a SB surface $\phi = n\pi$ is shadowed	$N^- = 0$
$\cot\left(\dfrac{\pi+(\phi+\phi')}{2n}\right)$	$\phi = (2n-1)\pi - \phi'$, a RB reflection from surface $\phi = n\pi$	$N^+ = 1$
$\cot\left(\dfrac{\pi-(\phi+\phi')}{2n}\right)$	$\phi = \pi - \phi'$, a RB reflection from surface $\phi = 0$	$N^- = 0$

$$F(x) = 2j\sqrt{x}\, e^{jx} \int_{\sqrt{x}}^{\infty} e^{-j\tau^2}\, d\tau \quad . \tag{2.52}$$

The magnitude and phase of this transition function $F(x)$ are shown in Figure 2.5.

When x is small, $F(x)$ is given by

$$F(x) \sim \left[\sqrt{\pi x} - 2x e^{j\pi/4} - 2/3\, x^2\, e^{-j\pi/4}\right] e^{j(\pi/4 + x)} \tag{2.53}$$

and when x is large, $F(x)$ is given by

$$F(x) \sim 1 + \frac{j}{2x} - \frac{3}{4}\frac{1}{x^2} - j\,\frac{15}{8}\frac{1}{x^3} + \frac{75}{16}\frac{1}{x^4} \quad . \tag{2.54}$$

$$F(KL_a) = 2 j \sqrt{KL_a} \; e^{jKL_a} \int_{\sqrt{KL_a}}^{\infty} e^{-j\tau^2} d\tau$$
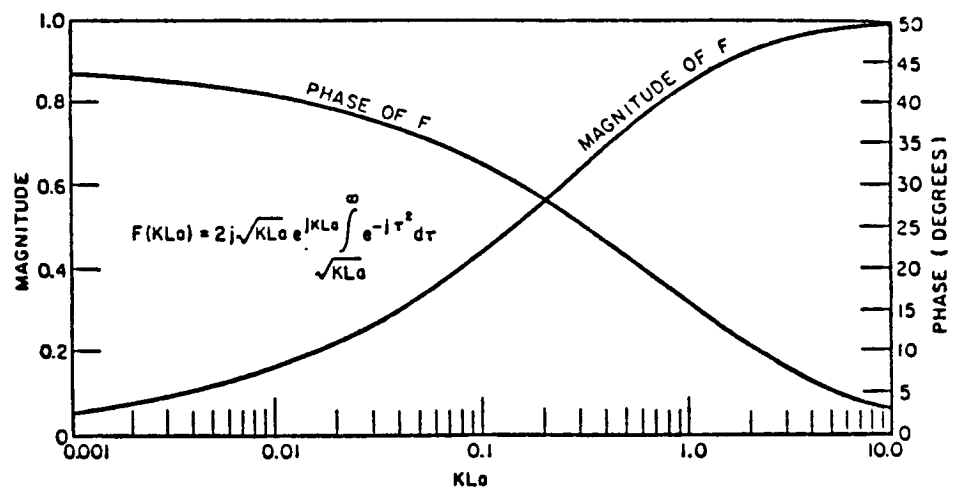
Figure 2.5. Transition function.

31

When $0.3 < x < 5.5$, i.e., in between those regions, a linear interpolation scheme is used such that

$$F(x) = F(x_i) + (F(x_{i+1}) - F(x_i)) \frac{(x-x_i)}{(x_{i+1}-x_i)} \qquad (2.55)$$

where the $F(x_i)$, $\dfrac{F(x_{i+1})-F(x_i)}{(x_{i+1}-x_i)}$ and x_i can be tabulated. These solutions can be used to conveniently compute the transition function. The L is a distance parameter, which is dependent on the type of illumination, and is given by

$$L = \begin{cases} s \sin^2 \beta_0 & \text{for plane wave incidence} \\[2mm] \dfrac{ss'}{s+s'} & \text{for cylindrical wave incidence, and} \\[2mm] \dfrac{ss' \sin^2 \beta_0}{s+s'} & \text{for conical and spherical wave incidence.} \end{cases} \qquad (2.56)$$

The spreading factor A(s), which accounts for the spreading of the power along the diffracted ray, is given by

$$A(s) = \begin{cases} \sqrt{\dfrac{1}{s}} & \text{plane, cylindrical and concical wave incidence, and} \\[2mm] \sqrt{\dfrac{s'}{s(s+s')}} & \text{spherical wave incidence} \end{cases} \qquad (2.57)$$

32

2. Diffraction by a Corner

A corner is formed by the intersection of a pair of finite straight edges. Figure 2.6 shows the corner diffraction geometry. The diffraction of energy from these edges is based on diffraction from an infinite straight edge. To compensate for the finiteness of the edges, a diffraction coefficient associated with the corners of the plate is needed. An empirical corner diffraction solution proposed by Burnside and Pathak [21] is based on the asymptotic evaluation of the radiation integral which employs the equivalent edge currents [6,31] that would exist in the absence of the corners. The corner diffraction term is then found by appropriately (but at present empirically) modifying the asymptotic result for the radiation integral which is characterized by a saddle point near an endpoint [28]. Even though this corner diffraction coefficient is still in its development stages, it has been shown to be very successful in predicting the fields diffracted by a corner for a number of plate structures. For this reason, it is discussed here and has been used to obtain some interesting results.

The corner diffracted fields associated with one corner and one edge in the near field with spherical wave incidence are given by [21]

$$
\begin{bmatrix} E^c_{\beta_o} \\ E^c_{\phi} \end{bmatrix} = \begin{bmatrix} I\ Z_o \\ M\ Y_o \end{bmatrix} \frac{\sqrt{\sin\beta_c\ \sin\beta_{oc}}}{(\cos\beta_{oc} - \cos\beta_c)}\ F[kL_c a(\pi + \beta_{oc} - \beta_c)]\ \frac{e^{-jks}}{4\pi s}
$$

(2.58)
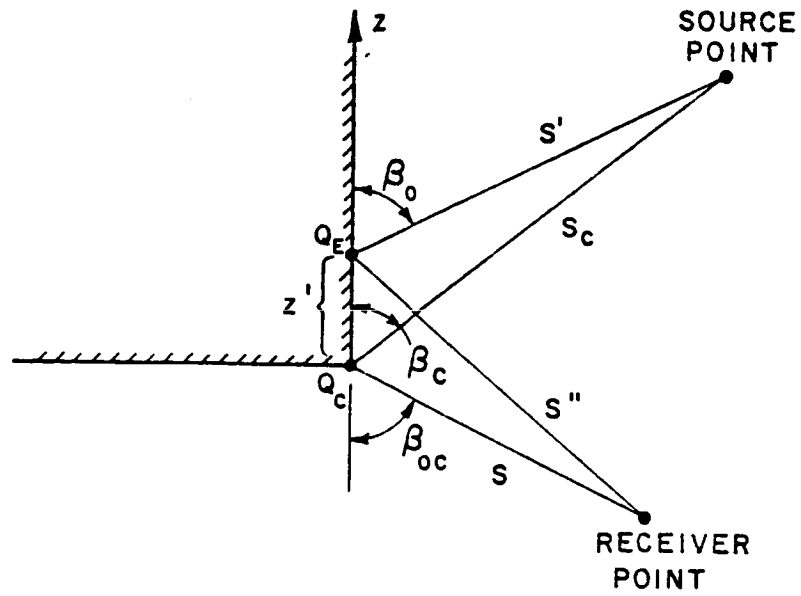
Figure 2.6. Geometry for corner diffraction problem.

where

$$\begin{bmatrix} I \\ M \end{bmatrix} = - \begin{bmatrix} E^i_{\beta_0}{}'(Q_c) \\ E^i_{\phi}{}'(Q_c) \end{bmatrix} \begin{bmatrix} C_S(Q_E)Y_0 \\ C_h(Q_E)Z_0 \end{bmatrix} \sqrt{\frac{8\pi}{k}} \; e^{-j\pi/4} \quad , \qquad (2.59)$$

and

$$C_{s_h}(Q_E) = \frac{-e^{-j\pi/4}}{2\sqrt{2\pi k}\sin\beta_0} \cdot \left[\frac{F(kLa(\beta^-))}{\cos(\frac{\beta^-}{2})} \left| F\left\{\frac{La(\beta^-)/\lambda}{kL_c a(\pi+\beta_{oc}-\beta_c)}\right\} \right| \right.$$

$$\left. \mp \frac{F(kLa(\beta^+))}{\cos(\frac{\beta^+}{2})} \left| F\left\{\frac{La(\beta^+)/\lambda}{kL_c a(\pi+\beta_{oc}-\beta_c)}\right\} \right| \right] \cdot \quad (2.60)$$

The angle parameters β_c and β_{oc} are shown in Figure 2.6. The function $F(x)$ was defined in the previous section, and

$$a(\beta) = 2\cos^2(\beta/2)$$

$$\beta^\pm = \phi \pm \phi'$$

$$\quad (2.61)$$

$$L = \frac{s's''}{(s'+s'')} \sin^2\beta_0 \quad \text{and} \quad L_c = \frac{s_c s}{s_c+s}$$

for spherical wave incidence. The function $C_{s,h}(Q)$ is a modified version of the ordinary edge diffraction coefficient for the half-plane case (n=2). The modification factor, which is given by

$$\left| F\left[\frac{La(\beta^\pm)/\lambda}{kL_c a(\pi+\beta_{oc}-\beta_c)}\right] \right|$$

$$\quad (2.62)$$

is a heuristic function that ensures that the diffraction coefficient will not change sign abruptly when it passes through the shadow boundaries of the edge, i.e., the corner diffracted field will ensure the continuity of the fields as the edge diffracted field shadow boundary is crossed. There is also a corner diffraction term associated with the other edge forming the corner and is found in a similar manner.

D. ELLIPSOID SURFACE PARAMETERS

In applying UTD to electromagnetic diffraction problems, some elementary knowledge of differential geometry of surfaces is necessary. The fuselage of an aircraft is modeled as a composite ellipsoid in order to better approximate general fuselage shapes. Using the ellipsoid geometry shown in Figure 2.7, the surface is defined by

$$\vec{R}(\theta,\phi) = R(\theta,\phi)\sin\theta\cos\phi\hat{x} + R(\theta,\phi)\sin\theta\sin\phi\hat{y} + R(\theta,\phi)\cos\theta\hat{z}$$

$$(2.63)$$

or,

$$\vec{R}(V_e,V_r) = a\cos V_e\cos V_r\hat{x} + b\cos V_e\sin V_r\hat{y} + c\sin V_e\hat{z} \qquad (2.64)$$

with

$$\tan V_e = \frac{\cot\theta}{c\sqrt{\frac{\cos^2\phi}{a^2} + \frac{\sin^2\phi}{b^2}}} \qquad \text{and} \qquad \tan V_r = \frac{a\sin\phi}{b\cos\phi} \quad . \qquad (2.65)$$
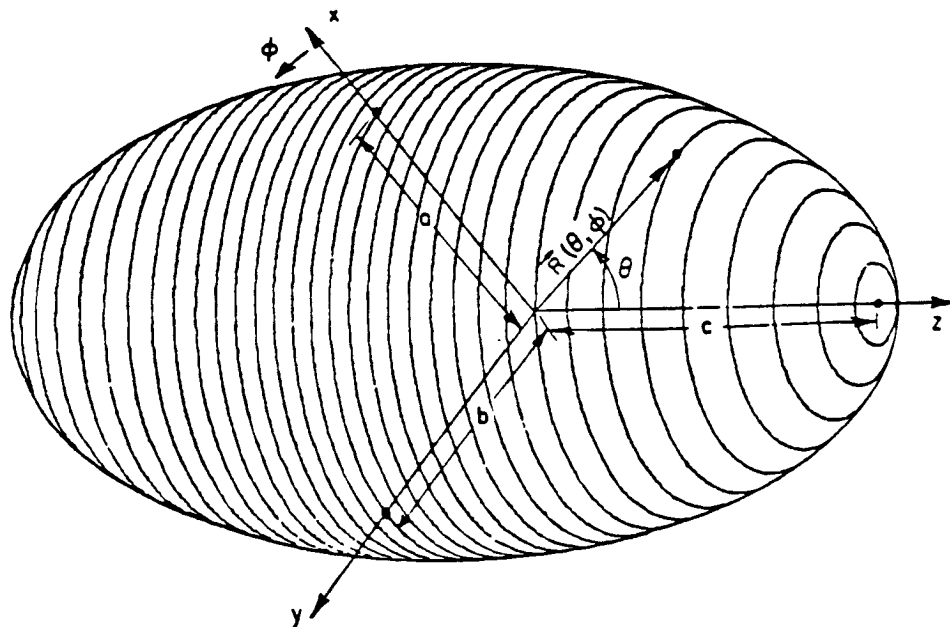
Figure 2.7. Geometry of an ellipsoid.

The V_r and V_e parameters are introduced because of their convenience in analyzing elliptic geometries.

Considering a ray which propagates along a geodesic path $\overline{Q'Q}$ on the ellipsoid surface as shown in Figure 2.8, the three unit vectors $\hat{t}$, $\hat{n}$, and $\hat{b}$ are, as defined earlier, the geodesic tangent, outward surface normal, and binormal at any point along the geodesic path. The outward surface unit normal ($\hat{n}$) is obtained from

$$\hat{n} = \frac{\vec{R}_{V_r} \times \vec{R}_{V_e}}{\left| \vec{R}_{V_r} \times \vec{R}_{V_e} \right|} \qquad (2.66)$$

where

$$\vec{R}_{V_e} = \frac{\partial \vec{R}}{\partial V_e} = -a\,\sin V_e \cos V_r \hat{x} - b\,\sin V_e \sin V_r \hat{y} + c\,\cos V_e \hat{z} \qquad (2.67)$$

and

$$\vec{R}_{V_r} = \frac{\partial \vec{R}}{\partial V_r} = -a\,\cos V_e \sin V_r\,\hat{x} + b\,\cos V_e \cos V_r\,\hat{y} \quad . \qquad (2.68)$$

Then,

$$\hat{n} = \frac{bc\,\cos^2 V_e \cos V_r\,\hat{x} + ac\,\cos^2 V_e \sin V_r\,\hat{y} + ab\,\cos V_e \sin V_e\,\hat{z}}{[b^2 c^2 \cos^4 V_e \cos^2 V_r + a^2 c^2 \cos^4 V_e \sin^2 V_r + a^2 b^2 \cos^2 V_e \sin^2 V_e]^{1/2}}$$

$$= \frac{\dfrac{\cos V_e \cos V_r}{a}\,\hat{x} + \dfrac{\cos V_e \sin V_r}{b}\,\hat{y} + \dfrac{\sin V_e}{c}\,\hat{z}}{A} \qquad (2.69)$$
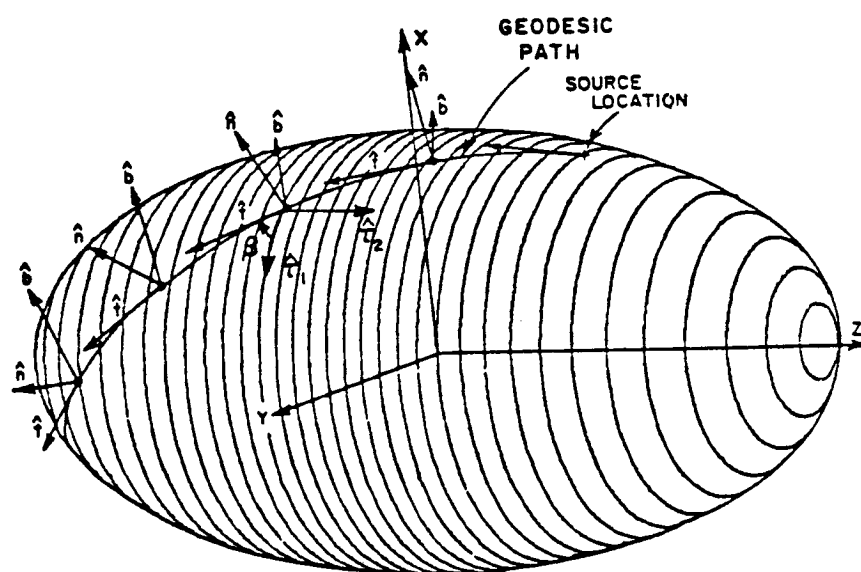
Figure 2.8. Geodesic path on an ellipsoid.

where

$$A \triangleq \left[(\frac{\cos V_e \cos V_r}{a})^2 + (\frac{\cos V_e \sin V_r}{b})^2 + (\frac{\sin V_e}{c})^2 \right]^{1/2} . \qquad (2.70)$$

The normal curvatures K_n on the surface are evaluated by introducing the first and second fundamental forms of differential geometry [17] such that

$$K_n = \frac{L \, dV_r^2 + 2M \, dV_r dV_e + N dV_e^2}{E \, dV_r^2 + 2F \, dV_r dV_e + G dV_e^2} \qquad (2.71)$$

$$L = \vec{R}_{V_r V_r} \cdot \hat{N} \,, \quad M = \vec{R}_{V_r V_e} \cdot \hat{N} \,, \quad N = \vec{R}_{V_e V_e} \cdot \hat{N}$$

$$(2.72)$$

$$E = \vec{R}_{V_r} \cdot \vec{R}_{V_r} \,, \quad F = \vec{R}_{V_r} \cdot \vec{R}_{V_e} \,, \quad G = \vec{R}_{V_e} \cdot \vec{R}_{V_e}$$

and $\hat{N} = -\hat{n}$. It can be shown that

$$\vec{R}_{V_e V_e} = -a \cos V_e \cos V_r \, \hat{x} - b \cos V_e \sin V_r \, \hat{y} - c \sin V_e \, \hat{z}$$

$$\vec{R}_{V_e V_r} = a \sin V_e \sin V_r \, \hat{x} - b \sin V_e \cos V_r \, \hat{y} \qquad (2.73)$$

and

$$\vec{R}_{V_r V_r} = -a \cos V_e \cos V_r \, \hat{x} - b \cos V_e \sin V_r \, \hat{y} \quad .$$

After some algebraic manipulation, one obtains

$$L = \frac{\cos^2 v_e}{A}$$

$$M = 0$$

$$N = \frac{1}{A}$$

$$E = a^2 \cos^2 v_e \sin^2 v_r + b^2 \cos^2 v_e \cos^2 v_r$$

$$F = (a^2 - b^2) \sin^2 v_e \sin^2 v_r \qquad\qquad (2.74)$$

$$G = a^2 \sin^2 v_e \cos^2 v_r + b^2 \sin^2 v_e \sin^2 v_r + c^2 \cos^2 v_e \quad .$$

A pair of orthogonal directions exists for which curvature, K, assumes maximum and minimum values, i.e., principal directions represented by two unit vectors $\hat{\tau}_1$ and $\hat{\tau}_2$. The two extreme values of K corresponding to the above directions are called principal curvatures denoted by K_1 and K_2 [26]. The mean curvature is given by

$$K_M = \frac{K_1 + K_2}{2} = \frac{EN - 2MF + LG}{2(EG - F^2)}$$

and the Gaussian curvature is

$$(2.75)$$

$$K_G = K_1 K_2 = \frac{LN - M^2}{EG - F^2} \quad .$$

Thus, the principal curvatures K_1 and K_2 are given by

$$K_{1,2} = K_M \pm \sqrt{K_M^2 - K_G} \qquad \cdot. \qquad\qquad (2.76)$$

The two principal directions $(\hat{\tau}_1, \hat{\tau}_2)$ are given by

$$\hat{\tau}_1 = \frac{1}{\gamma_1} \left[1 \vec{R}_{V_r} + \alpha \vec{R}_{V_e} \right]$$

and

$$\hat{\tau}_2 = \frac{1}{\gamma_2} \left[\beta \vec{R}_{V_r} + 1 \vec{R}_{V_e} \right] \qquad\qquad (2.77)$$

where

$$\alpha = \frac{L - K_1 E}{K_1 F - M} \qquad, \quad \beta = \frac{M - K_2 F}{K_2 E - L}$$

$$\qquad\qquad (2.78)$$

$$\gamma_1 = (E + 2\alpha F + \alpha^2 G)^{1/2} \;, \text{ and } \gamma_2 = (\beta^2 E + 2\beta F + G)^{1/2} \quad.$$

However, it is noticed that $K_1 \sim L/E$ and $K_2 \sim N/G$ within the significant energy region for most practical cases. That indicates approximate values of the two principal curvatures, $K_1 \sim L/E$ and $K_2 \sim N/G$ are good enough to be used for the geodesics on the ellipsoid surface for our radiation consideration. Thus, one obtains

42

$$K_1 \approx \frac{L}{E} = \frac{\cos^2 V_e}{A[a^2\cos^2 V_e \sin^2 V_r + b^2\cos^2 V_e \cos^2 V_r]}$$

$$= (A[a^2\sin^2 V_r + b^2\cos^2 V_r])^{-1} \qquad (2.79)$$

and

$$K_2 \approx \frac{N}{G} = \frac{1}{A[a^2\sin^2 V_e \cos^2 V_r + b^2\sin^2 V_e \sin^2 V_r + c^2\cos^2 V_e]} \quad . \quad (2.80)$$

It is noticed that the principal radii of curvature are by
$R_1 = \frac{1}{K_1}$ and $R_2 = \frac{1}{K_2}$. If β' denotes the angle between $\hat{t}$ and $\hat{\tau}_1$, then
$\hat{t} = \hat{\tau}_1 \cos\beta' + \hat{\tau}_2 \sin\beta'$. From Euler's theorem, the normal curvature along the geodesic path is specified by

$$K_g = K_1\cos^2\beta' + K_2\sin^2\beta' \qquad (2.81)$$

with the radius of curvature, ρ_g, being $\frac{1}{K_g}$. The torsion term (T_o) introduced in Section (B) is given by

$$T_o = T \cdot \rho_g \qquad (2.82)$$

where the surface torsion is given by

$$T = \frac{\sin^2\beta'}{2} (K_2 - K_1) \qquad (2.83)$$

with K_1 and K_2 being defined in Equations (2.79) and (2.80).

CHAPTER III

FUSELAGE SIMULATION TECHNIQUE

A. INTRODUCTION

For airborne antennas mounted on the fuselage of an aircraft, the
fuselage has been previously modeled as an elliptic cylinder [7,8,9] or
a prolate spheroid [10,11]. However, the elliptic cylinder model could
not predict the pattern close to the nose or tail sectors, where the
deviation from the physical situation becomes very prominent, and the
prolate spheroid model is not general enough to satisfactorily
approximate the wide variety of aircraft cross sectional shapes. The
inadequacy associated with the prolate spheroid results from its
circular cross-section. It has been shown in reference [8] that an
elliptic cross-section is necessary to successfully simulate the wide
variety of aircraft fuselage shapes. In addition, the dominant
structural effect in the elevation plane pattern is the profile of the
aircraft fuselage. Note that the UTD solution in the lit region does

44

not depend on the surface parameters in that it is assumed the source is mounted on an infinite ground plane tangent to the surface at the source point. On the other hand, the transition and deep-shadow region solutions are modified due to their dependence upon the surface parameters. Therefore, the composite ellipsoid fuselage model becomes necessary and will be discussed in detail in Section III-B. In fact, the fuselage has a dominant effect on the resulting radiation pattern of a flush-mounted airborne antenna.

In applying the UTD to antenna radiation problems involving curved surfaces, a major task is to determine the geodesic paths on the curved surface. Among the solutions for obtaining the goedesic paths of the three models, i.e., the cylindrical, prolate spheroidal and ellipsoidal models, the ellipsoid case is the most involved and complex one. This is to be expected because the equation describing an ellipsoid can degenerate into that of a cylinder of a prolate spheroid by using appropriate simplifications.

According to the generalized Fermat's principle, a ray emanating from a source, which is located on the surface, follows a geodesic path on the surface and continually sheds energy into the shadow region. As the energy flows around the surface, it is continuously diffracted along the geodesic tangent toward the field point such that the significant effect of the surface is associated with a region around the source. In fact, for an ellipsoid, the significant portion of the surface, which is associated with the dominant energy, may look as shown in Figure 3.1.

ANTENNA

**REGION OF
SIGNIFICANT
GEODESIC PATHS**
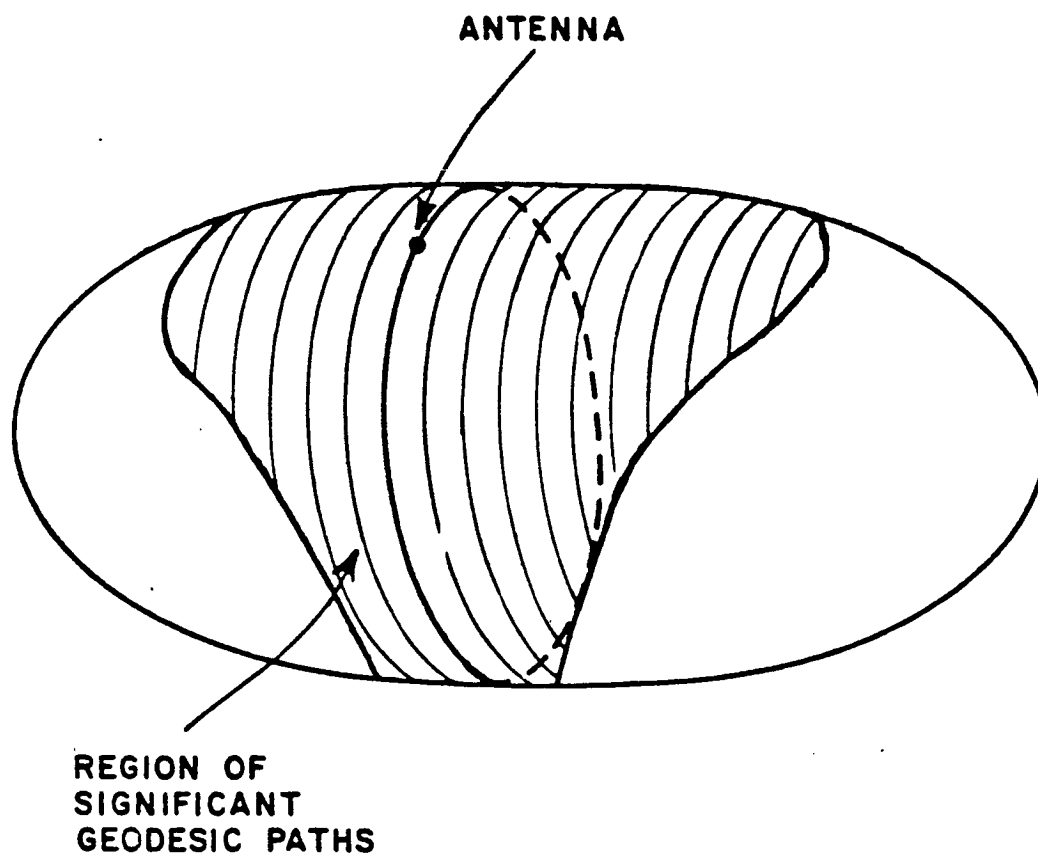
Figure 3.1. The region of significant energy flow from an antenna mounted on an ellipsoid.

Note that this region can be specified by following the various geodesic paths until the radiation level along a given path becomes insignificant, i.e., more than 40 dB below the source magnitude. With this in mind, it is clear that one could represent the ellipsoid by a structure which simulates the elliptic cross-section completely; however, the profile could be approximated by a simpler shape since the significant energy region does not cover a large portion of the profile shape. An elliptic cone model is employed here to simulate the ellipsoid which in turn can be used to model a fuselage. This elliptic cone model is illustrated in Figure 3.2(a) for a source located near one end of the ellipsoid. Note that if the source is placed at the mid-section of the ellipsoid, the elliptic cone actually becomes a right elliptic cylinder.

Since the elliptic cone is a developed surface, one can unfold the elliptic cone such that a planar structure results. Then the geodesics associated with the elliptic cone are straight lines on this planar structure. In order to allow for a geodesic solution between the simplicity of the elliptic cone and the rigor of the ellipsoid, one can perturb the elliptic cone by bending it along its generator as illustrated in Figure 3.2(b). In that a perturbation technique is employed, the geodesic paths for the elliptic cone are simply modified such that the solution for the ellipsoid is basically straight-forward. It is obvious that one cannot use this perturbation technique if

47
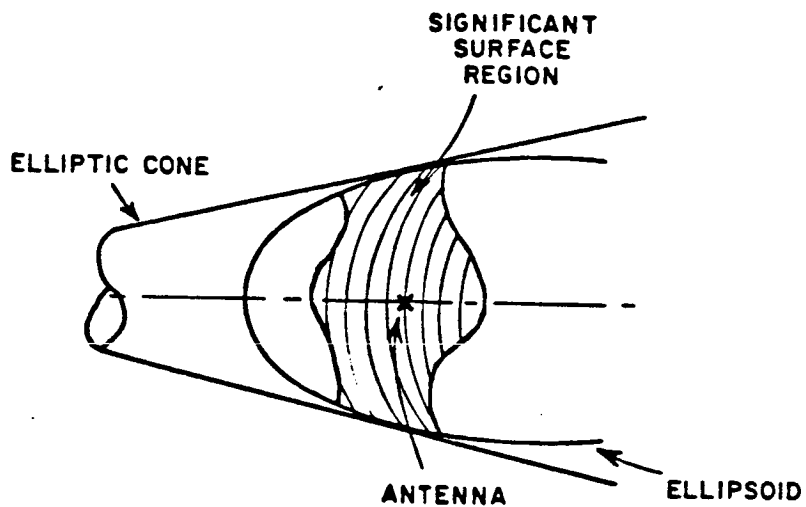
(a) Elliptic cone simulation.
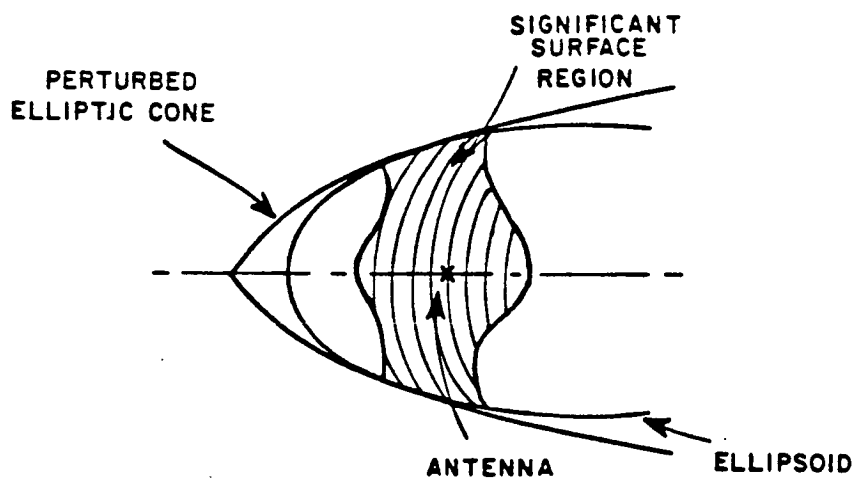
(b) Elliptic cone perturbation model.

Figure 3.2. Elliptic cone perturbation.

48

significant energy propagates far away from the source. However, as
mentioned previously, the energy which propagates great distances along
the ellipsoid surface becomes insignificant in magnitude such that one
need not solve for the true geodesic paths outside the significant
region shown in Figure 3.2(b). The simplicity of these perturbed
geodesic paths allows one to very efficiently determine the significant
ray paths on the ellipsoid. Thus, the efficient numerical technique,
which uses an elliptic cylinder and elliptic cone perturbation method to
find the creeping wave geodesic paths on an ellipsoid [13,14,22,23],
will be discussed and verified by comparing it with the exact solution
in Section III-C.

It is obvious that if one wishes to simulate an aircraft, one must
allow vertical or horizontal stabilizers, etc. to attach to the
fuselage. The algorithm to find the curved junction edge resulting from
attaching these plates to the ellipsoid is discussed in Section III-D.

B. COMPOSITE ELLIPSOID MODEL

The composite ellipsoid is used to model the general aircraft
fuselage in this study. The composite ellipspoid is constructed from
two ellipsoid sections positioned back to back and connected together
such that its surface is continuous and smooth at the cross-section of
the source location as shown in Figure 3.3. The composite ellipsoid
semi-major/minor axes are defined by a_0, b_0, c_0 and d_0 as shown in
Figure 3.3(a) and the source location is defined by z_s and ϕ_s. It is
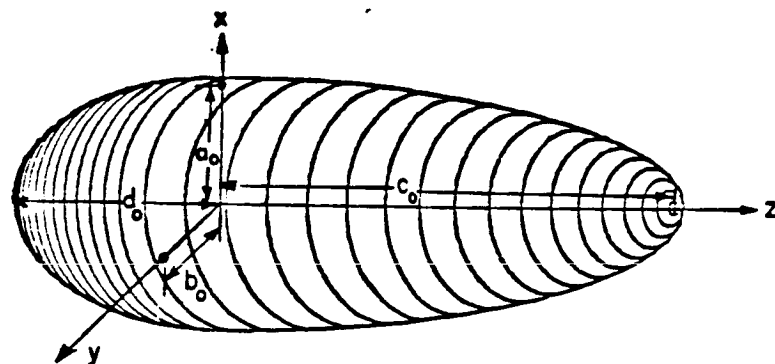
(a) Composite ellipsoid model.
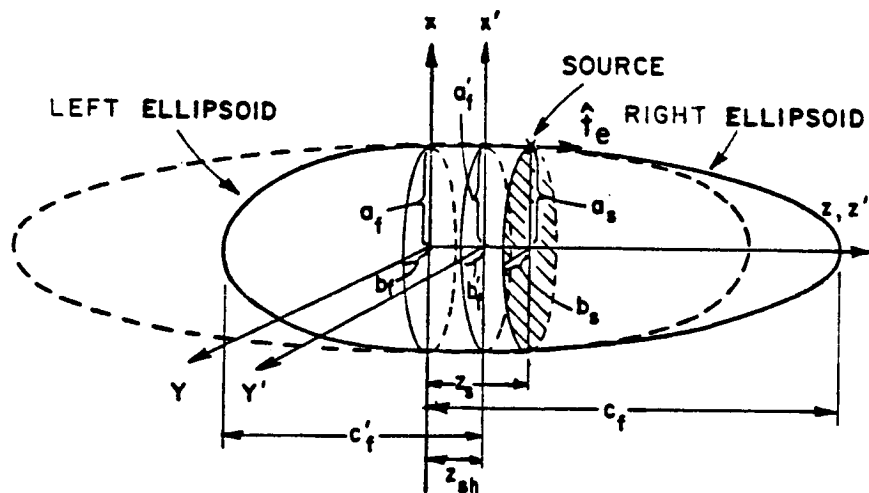
(b) Composite ellipsoid geometry.

Figure 3.3. Composite ellipsoid.

assumed here that both the right and left ellipsoid coordinate systems
are coincident. Then, the right side ellipsoid semi-major/minor axes
and the source location are defined as

$$(a_f, b_f, c_f, V_{es}, V_{rs}) = (a_0, b_0, c_0, V_{es}, V_{rs}) \tag{3.1}$$

where

$$V_{es} = \sin^{-1} \frac{z_s}{c_0} \quad \text{and} \quad V_{rs} = \frac{a_0 \sin\phi_s}{b_0 \cos\phi_s} \quad . \tag{3.2}$$

Now, one needs to define the parameters for the left side ellipsoid in
order to complete the composition. Since the surface of the composite
ellipsoid is continuous and smooth at the connection junction, the
geodesic tangents of both the right and left ellipsoids should be
continuous at the source location. For simplicity, let us consider the
connection in the the x-z plane first. Thus,

$$\hat{t}_e(a_f, b_f, c_f, V_{es}) = \hat{t}_e'(a_f', b_f', c_f', V_{es}') \tag{3.3}$$

with

$$\hat{t}_e(a_f, b_f, c_f, V_{es}) = \frac{-\hat{x} \, a_f \sin V_{es} + \hat{z} \, c_f \cos V_{es}}{[a_f^2 \, \sin^2 V_{es} + c_f^2 \, \cos^2 V_{es}]^{1/2}} \tag{3.4}$$

and

$$\hat{t}'_e(a'_f, b'_f, c'_f, V'_{es}) = \frac{-\hat{x} \, a'_f \, \sin V'_{es} + \hat{z} \, c'_f \, \cos V'_{es}}{[a'^2_f \, \sin^2 V'_{es} + c'^2_f \, \cos^2 V'_{es}]^{1/2}} \quad . \qquad (3.5)$$

From Equations (3.3) - (3.5) one obtains

$$\frac{a_f}{c_f} \tan V_{es} = \frac{a'_f}{c'_f} \tan V'_{es} \qquad (3.6)$$

with

$$c'_f = d_0 + z_{sh} \qquad (3.7)$$

where z_{sh} is the distance between the right and left ellipsoid coordinate origins as shown in Figure 3.3(b). Since the rim of the elliptic cross section at the source location is common to both the right and left ellipsoids, one can obtain the following relationships;

$$a_s = a_f \cos V_{es} = a'_f \cos V'_{es} \qquad (3.8)$$

and

$$b_s = b_f \cos V_{es} = b'_f \cos V'_{es} \quad . \qquad (3.9)$$

From Figure 3.3(b), one also finds that

$$c_f' \sin V_{es}' = z_s - z_{sh} \quad .$$

(3.10)

Now, from Equations (3.7) and (3.10) one obtains

$$z_{sh}(\sin V_{es}' + 1) = z_s - d_o \sin V_{es}' \quad ,$$

(3.11)

i.e.,

$$z_{sh} = \frac{z_s - d_o \sin V_{es}'}{1 + \sin V_{es}'} \quad .$$

(3.12)

After manipulation of Equations (3.3) - (3.12), the parameters needed to define the left ellipsoid are given by

$$V_{es}' = \sin^{-1} \left[\left[\frac{c_o \cos V_{es}}{\tan V_{es}(d_o + z_s)} + 1 \right]^{-1} \right] \quad ,$$

(3.13)

$$a_f' = \frac{a_o \cos V_{es}}{\cos V_{es}'} \quad ,$$

(3.14)

$$b_f' = \frac{b_o \cos V_{es}}{\cos V_{es}'} \quad ,$$

(3.15)

and c_f' was already given in Equation (3.7).

The smoothness through the whole elliptic rim at the connecting junction can be easily checked by applying Equations (3.6), (3.7), (3.14) and (3.15) to the x, y, and z components of $\hat{t}_e$ and $\hat{n}$, which will be given in Equations (3.24) and (3.26), respectively, for an arbitrary value of V_r. It is also noted that the two surfaces join together at the source location so creeping waves that propagate to the right side from the source will follow the geodesics on the right ellipsoid surface and those that propagate to the left side from the source will follow the geodesics on the left ellipsoid surface.

C. NUMERICAL TECHNIQUES FOR THE GEODESIC CALCULATION OF AN ELLIPSOID

It is seen that, for an antenna mounted on an ellipsoid, the geodesic paths associated with the UTD solution in the shadow region are extremely complex. An elaborate method employing calculus of variations to calculate the geodesic paths, which is very inefficient, is presented in Appendix A. An efficient numerical approach is examined in this section with the ellipsoid simulated by an elliptic cone or elliptic cylinder model. Since the elliptic cone and elliptic cylinder are developed surfaces, geodesics are efficiently obtained.

1. Surface Geodesics

The geodesics on the elliptic cylinder, elliptic cone and ellipsoid are presented in this section.

(a) Elliptic Cylinder Case:

The elliptic cylinder geometry used for this study is shown in Figure 3.4(a). Since the elliptic cylinder is a developed surface, the geodesic path $\overline{Q'Q}$ is a straight line on the unfolded planar surface as shown in Figure 3.4(b). Thus, the geodesic unit tangent $\hat{t}$ is given by

$$\hat{t} = \hat{V}_r \cos\gamma + \hat{z} \sin\gamma \tag{3.16}$$

where

$$\hat{V}_r = \frac{\hat{x}(-a \sin V_r) + \hat{y}b \cos V_r}{(a^2 \sin^2 V_r + b^2 \cos^2 V_r)^{1/2}} \quad . \tag{3.17}$$

It is noticed that $\hat{V}_r$ and $\hat{z}$ are the two principal directions on the elliptic cylinder surface. For a given geodesic $\overline{Q'Q}$, one can see that γ is a constant along the geodesic path.
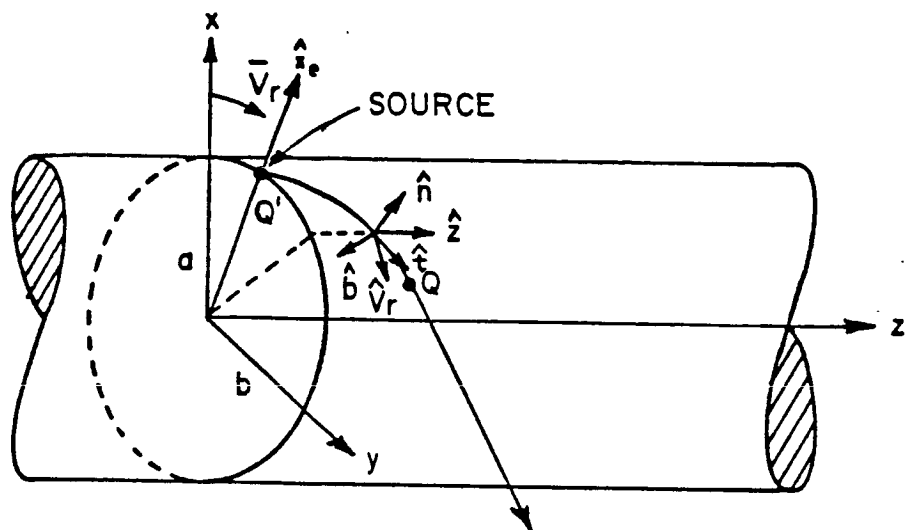
(a) TRUE ELLIPTIC CYLINDER
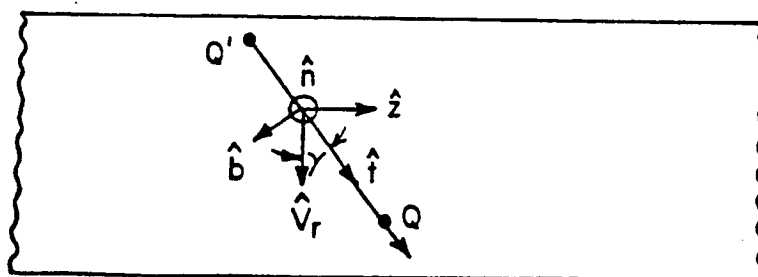
(b) UNFOLDED PLANAR SURFACE

Figure 3.4. Geodesic path on a developed elliptic cylinder.

(b) Elliptic Cone Case:

Consider a ray which propagates along a geodesic path $\overline{Q'Q}$ on the elliptic cone surface as shown in Figure 3.5(a). It is a straight line on the unfolded planar surface as shown in Figure 3.5(b). It is noticed that $\hat{t}_e$ and $\hat{t}_1$ are the two principal directions on the surface. The goedesic unit tangent $\hat{t}$ is, then, represented by

$$\hat{t} = \hat{t}_1 \cos\beta + \hat{t}_e \sin\beta \tag{3.18}$$

where

$$\hat{t}_e = -\hat{x}_e \sin\delta + \hat{z} \cos\delta \tag{3.19}$$

$$\hat{x}_e = \frac{\hat{x}a' \cos V_r + \hat{y}b' \sin V_r}{\sqrt{a'^2\cos^2V_r + b'\sin^2V_r}} \tag{3.20}$$

and δ is the half cone angle as shown in Figure 3.5(a). Note that β denotes the angle between $\hat{t}_1$ and the geodesic unit tangent $\hat{t}$ and is no longer a constant along the geodesic path $\overline{Q'Q}$.

(c) Ellipsoid Case:

Recall that the ellipsoid surface is defined by

$$\vec{R}(V_e,V_r) = a \cos V_e \cos V_r\hat{x} + b \cos V_e \sin V_r\hat{y} + c \sin V_e\hat{z} \tag{3.21}$$

with

(a) TRUE ELLIPTIC CONE

(b) UNFOLDED PLANAR SURFACE

Figure 3.5. Geodesic path on a developed elliptic cone.

$$\tan V_e = \frac{\cot \theta}{c \left[\frac{-\sin^2\phi}{b^2} + \frac{\cos^2\phi}{a^2} \right]^{1/2}} \tag{3.22}$$

and

$$\tan V_r = \frac{a \sin\phi}{b \cos\phi} \quad . \tag{3.23}$$

As shown in Figures 3.6(a) and (b), the unit vectors in the principal directions can be represented by

$$\hat{t}_e = \frac{\frac{\partial \vec{R}}{\partial V_e}}{\left| \frac{\partial \vec{R}}{\partial V_e} \right|} = \frac{-\hat{x}a \sin V_e \cos V_r - \hat{y}b \sin V_e \sin V_r + \hat{z}c \cos V_e}{[a^2\sin^2V_e\cos^2V_r + b^2\sin^2V_e\sin^2V_r + c^2\cos^2V_e]^{1/2}} \tag{3.24}$$

and

$$\hat{t}_1 = \hat{t}_e \times \hat{n}$$

$$= \frac{-\hat{x}a \sin V_r(b^2\sin^2V_e + c^2\cos^2V_e) + \hat{y}b \cos V_r(a^2\sin^2V_e + c^2\cos^2V_e)}{[a^2b^2\sin^2V_e + c^2\cos^2V_e(a^2\sin^2V_r + b^2\cos^2V_r)]^{1/2}}$$

$$+ \frac{\hat{z}c(b^2 - a^2) \sin V_r \cos V_r \sin V_e \cos V_e}{[c^2\cos^2V_e + \sin^2V_e(a^2\cos^2V_r + b^2\sin^2V_r)]^{1/2}} \tag{3.25}$$
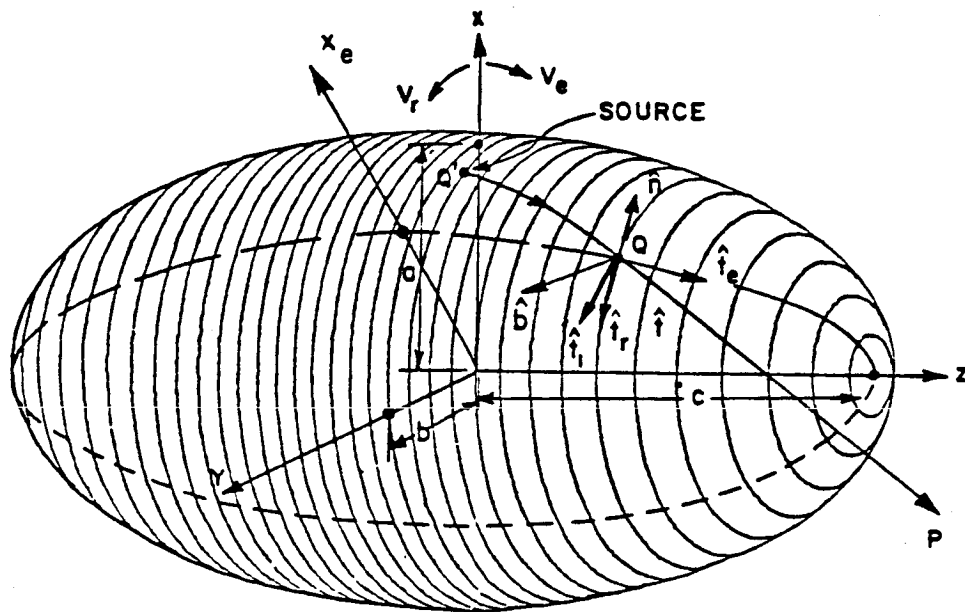
(a) Geodesic path on an ellipsoid.
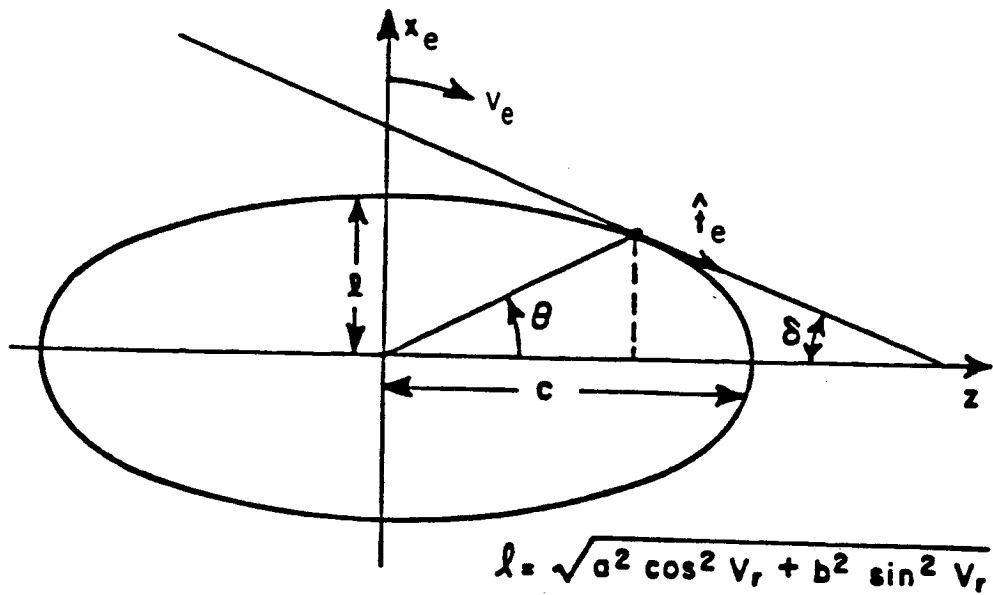
$$\ell = \sqrt{a^2 \cos^2 V_r + b^2 \sin^2 V_r}$$

(b) Elliptic profile.

Figure 3.6. Definition of the unit vectors on an ellipsoid.

with

$$\hat{n} = \frac{\hat{t}_r \times \hat{t}_e}{|\hat{t}_r \times \hat{t}_e|}$$

$$= \frac{\hat{x}bc\,\cos V_e\,\cos V_r + \hat{y}ac\,\cos V_e\,\sin V_r + \hat{z}ab\,\sin V_e}{[a^2 b^2 \sin^2 V_e + c^2 \cos^2 V_e (a^2 \sin^2 V_r + b^2 \cos^2 V_r)]^{1/2}} \qquad (3.26)$$

and

$$\hat{t}_r = \frac{\dfrac{\partial \vec{R}}{\partial V_r}}{\left|\dfrac{\partial \vec{R}}{\partial V_r}\right|} = \frac{-\hat{x}a\,\cos V_e\,\sin V_r + \hat{y}b\,\cos V_e\,\cos V_r}{[a^2 \cos^2 V_e\,\sin^2 V_r + b^2 \cos^2 V_e\,\cos^2 V_r]^{1/2}} \quad . \qquad (3.27)$$

If β denotes the angle between $\hat{t}_1$ and the geodesic unit tangent $\hat{t}$, then $\hat{t}$ is represented by

$$\hat{t} = \hat{t}_1 \cos\beta + \hat{t}_e \sin\beta \qquad (3.28)$$

which is identical to the form used for the elliptic cylinder and elliptic cone geodesics. This suggests that one might be able to develop a perturbation solution which gives a simplified form for β on an ellipsoid using the elliptic cylinder or elliptic cone expressions for β.

2. Elliptic Cylinder Perturbation

In order to solve for the geodesics on an ellipsoid, the elliptic cylinder perturbation technique is used when the source is located at or near $\theta_s = 90°$. Recalling that γ is a constant along a given geodesic path on an elliptic cylinder, one obtains a geodesic equation which is given by

$$\tan \gamma = \frac{S_e}{S_r} \quad . \tag{3.29}$$

The elliptic cross-section in the x_e - z plane is described by

$$x_e = \sqrt{a^2\cos^2 V_r + b^2\sin^2 V_r} \ \cos V_e \tag{3.30}$$

and

$$z = c \sin V_e \quad . \tag{3.31}$$

The arc length in the t_e direction is given by

$$S_e = \int_0^{V_e} \sqrt{\left(\frac{dx_e}{dV_e'}\right)^2 + \left(\frac{dz}{dV_e'}\right)^2} \ dV_e'$$

$$= \int_0^{V_e} \{c^2\cos^2 V_e' + (a^2\cos^2 V_r + b^2\sin^2 V_r) \sin^2 V_e'\}^{1/2} dV_e' \quad . \tag{3.32}$$

The elliptic cross-section in the x-y plane is described by

$$x = a \cos V_{es} \cos V_r \quad , \text{ and}$$
(3.33)

$$y = b \cos V_{es} \sin V_r \quad .$$
(3.34)

The arc length in the t_r direction is given by

$$S_r = \int_{V_{r_s}}^{V_r} \sqrt{\left(\frac{dx}{dV_r'}\right)^2 + \left(\frac{dy}{dV_r'}\right)^2} \; dV_r'$$

$$= \int_{V_{r_s}}^{V_r} \cos V_{es} \left\{ a^2 \sin^2 V_r' + b^2 \cos^2 V_r' \right\}^{1/2} dV_r' \quad .$$
(3.35)

Thus, the geodesic equation becomes

$$\tan \gamma = \frac{\displaystyle\int_{0}^{V_e} \left[(a^2 \cos^2 V_r + b^2 \sin^2 V_r) \sin^2 V_e' + c^2 \cos^2 V_e' \right]^{1/2} dV_e'}{\displaystyle\int_{V_{r_s}}^{V_r} \left[a^2 \cos^2 V_{es} \sin^2 V_r' + b^2 \cos^2 V_{es} \cos^2 V_r' \right]^{1/2} dV_r'} \quad .$$
(3.36)

Assuming the diffraction point is located at Q (a $\cos V_e \cos V_r$, b $\cos V_e \sin V_r$, c $\sin V_e$) and the field point at P ($R_t \sin \theta_t \cos \phi_t$, $R_t \sin \theta_t \sin \phi_t$, $R_t \cos \theta_t$), then at the diffraction point Q, the

63

radiation direction (θ_t, ϕ_t) should coincide with the geodesic tangent $\hat{t}$ given in Equation (3.28). Thus, the radiation direction is given by

$$\hat{t} = \hat{x}t_x + \hat{y}t_y + \hat{z}t_z$$

$$= \hat{t}_1 \cos\gamma + \hat{t}_e \sin\gamma \qquad , \tag{3.37}$$

where

$$t_x = \frac{\sin\theta_t \cos\phi_t - \dfrac{a}{R_t} \cos V_e \cos V_r}{D} \tag{3.38}$$

$$t_y = \frac{\sin\theta_t \sin\phi_t - \dfrac{b}{R_t} \cos V_e \cos V_r}{D} \tag{3.39}$$

and

$$t_z = \frac{\cos\theta_t - \dfrac{c}{R_t} \sin V_e}{D} \qquad . \tag{3.40}$$

Note that

$$D^2 = (\sin\theta_t \cos\phi_t - \frac{a}{R_t} \cos V_e \cos V_r)^2 + (\sin\theta_t \sin\phi_t$$

$$- \frac{b}{R_t} \cos V_e \sin V_r)^2 + (\cos\theta_t - \frac{c}{R_t} \sin V_e)^2$$

$$= 1 - 2 [\sin\theta_t \cos V_e (\frac{a}{R_t} \cos\phi_t \cos V_r + \frac{b}{R_t} \sin\phi_t \sin V_r)$$

$$+ \frac{c}{R_t} \cos\theta_t \sin V_e] + [\cos^2 V_e (\frac{a^2}{R_t^2} \cos^2 V_r + \frac{b^2}{R_t^2} \sin^2 V_r)$$

$$+ \frac{c^2}{R_t^2} \sin^2 V_e] \tag{3.41}$$

and $\hat{t}_e$ and $\hat{t}_1$ were given in Equations (3.24) and (3.25), respectively.
Equating the x-, y-, and z- cmponents, respectively, one obtains

$$t_x = \frac{- a \sin V_r \cos\gamma (b^2 \sin^2 V_e + c^2 \cos^2 V_e)}{[a^2 b^2 \sin^2 V_e + c^2 \cos^2 V_e (a^2 \sin^2 V_r + b^2 \cos^2 V_r)]^{1/2}}$$

$$\cdot \frac{1}{[c^2 \cos^2 V_e + \sin^2 V_e (a^2 \cos^2 V_r + b^2 \sin^2 V_r)]^{1/2}}$$

$$- \frac{a \sin V_e \cos V_r \sin\gamma}{[c^2 \cos^2 V_e + \sin^2 V_e (a^2 \cos^2 V_r + b^2 \sin^2 V_r)]^{1/2}}$$

$$= \frac{\sin\theta_t \cos\phi_t - \frac{a}{R_t} \cos V_e \cos V_r}{D} \quad , \tag{3.42}$$

$$t_y = \frac{b \cos V_r \cos\gamma (a^2 \sin^2 V_e + c^2 \cos^2 V_e)}{[a^2 b^2 \sin^2 V_e + c^2 \cos^2 V_e (a^2 \sin^2 V_r + b^2 \cos^2 V_r)]^{1/2}}$$

$$\cdot \frac{1}{[c^2 \cos^2 V_e + \sin^2 V_e (a^2 \cos^2 V_r + b^2 \sin^2 V_r)]^{1/2}}$$

$$- \frac{b \sin V_e \sin V_r \sin\gamma}{[c^2 \cos^2 V_e + \sin^2 V_e (a^2 \cos^2 V_r + b^2 \sin^2 V_r)]^{1/2}}$$

$$= \frac{\sin\theta_t \sin\phi_t - \dfrac{b}{R_t} \cos V_e \sin V_r}{D} , \qquad (3.43)$$

and

$$t_z = \frac{c(b^2 - a^2)\sin V_r \cos V_r \sin V_e \cos V_e \cos\gamma}{[a^2 b^2 \sin^2 V_e + c^2 \cos^2 V_e (a^2 \sin^2 V_r + b^2 \cos^2 V_r)]^{1/2}}$$

$$\cdot \frac{1}{[c^2 \cos^2 V_e + \sin^2 V_e (a^2 \cos^2 V_r + b^2 \sin^2 V_r)]^{1/2}}$$

$$+ \frac{c \cos V_e \sin\gamma}{[c^2 \cos^2 V_e + \sin^2 V_e (a^2 \cos^2 V_r + b^2 \sin^2 V_r)]^{1/2}}$$

$$= \frac{\cos\theta_t - \dfrac{c}{R_t} \sin V_e}{D} . \qquad (3.44)$$

66

Now, $[t_x b \cos V_r + t_y a \sin V_r] \, c \cos V_e + t_z \, ab \sin V_e$ yields

$H(\theta_t, \phi_t, V_e, V_r, R_t)$

$= ab \sin V_e \cos \theta_t + c \sin \theta_t \cos V_e (a \sin \phi_t \sin V_r + b \cos \phi_t \cos V_r)$

$$-\frac{abc}{R_t} = 0 \quad . \tag{3.45}$$

Next, from Equations (3.42) and (3.43) one obtains

$t_x (-b \sin V_r) + t_y (a \cos V_r)$:

$$\frac{ab \cos \gamma \{\sin^2 V_e (b^2 \sin^2 V_r + a^2 \cos^2 V_r) + c^2 \cos^2 V_e\}^{1/2}}{\{a^2 b^2 \sin^2 V_e + c^2 \cos^2 V_e (a^2 \sin^2 V_r + b^2 \cos^2 V_r)\}^{1/2}}$$

$$= \frac{1}{D} \{a \cos V_r \sin \theta_t \sin \phi_t - b \sin V_r \sin \theta_t \cos \phi_t\} \quad . \tag{3.46}$$

Accordingly,

$$\cos \gamma = [a^2 b^2 \sin^2 V_e + c^2 \cos^2 V_e (a^2 \sin^2 V_r + b^2 \cos^2 V_r)]^{1/2}$$

$$\cdot \frac{\sin \theta_t (a \cos V_r \sin \phi_t - b \sin V_r \cos \phi_t)}{D ab \{\sin^2 V_e (b^2 \sin^2 V_r + a^2 \cos^2 V_r) + c^2 \cos^2 V_e\}^{1/2}} \quad . \tag{3.47}$$

67

Substituting Equation (3.47) into Equation (3.44), one obtains

$$
\frac{\begin{aligned}
&[c(b^2-a^2)\sin V_r \cdot \cos V_r \, \sin V_e \, \cos V_e \, \sin\theta_t \\[4pt]
&\quad \cdot (a\cos V_r \, \sin\phi_t - b\sin V_r \, \cos\phi_t) \\[4pt]
&+ c\cos V_e \, \frac{S_e}{S_r} \, \sin\theta_t \, (a\cos V_r \, \sin\phi_t - b\sin V_r \, \cos\phi_t) \\[4pt]
&\quad \cdot \{a^2b^2\sin V_e + c^2\cos^2 V_e(a^2\sin^2 V_r + b^2\cos^2 V_r)\}^{1/2}]
\end{aligned}}{ab[c^2\cos^2 V_e + \sin^2 V_e(a^2\cos^2 V_r + b^2\sin^2 V_r)]}
$$

$$
= \cos\theta_t - \frac{c}{R_t}\sin V_e
$$

$$
\cdot \tag{3.48}
$$

Thus, one finds that

$$
\begin{aligned}
G(\theta_t,\phi_t,V_e,V_r,R_t) &= S_r \, c(b^2-a^2)\,\sin V_r \, \cos V_r \, \sin V_e \, \cos V_e \, \sin\theta_t \\[4pt]
&\quad \cdot (a\cos V_r \, \sin\phi_t - b\sin V_r \, \cos\phi_t) \\[4pt]
&\quad + S_e \, c\cos V_e \, [a^2b^2\sin^2 V_e + c^2\cos^2 V_e(a^2\sin^2 V_r + b^2\cos^2 V_r)]^{1/2} \\[4pt]
&\quad \cdot \sin\theta_t \, (a\cos V_r \, \sin\phi_t - b\sin V_r \, \cos\phi_t) \\[4pt]
&\quad - S_r \, ab\cos\theta_t \, [c^2\cos^2 V_e + \sin^2 V_e(a^2\cos^2 V_r + b^2\sin^2 V_r)] \\[4pt]
&\quad + \frac{S_r}{R_t} \, abc\,\sin V_e \, [c^2\cos^2 V_e + \sin^2 V_e(a^2\cos^2 V_r + b^2\sin^2 V_r)] \\[4pt]
&= 0 \; .
\end{aligned}
\tag{3.49}
$$

Note that S_e and S_r were given in Equations (3.32) and (3.35), respectively.

Provided that one has obtained a diffraction point (V_e, V_r) for a receiver location (R_t, θ_t, ϕ_t), a numerical technique can now be developed from Equations (3.45) and (3.49) to solve for $(V_e + \Delta V_e, V_r + \Delta V_r)$ associated with a new receiver location $(R_t + \Delta R_t, \theta_t + \Delta \theta_t, \phi_t + \Delta \phi_t)$. Assuming that the ith set of $(R_t, \theta_t, \phi_t, V_e, V_r)$ is first known to satisfy $H_i = G_i = 0$, or at least approximately so, the next set $(R_t + \Delta R_t, \theta_t + \Delta \theta_t, \phi_t + \Delta \phi_t, V_e + \Delta V_e, V_r + \Delta V_r)$ is obtained by enforcing $H_{i+1} = G_{i+1} = 0$, such that

$$H_{i+1} = H_i + H_{R_t} \Delta R_t + H_{\theta_t} \Delta \theta_t + H_{\phi_t} \Delta \phi_t +$$

$$H_{V_e} \Delta V_e + H_{V_r} \Delta V_r$$

$$= 0 \qquad\qquad (3.50)$$

and

$$G_{i+1} = G_i + G_{R_t} \Delta R_t + G_{\theta_t} \Delta \theta_t + G_{\phi_t} \Delta \phi_t +$$

$$+ G_{V_e} \Delta V_e + G_{V_r} \Delta V_r$$

$$\qquad\qquad (3.51)$$

$$= 0 \quad .$$

In matrix form, these equations are satisfied

$$
\begin{bmatrix} H_{V_e} & H_{V_r} \\ G_{V_e} & G_{V_r} \end{bmatrix} \begin{bmatrix} \Delta V_e \\ \Delta V_r \end{bmatrix} = \begin{bmatrix} -H_i - H_{R_t}\Delta R_t - H_{\theta_t}\Delta\theta_t - H_{\phi_t}\Delta\phi_t \\ -G_i - G_{R_t}\Delta R_t - G_{\theta_t}\Delta\theta_t - G_{\phi_t}\Delta\phi_t \end{bmatrix} \quad (3.52)
$$

Note that the partial derivatives are given by the following:

$$
H_{V_e} = ab \cos V_e \cos \theta_t - c \sin V_e \sin \theta_t (a \sin \phi_t \sin V_r + b \cos \phi_t \cos V_r) \quad (3.53)
$$

$$
H_{V_r} = c \cos V_e \sin \theta_t (a \sin \phi_t \cos V_r - b \cos \phi_t \sin V_r) \quad (3.54)
$$

$$
H_{\theta_t} = -ab \sin V_e \sin \theta_t + c \cos V_e \cos \theta_t (a \sin \phi_t \sin V_r + b \cos \phi_t \cos V_r) \quad (3.55)
$$

$$
H_{\phi_t} = c \cos V_e \sin \theta_t (a \cos \phi_t \sin V_r - b \sin \phi_t \cos V_r) \quad (3.56)
$$

$$
H_{R_t} = abc/R_t^2 \quad (3.57)
$$

$$G_{V_e} = S_r \ c(b^2-a^2) \ \sin V_r \cos V_r (\cos^2 V_e - \sin^2 V_e)$$

$$\cdot \ \sin\theta_t (a \ \cos V_r \ \sin\phi_t - b \ \sin V_r \ \cos\phi_t)$$

$$+ \frac{dS_e}{dV_e} \ c \ \cos V_e [a^2 b^2 \sin^2 V_e + c^2 \cos^2 V_e (a^2 \sin^2 V_r + b^2 \cos^2 V_r)]^{1/2}$$

$$\cdot \ \sin\theta_t (a \ \cos V_r \ \sin\phi_t - b \ \sin V_r \ \cos\phi_t)$$

$$+ S_e \ c \ \sin\theta_t (a \ \cos V_r \ \sin\phi_t - b \ \sin V_r \ \cos\phi_t) \sin V_e$$

$$\cdot \ \frac{a^2 b^2 (\cos^2 V_e - \sin^2 V_e) - 2c^2 \cos^2 V_e (a^2 \sin^2 V_r + b^2 \cos^2 V_r)}{[a^2 b^2 \sin^2 V_e + c^2 \cos^2 V_e (a^2 \sin^2 V_r + b^2 \cos^2 V_r)]^{1/2}}$$

$$+ 2 \ S_r \ ab \cos\theta_t \ \cos V_e \ \sin V_e \ (c^2 - a^2 \cos^2 V_r - b^2 \sin^2 V_r)$$

$$+ \frac{S_r}{R_t} \ abc \ \cos V_e [c^2 \ \cos^2 V_e + \sin^2 V_e (a^2 \cos^2 V_r + b^2 \sin^2 V_r)$$

$$+ 2\sin^2 V_e (a^2 \cos^2 V_r + b^2 \sin^2 V_r - c^2)]$$

$$(3.58)$$

where

$$\frac{dS_e}{dV_e} = \{c^2 \cos^2 V_e + (a^2 \cos^2 V_r + b^2 \sin^2 V_r) \sin^2 V_e\}^{1/2} \qquad ,$$

$$(3.59)$$

71

and

$$G_{V_r} = \{ \frac{dS_r}{dV_r} \sin V_r \cos V_r + S_r(\cos^2 V_r - \sin^2 V_r) \}$$

$$\cdot c(b^2 - a^2) \sin V_e \cos V_e \sin \theta_t (a \cos V_r \sin \phi_t - b \sin V_r \cos \phi_t)$$

$$- S_r c(b^2 - a^2) \sin V_r \cos V_r \sin V_e \cos V_e \sin \theta_t$$

$$\cdot (a \sin V_r \sin \phi_t + b \cos V_r \cos \phi_t) +$$

$$+ \frac{dS_e}{dV_r} c \cos V_e [a^2 b^2 \sin^2 V_e + c^2 \cos^2 V_e (a^2 \sin^2 V_r + b^2 \cos^2 V_r)]^{1/2}$$

$$\cdot \sin \theta_t (a \cos V_r \sin \phi_t - b \sin V_r \cos \phi_t)$$

$$+ \frac{S_e c^3 \cos^3 V_e (a^2 - b^2) \sin V_r \cos V_r \sin \theta_t (a \cos V_r \sin \phi_t - b \sin V_r \cos \phi_t)}{[a^2 b^2 \sin^2 V_e + c^2 \cos^2 V_e (a^2 \sin^2 V_r + b^2 \cos^2 V_r)]^{1/2}}$$

$$- S_e c \cos V_e [a^2 b^2 \sin^2 V_e + c^2 \cos^2 V_e (a^2 \sin^2 V_r + b^2 \cos^2 V_r)]^{1/2}$$

$$\cdot \sin \theta_t (a \sin V_r \sin \phi_t + b \cos V_r \cos \phi_t)$$

$$- \frac{dS_r}{dV_r} ab \cos \theta_t [c^2 \cos^2 V_e + \sin^2 V_e (a^2 \cos^2 V_r + b^2 \sin^2 V_r)]$$

$$+ 2S_r ab(a^2 - b^2) \cos \theta_t \sin^2 V_e \cos V_r \sin V_r$$

$$+ \frac{dS_r}{dV_r} \frac{abc}{R_t} \sin V_e [c^2 \cos^2 V_e + \sin^2 V_e (a^2 \cos^2 V_r + b^2 \sin^2 V_r)]$$

$$+ \frac{2S_r}{R_t} abc \sin^3 V_e (b^2 - a^2) \cos V_r \sin V_r \qquad (3.60)$$

72

where

$$\frac{dS_r}{dV_r} = \cos V_{es} \{a^2 \sin^2 V_r + b^2 \cos^2 V_r\}^{1/2} \quad , \tag{3.61}$$

and

$$\frac{dS_e}{dV_r} = \int_0^{V_e} \frac{(b^2-a^2) \sin V_r \cos V_r \sin^2 V_e'}{[c^2 \cos^2 V_e' + (a^2 \cos^2 V_r + b^2 \sin^2 V_r) \sin^2 V_e']^{1/2}} \, dV_e' \tag{3.62}$$

and

$$G_{\theta_t} = S_r c(b^2-a^2) \sin V_r \cos V_r \sin V_e \cos V_e \cos \theta_t$$

$$\cdot (a \cos V_r \sin \phi_t - b \sin V_r \cos \phi_t)$$

$$+ S_e c \cos V_e [a^2 b^2 \sin^2 V_e + c^2 \cos^2 V_e (a^2 \sin^2 V_r + b^2 \cos^2 V_r)]^{1/2}$$

$$\cdot \cos \theta_t (a \cos V_r \sin \phi_t - b \sin V_r \cos \phi_t)$$

$$+ S_r ab \sin \theta_t [c^2 \cos^2 V_e + \sin^2 V_e (a^2 \cos^2 V_r + b^2 \sin^2 V_r)] \tag{3.63}$$

$$G_{\phi_t} = S_r c(b^2-a^2) \sin V_r \cos V_r \sin V_e \cos V_e \sin \theta_t$$

$$\cdot (a \cos V_r \cos \phi_t - b \sin V_r \sin \phi_t)$$

$$+ S_e c \cos V_e [a^2 b^2 \sin^2 V_e + c^2 \cos^2 V_e (a^2 \sin^2 V_r + b^2 \cos^2 V_r)]^{1/2}$$

$$\cdot \sin \theta_t (a \cos V_r \cos \phi_t + b \sin V_r \sin \phi_t) \tag{3.64}$$

73

and

$$G_{R_t} = -\frac{S_r}{R_t^2} \, abc \, \sin V_e [c^2 \cos^2 V_e + \sin^2 V_e (a^2 \cos^2 V_r + b^2 \sin^2 V_r)] \; .$$

(3.65)

It is seen that one can solve for $(\Delta V_e, \Delta V_r)$, for a known $(\Delta R_t, \Delta \theta_t, \Delta \phi_t)$, using Equation (3.52). To determine the initial diffraction point (V_e, V_r) for a given receiver location (R_t, θ_t, ϕ_t), one can always assume a diffraction point at the source $(0, V_{rs})$ with the radiation direction $(\theta_f, \phi_f = \pm \pi/2)$ with respect to the source coordinate system $(\hat{t}_N, \hat{t}_r, \hat{t}_e)$ and gradually add increments $(\Delta R_t, \Delta \theta_t, \Delta \phi_t)$ until the desired receiver location (R_t, θ_t, ϕ_t) is reached as depicted in Figure 3.7.

In this process one can construct a cone where the rim of the cone is traced out by the receiver trajectory with the tip of the cone at the source point Q' and the cone axis aligned with $\hat{t}_e$. The half cone angle θ_f is given by

$$\theta_f = \tan^{-1} \left[\frac{\sqrt{|\hat{t}_N \cdot \vec{P}_{OS}|^2 + |\hat{t}_r \cdot \vec{P}_{OS}|^2}}{\hat{t}_e \cdot \vec{P}_{OS}} \right]$$

(3.66)

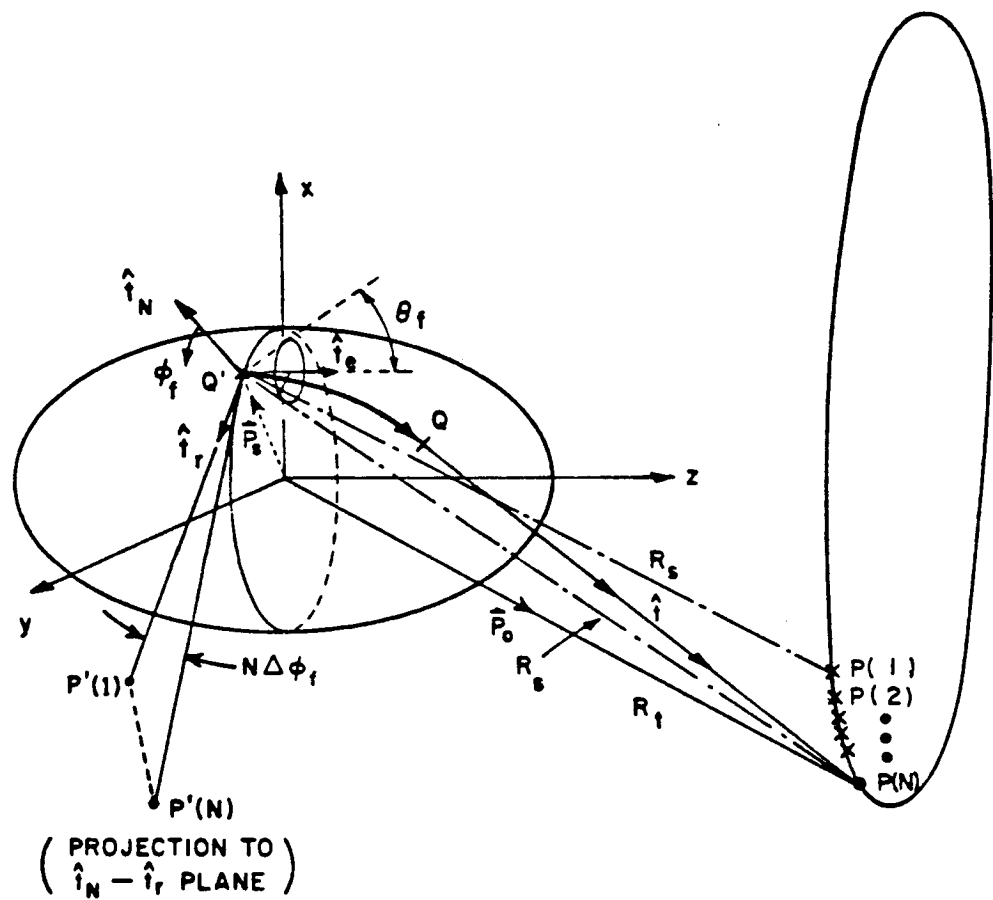with

$$\vec{P}_{OS} = \vec{P}_O - \vec{P}_S$$

(3.67)

74

Figure 3.7. Illustration of the diffraction point finding for a given receiver location.

and $\phi_f(N)$ is given by

$$\phi_f(N) = \tan^{-1}\left[\frac{\hat{t}_r \cdot \vec{P}_{OS}}{\hat{t}_N \cdot \vec{P}_{OS}}\right] \cdot \qquad (3.68)$$

Note that P(1) denotes the position vector of the assumed observation point tangential to the source, i.e., $(\theta_f, \phi_f = \pi/2)$ with respect to $(\hat{t}_N, \hat{t}_r, \hat{t}_e)$ and P(N) denotes the position vector of the actual observation point tangential to the diffraction point Q, i.e., $(\theta_f, \phi_f + N\Delta\phi_f)$ with respect to $(\hat{t}_N, \hat{t}_r, \hat{t}_e)$ or (θ_t, ϕ_t) with respect to $(\hat{x}, \hat{y}, \hat{z})$. It is observed that there exists a one-to-one correspondence between the points (from P(1) to P(N)) on the rim of the cone and the points on the ellipsoid surface.

After the initial diffraction point is identified by $(V_e, V_r); \gamma$, one knows the geodesic path as defined by the geodesic equation which was given by

$$\tan \gamma = \frac{S_e}{S_r} \qquad (3.69)$$

and γ is a constant along a given geodesic path on the perturbed elliptic cylinder. Such a numerical approach is illustrated in Figure 3.8. One need not trace out the complete geodesic path from the source location to the diffraction point for each new radiation direction. As
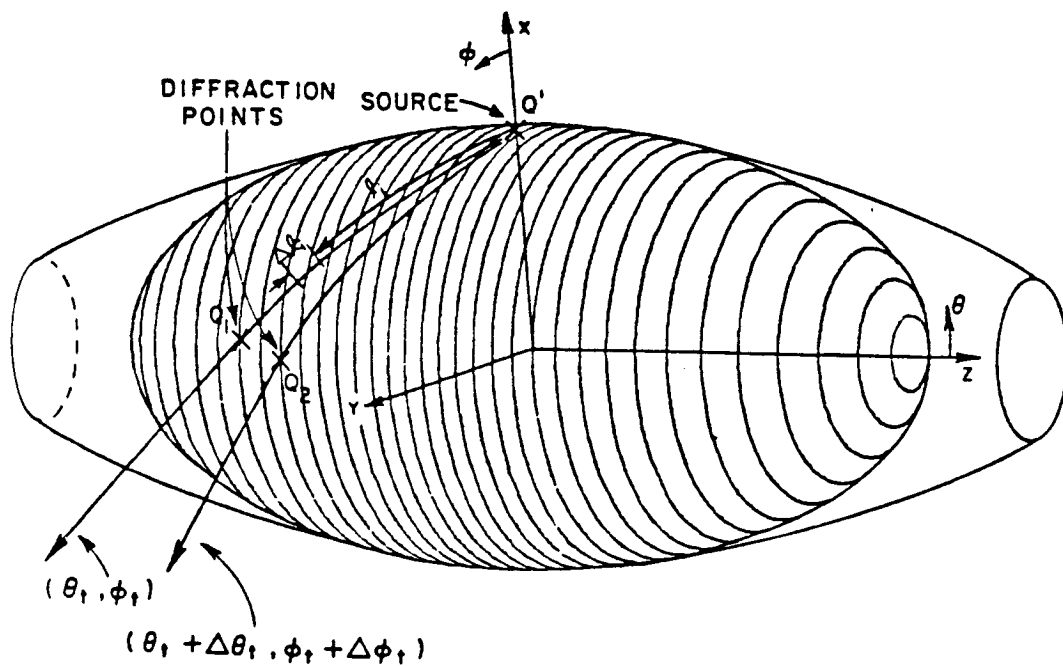
Figure 3.8. Elliptic cylinder perturbation.

shown in Figure 3.8, the diffraction point $(V_e + \Delta V_e, V_r + \Delta V_r)$ for the next receiver location is determined from (V_e, V_r), using Equation (3.52), if $(\Delta R_t, \Delta\theta_t, \Delta\phi_t)$ is small which is the case when a complete radiation pattern is computed.

After the geodesic path is determined, various other parameters associated with actual field calculations must be found. the Fock parameter ξ of Equation (2.15) is given by

$$\xi = \int_{Q'}^{Q} \frac{1}{\rho_g} \left(\frac{k\rho_g}{2}\right)^{1/3} d\ell \qquad , \qquad (3.70)$$

where the integral is evaluated along the geodesic path. Note that ℓ is the arc length along the geodesic and given by either of the following equations;

$$\ell = \frac{S_e}{\sin\gamma} \qquad \text{or} \qquad \ell = \frac{S_r}{\cos\gamma} \qquad . \qquad (3.71)$$

Accordingly,

$$d\ell = \frac{1}{\sin\gamma} \sqrt{(a^2\cos^2 V_r + b^2\sin^2 V_r)\sin^2 V_e + c^2\cos^2 V_e} \; dV_e \qquad (3.72)$$

or

$$d\ell = \frac{1}{\cos\gamma} \sqrt{a^2\cos^2 V_{es}\sin^2 V_r + b^2\cos^2 V_{es}\cos^2 V_r} \; dV_r \qquad (3.73)$$

78

and the integration can be rewritten as

$$\xi = \frac{1}{\cos\gamma} \int_{V_{r_s}}^{V_r} \frac{1}{\rho_g} \left(\frac{k\rho_g}{2}\right)^{1/3}$$

$$\cdot \sqrt{a^2\cos^2 V_{es} \sin^2 V_r' + b^2\cos^2 V_{es} \cos^2 V_r'} \quad dV_r' \tag{3.74}$$

or

$$\xi = \frac{1}{\sin\gamma} \int_0^{V_e} \frac{1}{\rho_g} \left(\frac{k\rho_g}{2}\right)^{1/3}$$

$$\cdot \sqrt{(a^2\cos^2 V_r + b^2\sin^2 V_r) \sin^2 V_e' + c^2\cos^2 V_e'} \quad dV_e' \tag{3.75}$$

where $\rho_g = 1/(K_1\cos^2\gamma + K_2\sin^2\gamma)$ and K_1, K_2 are two principal curvatures given in Equations (2.79) and (2.80), respectively.

Next, the ray divergence factor $\sqrt{d\psi_0(Q')/d\psi(Q)}$ is defined as the change in the separation of adjacent surface rays as shown in Figure 3.9. Since the ellipsoid simulating the aircraft fuselage will be long and slender, it is assumed that the ray divergence factor is unity in the analysis.

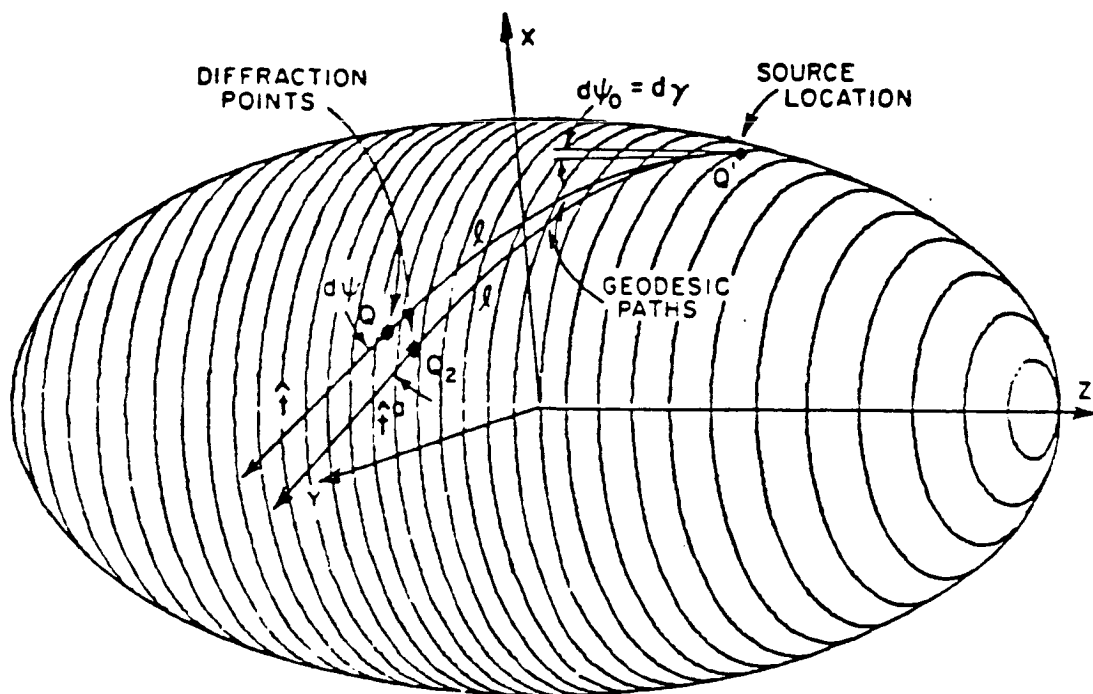This completes the elliptic cylinder perturbtion solution for an antenna mounted on the mid-section of the ellipsoid.

79

Figure 3.9. Illustration of the divergence factor ($\sqrt{d\psi_0/d\psi}$) terms.

3. Elliptic Cone Perturbation

When the source is not located at or near the mid-section ($\theta_s = 90°$), the elliptic cone perturbation method is used. The geodesic path on an ellipsoid using the elliptic cone perturbation method is shown in Figure 3.10(a) and the associated unfolded surface is shown in Figure 3.10(b). If γ and β denote the angle between $\hat{t}$ and $\hat{t}_1$ at Q' and Q, respectively, it was shown in Section III-C.1 that they are not the same as in the elliptic cylinder case. In fact,

$$\beta = \gamma - \alpha. \tag{3.76}$$

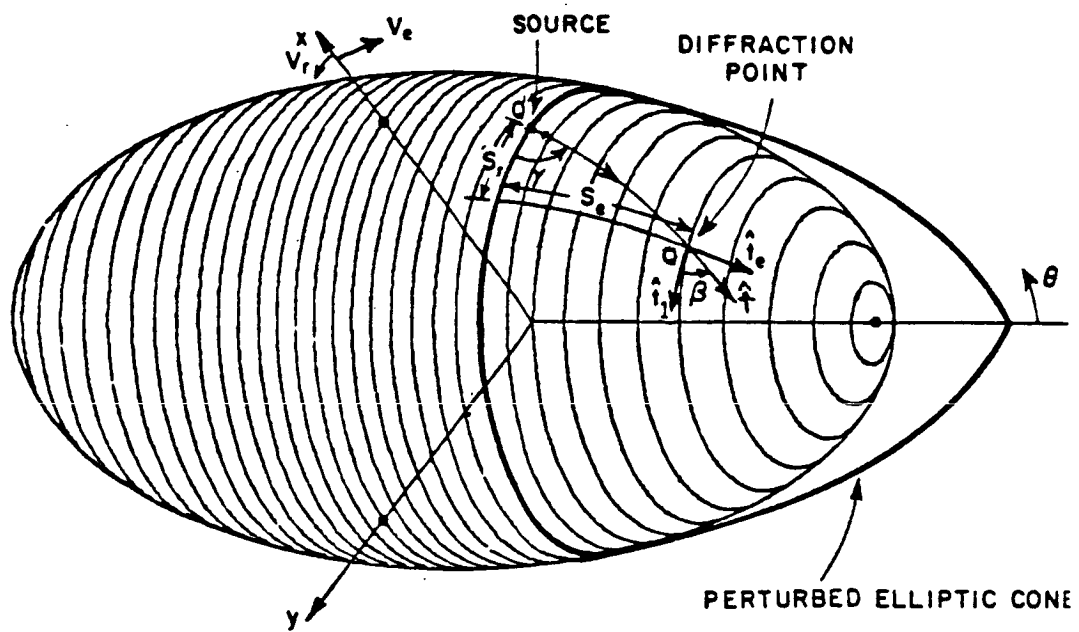The calculation of α will be discussed in detail in this section.

Recall that the ellipsoid surface is defined by

$$\vec{R}(V_e, V_r) = a \cos V_e \cos V_r \hat{x} + b \cos V_e \sin V_r \hat{y} + c \sin V_e \hat{z} \tag{3.77}$$
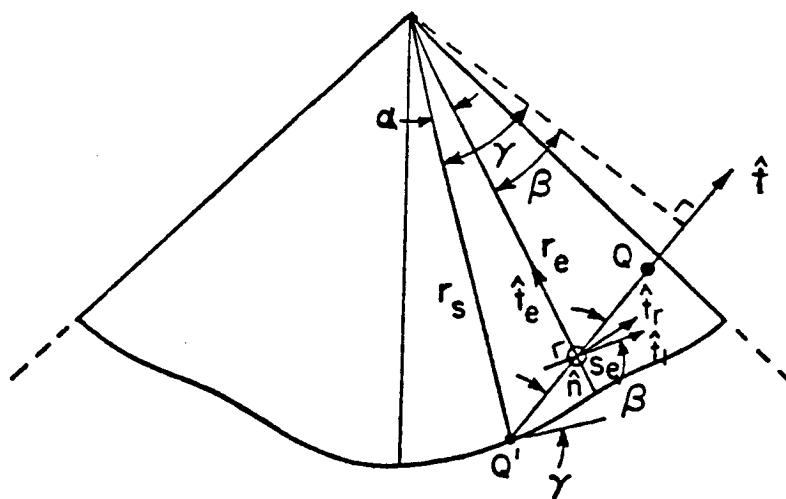
and the tangent vector $\vec{t}_e$ is defined by

$$\vec{t}_e = \frac{\partial \vec{R}}{\partial V_e} = -\hat{x} a \sin V_e \cos V_r - \hat{y} b \sin V_e \sin V_r + \hat{z} c \cos V_e \quad . \tag{3.78}$$

Therefore, one can show that

(a). Geodesic path on the perturbed elliptic cone.

(b). Geodesic path on a developed elliptic cone.

Figure 3.10. Illustration of the elliptic cone perturbation method.

c - 2

$$\frac{x-a\,\cos V_{es}\,\cos V_{rs}}{-a\,\sin V_{es}\,\cos V_{rs}} = \frac{y-b\,\cos V_{es}\,\sin V_{rs}}{-b\,\sin V_{es}\,\sin V_{rs}} = \frac{z-c\,\sin V_{es}}{c\,\cos V_{es}} \qquad . \qquad (3.79)$$

From Figure 3.11, $z = c\,\csc V_{es}$ for $x = y = 0$; thus one obtains

$$r_s = [a^2\cos^2 V_{es}\,\cos^2 V_{rs} + b^2\cos^2 V_{es}\,\sin^2 V_{rs}$$

$$+ (c\,\sin V_{es} - c\,\csc V_{es})^2]^{1/2}$$

$$= [a_s^2\,\cos^2 V_{rs} + b_s^2\,\sin^2 V_{rs} + z_s^2\,\cot^4 V_{es}]^{1/2} \qquad (3.80)$$

where

$$z_s = c\,\sin V_{es}$$

$$a_s = a\,\cos V_{es}$$

$$b_s = b\,\cos V_{es} \qquad .$$

From Figures 3.12(a) and (b),

$$\vec{\ell} = \hat{x}\,a_s\,\cos V_r + \hat{y}\,b_s\,\sin V_r \qquad (3.81)$$

and

$$\frac{\partial \vec{\ell}}{\partial V_r} = -\hat{x}\,a_s\,\sin V_r + \hat{y}\,b_s\,\cos V_r \qquad . \qquad (3.82)$$
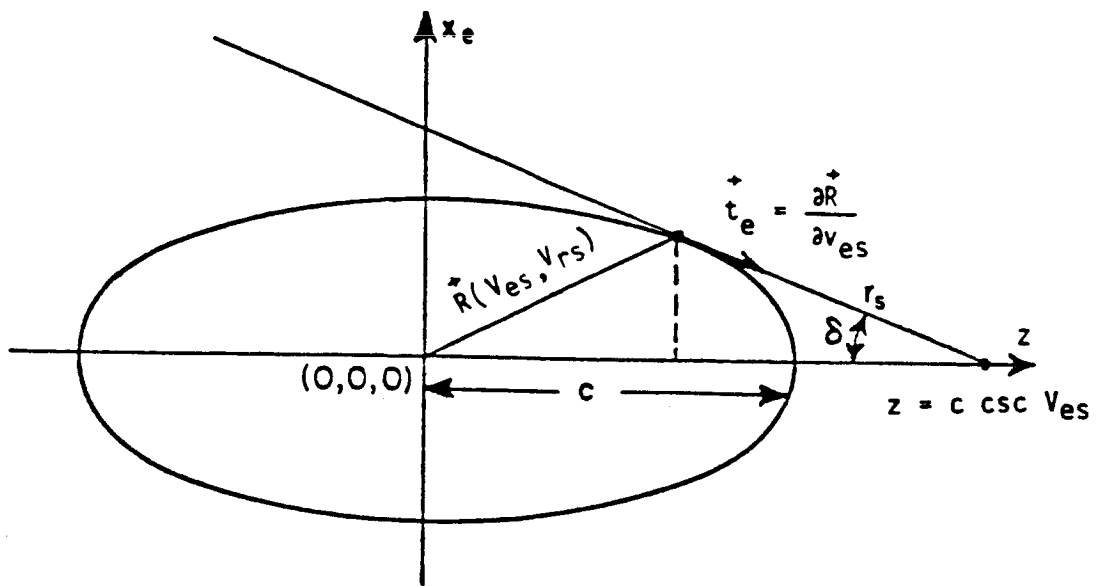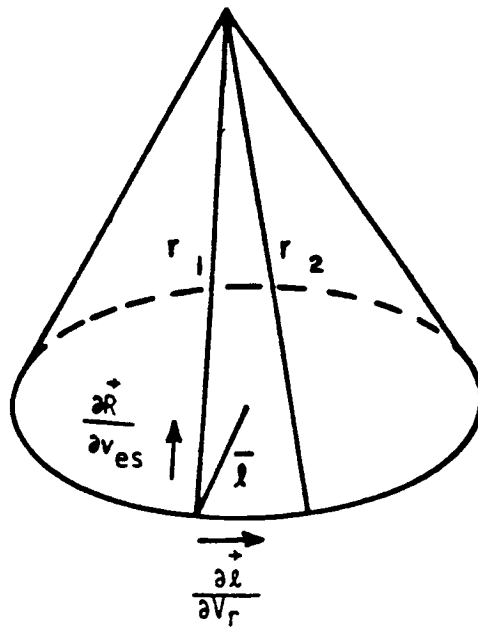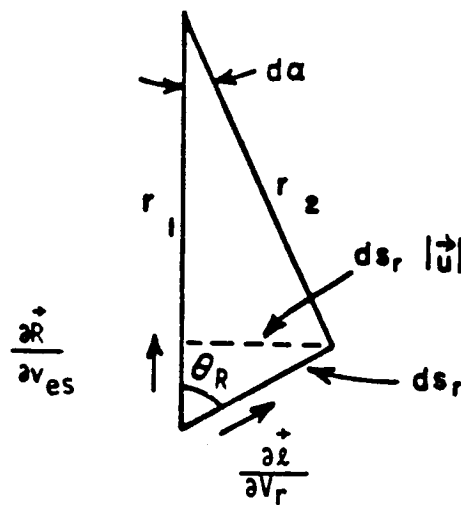
Figure 3.11. Elliptic profile.

(a). Elliptic cone model.

(b). Unfolded planar surface of the elliptic cone.

Figure 3.12. Illustration of the elliptic cone.

From the previous calculation, one can define a new vector $\vec{U}$ as follows:

$$\vec{U} = \left(\frac{\partial \vec{l}}{\partial V_r}\right) \times \left(\frac{\partial \vec{R}}{\partial V_{es}}\right)$$

$$= \frac{(-\hat{x}\, a\, \sin V_{es}\cos V_r - \hat{y}\, b\, \sin V_{es}\sin V_r + \hat{z}\, c\, \cos V_{es}) \cdot (-\hat{x}\, a_s\, \sin V_r + \hat{y}\, b_s\, \cos V_r)}{[a^2\sin^2 V_{es}\cos^2 V_r + b^2\sin^2 V_{es}\sin^2 V_r + c^2\cos^2 V_{es}]^{1/2} \cdot [a_s^2\sin^2 V_r + b_s^2\cos^2 V_r]^{1/2}}$$

$$= \frac{\hat{x}\, b_s\, c\, \cos V_{es}\cos V_r + \hat{y}\, a_s\, c\, \cos V_{es}\sin V_r + \hat{z}\, a_s\, b\, \sin V_{es}}{[a_s^2\sin^2 V_r + b_s^2\cos^2 V_r]^{1/2} \cdot [a^2\sin^2 V_{es}\cos^2 V_r + b^2\sin^2 V_{es}\sin^2 V_r + c^2\cos^2 V_{es}]^{1/2}}$$

(3.83)

The magnitude of vector $\vec{U}$ becomes

$$|\vec{U}| = \left| \frac{\widehat{\partial \vec{\ell}}}{\partial V_r} \right| \left| \frac{\widehat{\partial \vec{R}}}{\partial V_{es}} \right| \sin\theta_R = \sin\theta_R \qquad .$$

From Figure 3.12(b), one obtains the following equation;

$$d\alpha = \frac{ds_r |\vec{U}|}{r} \qquad . \qquad (3.85)$$

Therefore, α is given by

$$\alpha = \int_{V_{rs}}^{V_r}$$

$$\frac{\cos V_{es} \lfloor a^2 b^2 \sin^2 V_{es} + c^2 \cos^2 V_{es} \cdot (a^2 \sin^2 V_r' + b^2 \cos^2 V_r') \rfloor^{1/2} dV_r'}{r \lfloor c^2 \cos^2 V_{es} + \sin^2 V_{es} (a^2 \cos^2 V_r' + b^2 \sin^2 V_r') \rfloor^{1/2}}$$

$$= \int_{V_{rs}}^{V_r} \frac{\lfloor a_s^2 b_s^2 + z^2 \cos^4 V_{es} (a_s^2 \sin^2 V_r' + b_s^2 \cos^2 V_r') \rfloor^{1/2}}{a_s^2 \cos^2 V_r' + b_s^2 \sin^2 V_r' + z_s^2 \cot^4 V_{es}} dV_r' \quad , \qquad (3.86)$$

where

$$r = \lfloor a_s^2 \cos^2 V_r + b_s^2 \sin^2 V_r + z_s^2 \cot^4 V_{es} \rfloor^{1/2} \qquad . \qquad (3.87)$$

To obtain a diffraction point (V_e, V_r) for a radiation direction (θ_t, ϕ_t), one follows the same idea as that of the elliptic cylinder perturbation solution.

At the diffraction point Q, the radiation direction (θ_t, ϕ_t) should coincide with the geodesic tangent $\hat{t}$. Thus,

$$\hat{t} = \hat{x}\, t_x + \hat{y}\, t_y + \hat{z}\, t_z$$

$$= \hat{t}_1 \cos\beta + \hat{t}_e \sin\beta , \tag{3.88}$$

Note that t_x, t_y, t_z, t_e, and t_1 were already given in the Equations (3.38)-(3.40) and (3.24) and (3.25), respectively. Equating the x-, y-, and z-components, respectively, one obtains

$$t_x = \frac{-a \sin V_r \cos\beta (b^2 \sin^2 V_e + c^2 \cos^2 V_e)}{[a^2 b^2 \sin^2 V_e + c^2 \cos^2 V_e (a^2 \sin^2 V_r + b^2 \cos^2 V_r)]^{1/2}}$$

$$\cdot \frac{1}{[c^2 \cos^2 V_e + \sin^2 V_e (a^2 \cos^2 V_r + b^2 \sin^2 V_r)]^{1/2}}$$

$$- \frac{a \sin V_e \cos V_r \sin\beta}{[c^2 \cos^2 V_e + \sin^2 V_e (a^2 \cos^2 V_r + b^2 \sin^2 V_r)]^{1/2}}$$

$$= \frac{\sin\theta_t \cos\phi_t - \dfrac{a}{R_t} \cos V_e \cos V_r}{D} , \tag{3.89}$$

$$t_y = \frac{b \cos V_r \cos\beta (a^2 \sin^2 V_e + c^2 \cos^2 V_e)}{[a^2 b^2 \sin^2 V_e + c^2 \cos^2 V_e (a^2 \sin^2 V_r + b^2 \cos^2 V_r)]^{1/2}}$$

$$\cdot \frac{1}{[c^2 \cos^2 V_e + \sin^2 V_e (a^2 \cos^2 V_r + b^2 \sin^2 V_r)]^{1/2}}$$

$$- \frac{b \sin V_e \sin V_r \sin\beta}{[c^2 \cos^2 V_e + \sin^2 V_e (a^2 \cos^2 V_r + b^2 \sin^2 V_r)]^{1/2}}$$

$$= \frac{\sin\theta_t \cos\phi_t - \dfrac{b}{R_t} \cos V_e \sin V_r}{D} \quad , \qquad (3.90)$$

and

$$t_z = \frac{c(b^2 - a^2) \sin V_r \cos V_r \cos V_e \cos\beta}{[a^2 b^2 \sin^2 V_e + c^2 \cos^2 V_e (a^2 \sin^2 V_r + b^2 \cos^2 V_r)]^{1/2}}$$

$$\cdot \frac{1}{[c^2 \cos^2 V_e + \sin^2 V_e (a^2 \cos^2 V_r + b^2 \sin^2 V_r)]^{1/2}}$$

$$+ \frac{c \cos V_e \sin\beta}{[c^2 \cos^2 V_e + \sin^2 V_e (a^2 \cos^2 V_r + b^2 \sin^2 V_r)]^{1/2}}$$

$$= \frac{\cos\theta_t - \dfrac{c}{R_t} \sin V_e}{D} \quad . \qquad (3.91)$$

From Figure 3.10(b), one can show that the perturbed geodesic path can be expressed as follows:

$$r_e \cos(\gamma - \alpha) = r_s \cos\gamma \qquad (3.92)$$

where

$$r_s = (a_s^2 \cos^2 V_{rs} + b_s^2 \sin^2 V_{rs} + z_s^2 \cot^4 V_{es})^{1/2} \quad , \qquad (3.93)$$

$$r_e = (a_s^2 \cos^2 V_r + b_s^2 \sin^2 V_r + z_s^2 \cot^4 V_{es})^{1/2} - S_e \quad , \qquad (3.94)$$

and

$$S_e = \int_{V_{es}}^{V_e} [c^2 \cos^2 V_e' + (a^2 \cos^2 V_r + b^2 \sin^2 V_r)\sin^2 V_e']^{1/2} dV_e' \quad . \qquad (3.95)$$

Now, $[t_x(-b \sin V_r) + t_y \, a \cos V_r]$ yields

$$\frac{ab \cos(\gamma - \alpha) [c^2 \cos^2 V_e + \sin^2 V_e (a^2 \cos^2 V_r + b^2 \sin^2 V_r)]^{1/2}}{[a^2 b^2 \sin^2 V_e + c^2 \cos^2 V_e (a^2 \sin^2 V_r + b^2 \cos^2 V_r)]^{1/2}}$$

$$= \frac{\sin \theta_t \, (a\cos V_r \, \sin\phi_t - b\sin V_r \, \cos\phi_t)}{D} \quad . \qquad (3.96)$$

Next, $[(t_x \ b \ \cos V_r + t_y \ a \ \sin V_r) \ c \ \cos V_e + t_z \ a \ b \ \sin V_e]$ yields

$$\frac{ab\sin V_e \ \cos\theta_t + c\sin\theta_t \ \cos V_e \ (a\sin\phi_t\sin V_r + b\cos\phi_t\cos V_r)}{D}$$

$$-\frac{abc}{DR_t} = 0 \qquad . \qquad\qquad (3.97)$$

Three functions can, then, be constructed from Equations (3.92), (3.96), and (3.97) as follows:

$$F(V_e, V_r, \gamma) = r_e\cos(\gamma-\alpha) - r_s\cos\gamma = 0 \quad , \qquad\qquad (3.98)$$

$$G(R_t, \ \theta_t, \ \phi_t, \ V_e, \ V_r, \ \gamma)$$

$$= Dabc\cos(\gamma-\alpha)[c^2\cos^2 V_e + \sin^2 V_e(a^2\cos^2 V_r + b^2\sin^2 V_r)]^{1/2}$$

$$- \sin\theta_t \ (a\sin\phi_t \ \cos V_r - b\cos\phi_t \ \sin V_r)$$

$$\cdot \ [a^2b^2\sin^2 V_e + c^2\cos^2 V_e \ (a^2\sin^2 V_r + b^2\cos^2 V_r)]^{1/2}$$

$$= 0 \qquad\qquad (3.99)$$

and

$$H(R_t, \ \theta_t, \ \phi_t, \ V_e, \ V_r)$$

$$= ab\sin V_e \ \cos\theta_t + c\sin\theta_t \ \cos V_e \ (a\sin\phi_t \ \sin V_r + b\cos\phi_t \ \cos V_r)$$

$$-\frac{abc}{R_t} = 0 \quad . \qquad\qquad (3.100)$$

91

Provided that one has obtained a diffraction point (V_e, V_r) for a receiver location (R_t, θ_t, ϕ_t), a numerical technique can now be developed from Equations (3.90), (3.99), and (3.100) to solve for $(V_e + \Delta V_e, V_r + \Delta V_r)$ associated with a new receiver location $(R_t + \Delta R_t, \theta_t + \Delta \theta_t, \phi_t + \Delta \phi_t)$. Assuming that the ith set of $(R_t, \theta_t, \phi_t, V_e, V_r)$ is first known to satisfy $F_i = H_i = G_i = 0$, or at least approximately so, the next set $(R_t + \Delta R_t, \theta_t + \Delta \theta_t, \phi_t + \Delta \phi_t, V_e + \Delta V_e, V_r + \Delta V_r)$ is obtained by enforcing $F_{i+1} = H_{i+1} = G_{i+1} = 0$, such that

$$F_{i+1} = F_i + F_{V_e} \Delta V_e + F_{V_r} \Delta V_r + F_\gamma \Delta \gamma = 0 \quad , \tag{3.101}$$

$$G_{i+1} = G_i + G_{V_e} \Delta V_e + G_{V_r} \Delta V_r + G_\gamma \Delta \gamma$$
$$+ G_{\theta_t} \Delta \theta_t + G_{\phi_t} \Delta \phi_t + G_{R_t} \Delta R_t = 0 \quad , \tag{3.102}$$

and

$$H_{i+1} = H_i + H_{V_e} \Delta V_e + H_{V_r} \Delta V_r + H_{\theta_t} \Delta \theta_t$$
$$+ H_{\phi_t} \Delta \phi_t + H_{R_t} \Delta R_t = 0 \quad . \tag{3.103}$$

In matrix form, these equations are satisfied by

$$
\begin{bmatrix}
F_{V_e} & F_{V_r} & F_\gamma \\
G_{V_e} & G_{V_r} & G_\gamma \\
H_{V_e} & H_{V_r} & 0
\end{bmatrix}
\begin{bmatrix}
\Delta V_e \\
\Delta V_r \\
\Delta \gamma
\end{bmatrix}
=
\begin{bmatrix}
-F_i \\
-G_i - G_{\theta_t}\Delta\theta_t - G_{\phi_t}\Delta\phi_t - G_{R_t}\Delta R_t \\
-H_i - H_{\theta_t}\Delta\theta_t - H_{\phi_t}\Delta\phi_t - H_{R_t}\Delta R_t
\end{bmatrix} .
$$

(3.104)

Note that the partial derivations are given by the following:

$$
F_{V_e} = -[c^2\cos^2 V_e + (a^2\cos^2 V_r + b^2\sin^2 V_r)\sin^2 V_e]^{1/2}\cos(\gamma-\alpha) , \quad (3.105)
$$

$$
F_{V_r} = (b^2-a^2)\,\sin V_r \cos V_r \left[\frac{\cos^2 V_{es}}{(a_s^2\cos^2 V_r + b_s^2\sin^2 V_r + z_s^2\cot^4 V_{es})^{1/2}} \right.
$$

$$
\left. - \int_{V_{es}}^{V_e} \frac{\sin^2 V_e'}{[c^2\cos^2 V_e' + (a^2\cos^2 V_r + b^2\sin^2 V_r)\sin^2 V_e']^{1/2}}\, dV_e' \right] \cos(\gamma-\alpha)
$$

$$
+ \frac{r_e\sin(\gamma-\alpha)[a_s^2 b_s^2 + Z_s^2\cot^4 V_{es}\,(a_s^2\sin^2 V_r + b_s^2\cos^2 V_r)]^{1/2}}{a_s^2\cos^2 V_r + b_s^2\sin^2 V_r + Z_s^2\cot^4 V_{es}}
$$

(3.106)

93

$$F_\gamma = r_s \sin \gamma - r_e \sin (\gamma-\alpha) \quad ,$$

(3.107)

and

$$G_{V_e} = \frac{Dab(a^2\cos^2 V_r + b^2\sin^2 V_r - c^2)\sin V_e \cos V_e \cos(\gamma-\alpha)}{[c^2\cos^2 V_e + (a^2\cos^2 V_r + b^2\sin^2 V_r)\sin^2 V_e]^{1/2}}$$

$$- \frac{\sin\theta_t(a\sin\phi_t\cos V_r - b\cos\phi_t\sin V_r)[a^2b^2 - (a^2\sin^2 V_r + b^2\cos^2 V_r)c^2]\sin V_e\cos V_e}{[(a^2\sin^2 V_r + b^2\cos^2 V_r)c^2\cos^2 V_e + a^2b^2\sin^2 V_e]^{1/2}}$$

$$+ \frac{ab\cos(\gamma-\alpha)}{D}[c^2\cos^2 V_e + (a^2\cos^2 V_r + b^2\sin^2 V_r)\sin^2 V_e]^{1/2}$$

$$\cdot \left[\frac{c^2 - (a^2\cos^2 V_r + b^2\sin^2 V_r)}{R_t^2}\sin V_e\cos V_e \right.$$

$$\left. + \sin\theta_t\sin V_e(\frac{a}{R_t}\cos\phi_t\cos V_r + \frac{b}{R_t}\sin\phi_t\sin V_r) - \frac{c}{R_t}\cos\theta_t\cos V_e \right]$$

(3.108)

94

$$G_{V_r} = \frac{Dab\,\cos(\gamma-\alpha)(b^2-a^2)\sin V_r\,\cos V_r\,\sin^2 V_e}{[c^2\cos^2 V_e+(a^2\cos^2 V_r+b^2\sin^2 V_r)\sin^2 V_e]^{1/2}}$$

$$+ \,Dab[c^2\cos^2 V_e+(a^2\cos^2 V_r+b^2\sin^2 V_r)\sin^2 V_e]^{1/2}\,\sin(\gamma-\alpha)$$

$$\cdot\,\frac{[a_s^2 b_s^2+Z_s^2\cot^4 V_{es}(a_s^2\sin^2 V_r+b_s^2\cos^2 V_r)]^{1/2}}{a_s^2\cos^2 V_r+b_s^2\sin^2 V_r+Z_s^2\cot^4 V_{es}}$$

$$+ \,\frac{\sin\theta_t(a\sin\phi_t\cos V_r-b\cos\phi_t\sin V_r)(b^2-a^2)\sin V_r\cos V_r c^2\cos^2 V_e}{[(a^2\sin^2 V_r+b^2\cos^2 V_r)c^2\cos^2 V_e+a^2 b^2\sin^2 V_e]^{1/2}}$$

$$+ \,\sin\theta_t(a\sin\phi_t\sin V_r+b\cos\phi_t\cos V_r)[(a^2\sin^2 V_r+b^2\cos^2 V_r)$$

$$\cdot\,c^2\cos^2 V_e+a^2 b^2\sin^2 V_e]^{1/2}$$

$$+ \,\frac{ab\cos(\gamma-\alpha)}{D}\{c^2\cos^2 V_e+(a^2\cos^2 V_r+b^2\sin^2 V_r)\sin^2 V_e\}^{1/2}$$

$$\cdot\,\{\frac{(b^2-a^2)}{R_t^2}\sin V_r\cos V_r\cos^2 V_e-\sin\theta_t\cos V_e\,(\frac{b}{R_t}\sin\phi_t\cos V_r$$

$$- \,\frac{a}{R_t}\cos\phi_t\sin V_r)\,\}\qquad\qquad, \qquad (3.109)$$

$$G_\gamma = -Dab\sin(\gamma-\alpha)[c^2\cos^2 V_e+(a^2\cos^2 V_r+b^2\sin^2 V_r)\sin^2 V_e]^{1/2}$$

$$(3.110)$$

$$G_{\theta_t} = - \cos\theta_t(a\sin\phi_t\cos V_r - b\cos\phi_t\sin V_r)$$

$$\cdot \left[(a^2\sin^2 V_r + b^2\cos^2 V_r)c^2\cos^2 V_e + a^2 b^2\sin^2 V_e\right]^{1/2}$$

$$+ \frac{ab\cos(\gamma-\alpha)}{D}\left[c^2\cos^2 V_e + (a^2\cos^2 V_r + b^2\sin^2 V_r)\sin^2 V_e\right]^{1/2}$$

$$\cdot \left\{\frac{c}{R_t}\sin\theta_t\sin V_e - \cos\theta_t\cos V_e\left(\frac{a}{R_t}\cos\phi_t\cos V_r + \frac{b}{R_t}\sin\phi_t\sin V_r\right)\right\} ,$$

$$(3.111)$$

$$G_{\phi_t} = - \sin\theta_t(a\cos\phi_t\cos V_r + b\sin\phi_t\sin V_r)$$

$$\cdot \left[(a^2\sin^2 V_r + b^2\cos^2 V_r)c^2\cos^2 V_e + a^2 b^2\sin^2 V_e\right]^{1/2}$$

$$+ \frac{ab\cos(\gamma-\alpha)}{D}\left[c^2\cos^2 V_e + (a^2\cos^2 V_r + b^2\sin^2 V_r)\sin^2 V_e\right]^{1/2}$$

$$\cdot \left\{\sin\theta_t\cos V_e\left(\frac{a}{R_t}\sin\phi_t\cos V_r - \frac{b}{R_t}\cos\phi_t\sin V_r\right)\right\} , \qquad (3.112)$$

$$G_{R_t} = \frac{ab}{D}\cos(\gamma-\alpha)\left[c^2\cos^2 V_e + (a^2\cos^2 V_r + b^2\sin^2 V_r)\sin^2 V_e\right]^{1/2}$$

$$\cdot \left\{[\sin\theta_t\cos V_e(a\cos\phi_t\cos V_r + b\sin\phi_t\sin V_r) + c\cos\theta_t\sin V_e]/R_t^2\right.$$

$$\left. - [\cos^2 V_e(a^2\cos^2 V_r + b^2\sin^2 V_r) + c^2\sin^2 V_e]/R_t^3\right\} , \qquad (3.113)$$

$$H_{V_e} = ab \cos V_e \cos \theta_t - c \sin V_e \sin \theta_t (a \sin \phi_t \sin V_r + b \cos \phi_t \cos V_r) \tag{3.114}$$

$$H_{V_r} = c \cos V_e \sin \theta_t (a \sin \phi_t \cos V_r - b \cos \phi_t \sin V_r) \tag{3.115}$$

$$\tag{3.116}$$

$$H_\gamma = 0$$

$$H_\theta = -ab \sin V_e \sin \theta_t + c \cos V_e \cos \theta_t (a \sin \phi_t \sin V_r + b \cos \phi_t \cos V_r) \tag{3.117}$$

$$H_{\phi_t} = c \cos V_e \sin \theta_t (a \cos \phi_t \sin V_r - b \sin \phi_t \cos V_r) \tag{3.118}$$

and

$$H_{R_t} = \frac{abc}{R_t^2} \cdot \tag{3.119}$$

It is seen that one can solve for $(\Delta V_e, \Delta V_r, \Delta \gamma)$, for a known $(\Delta R_t, \Delta \theta_t, \Delta \phi_t)$, using Equation (3.104). To obtain a diffraction point (V_e, V_r) for a given receiver location (R_t, θ_t, ϕ_t), one can always assume the first diffraction point is at the source $(V_e, V_r) = (V_{es}, V_{rs})$ with the radiation direction $(\theta_f, \phi_f = \frac{\pi}{2})$ for the positive ray (in $+\hat{y}$ direction) or $(\theta_f, \phi_f = \frac{3}{2}\pi)$ for a negative ray (in $-\hat{y}$ direction), and gradually add the increments $(\Delta R_t, \Delta \theta_t, \Delta \phi_t)$ until the final radiation direction (θ_t, ϕ_t) is reached. The detailed description on this process was already given for the elliptic cylinder perturbation in Section III-C.2. One need not start out from the source everytime, but obtain the new diffraction point directly from Equation (3.104), provided that the new receiver location does not deviate greatly from the previous direction.

After the geodesic path is determined by this procedure, various other parameters associated with actual field calculations must be found. The Fock parameter ξ is given by

$$\xi = \int_{Q'}^{Q} \frac{1}{\rho_g} \left(\frac{k\rho_g}{2}\right)^{1/3} d\ell \quad .$$ (3.120)

From Figure 3.10(b), the geodesic arc length is obtained as follows:

$$\ell \cos\gamma = (r - S_e) \sin\alpha \quad .$$ (3.121)

or

$$\ell \sin\gamma = r_s - (r - S_e) \cos\alpha \quad .$$ (3.122)

Therefore,

$$d\ell = \frac{r_s \cos\gamma}{\cos^2(\gamma-\alpha)} \, d\alpha \quad ,$$ (3.123)

or

$$d\ell = \frac{1}{\sin(\gamma-\alpha)} \frac{dS_e}{dV_e} \cdot dV_e \quad .$$ (3.124)

98

The Fock parameter ξ is obtained by integrating along V_r or V_e, i.e.,

$$\xi = r_s \cos\gamma \int_0^\alpha \frac{1}{\rho_g} \left(\frac{k\rho_g}{2}\right)^{1/3} \frac{1}{\cos^2(\gamma-\alpha')} \, d\alpha'$$

$$= r_s \cos\gamma \int_{V_{rs}}^{V_r} \frac{1}{\rho_g} \left(\frac{k\rho_g}{2}\right)^{1/3} \frac{1}{\cos^2(\gamma-\alpha)} \frac{d\alpha}{dV_r'} \, dV_r' \qquad (3.125)$$

where

$$\frac{d\alpha}{dV_r'} = \frac{\left[a_s^2 b_s^2 + z_s^2 \cot^4 V_{es}(a_s^2 \sin^2 V_r' + b_s^2 \cos^2 V_r')\right]^{1/2}}{a_s^2 \cos^2 V_r' + b_s^2 \sin^2 V_r' + z_s^2 \cot^4 V_{es}} \qquad (3.126)$$

or

$$\xi = \int_{V_{es}}^{V_s} \frac{1}{\rho_g} \left(\frac{k\rho_g}{2}\right)^{1/3} \frac{1}{\sin(\gamma-\alpha)} \frac{dS_e}{dV_e'} \, dV_e' \qquad . \qquad (3.127)$$

Note that $\rho_g = 1/(K_1 \cos^2\beta + K_2 \sin^2\beta)$ and K_1, K_2 are two principal curvatures given in Equations (2.79) and (2.80), respectively.

This completes the elliptic cone perturbation solution for the antenna mounted off the mid section of the ellipsoid.

4. Comparison with Exact Solution

Geodesics for a source mounted on an ellipsoid can be analyzed precisely by computing the geodesic path defined by the surface parameters (θ_Q, ϕ_Q) and the geodesic tangent defined by the radial vector direction (θ_t, ϕ_t) as shown in Figures 3.13(a) and (b), respectively. The geodesic path indicates the actual diffraction point location on an ellipsoid; whereas, the geodesic tangent indicates the radiation direction at the corresponding diffraction point.

In order to show the validity of the perturbation solutions, a more elaborate numerical method for the geodesics employing calculus of variations, whose results are indicated as exact solutions here, is also studied and derived in Appendix A. Although this method provides accurate geodesics on the ellipsoid, it is far too complicated and inefficient to use for practical radiation applications. However, the exact solution is most appropriate for coupling problems where the exact path is desired between two known points on the surface.

To show the validity of the elliptic cylinder perturbation solution, the source is placed at $\theta_s = 90°$ and the geodesic paths and geodesic tangents associated with this source location are calculated as shown in Figures 3.14(a) and (b), respectively. In each figure, the elliptic cylinder perturbation solutions are compared with the exact solutions. Note that the $4\lambda \times 6\lambda \times 40\lambda$ ellipsoid was chosen for more

100
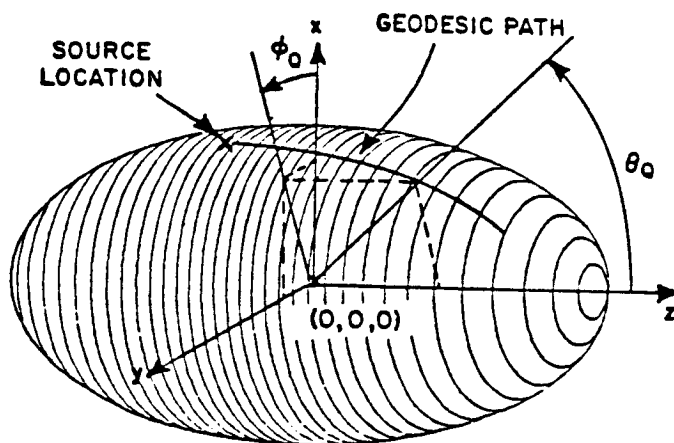
(a) Geodesic path defined by the surface parameters (θ_Q, ϕ_Q).
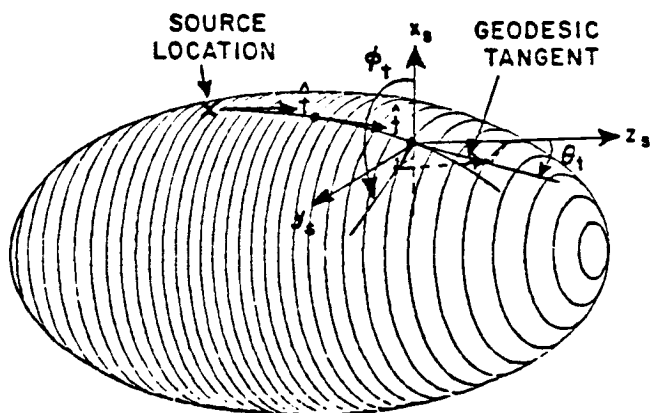
(b) Geodesic tangent defined by the radial vector direction (θ_t, ϕ_t).

Figure 3.13. Definition of geodesic path and geodesic tangent.
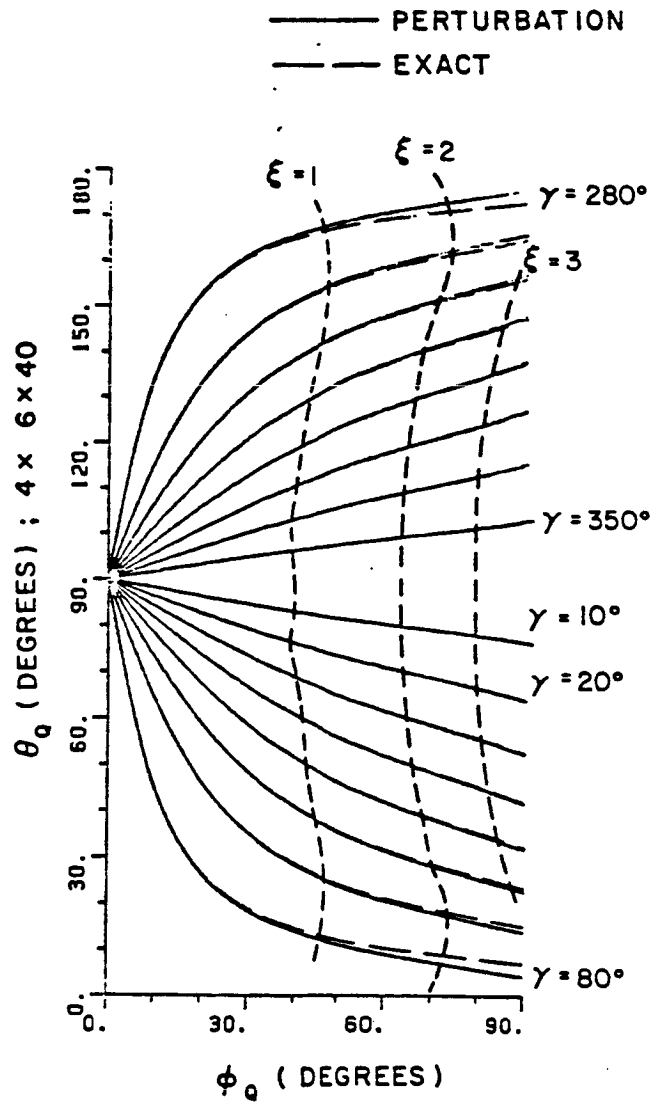
(a) Geodesic paths defined by surface parameters (θ_Q, ϕ_Q).

Figure 3.14. Comparison of geodesics for a source mounted at $\theta_S = 90°$ on a $4\lambda \times 6\lambda \times 40\lambda$ ellipsoid.
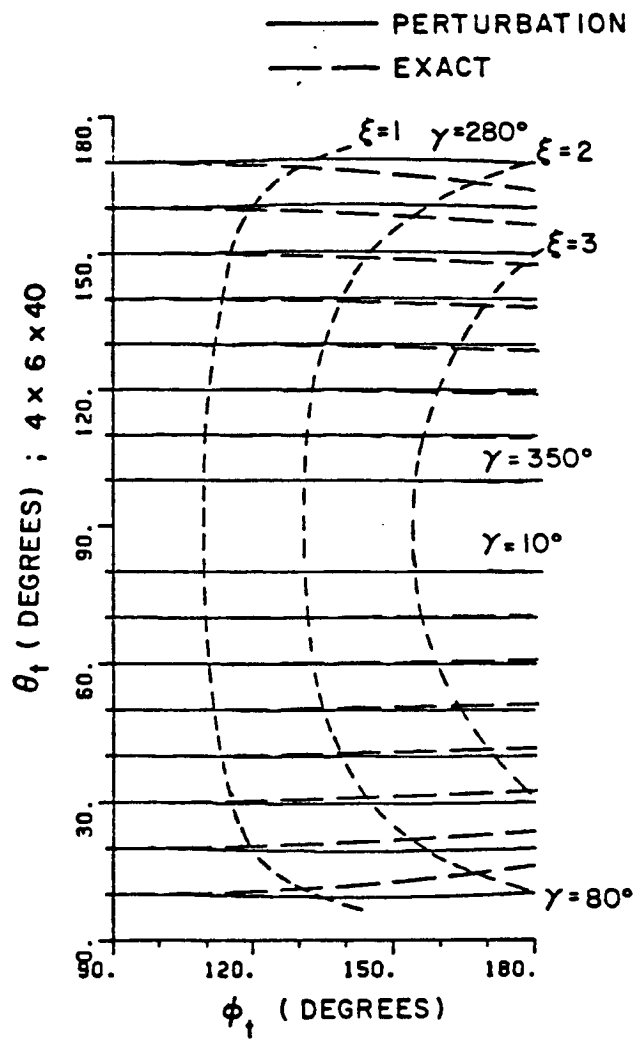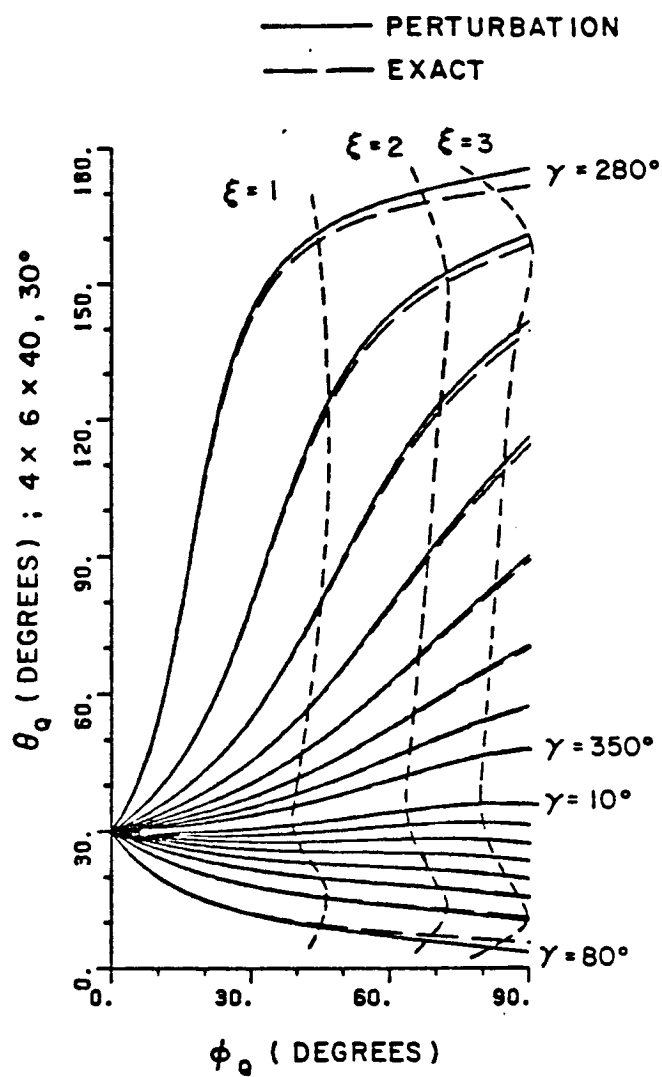
(b) Geodesic tangents defined by the radial vector direction (θ_t, ϕ_t).

Figure 3.14. (Continued).

realistic aircraft and missile shapes. It is also noted that γ is the angle between the geodesic tangent $\hat{t}$ and the principal direction $\hat{t}_1$ at the source location. Looking through those figures, one can see that the geodesic paths and the geodesic tangents of both methods coincide with each other within the significant energy region close to the source. This coincidence in the significant region can be checked more precisely by calculating the Fock parameter (ξ) along each geodesic path. Actually, the Fock functions associated with the solutions drop 8.6 dB, 16 dB, and 23 dB as the Fock parameter (ξ) reaches 1, 2, and 3, respectively, in the deep shadow region. This clearly shows the significant portion of the surface as discussed in Section III-A. Although one can see small discrepancies for the rays toward the tips of the ellipsoid, i.e., lines for $\gamma = 80°$ and $\gamma = 280°$ in these figures, they only happen when the caustic effects come into play. In the caustic region where virtually an infinite set of rays have significant effects on the radiation pattern, the basic GTD theory fails. The study of this caustic effect is beyond the scope of this study. If one neglects the caustic regions, the geodesic paths and geodesic tangents using the perturbation models coincide with the exact solution very well in the significant region.

The elliptic cone perturbation solutions can be examined by placing the source at $\theta_s = 30°$ as shown in Figures 3.15(a) and (b), where the geodesic paths and geodesic tangents of the elliptic cone perturbation solutions are compared with those of the exact solution

(a) Geodesic paths defined by surface parameters (θ_Q, ϕ_Q).

Figure 3.15. Comparison of geodesics for a source mounted at $\theta_s = 30°$ on a $4\lambda \times 6\lambda \times 40\lambda$ ellipsoid.
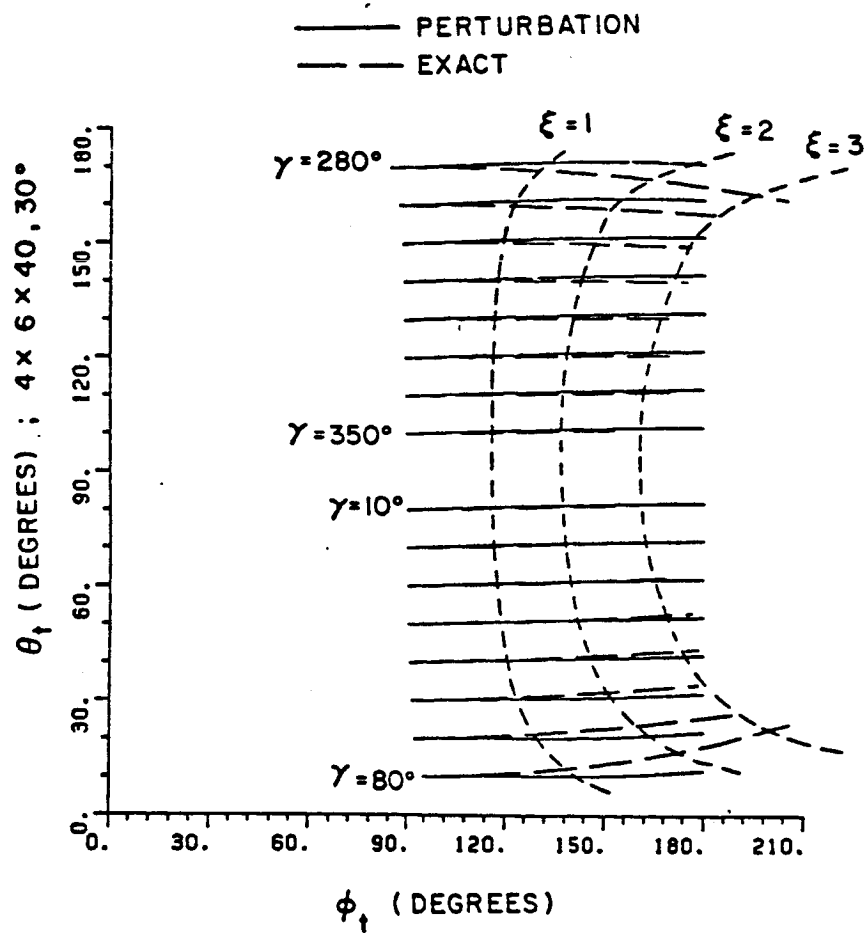
(b) Geodesic tangents defined by the radial vector direction (θ_t, ϕ_t).

Figure 3.15. (Continued).

for the same $4\lambda \times 6\lambda \times 40\lambda$ ellipsoid model. One should note the good agreement between the two results. The significant energy region of the geodesic path is also shown using the calculated Fock parameters (ξ) in the figures. For more detailed analysis with various source locations, one is referred to references [13,14].

To make sure that the solution switches correctly between the elliptic cylinder and the elliptic cone perturbation method, the source is placed at $\theta_S=85°$ and the geodesic paths are calculated as shown in Figure 3.16. Comparing Figures 3.16 with 3.14(a), one can see that the geodesic paths of the elliptic cone perturbation solution are very close to those of the elliptic cylinder perturbation solution for that source location.

These comparisons illustrate that the geodesic paths can be solved by using either numerical technique; however, the perturbation is much more efficient. In addition, one can easily relate the radiation direction with the desired geodesic path using the perturbation method. On the other hand, one is not sure which geodesic is necessary to achieve the desired radiation direction using the exact solution.
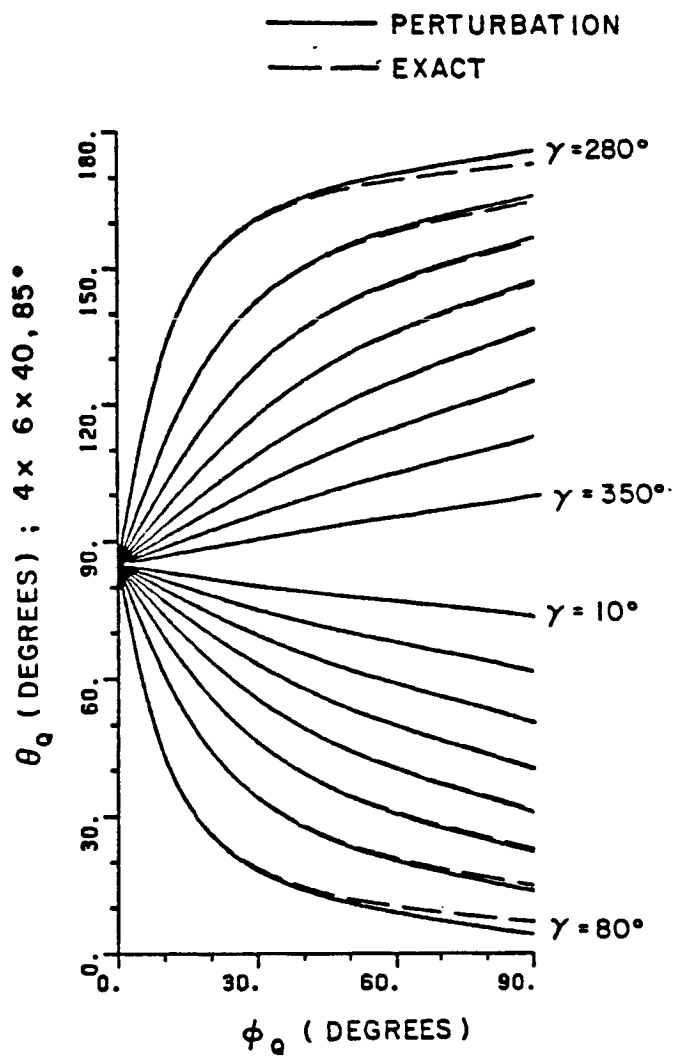
Figure 3.16. Geodesic paths defined by the surface parameters (θ_Q, ϕ_Q) for a source mounted at $\theta s=85°$ on a $4\lambda \times 6\lambda \times 40\lambda$ ellipsoid.

D. FLAT PLATE ATTACHMENT TO AN ELLIPSOID

The flat plates used to simulate the aircraft wings and stabilizers
are described by defining the location of the plate corners. The
corners are numbered in a counter clockwise sense with the first and
last corners being on the ellipsoid. The attachment of the flat plate
to the ellipsoid is essential in that the intersection represents the
wing-root section of the aircraft. The plates can be attached to the
ellipsoid as illustrated in Figure 3.17(a) and (b). However, when the
plates are attached on the lower half of the ellipsoid, the y component
of the first and last corners are set equal to the y dimension of the
ellipsoid center line as shown in Figure 3.17(c) and (d). This
modification is made to eliminate the interior wedge problem which leads
to multiple reflections and diffractions. Since the antenna is
restricted to be on the top or near the top of the ellipsoid, this
modification is reasonable. In addition, the field contribution from
this edge is small compared with the other edges of the plate. This is
due to the great attenuation of the surface wave propagating along the
ellipsoid surface in reaching the edge. Note that the plates are not
restricted to lie horizontally. The flat plate attachment above and
below the center line of the ellipsoid will be discussed separately in
this section.

Now, the first approach to this problem is to find the intersection
point between a line (i.e., one edge of the plate) and the ellipsoid.
Then one can follow the same concept to find the curved junction edge
between a flat plate and the ellipsoid.

109
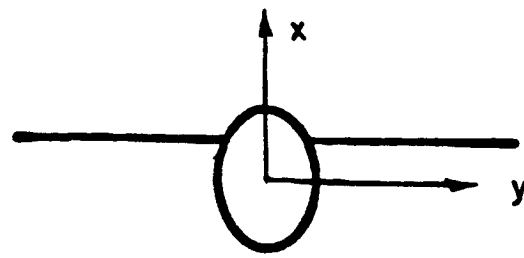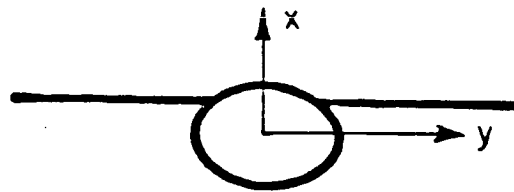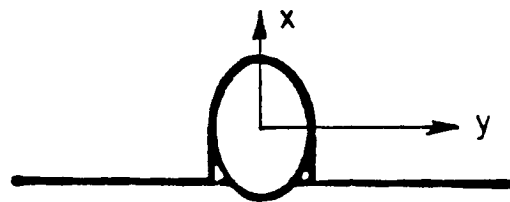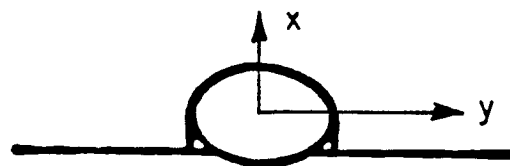
Figure 3.17. Fuselage and wing geometries for aircraft model looking from the front. The antenna is assumed to be on the top portion of the models.

Using the geometry as shown in Figure 3.18(a), the ellipsoid surface is defined by

$$\vec{R}(V_e, V_r) = a \cos V_e \cos V_r \hat{x} + b \cos V_e \sin V_r \hat{y} + c \sin V_e \hat{z} \qquad (3.128)$$

and the unit edge vector is given by

$$\hat{e}_1 = \frac{\vec{P}_2 - \vec{P}_1}{|\vec{P}_2 - \vec{P}_1|} = \hat{x} \, e_{1x} + \hat{y} \, e_{1y} + \hat{z} \, e_{1z} \qquad (3.129)$$

where $\vec{P}(x_1, y_1, z_1)$ and $\vec{P}_2(x_2, y_2, z_2)$ are the position vectors of two corners with respect to the origin of the coordinate system. From Figure 3.18(a), the position vector of the first intersection point $\vec{P}_{HI}$ can be easily defined by

$$\vec{P}_{HI} = \vec{P}_1 - \ell_I \hat{e}_1 \qquad . \qquad (3.130)$$

Since $\vec{P}_{HI}(x_h, y_h, z_h)$ is on the surface of an ellipsoid, one obtains the following equations:

$$a \cos V_e \cos V_r = x_1 - \ell_I e_{1x}$$
$$b \cos V_e \sin V_r = y_1 - \ell_I e_{1y}$$

and

$$c \sin V_e = z_1 - \ell_I e_{1z} \qquad . \qquad (3.131)$$

From these equations, one finds

111

(a) Flat plate attachment above the center line of an ellipsoid.

$$\hat{t}_b = \hat{e}_{FI} \times \hat{N}_P$$

$$\hat{N}_P = \hat{e}_1 \times \hat{e}_2$$

(b) Geometry of the curved junction edge.
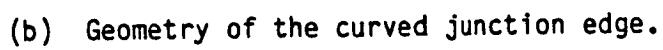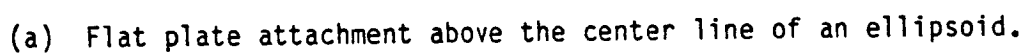
Figure 3.18. Flat plate attachment to an ellipsoid.

$$\frac{(x_1 - \ell_I e_{1x})^2}{a^2} + \frac{(y_1 - \ell_I e_{1y})^2}{b^2} + \frac{(z_1 - \ell_I e_{1z})^2}{c^2} = 1 \quad . \tag{3.132}$$

Defining

$$A = b^2 c^2 e_{1x}^2 + a^2 c^2 e_{1y}^2 + a^2 b^2 e_{1z}^2$$

$$B = - b^2 c^2 x_1 e_{1x} - a^2 c^2 y_1 e_{1y} - a^2 b^2 z_1 e_{1z}$$

$$C = b^2 c^2 x_1^2 + a^2 c^2 y_1^2 + a^2 b^2 z_1^2 - a^2 b^2 c^2 \tag{3.133}$$

and employing Equations (3.132) and (3.133), one obtains the distance between the points $\vec{P}_1$ and $\vec{P}_{HI}$ such that

$$\ell_1 = \frac{-B + \sqrt{B^2 - AC}}{A} \quad , \tag{3.134}$$

and

$$\ell_2 = \frac{-B - \sqrt{B^2 - AC}}{A} \quad . \tag{3.135}$$

The smaller one of (ℓ_1, ℓ_2) will be used in Equation (3.130) to define the position vector $\vec{P}_{HI}(x_h, y_h, z_h)$. One can follow the same procedure to obtain the second attachment point $\vec{P}_{HF}$. Then, as shown in Figure 3.18(b), one can define the unit vector

$$\hat{e}_{FI}(x, y, z) = \frac{\vec{P}_{HF}(x_{hf}, y_{hf}, z_{hf}) - \vec{P}_{HI}(x_{hi}, y_{hi}, z_{hi})}{|\vec{P}_{HF}(x_{hf}, y_{hf}, z_{hf}) - \vec{P}_{HI}(x_{hi}, y_{hi}, z_{hi})|} \quad , \tag{3.136}$$

and the binormal unit vector which is given by

$$\hat{t}_b(x,y,z) = \hat{e}_{FI}(x,y,z) \times \hat{N}_p(x,y,z) \qquad (3.137)$$

where the unit normal vector of the plate is given by

$$\hat{N}_p(x,y,z) = \frac{\hat{e}_1(x_1,y_1,z_1) \times \hat{e}_2(x_2,y_2,z_2)}{|\hat{e}_1(x_1,y_1,z_1) \times \hat{e}_2(x_2,y_2,z_2)|} \cdot \qquad (3.138)$$

According to the variation of the ellipsoid surface, one can divide the line $\overline{P_{HI}P_{HF}}$ into N-1 unequal length segments (ℓ'_i) with i = 1,2...,N-1. The position vectors $\vec{P}_i$ along $\overline{P_{HI}P_{HF}}$ are given by the recursive equation such that

$$\vec{P}_i = \vec{P}_{i-1} + \ell'_i \hat{e}_{FI}, \quad i = 2,...,N-1 \qquad (3.139)$$

By using the position vectors $\vec{P}_i$ just found, one can attain N position vectors along the curved junction edge,i.e.,

$$\vec{P}_{CE_i} = \vec{P}_i + \ell''_i \hat{t}_b \quad \text{for } i = 2,3,....,N-1 \qquad (3.140)$$

with

$$\vec{P}_{CE_1} = \vec{P}_{HI} \quad \text{and} \quad \vec{P}_{CE_N} = \vec{P}_{HF} \cdot \qquad (3.141)$$

Note that ℓ_i'' can be found by using the same idea employed to compute ℓ_I. Therefore, the curved junction edge is found by connecting all N position vectors $P_{CE_i}(x,y,z)$.

Next, consider the plate attachment below the center line of the ellipsoid. The first intersecting point $P_{HI}(x_h,y_h,z_h)$ can be defined by

$$\vec{P}_{HI} = \vec{P}_1 - \ell_I \, \hat{e}_1 \qquad\qquad (3.142)$$

with

$$x_h = x_1 - \ell_I \, e_{1x}$$

$$y_h = y_1 - \ell_I \, e_{1y}$$

and

$$z_h = z_1 - \ell_I \, e_{1z} \qquad . \qquad\qquad (3.143)$$

Considering the attachment to the elliptic cylinder as shown in Figure 3.19, one finds

$$\frac{(y_1-\ell_I e_{1y})^2}{b^2} + \frac{(z_1-\ell_I e_{1z})^2}{c^2} = 1 \qquad . \qquad\qquad (3.144)$$
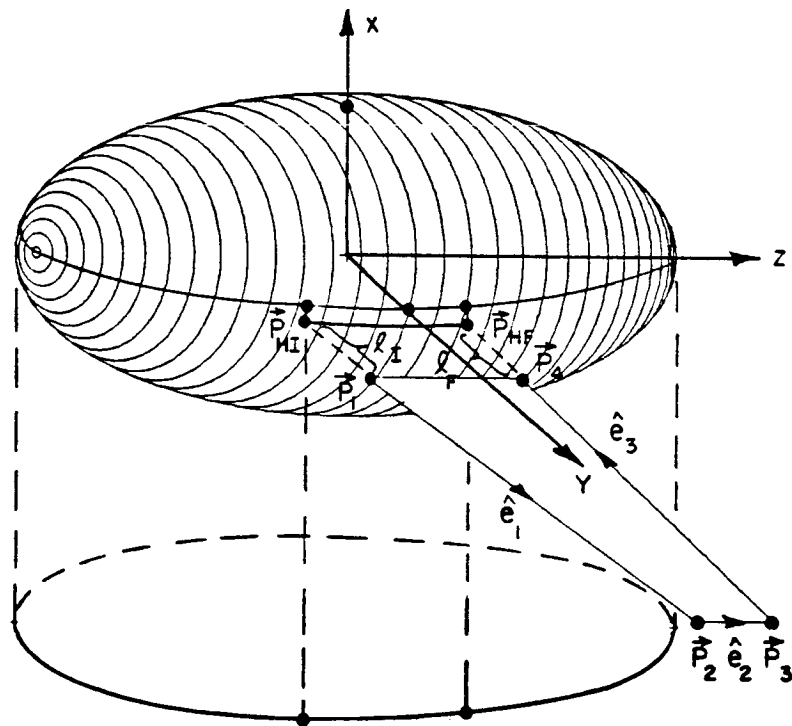
Figure 3.19. Flat plate attachment below the center line of an ellipsoid.

Defining

$$A = c^2 e_{1y}^2 + b^2 e_{1z}^2$$

$$B = -c^2 y_1 e_{1y} - b^2 z_1 e_{1z}$$

$$C = c^2 y_1^2 + b^2 z_1^2 - b^2 c^2 \qquad (3.145)$$

and employing Equations (3.144) and (3.145), one obtains the distance between the points $\vec{P}_1$ and $\vec{P}_{HI}$ such that

$$\ell_1 = \frac{-B + \sqrt{B^2 - AC}}{A} \qquad (3.146)$$

and

$$\ell_2 = \frac{-B - \sqrt{B^2 - AC}}{A} \qquad . \qquad (3.147)$$

The smaller one of (ℓ_1, ℓ_2) is used in Equation (3.142) to define the position vector $\vec{P}_{HI}(x_h, y_h, z_h)$. One can follow the same procedure to obtain the second attachment point $\vec{P}_{HF}$. The procedure to obtain the curved junction edge is the same as the attachment above the center line of the ellipsoid.

This completes the derivation of the curved edge junction between a flat plate and the ellipsoid. Note that the plates simulate the wings, stabilizers, etc.

117

CHAPTER IV

RADIATION FIELD CALCULATION ALGORITHMS

A. INTRODUCTION

This chapter presents details of the techniques to determine each
of the individual Uniform Geometrical Theory of Diffraction (UTD) terms
which contributes to the total field. It is noted that, since UTD is a
high frequency method, the lower frequency limit of this solution is
dictated by the electrical dimensions of the ellipsoid and plate
structures, i.e., the semi-minor axes of the ellipsoid are required to
be at least a wavelength and each plate should have edges at least a
wavelength long. In addition, each antenna element should be at least a
wavelength away from all edges. With the antenna mounted on the
fuselage it is obvious that the rest of the structure is very close to
the soruce. That is to say, the antenna is in the near field of the
structure. However, it is assumed that any point on the scattering body
is in the far field of the source.

As depicted in Figure 4.1, the total radiated field is the superposition of the following UTD field components: 1) direct field from the source; 2) curved surface diffracted fields from the composite ellipsoid (referred to as the source field here); 3) reflected fields from the finite flat plates (i.e., wings or stabilizers); 4) diffracted fields from the edges of the plates, including diffraction from the curved junction edges formed by the intersection of the plates with the composite ellipsoid; 5) and vertex diffraction from each of the plate corners. In addition to the above direct scattering from a structure, the rays reflected or diffracted from one structure tend to interact with the other structures causing various higher order UTD terms such as double reflected, reflected-diffracted, diffracted-reflected, and double diffracted, etc. Thus, the total radiated field of an antenna in a complex environment can be expressed as a summation of individual UTD terms as follows:

$$\bar{E}_{total} = \bar{E}_s + \bar{E}_r + \bar{E}_d + \bar{E}_c + \bar{E}_{rr} + \bar{E}_{rd} + \bar{E}_{dr} + \bar{E}_{dd} \; . \qquad (4.1)$$

Superimposing all of these scattered field terms is not unduly time consuming in that only a few contribute significantly in a given radiation direction.

The first step in obtaining the solution of each UTD term is to determine the ray path using the laws of reflection and/or diffraction. After the ray path is identified, one must then examine the total ray
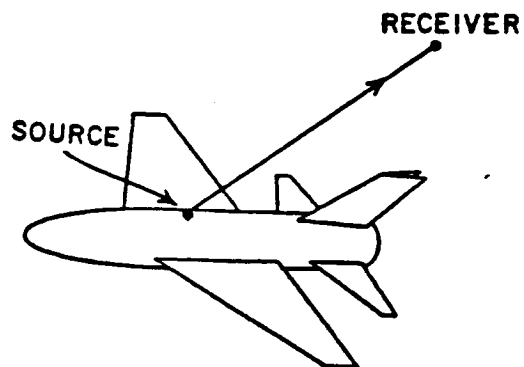
(a) DIRECT SOURCE FIELD
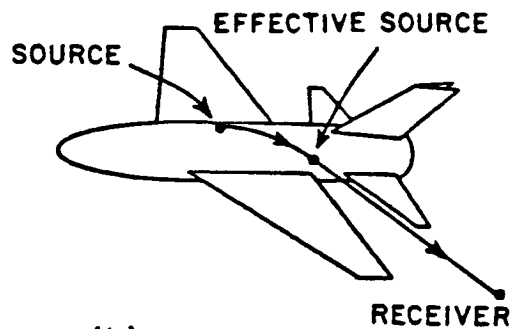
(b) SOURCE FIELD
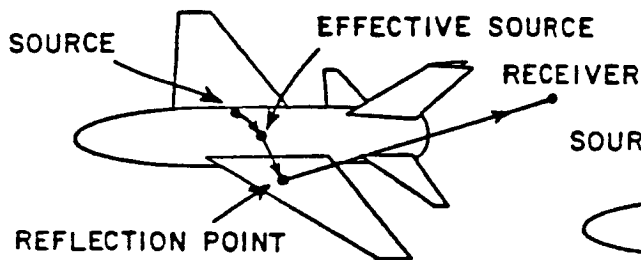
(c) REFLECTED FIELD
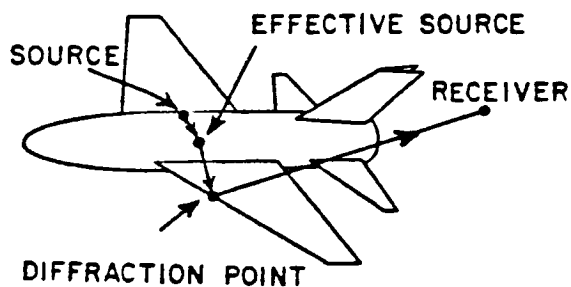
(d) EDGE DIFFRACTED FIELD
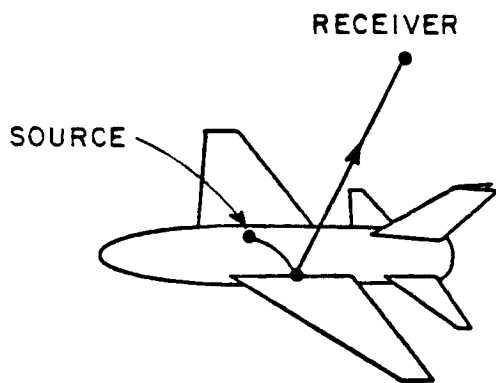
(e) CURVED JUNCTION EDGE DIFFRACTED FIELD
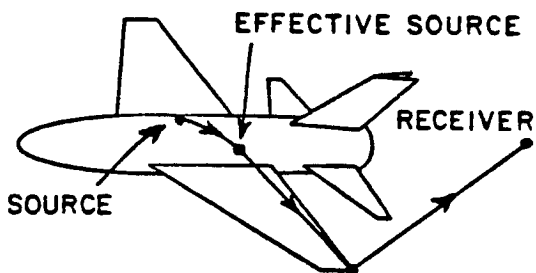
(f) CORNER DIFFRACTED FIELD

Figure 4.1. Various first order UTD terms.

120

path to see whether or not it intersects an obstacle. If the ray path is not interrupted, the field value is computed and superimposed with other terms. On the other hand, if the ray path is interrupted, the field is not computed. A complete computer simulation program has been written which takes advantage of this feature and was used to provide the calculated results presented in the next chapter.

Each UTD mechanism, which is expressed in terms of the x-y-z components of the electric field, will be discussed in detail in the following sections.

B. SOURCE FIELD

This section presents details of the techniques employed in the computer routines to obtain the direct and curved surface diffracted fields for a near field or a far field receiver. Both fields will be referred to as the source fields in the rest of this dissertation. The surface is assumed to be perfectly conducting and the surrounding medium is free space. An exp $(j\omega t)$ time dependence will be assumed and suppressed in the following formulations.

The solution of the radiated field for an infinitesimal electric or magnetic dipole (i.e., $d\bar{P}_e(Q')$ or $d\bar{P}_m(Q')$, respectively) mounted on a perfectly conducting convex surface was presented in Sections II-B.(1,2) and the pattern factors $\bar{P}_e$ and $\bar{P}_m$ for an extended aperture (i.e., slot) and linear antenna (i.e., monopole), respectively, were given in Section II-B.3. Thus, the source field solutions can be obtained by replacing

121

$d\bar{P}_e(Q')$ and $d\bar{P}_m(Q')$ with the pattern factors $\bar{P}_e$ and $\bar{P}_m$, respectively. The source field solutions are then summarized as follows:

a) when the receiver is in the lit region,

(i) for aperture type sources,

$$\bar{E}_m^\ell = (L_m^n \hat{n} + L_m^b \hat{b}) \left| \begin{array}{ll} \dfrac{e^{-jks}}{s} & \text{in the near field, and} \\[3ex] e^{jk\vec{P}_s \cdot \hat{P}_r} & \text{in the far field} \end{array} \right. \tag{4.2}$$

where

$$L_m^n = \frac{-jk}{4\pi} \left[(\bar{P}_m \cdot \hat{b}')(H^\ell + T_0^2 F \cos\theta^i) + (\bar{P}_m \cdot \hat{t}') T_0 F \cos\theta^i \right] \quad , \tag{4.3}$$

$$L_m^b = \frac{-jk}{4\pi} \left[(\bar{P}_m \cdot \hat{b}') T_0 F + (\bar{P}_m \cdot \hat{t}')(S^\ell - T_0^2 F \cos^2\theta^i) \right] \tag{4.4}$$

(ii) for monopole type sources,

$$\bar{E}_e^\ell = (L_e^n \hat{n} + L_e^b \hat{b}) \left| \begin{array}{ll} \dfrac{e^{-jks}}{s} & \text{in the near field, and} \\[3ex] e^{jk\vec{P}_s \cdot \hat{P}_r} & \text{in the far field} \end{array} \right. \tag{4.5}$$

$$L_e^n = \frac{-jkZ_0}{4\pi} \bar{P}_e \sin\theta^i [H^\ell + T_0^2 F \cos\theta^i] \tag{4.6}$$

$$L_e^b = \frac{-jkZ_0}{4\pi} \bar{P}_e \sin\theta^i T_0 F \quad . \tag{4.7}$$

b) When the receiver is in the shadow region,

    (i) for aperture type sources,

$$\bar{E}_m^s = (D_m^n \hat{n} + D_m^b \hat{b}) \begin{vmatrix} \dfrac{e^{-jks}}{\sqrt{s(\rho_c + s)}} & \text{in the near field, and} \\[4mm] e^{jk\vec{P}_{es} \cdot \hat{P}_r} & \text{in the far field} \end{vmatrix} \tag{4.8}$$

$$D_m^n = \frac{-jk}{4\pi} (\bar{P}_m \cdot \hat{b}') H e^{-jkt} \left[\frac{\rho_g(Q')}{\rho_g(Q)} \right]^{-1/6} \tag{4.9}$$

$$D_m^b = \frac{-jk}{4\pi} [(\bar{P}_m \cdot \hat{b}') T_0 S + (\bar{P}_m \cdot \hat{t}') S] e^{-jkt} \left[\frac{\rho_g(Q')}{\rho_g(Q)} \right]^{-1/6} \tag{4.10}$$

(ii) for the monopole type sources,

$$\bar{E}_e^s = (D_e^n \hat{n} + D_e^b \hat{b}) \begin{vmatrix} \dfrac{e^{-jks}}{\sqrt{s(\rho_c + s)}} & \text{in the near field, and} \\[2em] e^{jk\vec{P}_{es} \cdot \hat{P}_r} & \text{in the far field} \end{vmatrix} \qquad (4.11)$$

$$D_e^n = \frac{-jkZ_0}{4\pi} \bar{P}_e H e^{-jkt} \left[\frac{\rho_g(Q')}{\rho_g(Q)} \right]^{-1/6} , \qquad (4.12)$$

$$D_e^b = \frac{-jkZ_0}{4\pi} \bar{P}_e T_0 S e^{-jkt} \left[\frac{\rho_g(Q')}{\rho_g(Q)} \right]^{-1/6} . \qquad (4.13)$$

It is noted that the caustic distance, ρ_c, [30] is approximated by the geodesic arc length given in Equations (3.71), (3.121) and (3.122). It is a reasonable approximation in that the dimensions of the ellipsoid are assumed to be large in terms of the wavelength. The other parameters used in the above equations were defined in Section II-B.

Through an extensive study [7] of geodesic paths on a surface of revolution, the dominant rays needed to be considered would not exceed four rays. These four rays are illustrated in Figure 4.2. However, the significant effect of the ellipsoid surface is associated with a region

124
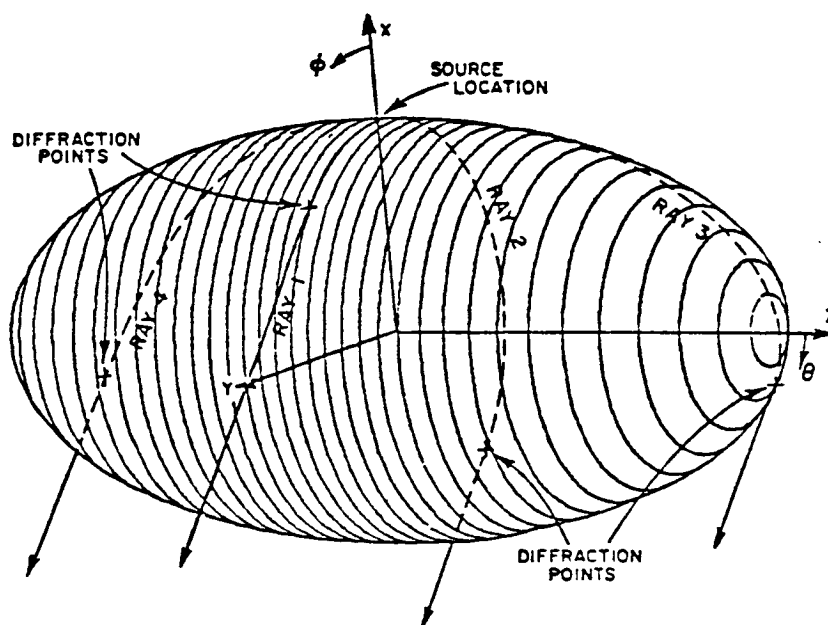
Figure 4.2. The four dominant GTD terms that radiate at
(θ=90°, φ=145°).

around the source. Since the fuselage of the usual aircraft is very

long and slender, only two dominant rays are included in the

computation of the source field in the deep shadow region. It·is also

observed that rays 3 and 4 in the figure fall into the caustic region

where the basic UTD theory fails. In order to avoid this caustic

problem, the cone boundary shown in Figure 4.3 is used in determining

whether one or two rays are used in the solution. Note that β_{12} is

defined automatically by determining the caustic angle in the elevation

pattern (β_c) and adding a few additional degrees to that value, i.e.,

$\beta_{12} = \beta_c + \Delta\beta$ where $2° < \Delta\beta < 10°$. The caustic angle β_c can be
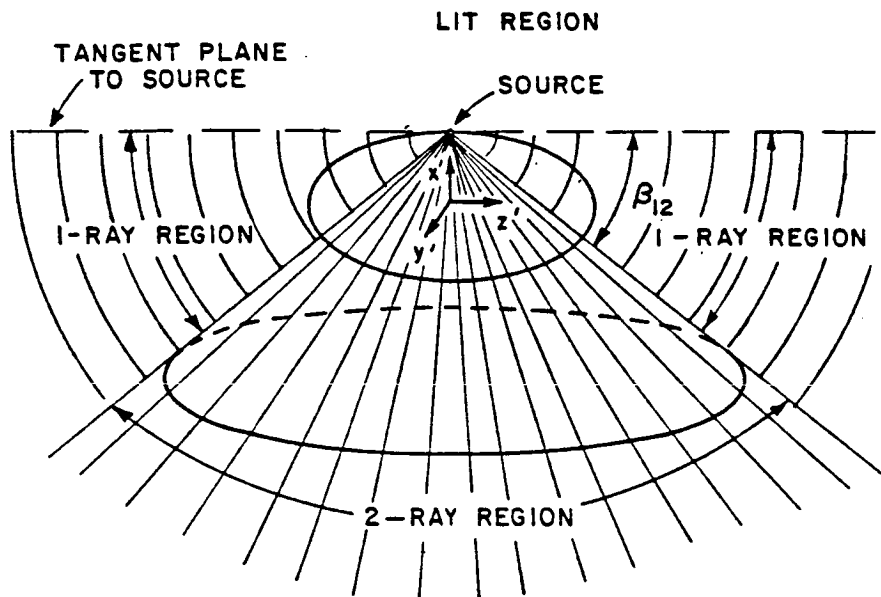
Figure 4.3. Cone boundary used to define terms to be included in the shadow region.

obtained by enforcing the determinant of the first matrix in Equation (3.104) to zero with the following assumptions:

$$r_s \approx S_e, \quad \theta_t \approx \gamma \approx \beta \approx \pi/2, \quad \alpha \approx 0 \text{ and } \phi_t \approx 0 \text{ or } \pi .$$

Note that the above parameters were defined in Section III-C.3. One would expect to observe slight discontinuities somewhere, because various numbers of rays are included in different regions.

This completes the source field calculation and this source field will also be used as an incident field at the scattering body of the aircraft structure in the following sections.

C. REFLECTED FIELD

The reflected field from each of the finite flat plates is determined using image theory [24]. As shown in Figure 4.4, the receiver image position with respect to j^{th} plate is given by

$$\vec{P}_r^{I_j} = \vec{P}_r - 2\hat{n}_j \cdot (\vec{P}_r - \vec{P}_{c_{1,j}}) \quad . \tag{4.14}$$

The source field solution is, then, used to compute the electric field (E_x^s, E_y^s, E_z^s) at the image position $\vec{P}_r^{I_j}$. This field would exist at that point if the plate were not present. The second step is to ascertain if the ray path from the effective source to the image position intersects the plate. This ray path shadowing algorithm will be discussed in detail in Section IV-F. If the ray path is not interrupted by the plate, a reflection by that plate does not occur for that receiver position. If the ray does pass through the plate, then the reflected field ($\bar{E}^r = E_x^r \hat{x} + E_y^r \hat{y} + E_z^r \hat{z}$) is given by

$$\begin{bmatrix} E_x^r(\vec{P}_r) \\ E_y^r(\vec{P}_r) \\ E_z^r(\vec{P}_r) \end{bmatrix} = \begin{bmatrix} T_{xx} & T_{xy} & T_{xz} \\ T_{yx} & T_{yy} & T_{yz} \\ T_{zx} & T_{zy} & T_{zz} \end{bmatrix} \begin{bmatrix} E_x^s(\vec{P}_r^{I_j}) \\ E_y^s(\vec{P}_r^{I_j}) \\ E_z^s(\vec{P}_r^{I_j}) \end{bmatrix} \tag{4.15}$$

127
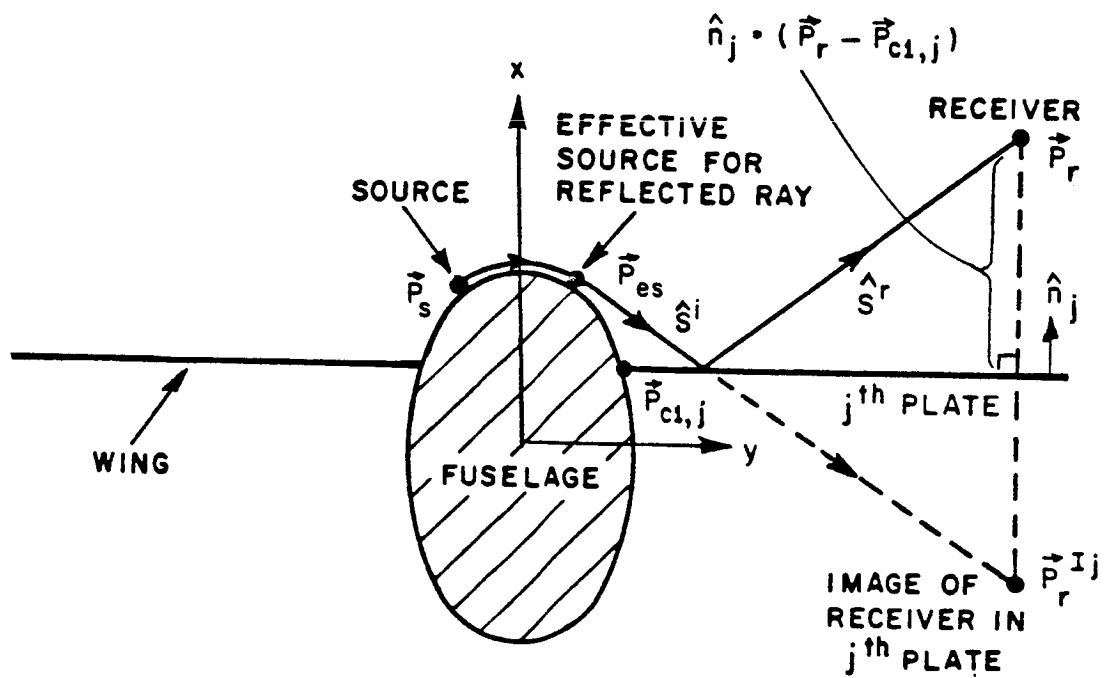
Figure 4.4. Geometry used to determine reflected field from plates (wings, etc.).

where [T] represents the reflected field polarization transformation matrix which satisfies the boundary conditions [32] on the given plate. This matrix is determined using the normal $\hat{n}$ and tangent $\hat{t}$ unit vectors of the electric field to the given plate as follows:

$$\vec{E}^r = (\hat{n} \cdot \vec{E}^s)\hat{n} - (\hat{t} \cdot \vec{E}^s)\hat{t} \quad \text{on plate} \tag{4.16}$$

$$(\hat{t} \cdot \vec{E}^s)\hat{t} = \vec{E}^s - (\hat{n} \cdot \vec{E}^s)\hat{n} \tag{4.17}$$

$$\vec{E}^r = 2(\hat{n} \cdot \vec{E}^s)\hat{n} - \vec{E}^s \tag{4.18}$$

or

$$T_{xx}\hat{x} + T_{yx}\hat{y} + T_{zx}\hat{z} = 2(\hat{n} \cdot \hat{x})\,\hat{n} - \hat{x} \tag{4.19}$$

$$T_{xy}\hat{x} + T_{yy}\hat{y} + T_{zy}\hat{z} = 2(\hat{n} \cdot \hat{y})\,\hat{n} - \hat{y} \tag{4.20}$$

$$T_{xz}\hat{x} + T_{yz}\hat{y} + T_{zz}\hat{z} = 2(\hat{n} \cdot \hat{z})\,\hat{n} - \hat{z} \quad . \tag{4.21}$$

Since the T-matrix is independent of the receiver location, it is stored for each plate in order to optimize the computational efficiency of the numerical solution. The total reflected field for a given receiver position is, then, the superposition of the reflected fields from the individual plates.

D. DIFFRACTED FIELD

The diffracted field is obtained by using the UTD formulation presented in Section II-C. The shadowing of the incident and reflected rays by the flat plates is compensated by the addition of the diffracted fields which cause the total field to be smooth and continuous at the incident and reflection shadow boundaries. The most difficult part in computing the edge diffracted field is to determine the ray path. For any particular source, plate edge, and receiver location, the diffracted ray path is unique [25]. The key in finding this unique path is to determine the actual diffraction point along the given edge.

Typical geometries for the diffraction point in the illuminated and shadow region are depicted in Figures 4.5(a) and (b), respectively, and will be discussed separately in the following sections.

1. Diffraction Point in the Lit Region

As shown in Figure 4.5(a), the diffraction point in the lit region must be located at a position along the edge such that the angle β between the incident ray and the edge equals the angle β' between the diffracted ray and the edge. With $\hat{i}$ and $\hat{d}$ defined as unit vectors in the direction of the incident and diffracted rays, respectively, and $\hat{e}$ defined as a unit vector lying along the edge, the above noted basic law
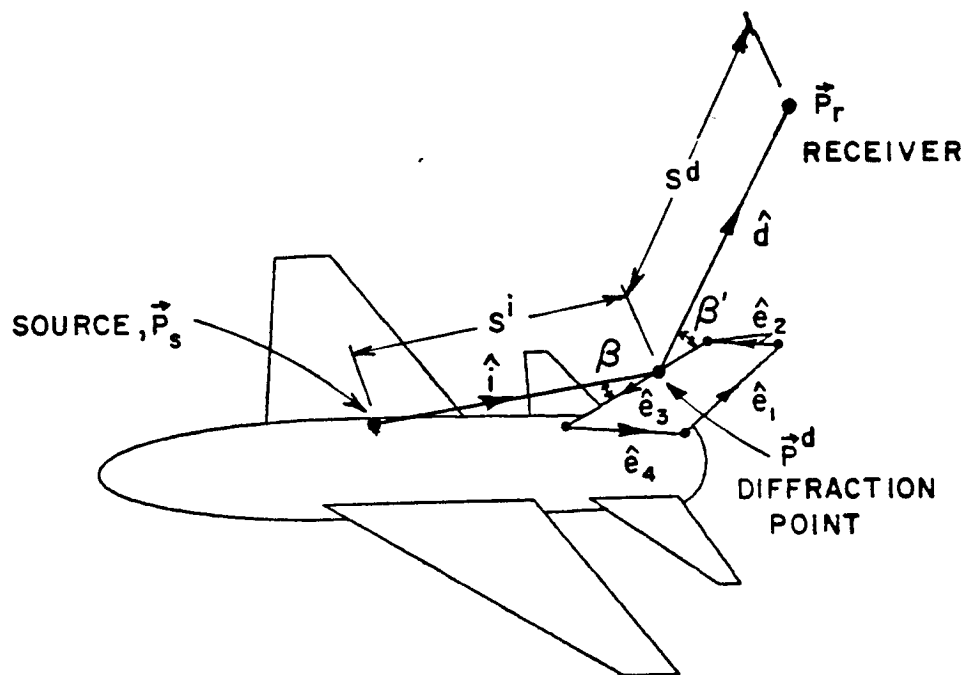
(a) Diffraction point in the lit region.
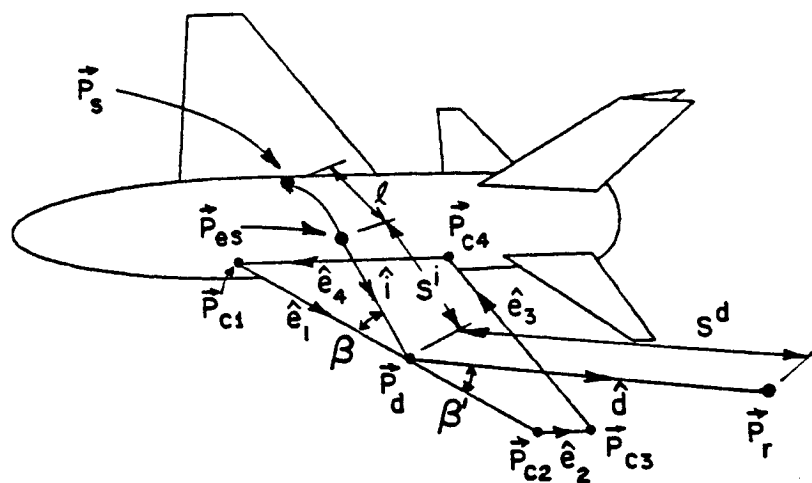
(b) Diffraction point in the shadow region.

Figure 4.5. Illustrations of the diffracted field by the straight
edge.

131

of edge diffraction [27] (i.e., $\beta = \beta'$) can be stated equivalently by the requirement that

$$\hat{i} \cdot \hat{e} = \hat{d} \cdot \hat{e} \qquad . \tag{4.22}$$

The edge unit vector $\hat{e}$ in Equation (4.22) can readily be computed from the specified corner coordinates of the plate. From the procedure depicted in Figure 4.6, the diffraction point is given by

$$\vec{P}_d = \vec{P}_s' + \frac{|\vec{P}_s - \vec{P}_s'|}{|\vec{P}_s - \vec{P}_s'| + |\vec{P}_r - \vec{P}_r'|} |(\vec{P}_r - \vec{P}_s) \cdot \hat{e}_i| \hat{e}_i$$

$$\text{in the near field case,} \tag{4.23}$$

or,

$$\vec{P}_d = \vec{P}_s' + |\vec{P}_s - \vec{P}_s'| \cos\beta \, \hat{e}_i \quad \text{in the far field case,} \tag{4.24}$$

where

$$\vec{P}_s' = \vec{P}_{c_i} + \{(\vec{P}_s - \vec{P}_{c_i}) \cdot \hat{e}_i\} \hat{e}_i \tag{4.25}$$

$$\vec{P}_r' = \vec{P}_{c_i} + \{(\vec{P}_r - \vec{P}_{c_i}) \cdot \hat{e}_i\} \hat{e}_i \tag{4.26}$$

and

$$\cot\beta = \frac{\hat{d} \cdot \hat{e}_i}{\sqrt{1 - (\hat{d} \cdot \hat{e}_i)^2}} \qquad . \tag{4.27}$$

132
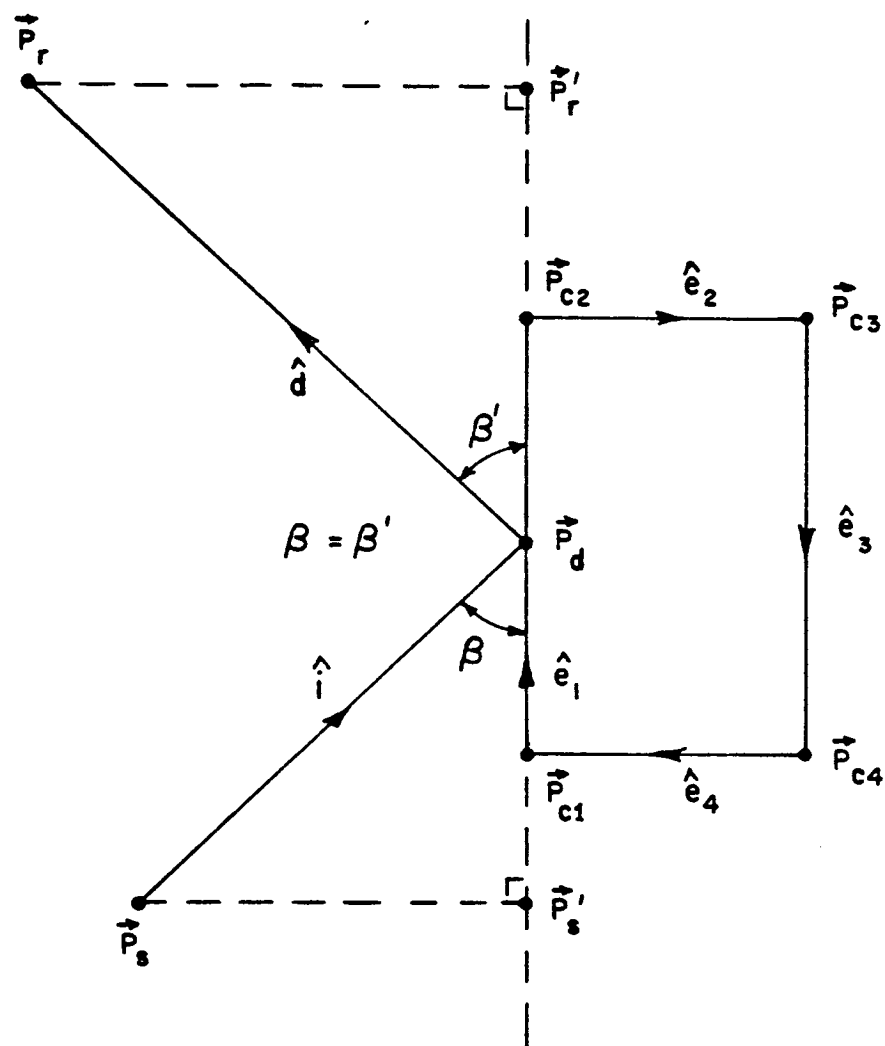
Figure 4.6. Geometry for the diffraction point search algorithm in the lit region.

2. Diffraction Point in the Shadow Region

If the edge of the plate is not located in the lit region of the source as shown in Figure 4.5(b), the diffraction point cannot be obtained directly in that one has to resort to a numerical approach. An iterative numerical search procedure is employed here to determine the diffraction point which satisfies the diffraction law (i.e., $\hat{i} \cdot \hat{e} = \hat{d} \cdot \hat{e}$). As an initial step in the routine prior to initiating the actual search procedure, values of $\hat{i} \cdot \hat{e}$ are computed and stored for a sequence of N sample points along the plate edge. The coordinates (x,y,z) of the sample points are selected and defined in the following manner. For an edge of length ℓ, the N sample points effectively subdivide the edge into (N-1) segments of length $\Delta\ell$, where $\Delta\ell = \ell/(N-1)$. The distance t between the one reference end of the edge and the nth sample point along the edge is then given by

$$t(n) = (n-1)\Delta\ell \; ; \quad n=1,2,3,\ldots,N \quad . \tag{4.28}$$

These distances define the coordinates (x_n, y_n, z_n) for each of the N sample points. It is noted that the $\hat{i} \cdot \hat{e}$ curve for the straight edges which attach to the fuselage varies rapidly near the fuselage. So for these edges, the sample points are taken in a nonlinear way with more samples near the fuselage, i.e., the distance t is given by

$$t(n) = \sum_{i=0}^{n-1} i\Delta s \; ; \quad n=1,2,3,\ldots,N \tag{4.29}$$

where

$$\Delta S = \frac{\ell}{\sum\limits_{i=0}^{N-1} i} \quad .$$

(4.30)

Except for this variation, the routine follows the detailed approach which was given previously.

After the $\hat{i} \cdot \hat{e}$ values are computed and stored at the N sample points along each plate edge, the routine initiates a search to determine which one (if any) of the (N-1) segments contains the diffraction point. The test to determine whether the diffraction point is within the limits of the physical edge or not can be done by computing $\hat{d} \cdot \hat{e}$ at two ends of each physical edge for a specified receiver point and then comparing them with stored data $\hat{i} \cdot \hat{e}$ at the two ends. A diffraction point lies along the physical edge if $\hat{d} \cdot \hat{e} > \hat{i} \cdot \hat{e}$ at one end of the physical edge and $\hat{d} \cdot \hat{e} < \hat{i} \cdot \hat{e}$ at the other end. Otherwise, the diffraction point does not exist on the physical edge. If the diffraction point falls within the limits of the physical edge, the routine selects the midpoint of the edge as the next test point. Note that a selected test point in the search routine always coincides with one of the N sample points in the list of previously computed $\hat{i} \cdot \hat{e}$ values. Noting the sign of the inequality between $\hat{i} \cdot \hat{e}$ and $\hat{d} \cdot \hat{e}$ at the midpoint and two endpoints of the edge, the routine selects the half of the total edge which contains the diffraction point as the second search interval. The routine continues

135

to halve the search interval in this manner until, after several cycles in the iteration, the length of the search interval is reduced to the segment length $\Delta\ell$ between successive sample points. This situation is depicted in Figure 4.7, which shows the diffraction point located within the segment bounded by distances $t(m)$ and $t(m+1)$. At this stage of the search, the routine uses linear interpolation to compute the distance h_d to the true diffraction point. The value of h_d is then used to compute the diffraction point coordinates $\vec{P}_d(x_d, y_d, z_d)$, as given by

$$x_d = x_1 + h_d \cdot e_x \tag{4.31}$$

$$y_d = y_1 + h_d \cdot e_y \tag{4.32}$$

and

$$z_d = z_1 + h_d \cdot e_z \tag{4.33}$$

3. Curved Edge Diffraction Point

This section presents a discussion of the routine for computing the diffraction point on a curved edge of a finite flat plate. In general, a curved edge solution is needed in the analytical aircraft model to treat the diffraction which occurs at the junction of the finite flat plates and the ellipsoid, and the chopped fuselage curved edge.
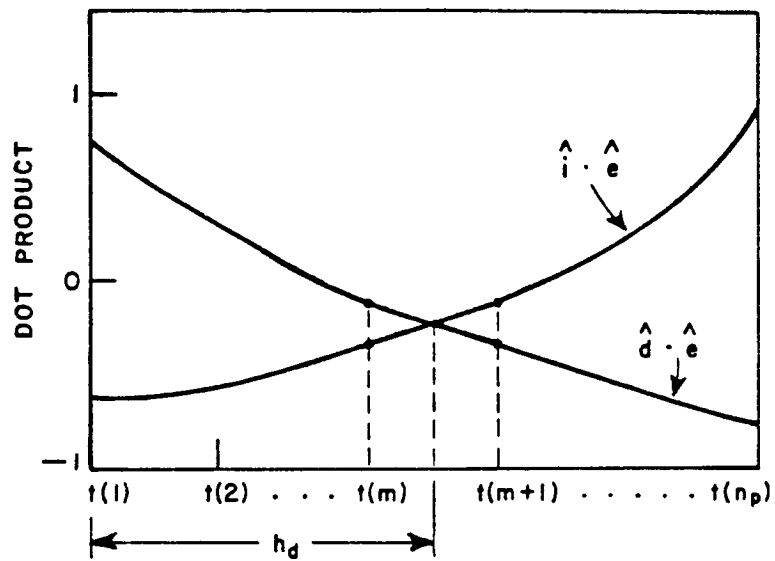
Figure 4.7. Graphical representation of how the diffraction point location is determined.

The basic approach used to determine the diffraction point along the curved junction edge is essentially the same as that for the straight edge diffraction point in the shadow region which was discussed in the previous section. The only difference is that the edge unit vector $\hat{e}$ is a function of position along the curved edge and the determination of the incident unit vector $\hat{i}$ is more complicated in that the curved junction edge lies on the ellipsoid surface as shown in Figure 4.8(a). The position vectors of the N sample points along the curved junction edge are easily computed using the attachment algorithm which was discussed in Section III-D. Accordingly, the ith edge unit is obtained as follows

$$\hat{e}_i = \frac{\vec{P}_{CE_{i+1}} - \vec{P}_{CE_i}}{|\vec{P}_{CE_{i+1}} - \vec{P}_{CE_i}|} \quad ; \quad i = 1,2,3,\ldots,N. \tag{4.34}$$

The unit vector $\hat{i}$ is determined in the following manner. Since the curved junction edge lies on the ellipsoid surface, one must use the elliptic perturbed cylinder or elliptic cone method which was discussed in Section III-C to find the incident unit vectors. The unit vector $\hat{i}$ for each of N sample points along the curved junction edge is expressed by

$$\tag{4.35}$$

$$\hat{i} = \hat{t}_1 \cos\beta + \hat{t}_e \sin\beta$$

138

(a) Diffraction from the curved junction edge.

Figure 4.8. Illustration of the diffracted field by the curved junction edge.
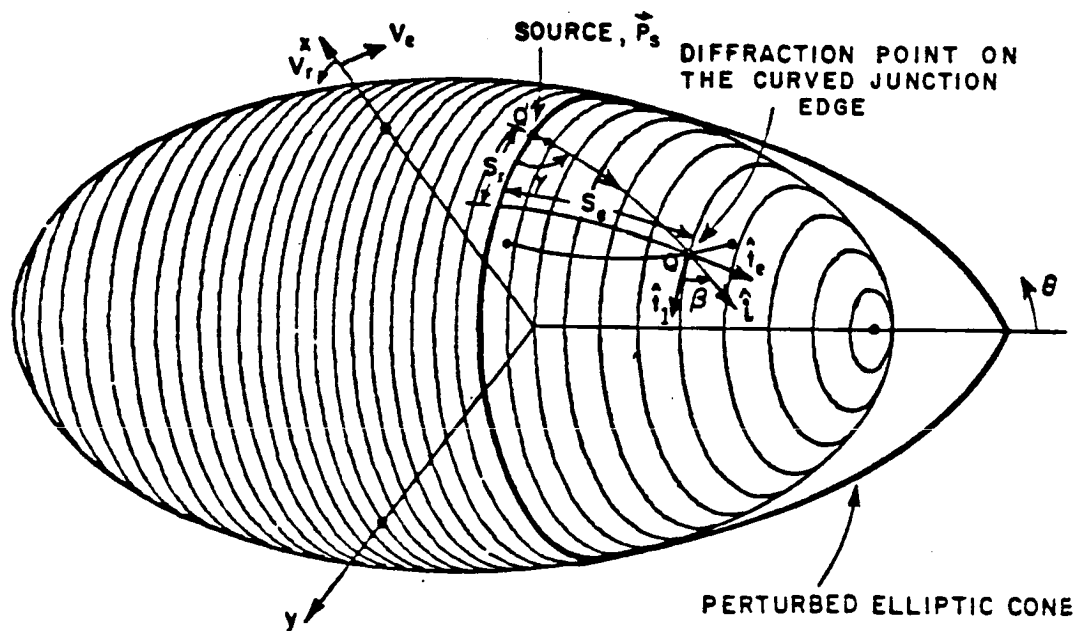
(b)   Incident unit vector on the curved junction edge.
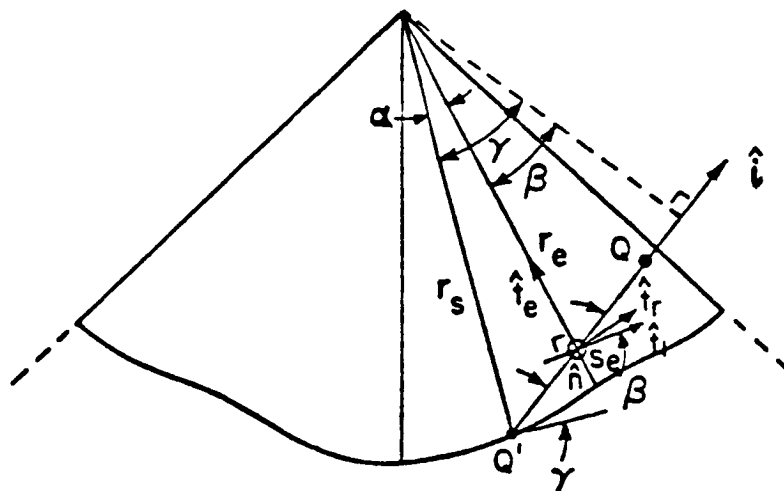
(c)   Incident unit vector on a developed elliptic cone.

Figure 4.8.   (Continued).

where β denotes the angle between $\hat{t}_1$ and the unit vector $\hat{i}$. The location of the source and the ith sample point on the curved junction edge are defined as $\vec{P}_s(V_{es}, V_{rs})$ and $\vec{P}_i(V_{ei}, V_{ri})$, respectively.

For the antennas mounted on the off-mid section of an ellipsoid, the perturbed cone method is used in the calculation of incident unit vectors as shown in Figures 4.8(b) and (c). The β angle is, then, given by

$$\beta = \gamma - \alpha \quad , \tag{4.36}$$

where α was given in Equation (3.86). The γ is obtained from the following geodesic equation:

$$r_e \cos(\gamma - a) = r_s \cos\gamma \quad , \tag{4.37}$$

where

$$r_s = (a_s^2 \cos^2 V_{rs} + b_s^2 \sin^2 V_{rs} + z_s^2 \cot^4 V_{es})^{1/2} \quad , \tag{4.38}$$

$$r_e = (a_s^2 \cos^2 V_{ri} + b_s^2 \sin^2 V_{ri} + z_s^2 \cot^4 V_{es})^{1/2} - S_e \quad , \tag{4.39}$$

and

$$S_e = \int_{V_{es}}^{V_{ei}} [c^2 \cos^2 V_e' + (a^2 \cos^2 V_{ri} + b^2 \sin^2 V_{ri}) \sin^2 V_e']^{1/2} \cdot dV_e' \quad , \tag{4.40}$$

with

141

$$a_s = a \cos V_{es}$$

$$b_s = b \cos V_{es} \qquad .$$

and

$$z_s = a \sin V_{es} \qquad . \qquad (4.41)$$

Thus, γ is given by

$$\gamma = \tan^{-1} \left(\frac{r_s - r_e \cos\alpha}{r_e \sin\alpha} \right) \qquad . \qquad (4.42)$$

Combining Equations (4.35), (4.36) and (4.42), the unit vector $\hat{i}$ at each of N sample points along the curved junction edge is then computed.

For the antennas mounted on the mid-section of an ellipsoid, the elliptic cylinder perturbation method is used in the calculation of the incident unit vector $\hat{i}$ along the curved edge. Note that the angles β and γ are the same for the elliptic cylinder case. The geodesic equation is, then, given by

$$\beta = \tan^{-1} \frac{S_e}{S_r} \qquad (4.43)$$

where

$$S_e = \int_0^{V_{ei}} \{c^2 \cos^2 V_e' + (a^2 \cos^2 V_r + b^2 \sin^2 V_r) \sin^2 V_e'\}^{1/2} \, dV_e' \qquad (4.44)$$

142

and

$$S_r = \int_{V_{rs}}^{V_{ri}} \cos V_{es} \left\{ a^2 \sin^2 V_r' + b^2 \cos^2 V_r' \right\}^{1/2} dV_r' \quad . \tag{4.45}$$

Combining Equations (4.35) and (4.43), the incident unit vector $\hat{i}$ at each of the N sample points along the curved junction edge is, then, computed.

After the edge unit vector and the incident unit vector at each of the N sample points on the curved edge are computed and stored, the actual diffraction point on the curved edge is determined using the diffraction point search algorithm for the shadow region.

4. Diffracted Field Calculation

Assuming that the ray path is identified, the diffracted field for the mth edge of the jth plate is given by

$$\begin{bmatrix} E_\parallel^d(\vec{P}_r) \\ E_\perp^d(\vec{P}_r) \end{bmatrix} = - \begin{bmatrix} D_s(L,\phi',\phi,\beta_0,n) & 0 \\ 0 & D_h(L,\phi',\phi,\beta_0,n) \end{bmatrix} \begin{bmatrix} E_\parallel^s(\vec{P}_d) \\ E_\perp^s(\vec{P}_d) \end{bmatrix} Ae^{-jks} \quad . \tag{4.46}$$

The parameters needed for the diffracted field calculation are given as follows:

$$L = \frac{s^d(s^i + \ell)}{s^d + s^i + \ell} \sin^2 \beta_0 \quad , \tag{4.47}$$

143

$$\beta_o = \sin^{-1} \left(\sqrt{1-(\hat{d}\cdot\hat{e}_{m,j})^2} \right) \tag{4.48}$$

$$\phi = \tan^{-1} \left[\frac{\hat{d}\cdot\hat{n}_j}{\hat{d}\cdot\hat{b}_{m,j}} \right] \tag{4.49}$$

$$\phi' = \tan^{-1} \left[\frac{-\hat{i}\cdot\hat{n}_j}{-\hat{i}\cdot\hat{b}_{m,j}} \right] \tag{4.50}$$

$$A = \sqrt{\frac{s^i}{s^d(s^d+s^i)}} \tag{4.51}$$

and

$$s = \left[\begin{array}{l} s^d \text{ in the near field, and} \\ -\hat{P}_r\cdot\vec{P}_d \text{ in the far field.} \end{array} \right. \tag{4.52}$$

Note that $\bar{E}^s(\vec{P}_d)$ is the field incident on the edge at the diffraction point and is obtained using the source field solution which was discussed in Section IV-B. The incident field can then be expressed as

$$E_i^s(\vec{P}_d) = E^n(\hat{n}\cdot\hat{\beta}') + E^b(\hat{b}\cdot\hat{\phi}') \tag{4.53}$$

and

144

$$E_{\perp}^{s}(\vec{P}_d) = E^n(\hat{n}\cdot\hat{\beta}') + E^b(\hat{b}\cdot\hat{\phi}') \qquad . \tag{4.54}$$

The unit vectors of the edge fixed coordinate system for the incident ray are given by

$$\hat{\phi}' = \hat{n}_j \cos\phi' - \hat{b}_{m,j} \sin\phi' \tag{4.55}$$

and

$$\hat{\beta}' = \hat{\phi}' \times \hat{i} \qquad . \tag{4.56}$$

Now, the diffracted field in terms of the rectangular coordinate system for the mth edge of the jth plate is given by

$$\bar{E}_{m,j}^{d} = \hat{\beta} E_{\parallel}^{d} + \hat{\phi} E_{\perp}^{d} \tag{4.57}$$

with

$$\hat{\phi} = \hat{n}_j \cos\phi - \hat{b}_{m,j} \sin\phi \tag{4.58}$$

and

$$\hat{\beta} = \hat{\phi} \times \hat{d} \qquad . \tag{4.59}$$

These unit vectors $(\hat{\phi}', \hat{\beta}', \hat{\phi}, \hat{\beta})$ will be used in the following sections without defining them again.

145

5. Corner Diffracted Field Calculation

The corner diffracted field is usually very small except near the edge diffraction shadow boundaries. Therefore, the physical edge length is extended by 5 wavelengths for the corner diffracted field calculation in that the current corner diffraction coefficients are based on the concept of equivalent edge current [31,33], which would exist on this edge when extended to infinity, as discussed in Section II-C.2.

There are two corner diffraction terms associated with each finite plate edge. However, for the edges attached to the fuselage, there is only one corner diffraction term involved in the calculation. The corner diffracted field and its related parameters are defined in Section II-C.2. Some parameters related to the geometry given in Figure 4.9 are defined as follows:

$$\beta_c = \cos^{-1} (\hat{s}_c \cdot \hat{e}_{m,j}) \quad , \tag{4.60}$$

$$\beta_{oc} = \cos^{-1} (\hat{s} \cdot \hat{e}_{m,j}) \tag{4.61}$$

and

$$L_c = \frac{s_c s}{s_c + s} \quad . \tag{4.62}$$

The total corner diffracted field is obtained by superimposing the corner diffracted fields from each of the corners.
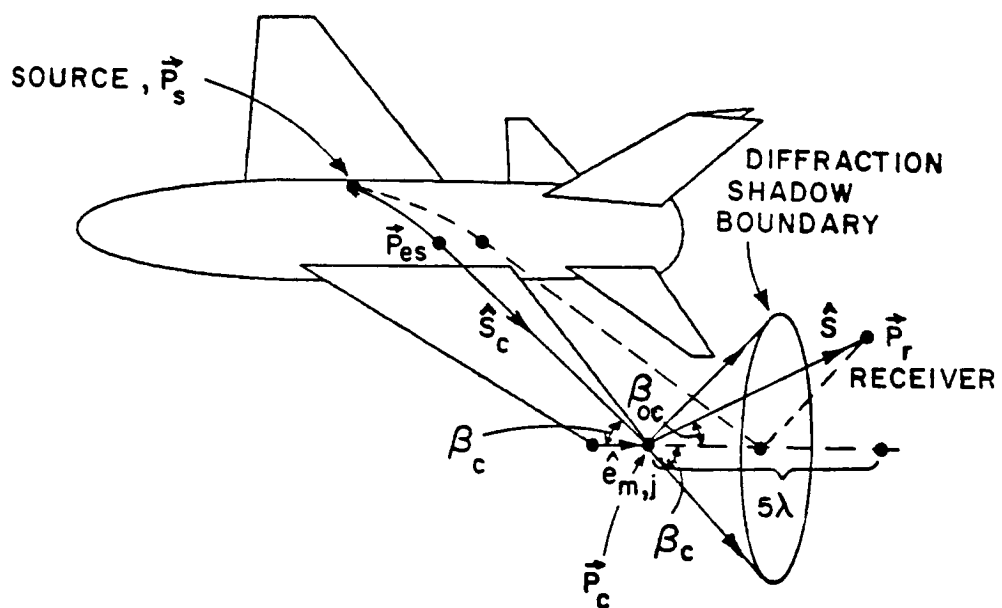
Figure 4.9. Illustration of the corner diffracted field.

E. FIELD CALCULATION FOR HIGHER ORDER TERMS

In addition to the above direct scattering from a structure, the rays reflected or diffracted from one structure tend to interact with the other structures causing various higher order UTD terms (i.e., double reflected, reflected-diffracted, diffracted-reflected, and double diffracted).

1. Double Reflected Field

The double reflected field $\bar{E}^{rr}$ can be obtained following a procedure similar to the single reflected field in Section IV-C. As shown in Figure 4.10, the images of the receiver location with respect to the jth plate and j^{th}-k^{th} plates are given, respectively, by

$$\vec{P}_r^{I_j} = \vec{P}_r - 2\hat{n}_j \cdot (\vec{P}_r - \vec{P}_{c_{1,j}}) \quad , \tag{4.63}$$

and

$$\vec{P}_r^{I_j,k} = \vec{P}_r^{I_j} - 2\hat{n}_k \cdot (\vec{P}_r^{I_j} - \vec{P}_{c_{1,k}}) \quad . \tag{4.64}$$

The source field solution is, then, used to compute the electric field $\bar{E}^s$ at the image position $\vec{P}_r^{I_j,k}$. This field would exist at that point if the jth and k^{th} plates were not present. Then the double reflected field is, then, given by

$$[\bar{E}^{r_k r_j}(\vec{P}_r)] = [T]_j [T]_k [\bar{E}^s(\vec{P}_r^{I_j,k})] \quad . \tag{4.65}$$

148

Figure 4.10. Double reflection geometry.

Note that $[T]_j$ and $[T]_k$ satisfy the boundary conditions on the jth and k^{th} plates, respectively, and the matrix $[T]$ was defined in Section IV-C.

2. Reflected - Diffracted Field

A typical geometry for the reflected diffracted field is illustrated in Figure 4.11. To begin the solution, one needs to define the images of the second plate corners and the receiver location with respect to the first plate. From the geometry of Figure 4.11, the image point of the receiver with respect to the kth plate is given by

$$\vec{P}_r^{I_k} = \vec{P}_r - 2\hat{n}_k \cdot (\vec{P}_r - \vec{P}_{c_{1,k}})\ .$$

(4.66)

The images of the mth corner of the mth edge of the jth plate with respect to the kth plate are given by

$$\vec{P}_{c_{m,j}}^{I_k} = \vec{P}_{c_{m,j}} - 2\hat{n}_k \cdot (\vec{P}_{c_{m,j}} - \vec{P}_{c_{1,k}})$$

(4.67)

and

$$\hat{e}_{m,j}^{I_k} = \frac{\vec{P}_{c_{m+i,j}}^{I_k} - \vec{P}_{c_{m,j}}^{I_k}}{|\vec{P}_{c_{m+i,j}}^{I_k} - \vec{P}_{c_{m,j}}^{I_k}|}\ ,$$

(4.68)

Figure 4.11. Reflected-diffracted geometry.
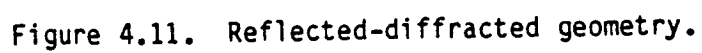
respectively. The value $\hat{i} \cdot \hat{e}_{m,j}^{I_k}$ is then computed and stored at the N

sample points along each edge of the image plate. The iterative

numerical technique which was discussed in Section IV-D is used to find

the diffraction point $\vec{P}_d^{I_k}$ on the edge of the image plate. From the

diffraction point on the image plate, the actual diffraction point $\vec{P}_d$ at

the mth edge of the jth plate is obtained as follows:

$$\vec{P}_d = \vec{P}_d^{I_k} + 2\hat{n}_k \cdot (\vec{P}_d^{I_k} - \vec{P}_{c_{1,k}}) \quad . \tag{4.69}$$

After the ray path is identified, the source field $\bar{E}^S$ is computed at the

diffraction point $\vec{P}_d^{I_k}$ on the image plate. Next, the reflected field $\bar{E}^{r_k}$

at the actual diffraction point $\vec{P}_d$ is obtained using the single

reflection solution which was discussed in Section IV-C, and is given

by

$$[\bar{E}^{r_k}(\vec{P}_d)] = [T]_k \, [\bar{E}^S(\vec{P}_d^{I_k})] \quad . \tag{4.70}$$

Then the reflected-diffracted field is given by

$$\begin{bmatrix} E_{\|}^{r_k d_{m,j}}(\vec{P}_r) \\ \\ E_{\perp}^{r_k d_{m,j}}(\vec{P}_r) \end{bmatrix} = - \begin{bmatrix} D_s(L,\phi',\phi,\beta_0,n) & 0 \\ \\ 0 & D_h(L,\phi',\phi,\beta_0,n) \end{bmatrix} \begin{bmatrix} E_{\|}^{r_k}(\vec{P}_d) \\ \\ E_{\perp}^{r_k}(\vec{P}_d) \end{bmatrix} Ae^{-jks} \quad . \tag{4.71}$$

152

The parameters needed for the diffracted field calculation are given as follows:

$$L = \frac{s^{rd}(s^r + s^i + \ell)}{s^{rd} + s^r + s^i + \ell} \sin^2\beta_0 \quad , \tag{4.72}$$

$$\phi' = \tan^{-1} \left[\frac{-\hat{s}^r \cdot \hat{n}_j}{-\hat{s}^r \cdot \hat{b}_{m,j}} \right] \quad , \tag{4.73}$$

$$\phi = \tan^{-1} \left[\frac{\hat{s}^{rd} \cdot \hat{n}_j}{\hat{s}^{rd} \cdot \hat{b}_{m,j}} \right] \quad , \tag{4.74}$$

$$\beta_0 = \sin^{-1} \left(\sqrt{1 - |\hat{s}^{rd} \cdot \hat{e}_{m,j}|^2} \right) \quad , \tag{4.75}$$

$$A = \sqrt{\frac{s^r + s^i}{s^{rd}(s^{rd} + s^r + s^i)}} \quad , \tag{4.76}$$

and

$$s = \left[\begin{array}{l} s^{rd} \quad \text{in the near field, and} \\ -\hat{p}_r \cdot \vec{p}_d \quad \text{in the far field} \end{array} \right. \quad . \tag{4.77}$$

153

The reflected-corner diffracted field can be computed following the same procedure as that of the reflected-diffracted field except using the corner diffraction coefficient rather than the edge diffraction coefficient, and is not repeated here.

3. Diffracted-Reflected Field

The geometry for the diffracted-reflected calculation is illustrated in Figure 4.12. To begin the solution, one needs to define the image point of the receiver location with respect to the jth plate which is given by

$$\vec{P}_r^{Ij} = \vec{P}_r - 2\hat{n}_j \cdot (\vec{P}_r - \vec{P}_{c_{1,j}}) \; . \tag{4.78}$$

If one assumes the image point $\vec{P}_r^{Ij}$ as the receiver location, the diffraction point $\vec{P}_d$ along the mth edge of the kth plate can be found through the single diffraction point search technique which was discussed in Section IV-D. The diffracted field at the image point $\vec{P}_r^{Ij}$ is, then, given by

$$\begin{bmatrix} E_{\parallel}^d(\vec{P}_r^{Ij}) \\ E_{\perp}^d(\vec{P}_r^{Ij}) \end{bmatrix} = - \begin{bmatrix} D_s(L,\phi',\phi,\beta_0,n) & 0 \\ 0 & D_h(L,\phi',\phi,\beta_0,n) \end{bmatrix} \begin{bmatrix} E_{\parallel}^s(\vec{P}_d) \\ E_{\perp}^s(\vec{P}_d) \end{bmatrix} Ae^{-jks} \; . \tag{4.79}$$

Figure 4.12. Diffracted-reflected geometry.
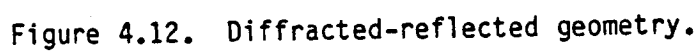
Some interesting parameters for this diffracted field calculation are given as follows:

$$L = \frac{(s^d + s^{dr})(s^i + \ell)}{s^d + s^{dr} + s^i + \ell} \sin^2 \beta_0 \quad , \tag{4.80}$$

$$\beta_0 = \sin^{-1} \left(\sqrt{1 - |\hat{s}^d \cdot \hat{e}_{m,k}|^2} \right) \quad , \tag{4.81}$$

$$\phi' = \tan^{-1} \left[\frac{-\hat{s}^i \cdot \hat{n}_k}{-\hat{s}^i \cdot \hat{b}_{n,k}} \right] \quad , \tag{4.82}$$

$$\phi = \tan^{-1} \left[\frac{\hat{s}^d \cdot \hat{n}_k}{\hat{s}^d \cdot \hat{b}_{n,k}} \right] \tag{4.83}$$

$$A = \sqrt{\frac{s^i}{(s^d + s^{dr})(s^d + s^{dr} + s^i)}} \quad , \tag{4.84}$$

and

$$s = \begin{bmatrix} |\vec{P}_r^{Ij} - \vec{P}_d| & \text{in the near field, and} \\ -\hat{P}_r \cdot \vec{P}_d^{Ij} & \text{in the far field} \end{bmatrix} \quad . \tag{4.85}$$

156

Finally, the diffracted-reflected field is obtained by multiplying the reflected field polarization transformation matrix to the above diffracted field, and is given by.

$$[\bar{E}^{d_m,k^r j}(\vec{P}_r)] = [T]_j \; [\bar{E}^{d_m,k}(\vec{P}_r^{Ij})] \quad . \tag{4.86}$$

For the corner diffracted-reflected field calculation, one needs to use the corner diffraction coefficient rather than the wedge diffraction coefficient. Beside that, the corner diffracted-reflected field can be computed following the same procedure as that for the diffracted-reflected field, and is not repeated here.

4. Double Diffracted Field

The double diffracted field contribution is usually small compared with the other UTD terms. However, when one edge lies in the shadow boundary of the other edge or both diffracted edges are close to the source, a double diffracted field may be significant. A typical geometry for the double diffracted field calculation is illustrated in Figures 4.13(a) and (b). The key to solving for the double diffracted field is to determine the two diffraction points along the diffracting edges for specific source and receiver locations.

EFFECTIVE
SOURCE
$\vec{P}_{es}$ Ist DIFFRACTION

SOURCE   POINT, $\vec{P}_{di}$
$\vec{P}_s$

ℓ $\hat{s}^i$ $\hat{n}_i$ $\hat{b}_{m,j}$ jth PLATE

$\hat{e}_{n,k}$ $\hat{s}^{di}$ 2nd DIFFRACTION
                $\hat{n}_k$ POINT $\vec{P}_{d2}$

kth PLATE

$\hat{s}^{d2}$

$\hat{b}_{n,k}$

$\vec{P}_r$,RECEIVER
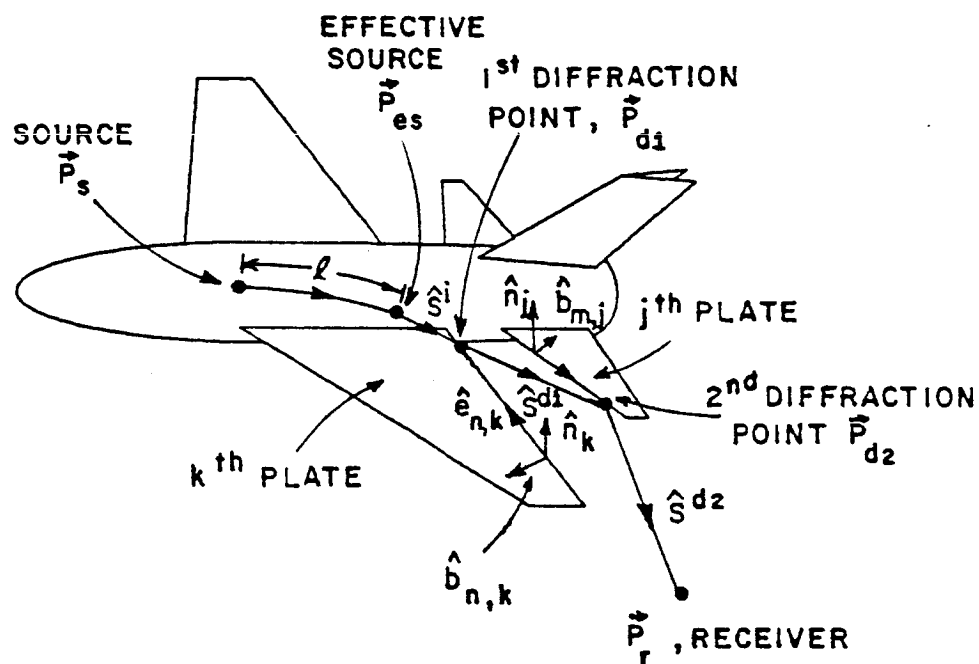
(a) Double diffracted field when the two diffraction points
    lie on the different plates.

Figure 4.13. Illustration of the double diffracted field.
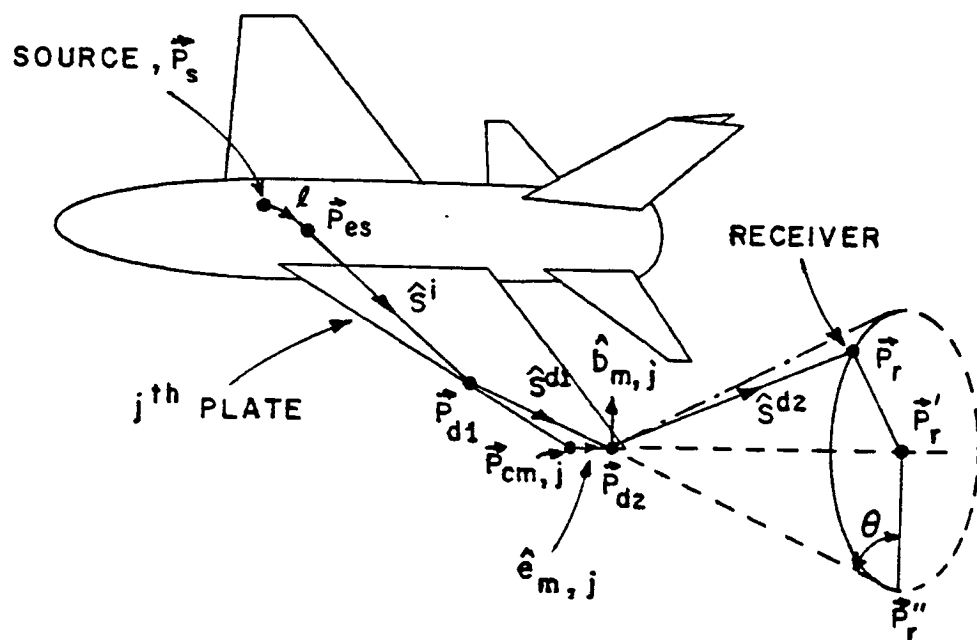
(b) Double diffracted field when both diffraction points
     lie on the same plate.

Figure 4.13. (Continued).

159

When the two diffraction points lie on different plates as shown in Figure 4.13(a), one needs to first compute and store the values $\hat{e}_{m,j} \cdot \hat{s}^{d_1}$ at the N sample points along the second edge $\hat{e}_{m,j}$. The N sample points along the second edge are assumed as the receiver locations and the first edge $\hat{e}_{n,k}$ as the diffracting edge. Then the value $\hat{e}_{m,j} \cdot \hat{s}^{d_1}$ at each sample point on the second edge can be computed using the usual single diffracted field algorithm and stored. In this procedure, the corresponding diffraction point $\vec{P}_{d_1}$ on the first diffraction edge for each sample point on the second edge is also determined using the diffraction point search technique which was discussed in Section IV-D. Next the diffraction point $\vec{P}_{d_2}$ on the second edge is found using the diffraction law, i.e., $\hat{e}_{m,j} \cdot \hat{s}^{d_1} = \hat{e}_{m,j} \cdot \hat{s}^{d_2}$. After the ray path is identified, the double diffracted field is computed in the following manner. The incident field $\bar{E}^{d_{m,j}}$ at the second diffraction point is given by

$$
\begin{bmatrix} E_{\parallel}^{d_{m,j}}(\vec{P}_{d_2}) \\ E_{\perp}^{d_{m,j}}(\vec{P}_{d_2}) \end{bmatrix} = - \begin{bmatrix} D_s(L_1,\phi_1',\phi_1,\beta_{01},n_1) & 0 \\ 0 & D_s(L_1,\phi_1',\phi_1,\beta_{01},n_1) \end{bmatrix} \begin{bmatrix} E_{\parallel}^{s}(\vec{P}_{d_1}) \\ E_{\perp}^{s}(\vec{P}_{d_1}) \end{bmatrix}
$$

$$
\cdot A_1 e^{jks^{d_1}}
$$

(4.87)

where $\bar{E}^s$ is the source field, which was discussed in Section IV-B at the first diffraction point $\vec{P}_{d_1}$. The parameters needed for this diffracted field calculation are given as follows:

160

$$L_1 = \frac{s^{d_1}(s^i + \ell)}{s^{d_1} + s^i + \ell} \sin^2 \beta_{o1} \quad , \tag{4.88}$$

$$\beta_{o1} = \sin^{-1} \left(\sqrt{1 - |\hat{s}^{d_1} \cdot \hat{e}_{m,j}|^2} \right) \quad , \tag{4.89}$$

$$\phi_1' = \tan^{-1} \left[\frac{-\hat{s}^i \cdot \hat{n}_j}{-\hat{s}^i \cdot \hat{b}_{m,j}} \right] \quad , \tag{4.90}$$

$$\phi = \tan^{-1} \left[\frac{\hat{s}^{d_1} \cdot \hat{n}_j}{\hat{s}^{d_1} \cdot \hat{b}_{m,j}} \right] \quad , \tag{4.91}$$

and

$$A = \sqrt{\frac{s^i}{s^{d_1}(s^{d_1} + s^i)}} \quad . \tag{4.92}$$

Finally, the double diffracted field at the receiver location is given by

$$\begin{bmatrix} E_{\parallel}^{d_m,j^{d_n},k}(\vec{P}_r) \\ E_{\perp}^{d_m,j^{d_n},k}(\vec{P}_r) \end{bmatrix} = - \begin{bmatrix} D_s(L_2, \phi_2', \phi_2, \beta_{o2}, n_2) & 0 \\ 0 & D_s(L_2, \phi_2', \phi_2, \beta_{o2}, n_2) \end{bmatrix} \begin{bmatrix} E_{\parallel}^{d_m,j}(\vec{P}_{d_2}) \\ E_{\perp}^{d_m,j}(\vec{P}_{d_2}) \end{bmatrix}$$

$$\cdot A_2 e^{-jks^{d_2}} \quad . \tag{4.93}$$

The parameters needed for this diffracted field calculation are given as follows:

$$L_2 = \frac{s^{d_2} s^{d_1}}{s^{d_2} + s^{d_1}} \sin^2 \beta_{02} \quad , \qquad (4.94)$$

$$\beta_{02} = \sin^{-1} \left(\sqrt{1 - |\hat{s}^{d_2} \cdot \hat{e}_{n,k}|^2} \right) \quad , \qquad (4.95)$$

$$\phi_2' = \tan^{-1} \left[\frac{-\hat{s}^{d_1} \cdot \hat{n}_k}{-\hat{s}^{d_1} \cdot \hat{b}_{n,k}} \right] \quad , \qquad (4.96)$$

$$\phi_2 = \tan^{-1} \left[\frac{\hat{s}^{d_2} \cdot \hat{n}_k}{\hat{s}^{d_2} \cdot \hat{b}_{n,k}} \right] \quad , \qquad (4.97)$$

$$A_2 = \sqrt{\frac{s^{d_1}}{s^{d_2}(s^{d_1} + s^{d_2})}} \quad , \qquad (4.98)$$

and

$$s^{d_2} = \left[\begin{array}{l} \vec{P}_r - \vec{P}_{d_2} \quad \text{in the near field, and} \\ \\ -\hat{P}_r \cdot \vec{P}_{d_2} \quad \text{in the far field} \quad . \end{array} \right. \qquad (4.99)$$

If both diffraction points lie on the same plate as shown in Figure 4.13(b), the ray path should be determined in a different way. The first step is to project the receiver onto the edge which contains the second diffraction point which is given by

$$\vec{P}_r^{\,\prime} = \vec{P}_{c_{m,j}} + [(\vec{P}_r - \vec{P}_{c_{m,j}}) \cdot \hat{e}_{m,j}] \, \hat{e}_{m,j} \quad . \tag{4.100}$$

Next, project the receiver onto the plane which contains the plate itself and the second incident ray path $\hat{s}^{d_1}$. Then, the projection of the receiver is given by

$$\vec{P}_r^{\,\prime\prime} = \vec{P}_r^{\,\prime} - |\vec{P}_r - \vec{P}_r^{\,\prime}| \, \hat{b}_{m,j} \quad . \tag{4.101}$$

Assuming that the receiver is located at $\vec{P}_r^{\,\prime\prime}$, one can find the first diffraction point $\vec{P}_{d_1}$ using the single diffraction point search technique which was discussed in Section IV-D. After the first diffraction point $\vec{P}_{d_1}$ is determined, the second diffraction point $\vec{P}_{d_2}$ is given by

$$\vec{P}_{d_2} = \vec{P}_{d_1} + \left| |\vec{P}_r^{\,\prime\prime} - \vec{P}_{d_1}| - \frac{|\vec{P}_r - \vec{P}_r^{\,\prime}|}{\cos\theta} \right| \, \hat{s}^{d_1} \quad , \tag{4.102}$$

where

$$\theta = \pi - \cos^{-1} (\hat{b}_{m,j} \cdot \hat{s}^{d_1}) \quad , \tag{4.103}$$

and

$$\hat{s}^{d_1} = \frac{\vec{P}_r'' - \vec{P}_{d_1}}{|\vec{P}_r'' - \vec{P}_{d_1}|} \qquad \cdot \, \, \tag{4.104}$$

After both diffraction points are determined, the double diffracted
field can be computed in the same way as done for the diffraction points
on the different plates.

It is noted that the parallel component of the field incident on
the second edge is always zero for this case, and if the diffracting
plate is a half plane (i.e., n=2) there are two perpendicular fields
incident on the second edge as shown in Figure 4.14.

The diffracted-corner diffracted, corner diffracted-diffracted and
double corner diffracted terms can be computed using the same procedure
as done for the double diffracted field, however, these terms are
usually very small.

F. SHADOWING ALGORITHM

After the ray path is determined using the previous field
calcualtion algorithms, one must then examine the total ray path to see
whether or not it intersects an obstacle. If the ray path is not
interrupted, the field value is computed and superimposed with other
terms. On the other hand, if the ray path is interrupted, the field is
not computed.
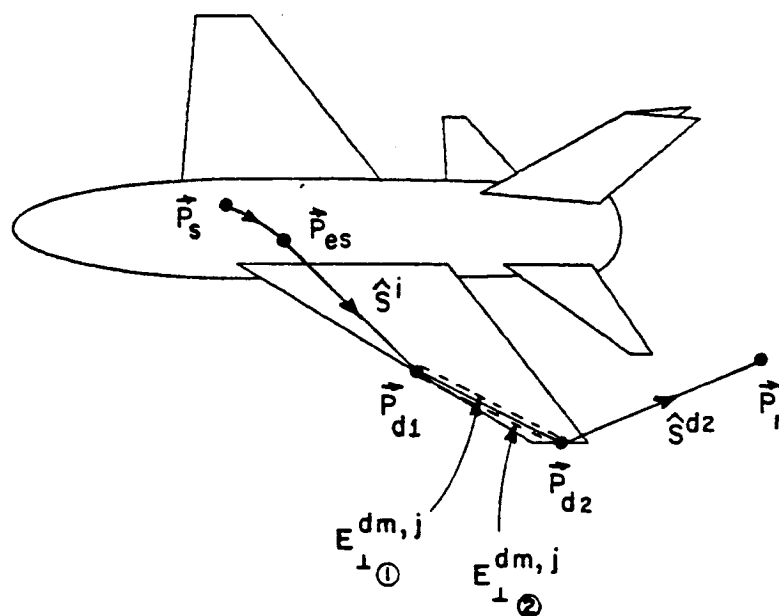
(a) 3- DIMENSIONAL VIEW
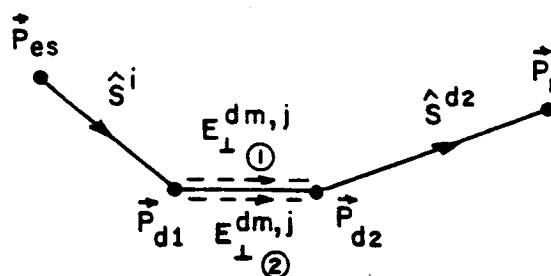
(b) SIDE VIEW

Figure 4.14. Two perpendicular components of the field incident to the second edge.

165

First of all, it is necessary to decide whether the incident ray is toward the plate. This can be done by determining the value of the parameter C_1 which is given by

$$C_1 = [\hat{n}_j \cdot (\vec{P}_r - \vec{P}_{es})] \cdot [\hat{n}_j \cdot (\vec{P}_{c_{1,j}} - \vec{P}_{es})] \quad . \qquad (4.105)$$

If the value of C_1 is less than or equal to zero, such as the point $\vec{P}_1$ in Figure 4.15, the ray cannot be interrupted by the plate. Otherwise, a next step is needed. From the geometry given in the figure, the intersection point between the incident ray and plate of the jth plate is given by

$$\vec{P}_H = \vec{P}_{es} + C_2(\vec{P}_r - \vec{P}_{es}) \quad , \qquad (4.106)$$

where

$$C_2 = \frac{\hat{n}_j \cdot (\vec{P}_{c_{1,j}} - \vec{P}_{es})}{\hat{n}_j \cdot (\vec{P}_r - \vec{P}_{es})} \quad . \qquad (4.107)$$

If the value of C_2 is greater than one, then the ray cannot reach to the jth plate such as the point $\vec{P}_2$ as shown in the figure. Otherwise, one more step is needed to decide whether the ray passes through the plate which is defined by corners. For this test, the parameter C_3 is used and given by

166

Figure 4.15. Illustration of the shadowing algorithm.

167

$$C_3 = \left| \sum_{m=1}^{N_j} \theta_m \right| - \pi \quad , \qquad \qquad (4.108)$$

where

$$\theta_m = \tan^{-1} \left[\frac{\hat{n}_j \cdot [(\vec{P}_{C_{m,j}} - \vec{P}_H) \times (\vec{P}_{C_{m+1,j}} - \vec{P}_H)]}{(\vec{P}_{C_{m-j}} - \vec{P}_H) \cdot (\vec{P}_{C_{m+1,j}} - \vec{P}_H)} \right] \quad , \qquad (4.109)$$

and N_j is the total number of corners used to define the jth plate. If the value of C_3 is less than zero, then the ray is not shadowed by the plate such as the point $\vec{P}_3$ in the figure. Otherwise, the ray is shadowed by the plate such as $\vec{P}_4$ in the figure.

All ray paths for each UTD term are tested with this shadowing algorithm to decide whether or not the UTD term is included in the total field. This completes the total field computation.

CHAPTER V

ANALYSIS OF AIRBORNE ANTENNA RADIATION PATTERNS

A. INTRODUCTION

Using the fuselage simulation techniques and the field calculation
algorithms presented earlier, the Ellipsoid-Model Aircraft Code [15] has
been developed to compute and superimpose the various UTD terms for an
arbitrary near or far field pattern.

To demonstrate the capability of this new analytic solution,
various airborne antenna radiation patterns are analyzed using the code.
Some radiation patterns that have been previously computed with old
programs (Elliptic cylinder-model Aircraft Code [40,45] or Prolate
spheroid-Model Aircraft Code [24]) are also computed and presented here
in that this new solution provides an improved result in most cases.
The validity of this analytic solution is also verified by the
comparisons between the calculated and measured data for the wide
variety of shapes such as commercial, private and fighter aircraft,
missiles, and spacecraft. Most of these comparisons are in terms of

actual aircraft simulations that have been used in the past for verification purposes. The solutions are presented in terms of the radiation patterns of the three basic elements (i.e., axial slot, circumferential slot, and monopole) which can be used to simulate an arbitrary fuselage mounted antenna if the aperture distribution is known.

In order to examine various conical pattern cuts, a cartesian coordinate system (x,y,z) originally defining the simulation model is now rotated into a new system (x_p,y_p,z_p) as shown in Figure 5.1. Note that the new cartesian coordinates are found by first rotating about the z-axis an angle ϕ_c and then about the y-axis an angle θ_c. The pattern is, then, taken in the (x_p,y_p,z_p) coordinate system with θ_p fixed. The coordinate systems that apply for the principal plane pattern cuts (i.e., roll, elevation, and azimuth patterns) are illustrated in Figure 5.2.

To begin any simulation of an aircraft, one needs to start with a set of scale model drawings. For our purposes, Jane's book [41] "All the World's Aircraft" is most appropriate in that it provides a reasonable line drawing for a wide variety of aircraft.

B. COMMERCIAL AIRCRAFT

This section presents various radiation pattern results for different antennas, locations and commercial aircraft. Measured radiation patterns were provided by NASA (Hampton, Virginia) for a
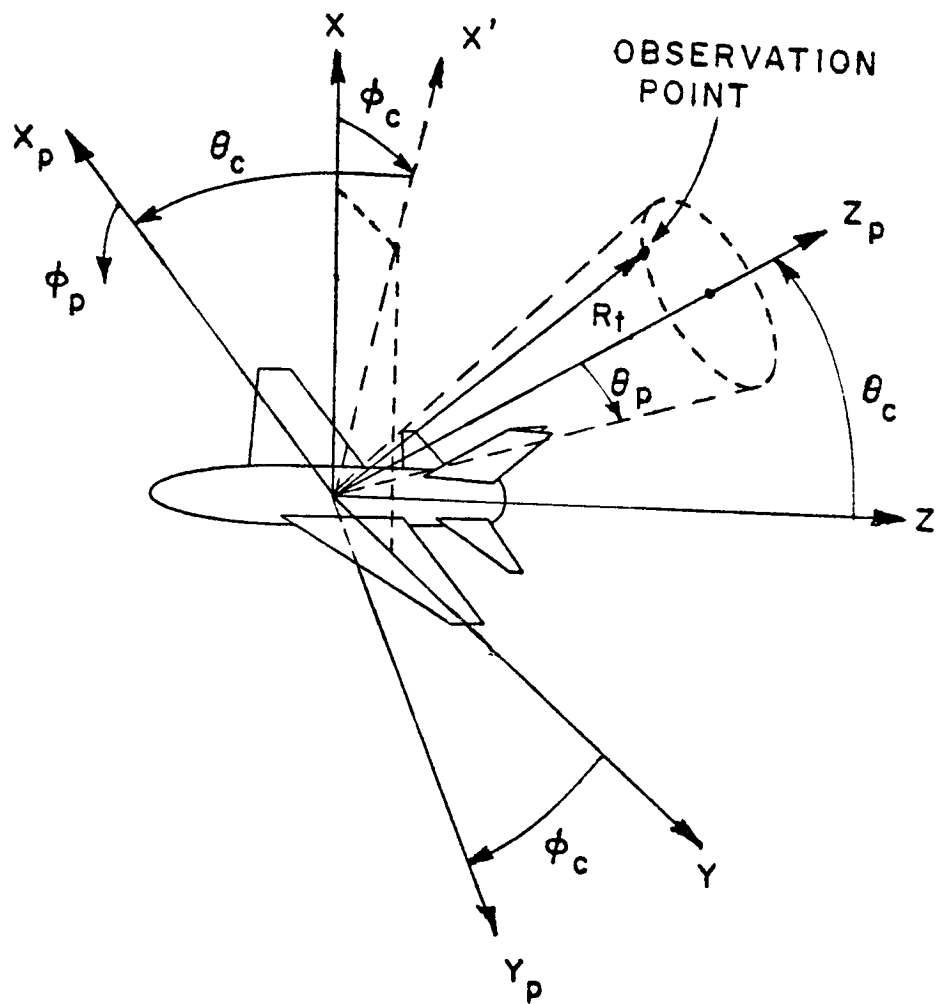
Figure 5.1. Definition of pattern axis.

171
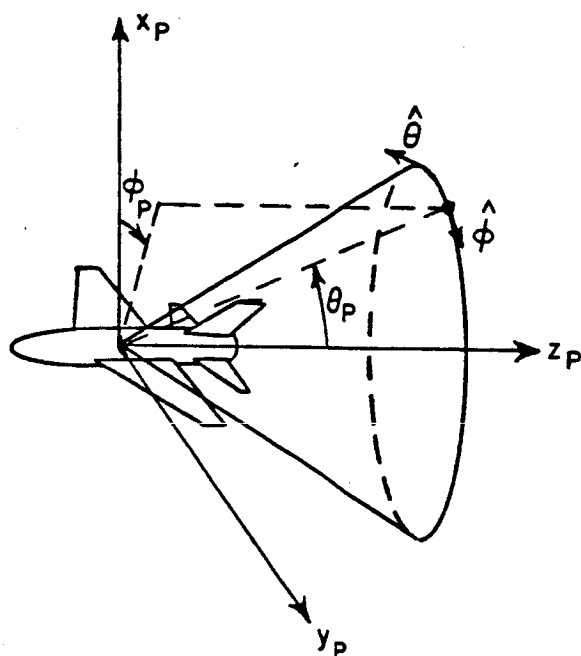
(a) ROLL PLANE PATTERN COORDINATES ($\theta_c = 0°, \phi_c = 0°$)
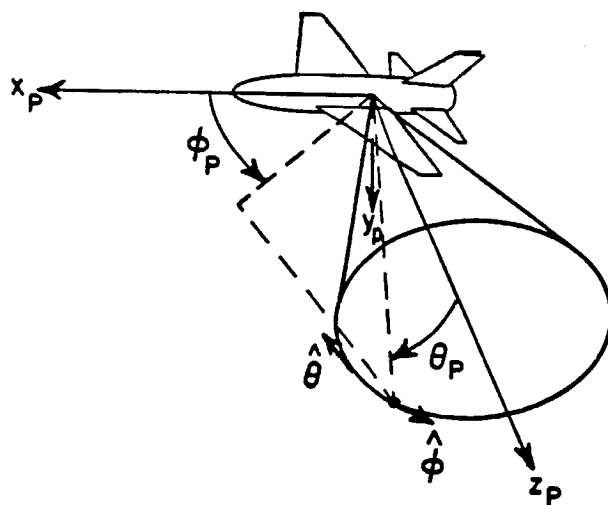
(b) ELEVATION PLANE PATTERN COORDINATES ($\theta_c = 90°, \phi_c = 90°$)

Figure 5.2. Transformed coordinate systems for the
principal plane pattern cuts.
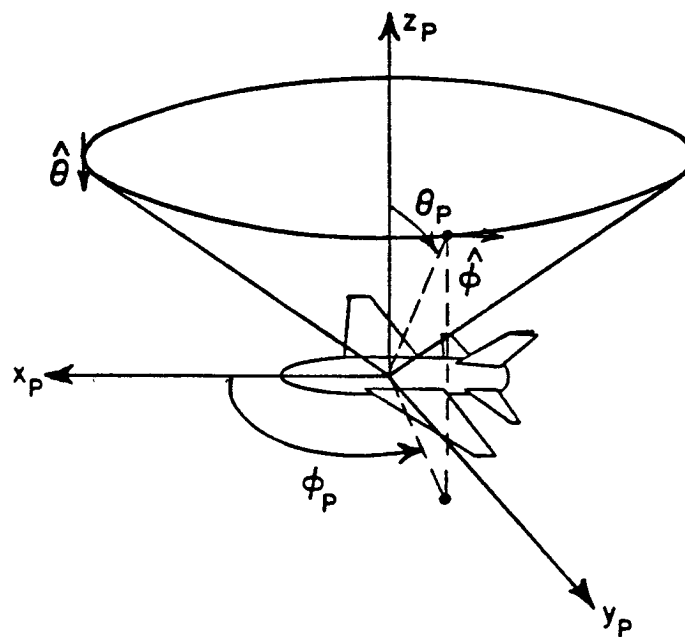
(c) AZIMUTH PLANE PATTERN COORDINATES $(\theta_c = 90°, \phi_c = 0°)$

Figure 5.2. (Continued.)

173

Boeing 737 and KC-135 aircraft. Since most commercial aircraft are similar to the 737 and KC-135, one can assume similar results would apply for other such structures., However, if the aircraft of interest deviates to a high degree from these geometries, one must verify his results before he can conclude their accuracy. Once that new configuration is verified, the class of geometries that can be treated increases accordingly.

1. Boeing 737 Aircraft

The Boeing 737 aircraft as shown in Figure 5.3 is most interesting in that extensive experimental work [42,43,44] is available.

One of the major problems in the design of a safe, reliable and accurate approach and landing system known as the Microwave Landing System (MLS) is the location of the antennas on the aircraft structure in order to achieve the desired radiation coverage. For the Beoing 737 aircraft, Stations 220, 250, and 305 on the top of the fuselage and Stations 222 and 950 on the bottom of the aircraft, as shown in Figure 5.4 were proposed as test locations for the antenna installation. In order to determine the best location for the MLS application, the radiation patterns for each test location was analyzed and measured.

Figure 5.5 illustrates the computer model which is used to simulate the Boeing 737 aircraft for the top mounted antennas. A composite ellipsoid (77" x 74" x 830" x 308") is chosen to simulate the fuselage

174
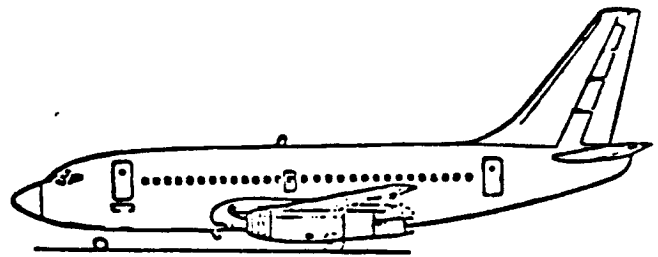
(a) SIDE VIEW
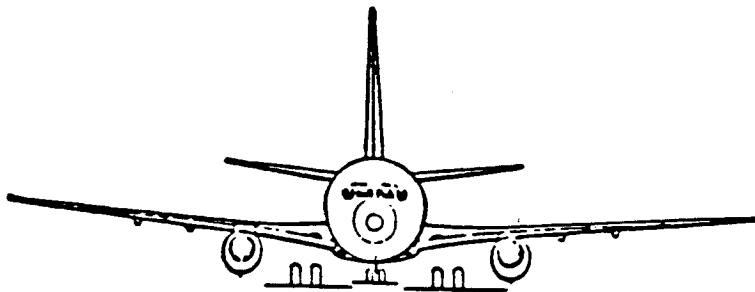
(b) FRONT VIEW
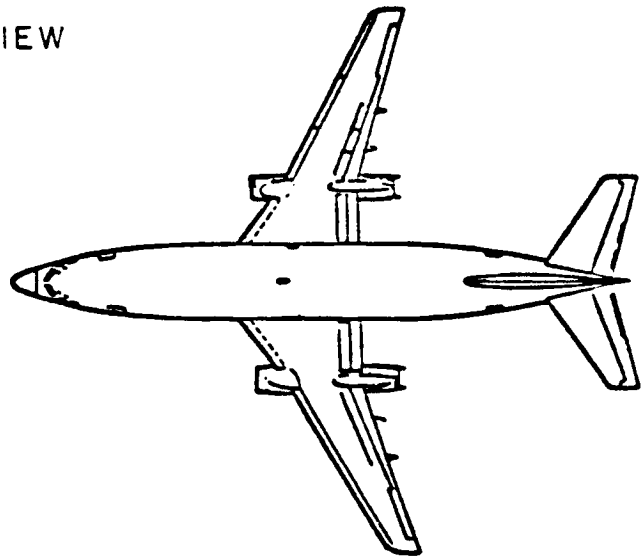
(c) TOP VIEW

Figure 5.3. Boeing 737 aircraft.

175

ANTENNA LOCATION

A – STATION 220
B – STATION 250
C – STATION 305
D – STATION 222
E – STATION 950
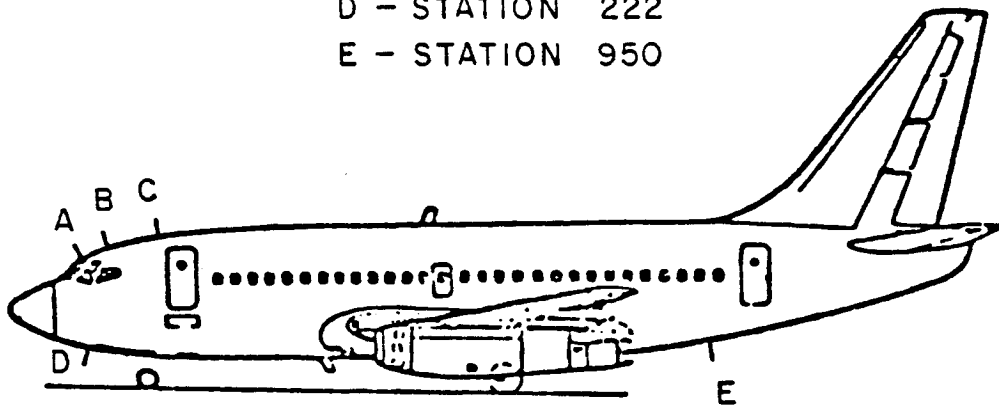
Figure 5.4. Test locations for the antenna installation on the Boeing 737 aircraft.

176

ANTENNA LOCATION

(a) SIDE VIEW

(b) FRONT VIEW

(c) TOP VIEW
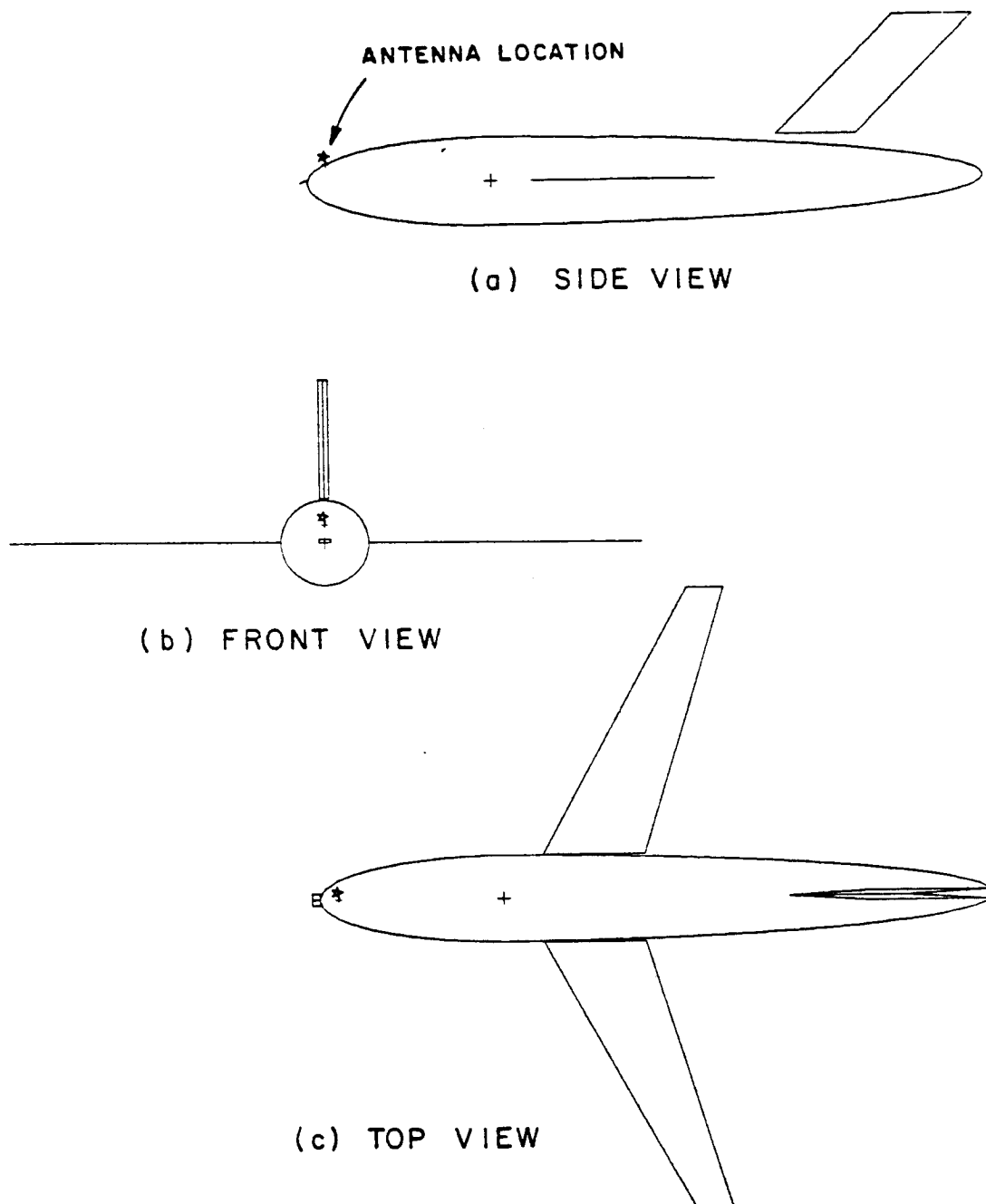
Figure 5.5. Computer simulated model of a Boeing 737 aircraft. The antenna is located at Station 220.

177 .

surface of the actual aircraft as accurately as possible, especially near the antenna location. It is assumed here that the radome is perfectly transparent. This leaves a short, blunt-looking nose section which extends out from the front of the aircraft. It was found that the nose section normally has little effect on the resulting pattern. Thus, the cockpit nose section for simplicity is simulated by a finite flat plate. The wings and vertical stabilizers are approximated by finite flat plates which results in a simple model for the aircraft. The significant features associated with the vertical stabilizer are the leading edge and thickness of the two flat plates used to approximate those features of the actual vertical stabilizer. The thickness is important in that it tends to shadow the direct field from the antenna for aft radiation directions. For the sake of efficiency, no horizontal stabilizers are included in this model.

The radiation patterns for a $\lambda/4$ monopole mounted at Station 220 above the cockpit on a Boeing 737 aircraft are, then, calculated using the model just described. The three principal plane results are shown in Figures 5.6 to 5.8 and found to be in very good agreement with measurements. The experimental work was performed by the technical staff at NASA (Hampton, Virginia) using a 1/11th scale model of a Boeing 737 aircraft. But it is noted that the measured results have some asymmetry in the patterns. This could be attributed to misalignment of
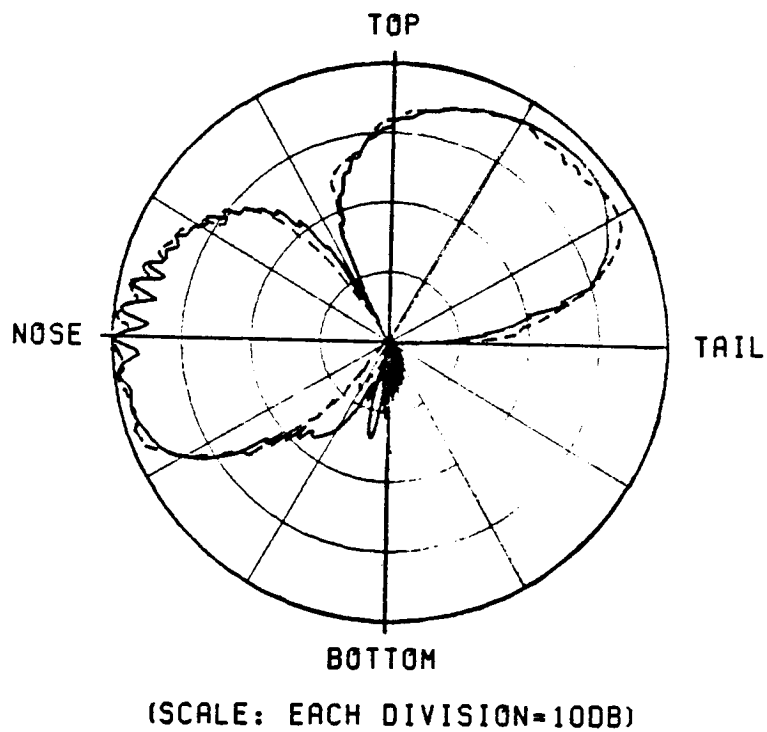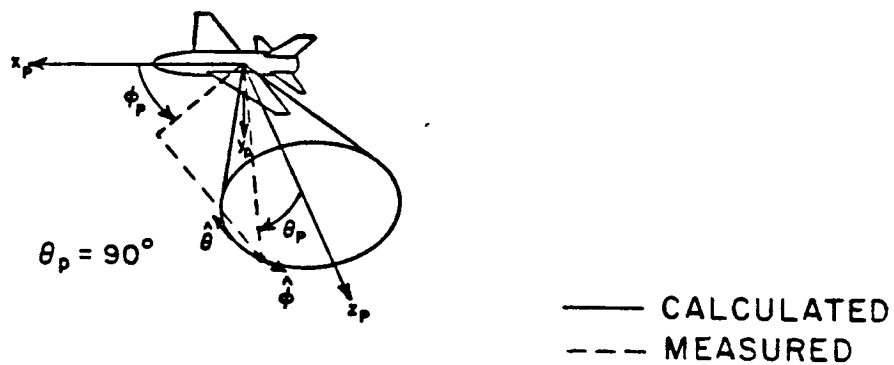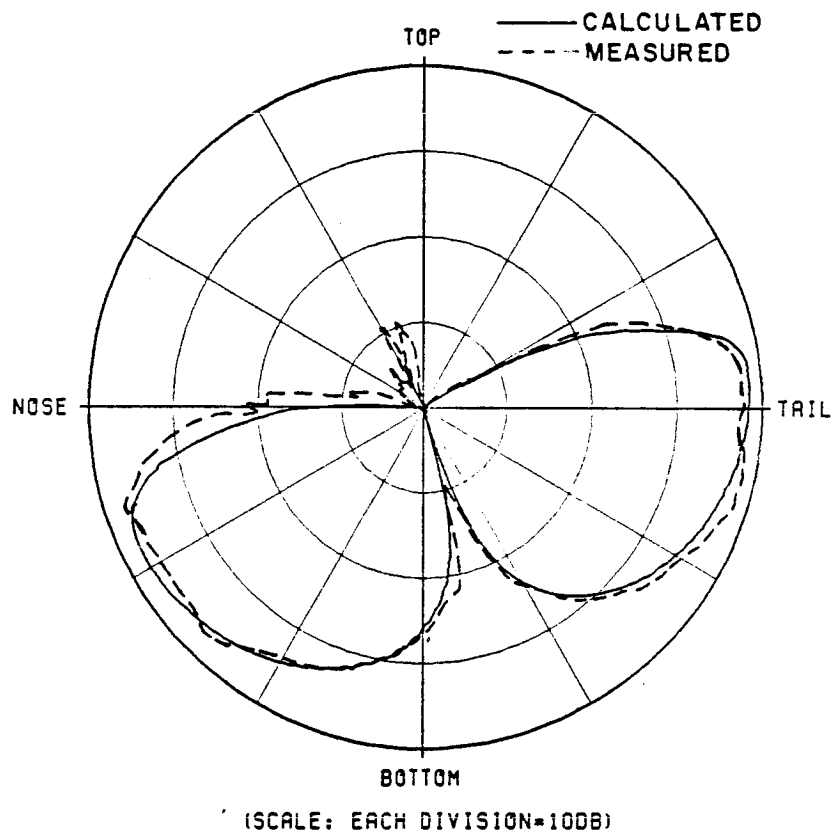
Figure 5.6. Elevation plane pattern of a λ/4 monopole mounted at Station 220 on top of a Boeing 737 aircraft.

179

C-3

$\theta_p = 90°$

—— CALCULATED

- - - MEASURED

TOP

LEFT WING — RIGHT WING

BOTTOM

(SCALE: EACH DIVISION=10DB)
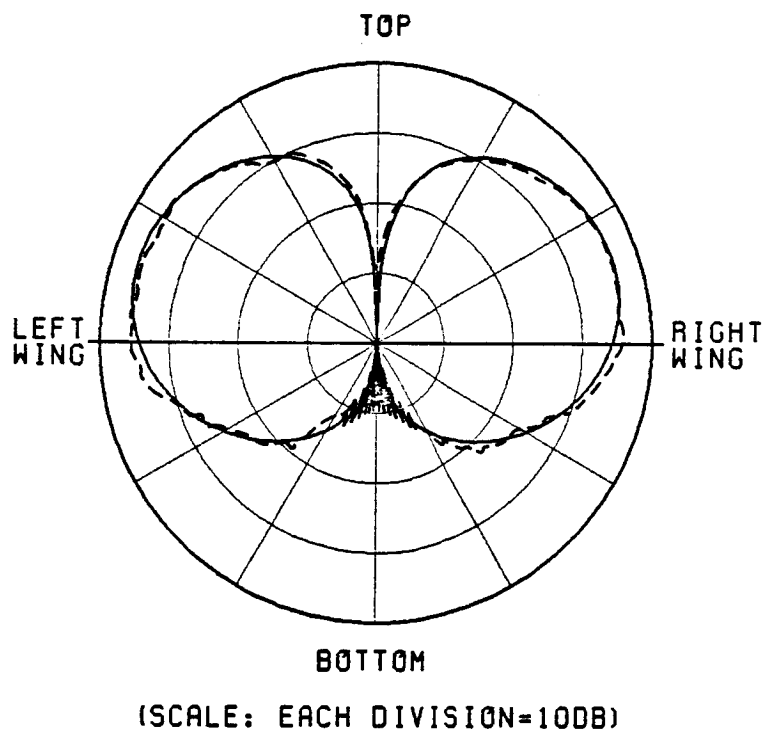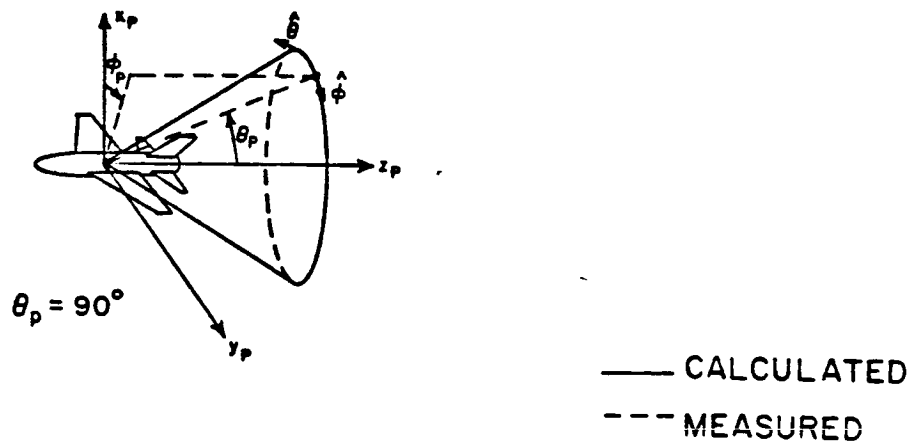
Figure 5.7. Roll plane pattern of a λ/4 monopole mounted at Station 220 on top of a Boeing 737 aircraft.

180

$\theta_p = 90°$

—— CALCULATED

--- MEASURED

NOSE

LEFT WING

RIGHT WING

TAIL
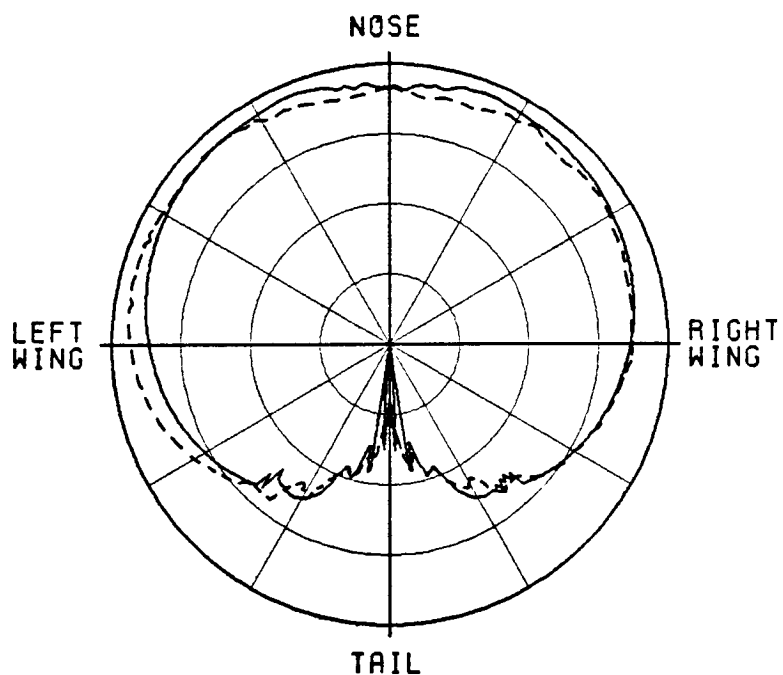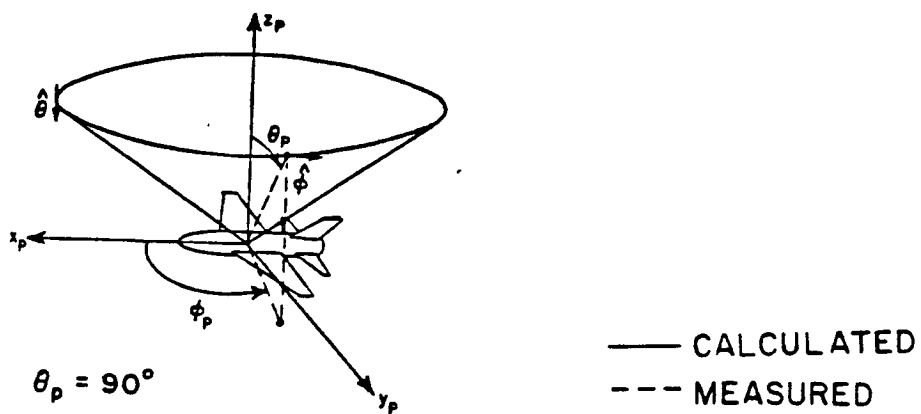
(SCALE: EACH DIVISION=10DB)

Figure 5.8. Azimuth plane pattern of a $\lambda/4$ monopole mounted at Station 220 on top of a Boeing 737 aircraft.

181

the monopole with respect to the surface normal or the movement of the model due to shifting weight during the measurement. This misalignment of the monopole (approximately 3° tilted to the nose section from the actual surface normal) was detected by the calculated elevation plane pattern and various azimuth plane patterns. To compensate this misalignment in the comparison with measured patterns, the conical pattern axes were rotated 3° toward the nose section. The various azimuth plane patterns for this antenna location are computed and shown in Figures 5.9(a) to (g). In each case, the calculated results compare very favorably with the measurements.

To evaluate the radiation coverage performance of the MLS antenna at Stations 250 and 305, the elevation plane patterns for a λ/4 monopole mounted at these locations are obtained. The elevation plane patterns are used in that it is the most critical MLS sector. It is noted that the antenna at Station 250 is mounted 4" off the fuselage centerline because of the structural problems that exist on the actual aircraft fuselage. Both calculated and experimental results for Stations 250 and 305 are presented in Figures 5.10 and 5.11, respectively. The results reveal good agreement between the theoretical predictions and scale model measurements. In addition, the results indicate that Station 220 appears to be the best choice since it gives the best forward coverage which satisfies the MLS performance requirement. However, due to structural problems, the antenna of interest had to be moved to Station 250.

NOSE

CALCULATED
MEASURED

LEFT
WING

RIGHT
WING

(SCALE: EACH DIVISION=10DB)

TAIL

NOSE

(a) $\theta_p = 50°$

LEFT
WING

RIGHT
WING

TAIL

(b) $\theta_p = 60°$
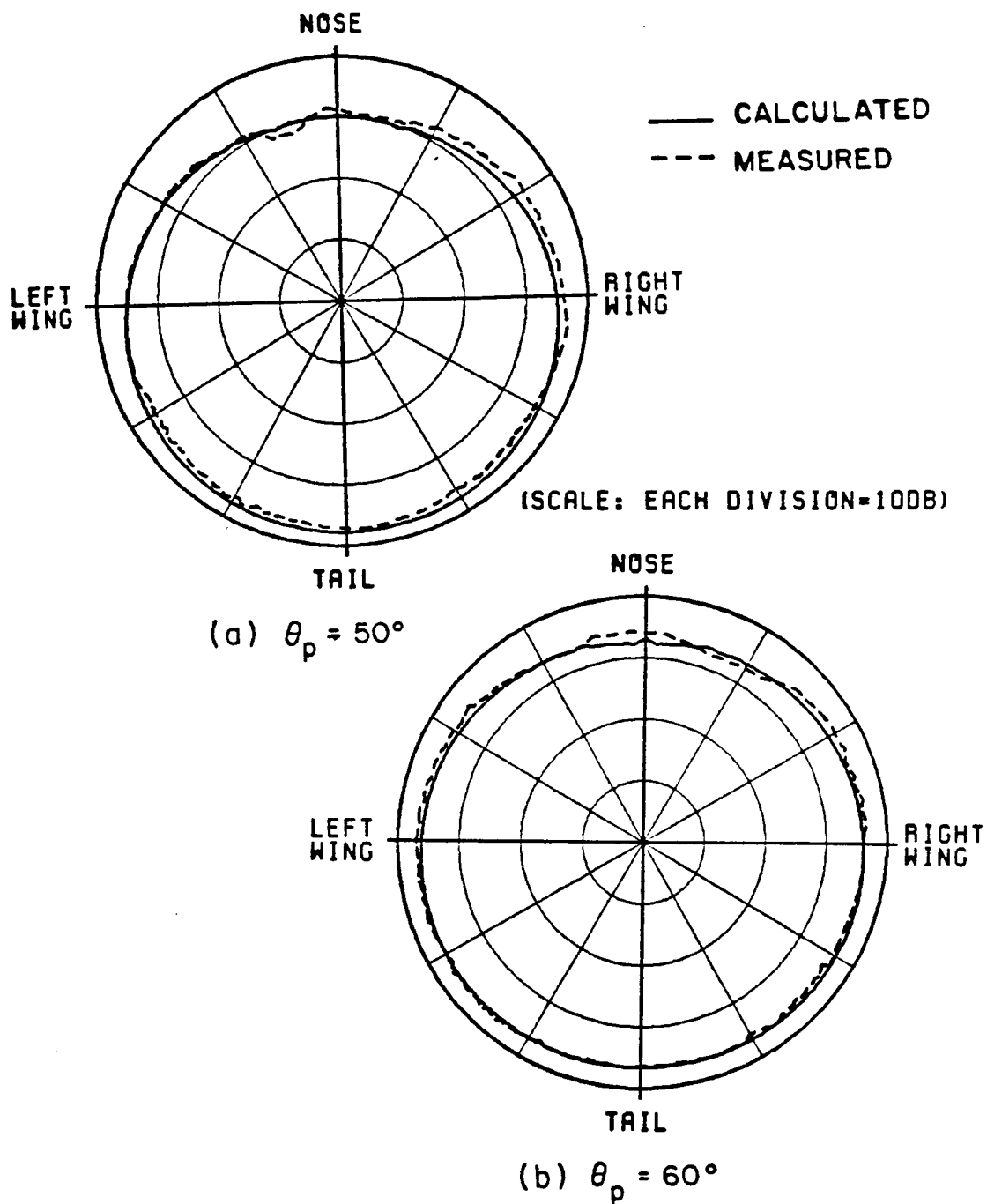
Figure 5.9. Azimuthal conical patterns of a $\lambda/4$ monopole mounted at
Station 220 on top of a Boeing 737 aircraft.

183

NOSE

— CALCULATED
--- MEASURED

LEFT WING   RIGHT WING

(SCALE: EACH DIVISION=10DB)

TAIL

(c) $\theta_p = 70°$

NOSE

LEFT WING   RIGHT WING

TAIL
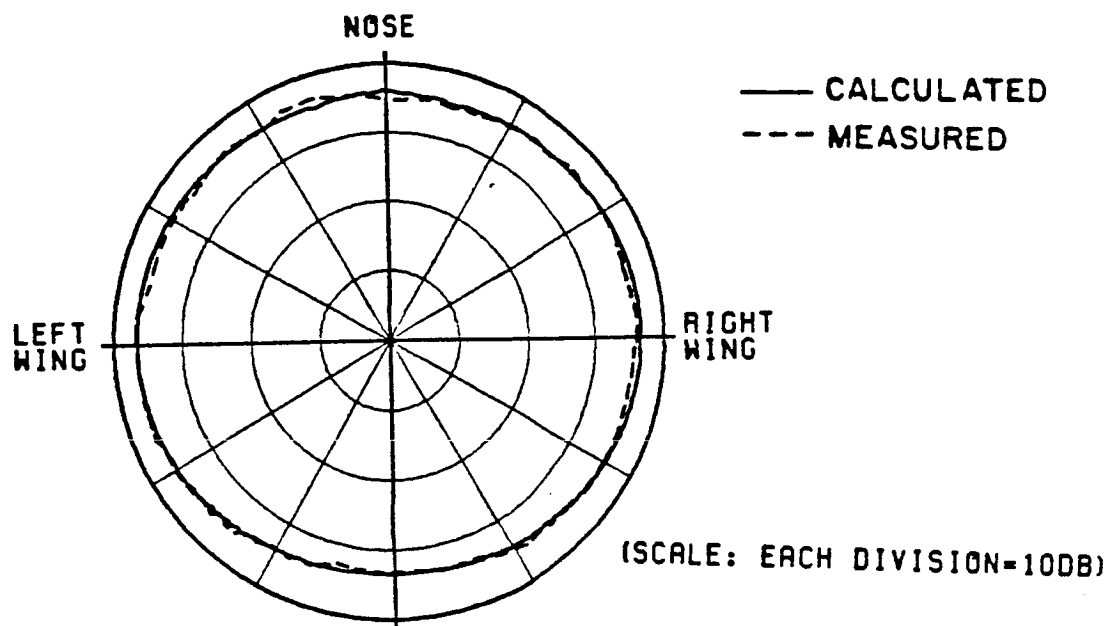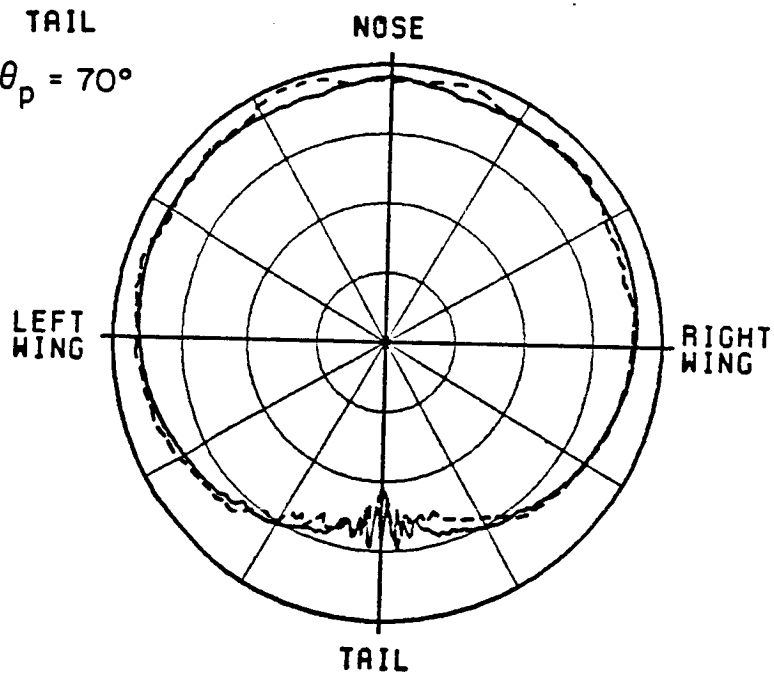
(d) $\theta_p = 80°$

Figure 5.9. (Continued).

184
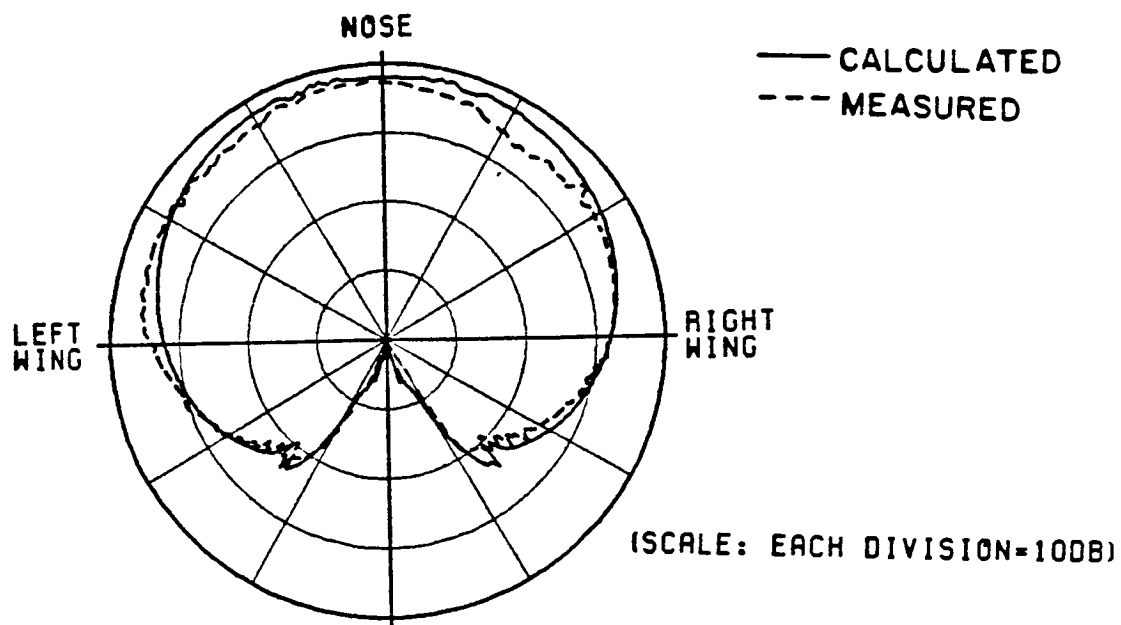
(e) $\theta_p = 100°$

(f) $\theta_p = 110°$

Figure 5.9. (Continued).

NOSE

LEFT
WING

RIGHT
WING

TAIL

(SCALE: EACH DIVISION=10DB)

(g) $\theta_p = 120°$
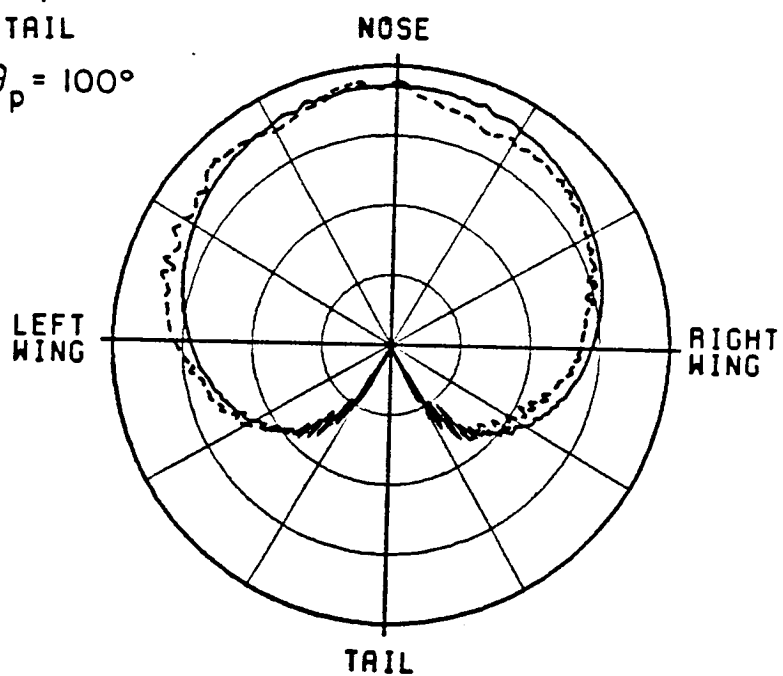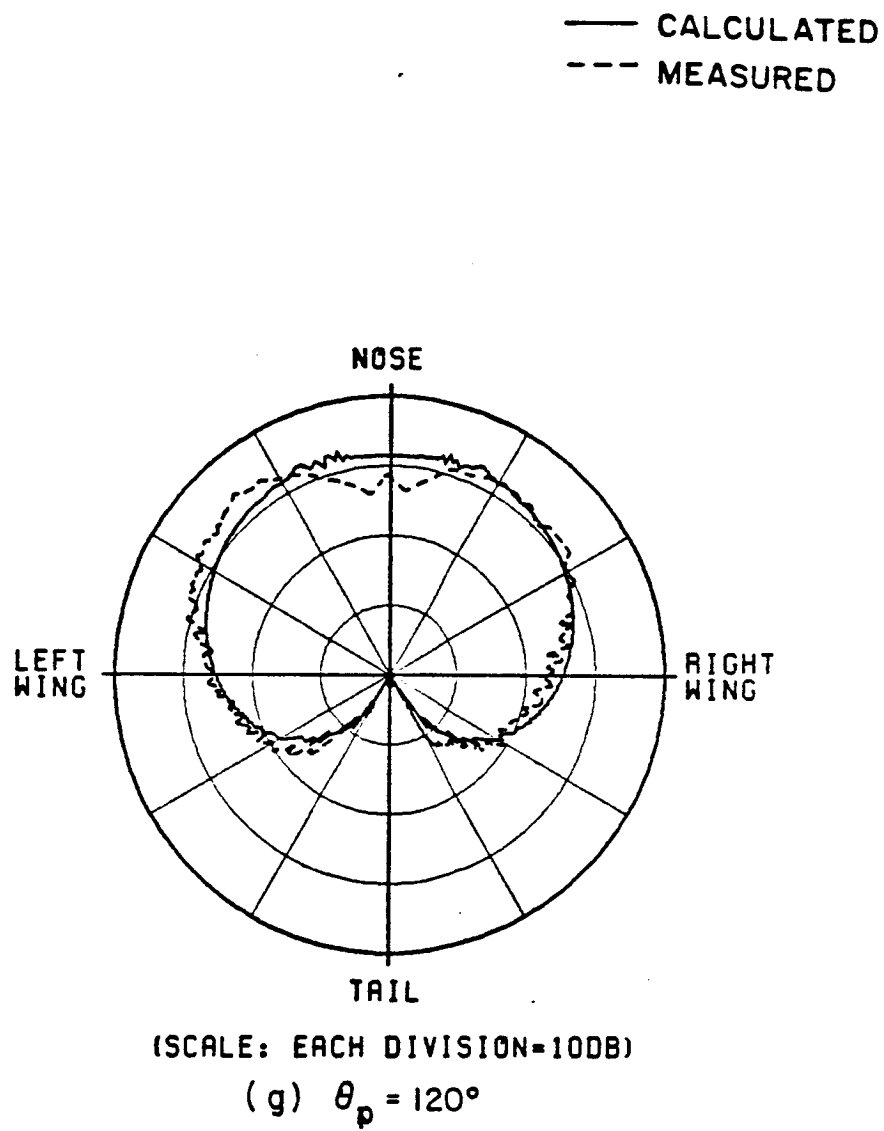
Figure 5.9.   (Continued).
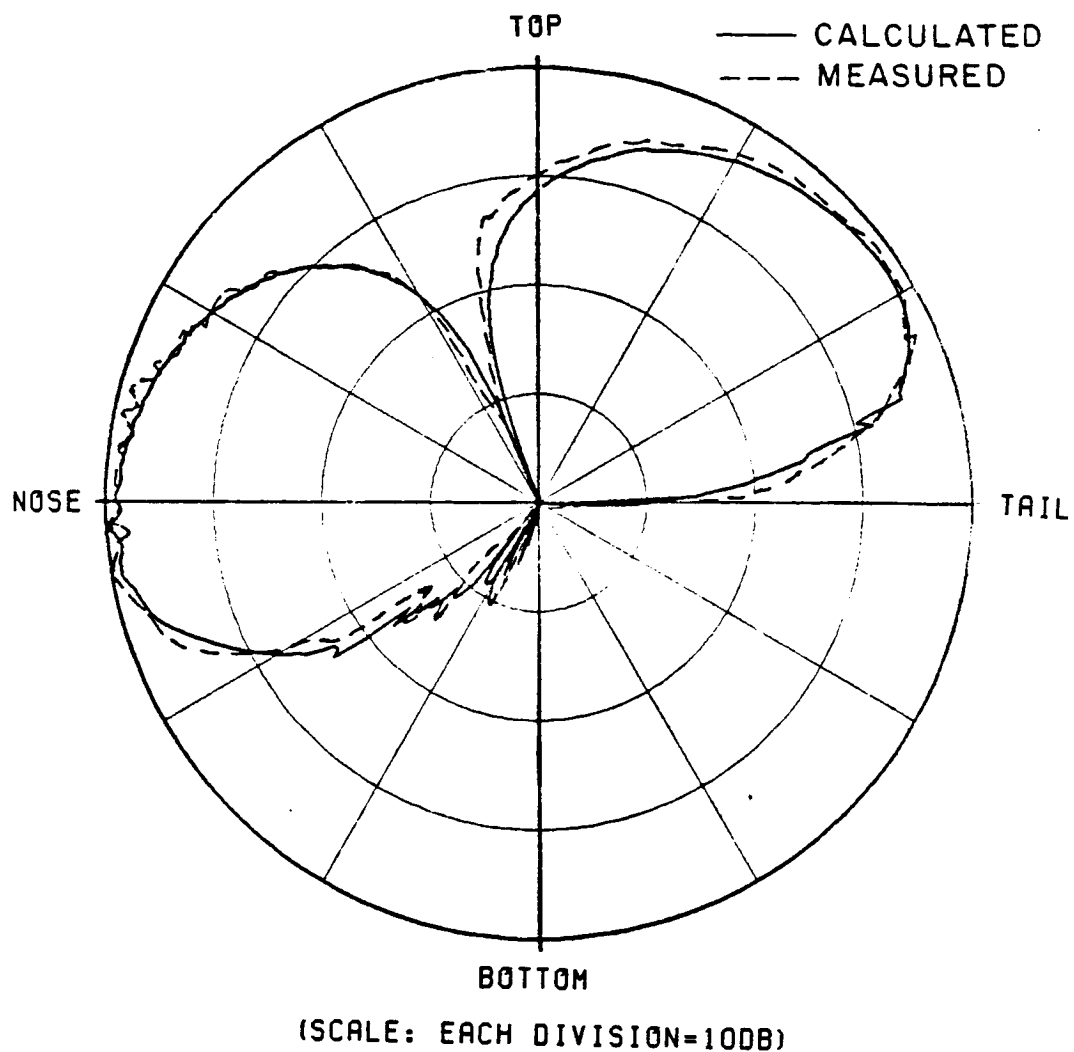
Figure 5.10. Elevation plane pattern of a λ/4 monopole mounted at Station 250 (off center) on top of a Boeing 737 aircraft.
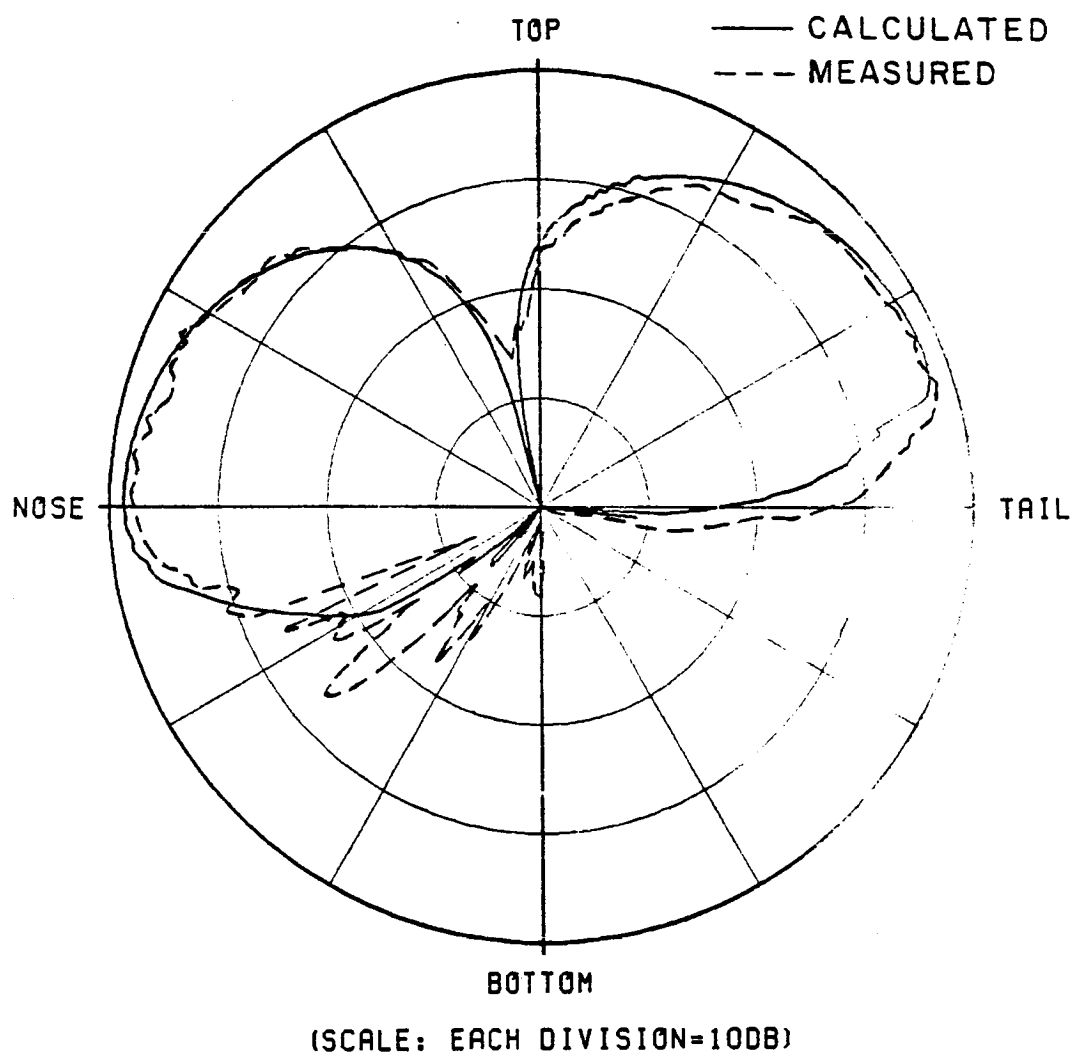
Figure 5.11. Elevation plane pattern of a λ/4 monopole mounted at Station 305 on top of a Boeing 737 aircraft.

Next, an antenna location on the bottom of an aircraft fuselage behind the radome was also proposed for the MLS application. Since the MLS is used for both for the approach and landing, this location appeared to be very attractive for the forward coverage requirement. For an antenna location at Station 222, the Boeing 737 aircraft was modeled by a composite ellipsoid (66" x 55" x 785" x 232"). It is noted that the fuselage dimensions associated with the bottom of the aircraft are different from the top, in that the aircraft has a definite shape change from top to bottom. The radome on the 737 aircraft is simulated by the truncated fuselage as shown in Figure 5.12.

In order to determine the appropriate polarization (horizontal or vertical) of the radiated field as well as the location of the antenna, the elevation plane patterns for a λ/4 monopole, a circumferential slot and an axial slot mounted at Station 222 are calculated and found to be in very good agreement with measurements as shown in Figures 5.13(a) to (c), respectively. In this case, vertical polarization has better forward coverage than horizontal polarization because horizontal polarization is shorted out by the perfect conducting fuselage.

Based on the MLS antenna coverage requirement, the radiation pattern of a single vertical polarization monopole is not quite adequate. Thus a tail mounted monopole was proposed to be mounted at Station 950 on the bottom of the Boeing 737 aircraft fuselage for missed approach purposes. This location is chosen because the slope of the fuselage surface at Station 950 is similar to that at Station 250 on the

189

RADOME

+

ANTENNA LOCATION
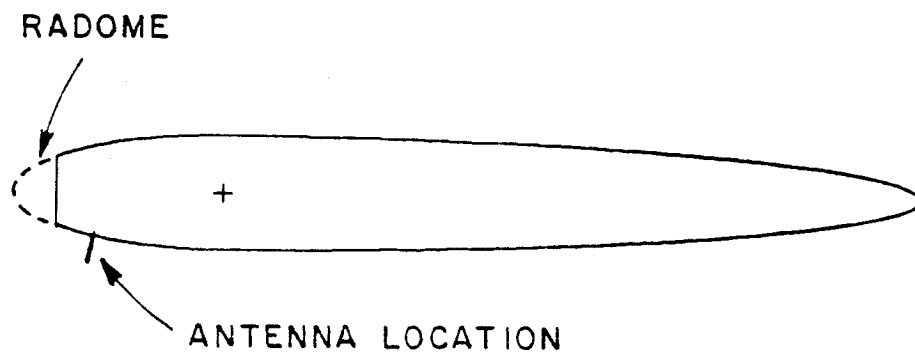
Figure 5.12. Computer simulated model for a $\lambda/4$ monopole mounted at
Station 222 on the bottom of the fuselage of a Boeing 737
aircraft.

TOP

NOSE

TAIL

BOTTOM

(SCALE: EACH DIVISION=10DB)
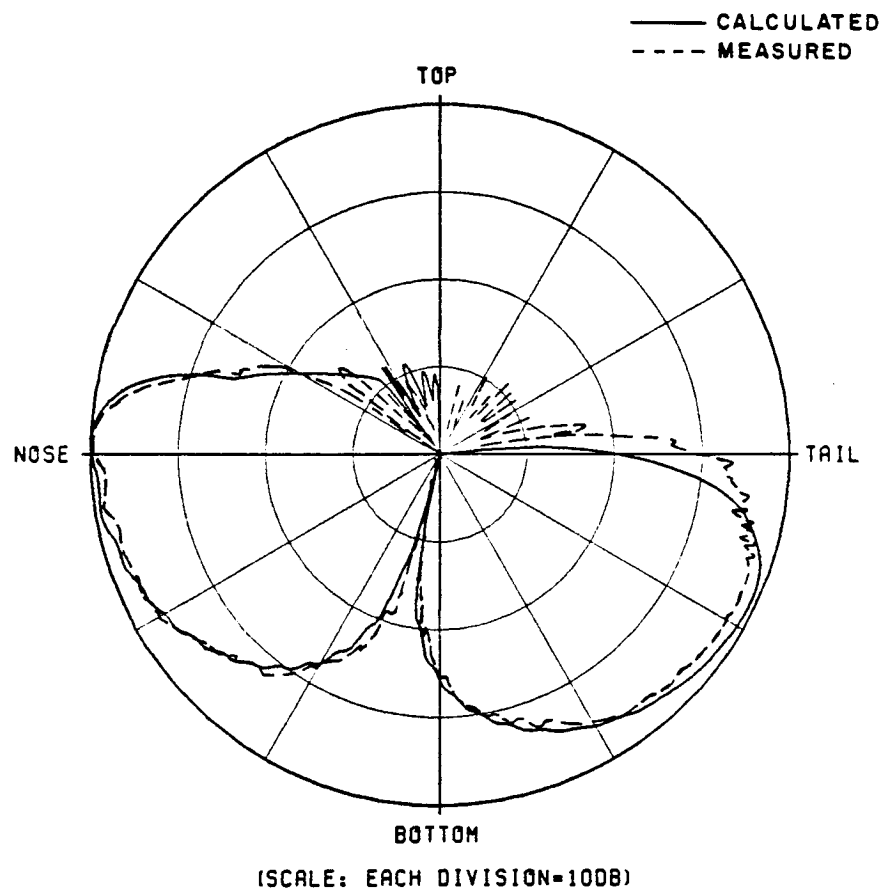
(a) λ/4 monopole case.

Figure 5.13. Elevation plane pattern of an antenna mounted at
Station 222 on the bottom of a Boeing 737 aircraft.
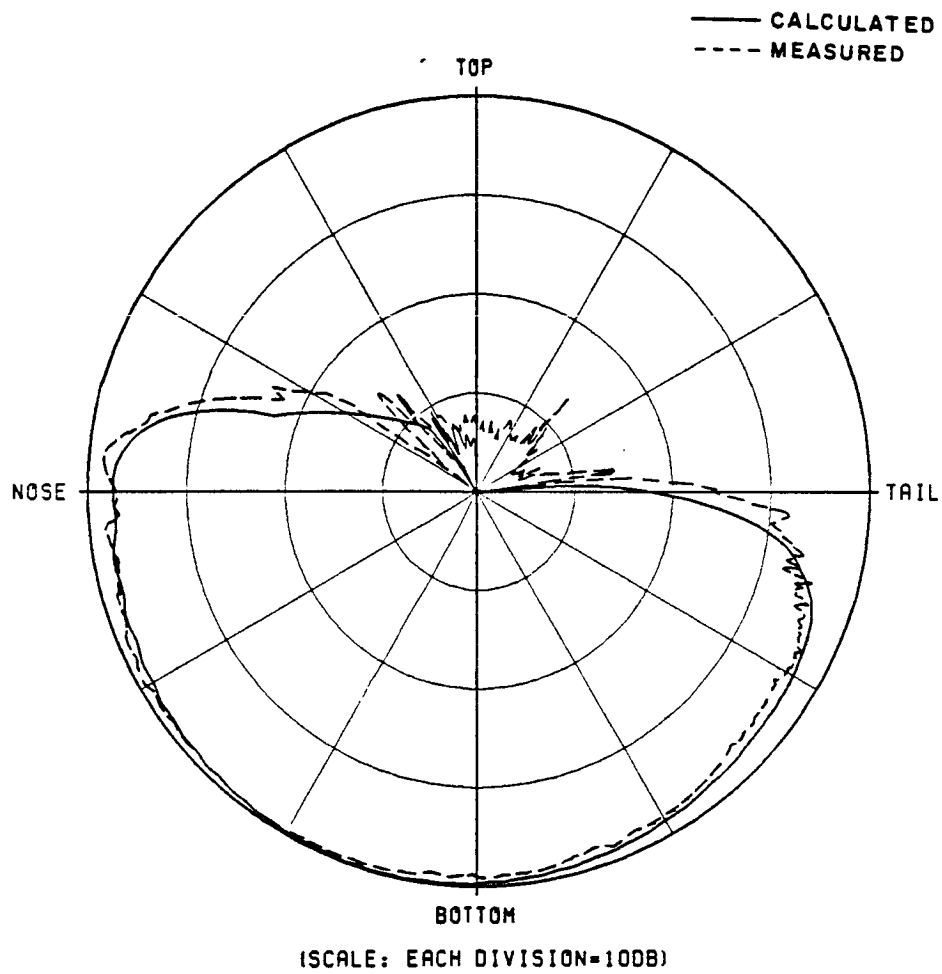
(b) Circumferential slot case.

Figure 5.13. (Continued).
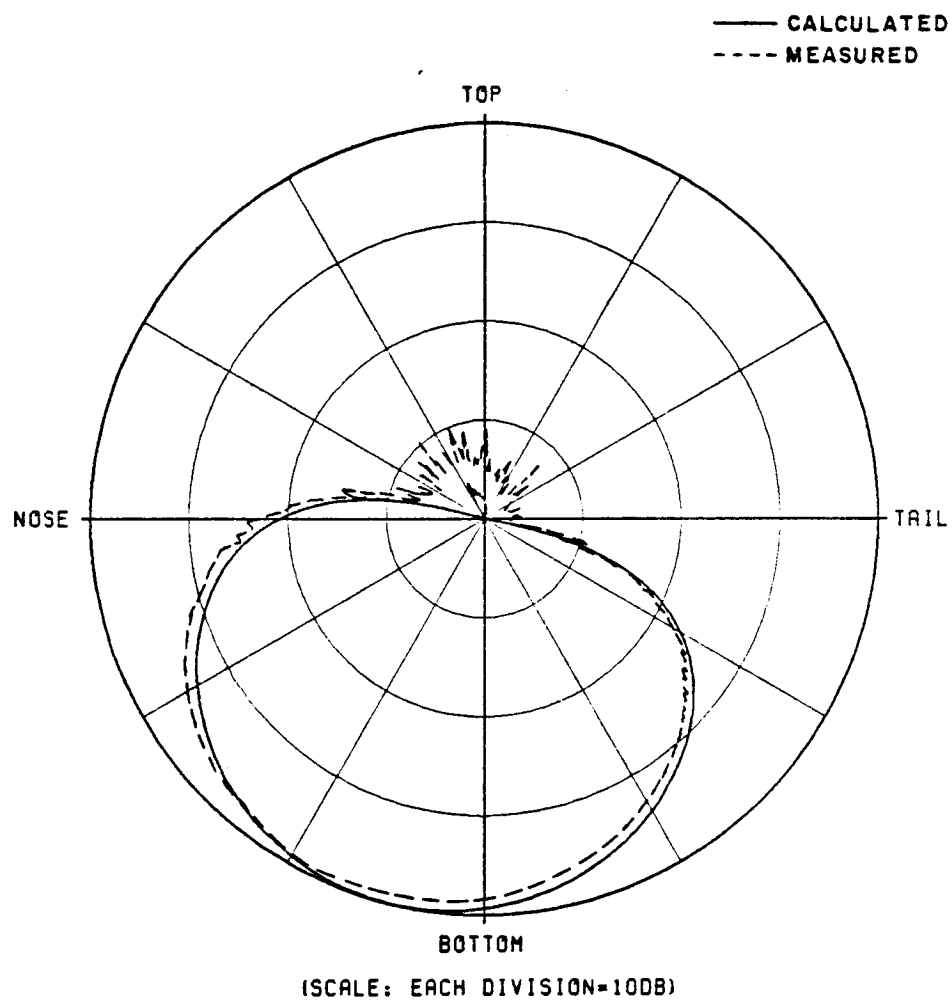
(c) Axial slot case.

Figure 5.13. (Continued).

top of the fuselage such that the space coverage of the two antennas tends to have a better match. The computer model as shown in Figure 5.14 is composed of a composite ellipsoid with four flat plates attached to the fuselage. Two flat plates are used to simulate the wings, and the other two simulate the horizonal stabilizers. The engines are neglected in the present model for simplicity. The elevation plane radiation pattern is computed and found to be in good agreement with the measurements as shown in Figure 5.15.

2. KC-135 (Boeing 707) Aircraft

The radiation patterns for the antennas mounted on the KC-135 aircraft are analyzed in this section. Precision pattern measurements (elevation and roll plane patterns) using a 1/25 scale model were taken at NASA (Hampton, Virginia) and will be used to verify our numerical solution.

The line drawings for the aircraft are shown in Figure 5.16. The computer simulated models of the KC-135 for antennas mounted forward of the wings and over wings are shown in Figures 5.17 and 5.18, respectively. The elevation plane patterns for a short monopole are illustrated in Figure 5.19. The patterns for a circumferential KA-band waveguide are illustrated in Figure 5.20. Finally, the patterns for an axial KA-band waveguide are shown in Figures 5.21. Next, the roll and azimuth plane patterns for a short monopole, a circumferential

194

ANTENNA LOCATION
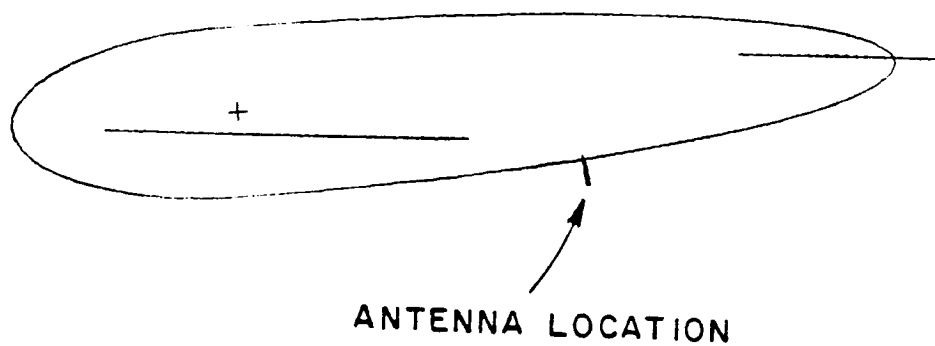
Figure 5.14. Computer simulated model for a λ/4 monopole mounted at Station 950 on the bottom of the fuselage of a Boeing 737 aircraft.

195

TOP

———— CALCULATED
— — — — MEASURED

NOSE

TAIL

BOTTOM

(SCALE: EACH DIVISION=10DB)

Figure 5.15.   Elevation plane pattern of a λ/4 monopole mounted at
Station 950 on the bottom of the fuselage of a Boeing
737 aircraft.

196
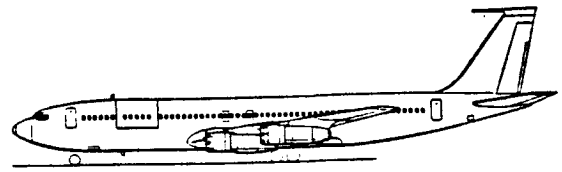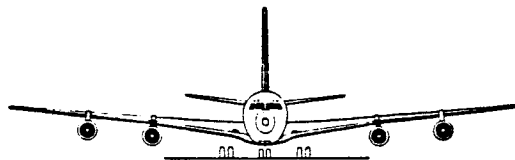
(a) SIDE VIEW
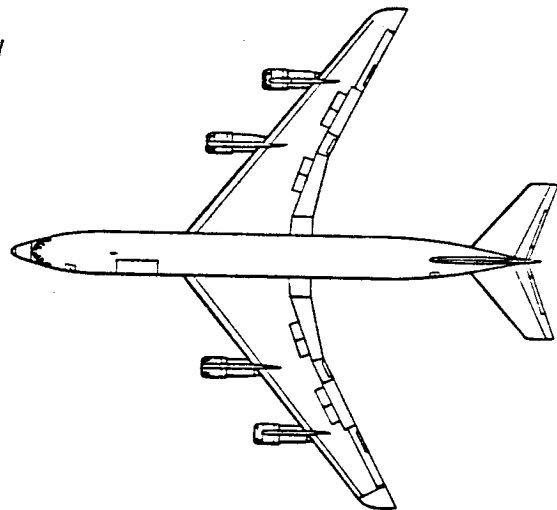
(b) FRONT VIEW

(c) TOP VIEW

Figure 5.16. KC-135 aircraft.
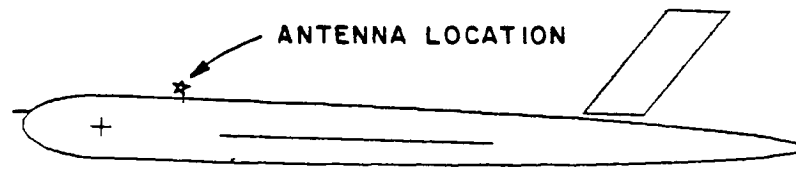
(a) SIDE VIEW
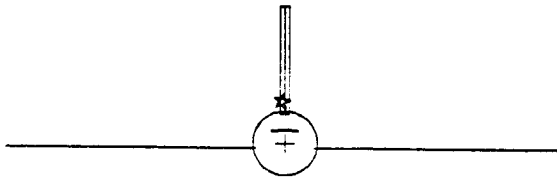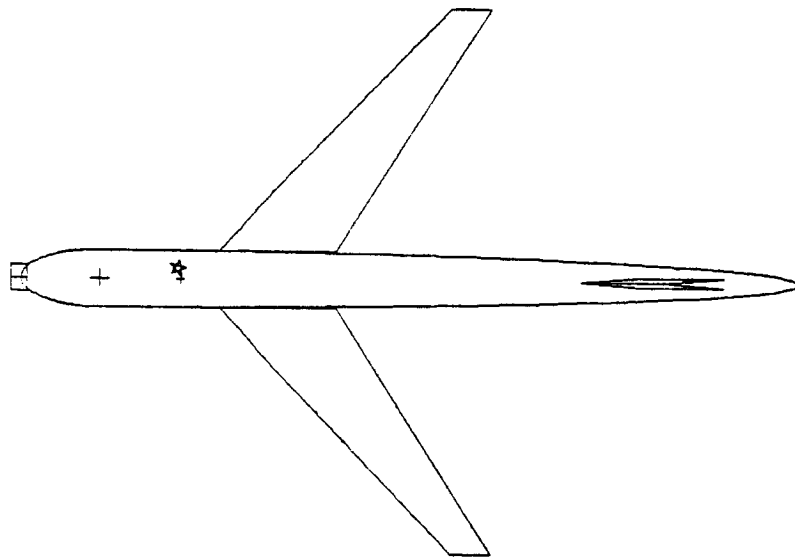
(b) FRONT VIEW

(c) TOP VIEW

Figure 5.17. Computer simulated model of a KC-135 aircraft. The antenna is located <u>forward</u> of the wings.
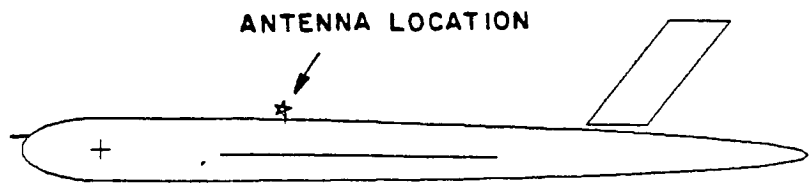
ANTENNA LOCATION

(a) SIDE VIEW
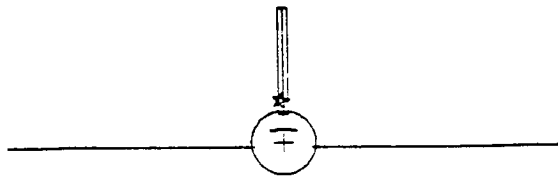
(b) FRONT VIEW
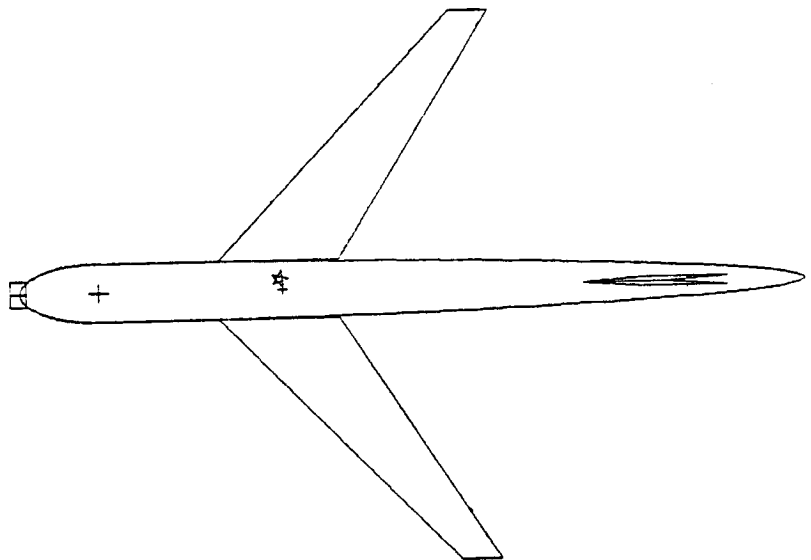
(c) TOP VIEW

Figure 5.18. Computer simulated model of a KC-135 aircraft.
The antenna is located <u>over</u> the wings.
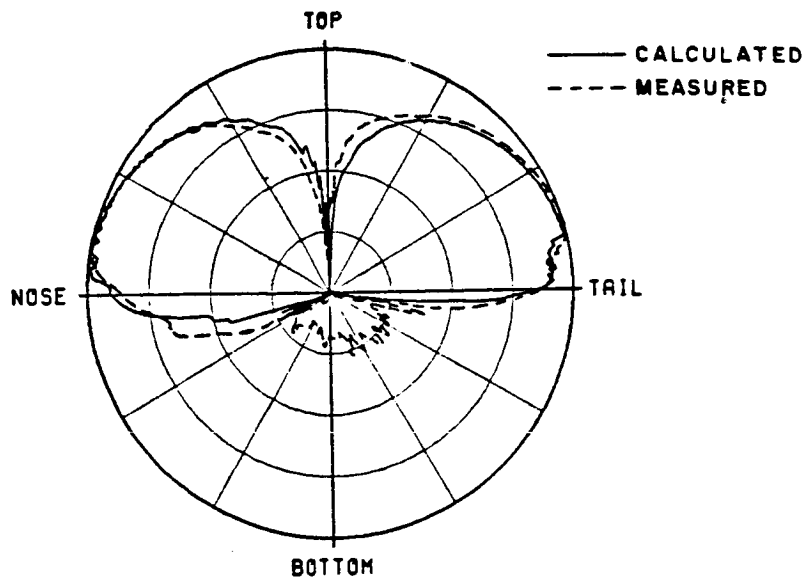
TOP

——— CALCULATED

- - - MEASURED

NOSE

TAIL

BOTTOM

(a) Antenna mounted forward of wings

TOP

NOSE

TAIL

BOTTOM
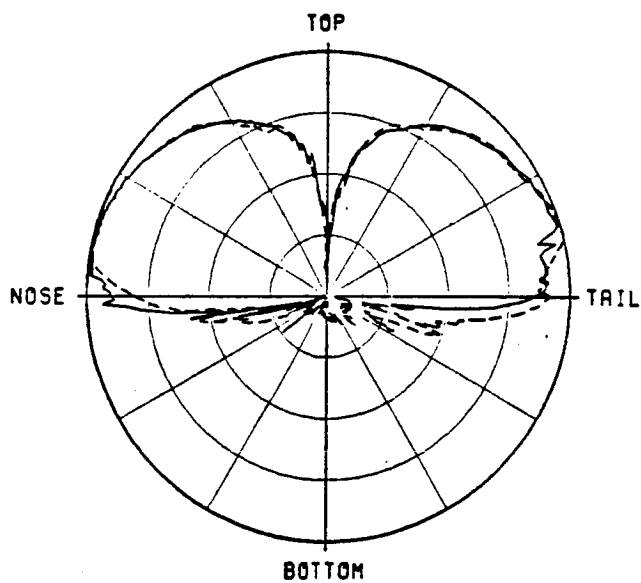
(SCALE: EACH DIVISION=10DB)

(b) Antenna mounted over wings

Figure 5.19. Elevation plane pattern for a λ/4 monopole mounted on a
KC-135 aircraft.
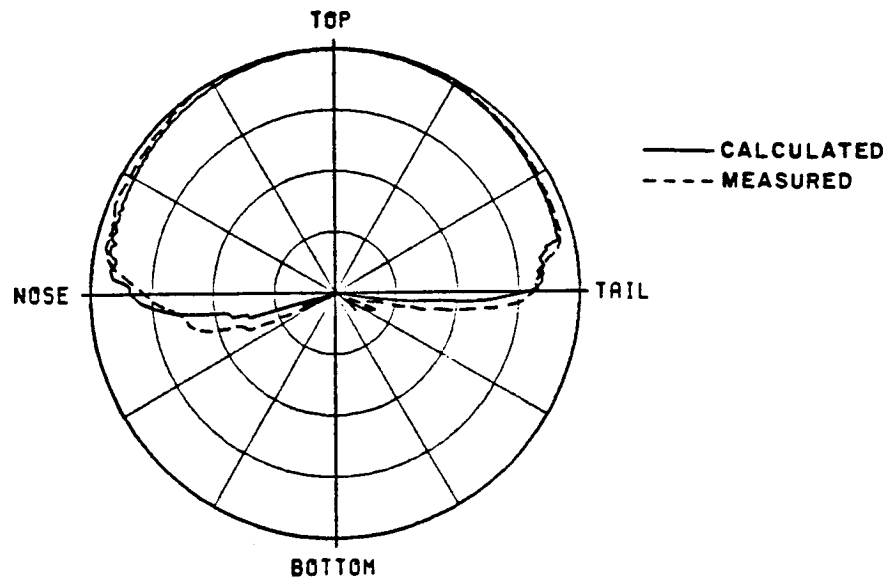
TOP

CALCULATED
MEASURED

NOSE

TAIL

BOTTOM

(a) Antenna mounted forward of wings

TOP

NOSE

TAIL

BOTTOM
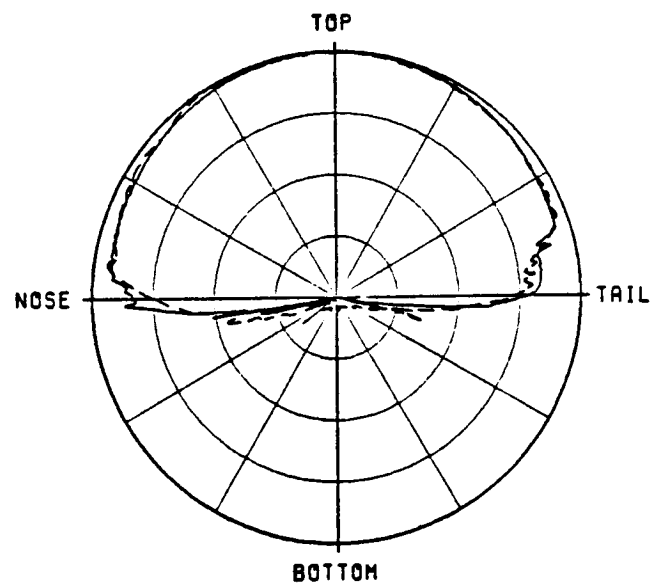
(SCALE: EACH DIVISION=10DB)

(b) Antenna mounted over wings

Figure 5.20. Elevation plane pattern for a circumferential KA-band
waveguide mounted on a KC-135 aircraft.
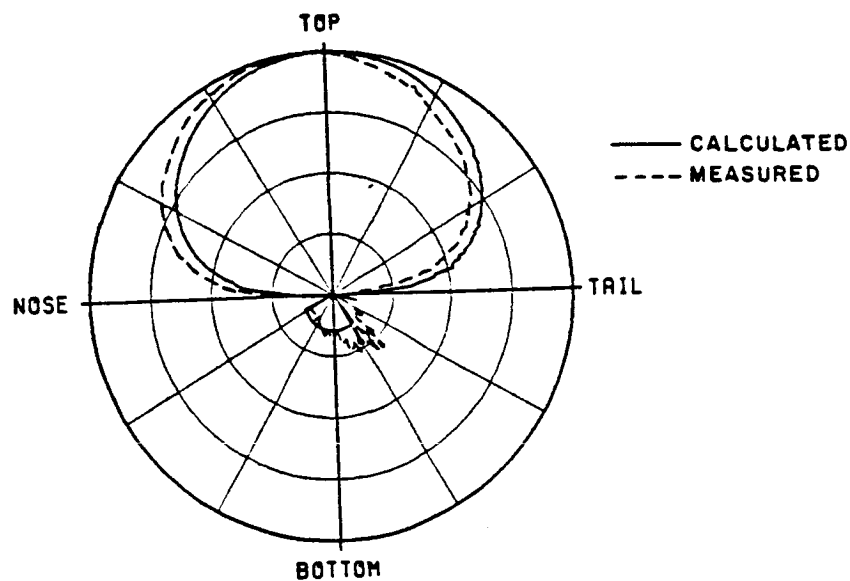
(a) Antenna mounted forward of wings
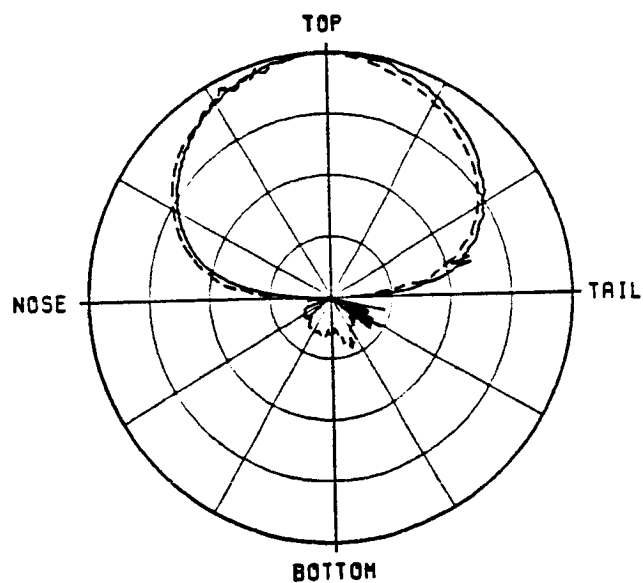
(SCALE: EACH DIVISION=10DB)

(b) Antenna mounted over wings

Figure 5.21. Elevation plane pattern for an axial KA-band waveguide mounted on a KC-135 aircraft.

202

ka-band waveguide, and an axial Ka-band waveguide mounted forward and over the wings are shown in Figures 5.22 to 5.27.

The computed results are found to be in very good agreement with the measurements in the elevation and roll planes. The comparisons of the azimuth plane radiation patterns are not shown here, since the measured data was not available.

To further demonstrate the versatility of this solution, the radiation patterns for the Lindberg crossed-slot antenna [46] mounted at Station 470 along the top center-line of a KC-135 aircraft is analyzed. The Lindberg antenna (crossed slots, 90° phase difference between two slots) is a UHF antenna designed for use in a satellite-to-aircraft communications link. Using the computer model as shown in Figure 5.28, the radiation patterns were computed for a right circularly polarized Lindberg antenna. Various calculated patterns along with the measured results as taken form reference [46] are presented in Figures 5.29 to Figures 5.32 and, again, good agreement is obtained. The gain level in each case is adjusted to compare with measurements. The E_θ pattern corresponds to the vertical component, E_ϕ to the horizontal component and E_{cp} pattern to the circularly polarized field. Note that all patterns are computed at a frequency of 6.25 GHz and $.039\lambda$ x $.78\lambda$ slots are considered in this calculation.
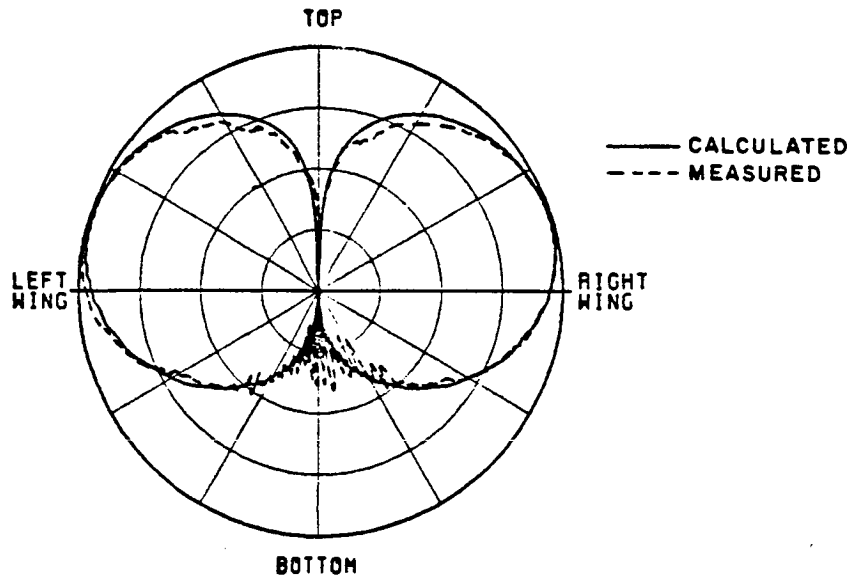
TOP

LEFT WING — CALCULATED
---- MEASURED

RIGHT WING

BOTTOM

(a) Antenna mounted forward of wings

TOP

LEFT WING

RIGHT WING

BOTTOM
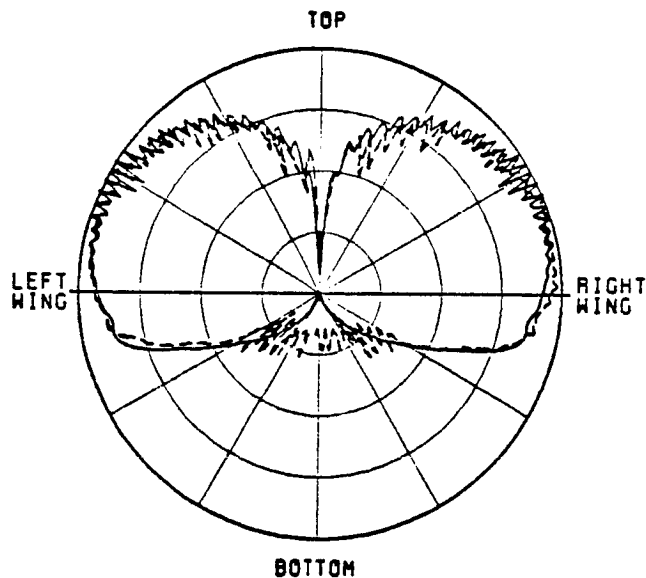
(SCALE: EACH DIVISION=10DB)

(b) Antenna mounted over wings

Figure 5.22.   Roll plane pattern for a λ/4 monopole mounted on a
KC-135 aircraft.

TOP

CALCULATED
---- MEASURED

LEFT
WING

RIGHT
WING

BOTTOM

(a) Antenna mounted forward of wings

TOP

LEFT
WING

RIGHT
WING

BOTTOM

(SCALE: EACH DIVISION=10DB)

(b) Antenna mounted over wings

Figure 5.23. Roll plane pattern for a KA-band circumferential
waveguide mounted on a KC-135 aircraft.
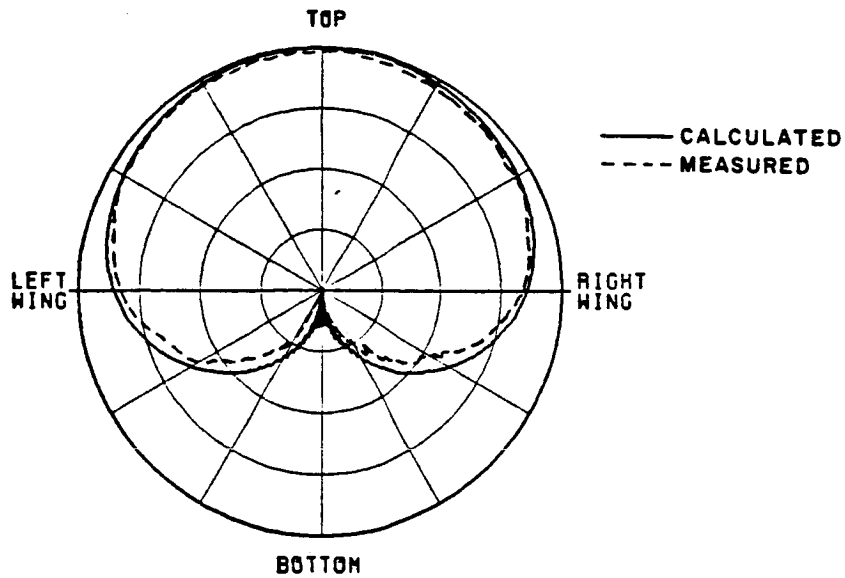
205

TOP

CALCULATED
---- MEASURED

LEFT
WING

RIGHT
WING

BOTTOM

(a) Antenna mounted forward of wings

TOP

LEFT
WING

RIGHT
WING

BOTTOM
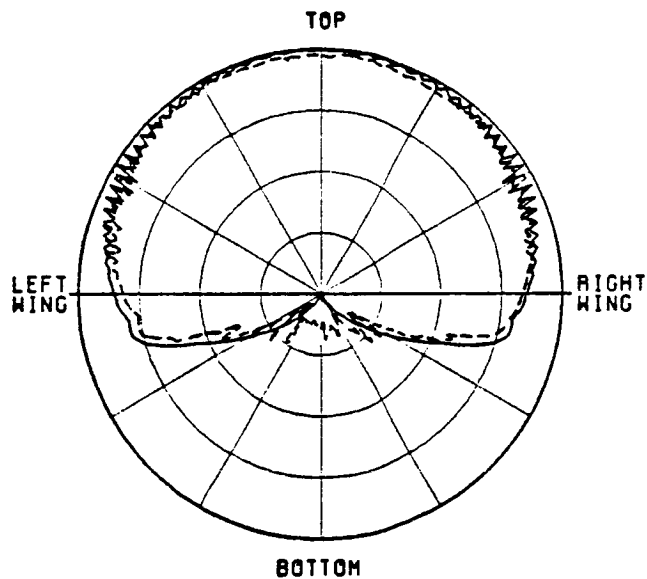
(SCALE: EACH DIVISION=10DB)

(b) Antenna mounted over wings

Figure 5.24. Roll plane pattern for a KA-band axial waveguide
mounted on a KC-135 aircraft.
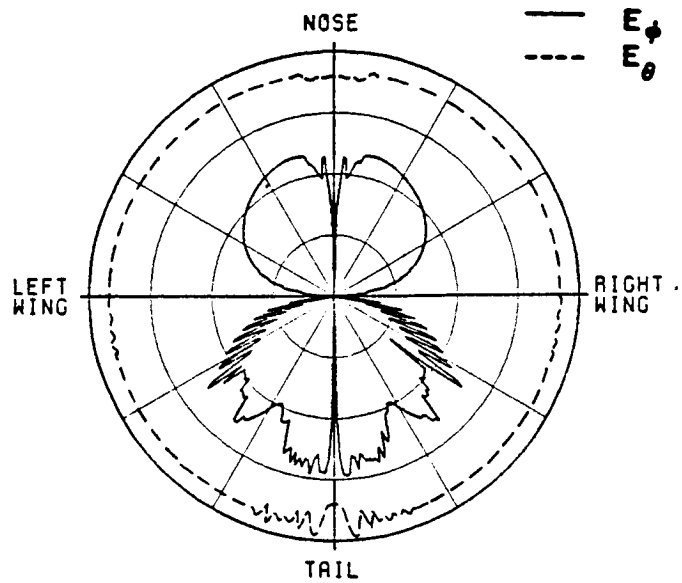
206

(a) Antenna mounted forward of wings
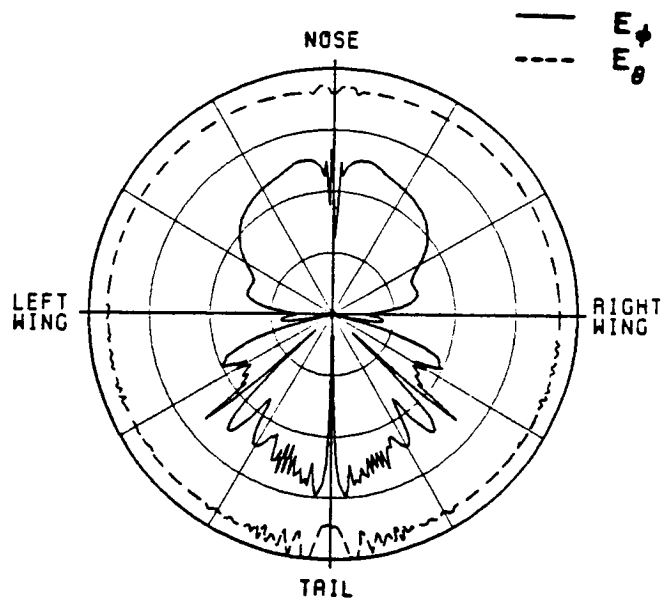
(SCALE: EACH DIVISION=10DB)

(b) Antenna mounted over wings

Figure 5.25. Azimuth plane pattern for a $\lambda/4$ monopole mounted on a KC-135 aircraft.
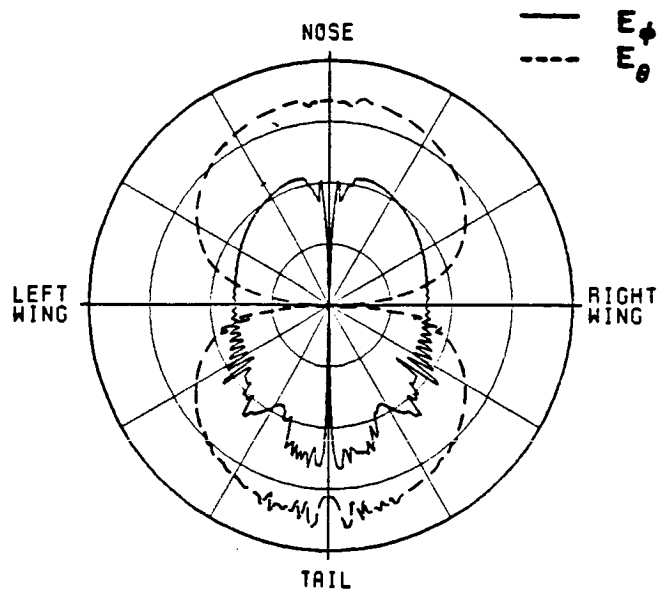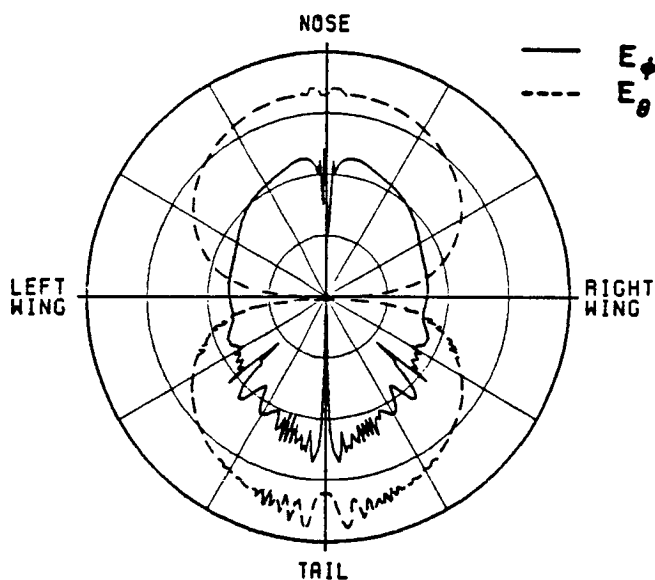
(a) Antenna mounted forward of wings

(b) Antenna mounted over wings

Figure 5.26. Azimuth plane pattern for a KA-band circumferential waveguide mounted on a KC-135 aircraft.

NOSE

LEFT
WING

RIGHT
WING

TAIL

(a) Antenna mounted forward of wings

NOSE

LEFT
WING

RIGHT
WING

TAIL
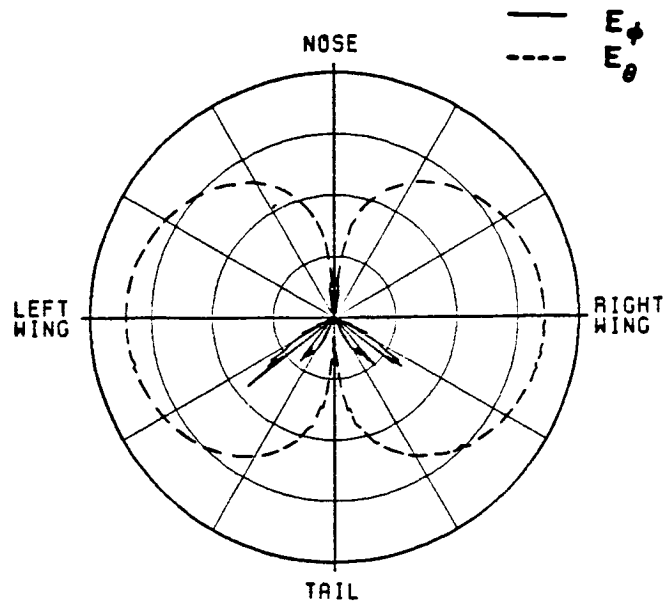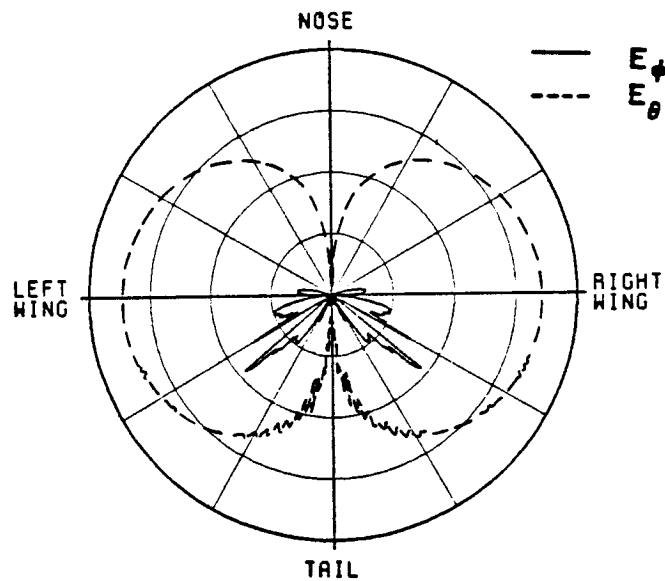
(SCALE: EACH DIVISION=10DB)

(b) Antenna mounted over wings

Figure 5.27. Azimuth plane pattern for a KA-band axial waveguide
mounted on a KC-135 aircraft.

(a) SIDE VIEW

(b) FRONT VIEW
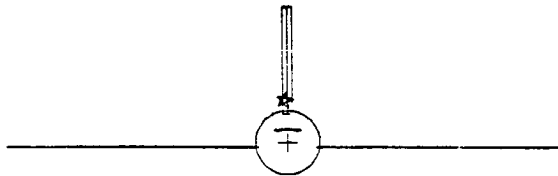
LINDBERG ANTENNA
(STATION 470)
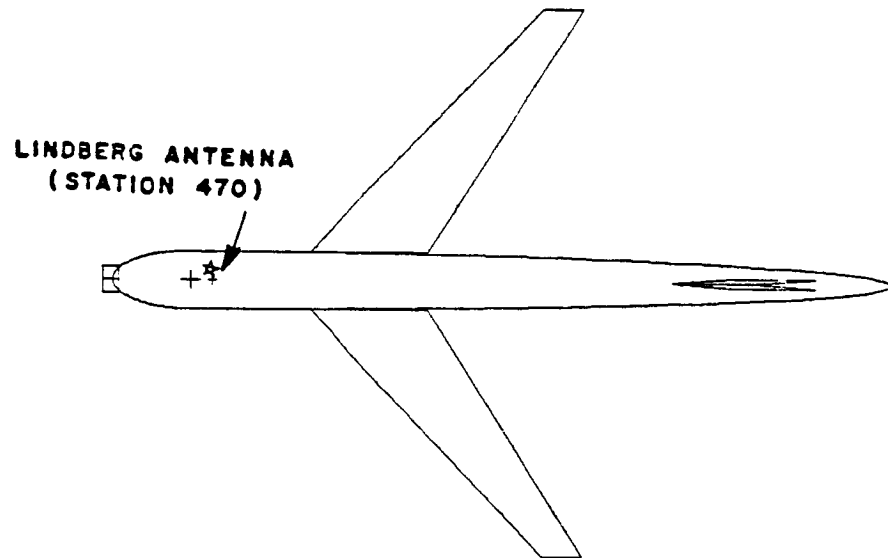
(c) TOP VIEW

Figure 5.28. Computer simulated model for a Lindberg antenna mounted on a KC-135 aircraft.

210

TOP

CALCULATED
MEASURED

NOSE

TAIL

BOTTOM

(SCALE: EACH DIVISION=10DB)

(a) E_ϕ

TOP

NOSE

TAIL

BOTTOM

(SCALE: EACH DIVISION=10DB)

(b) E_θ
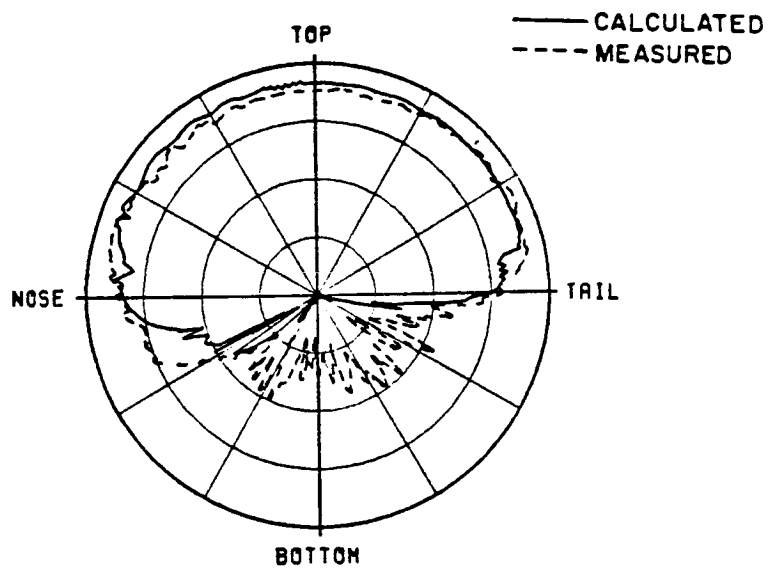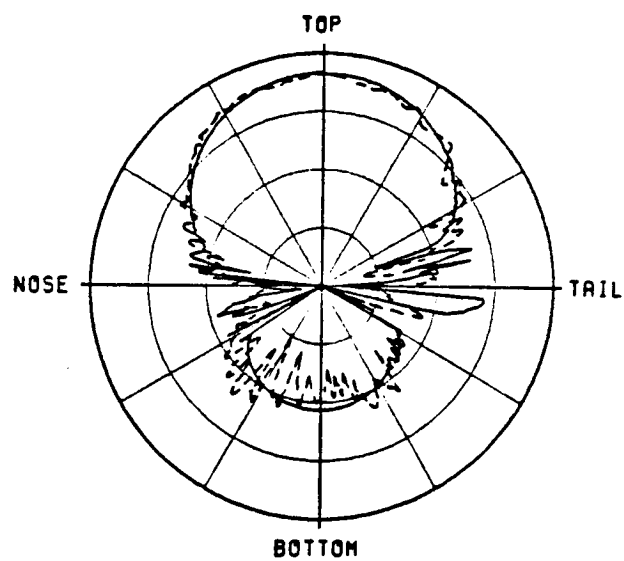
Figure 5.29. Elevation plane pattern for a Lindberg antenna
mounted on a KC-135 aircraft.

211

TOP

NOSE

TAIL

BOTTOM

(SCALE: EACH DIVISION=10DB)
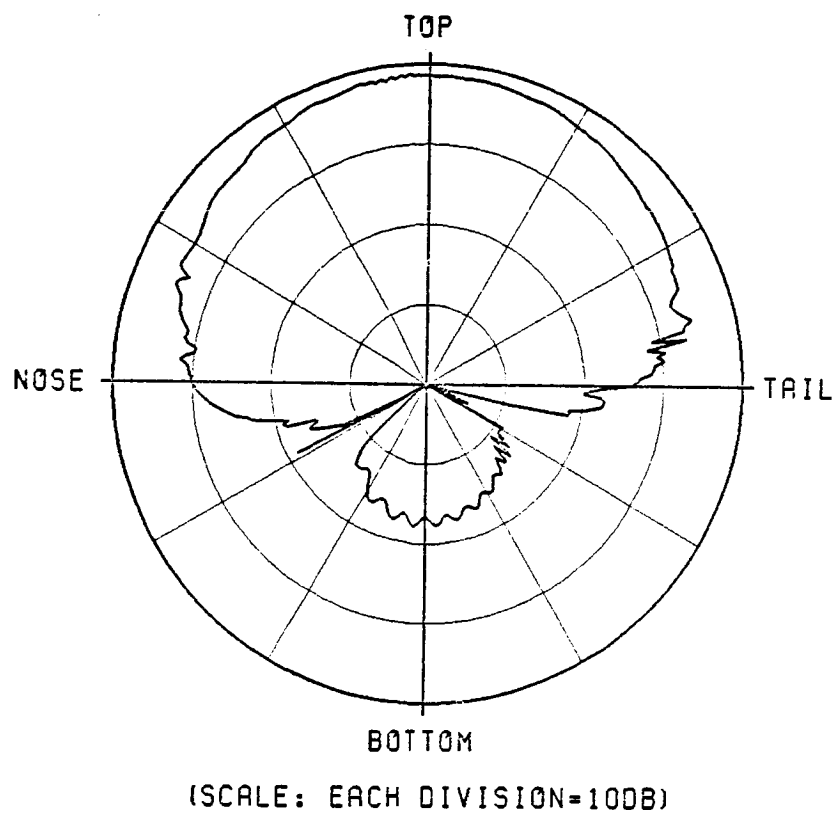
(c) E_{cp}

Figure 5.29.   (Continued.)

212

TOP

———— CALCULATED
– – – – MEASURED

LEFT
WING

RIGHT
WING

BOTTOM

(SCALE: EACH DIVISION=10DB)

(a) E_ϕ

TOP

LEFT
WING

RIGHT
WING

BOTTOM

(SCALE: EACH DIVISION=10DB)

(b) E_θ
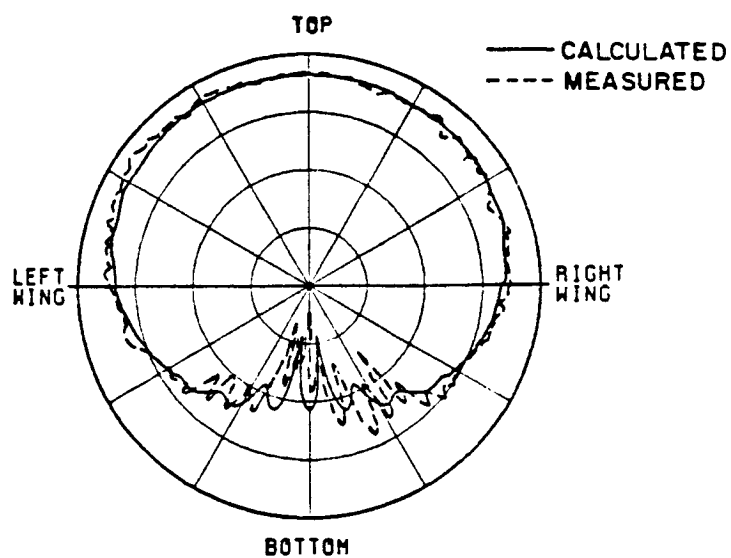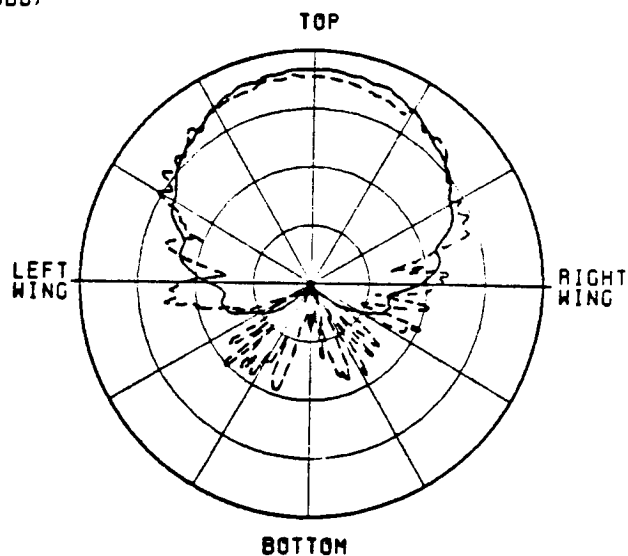
Figure 5.30. Roll plane pattern for a Lindberg antenna mounted on a KC-135 aircraft.

213

TOP

LEFT
WING

RIGHT
WING

BOTTOM

(SCALE: EACH DIVISION=10DB)
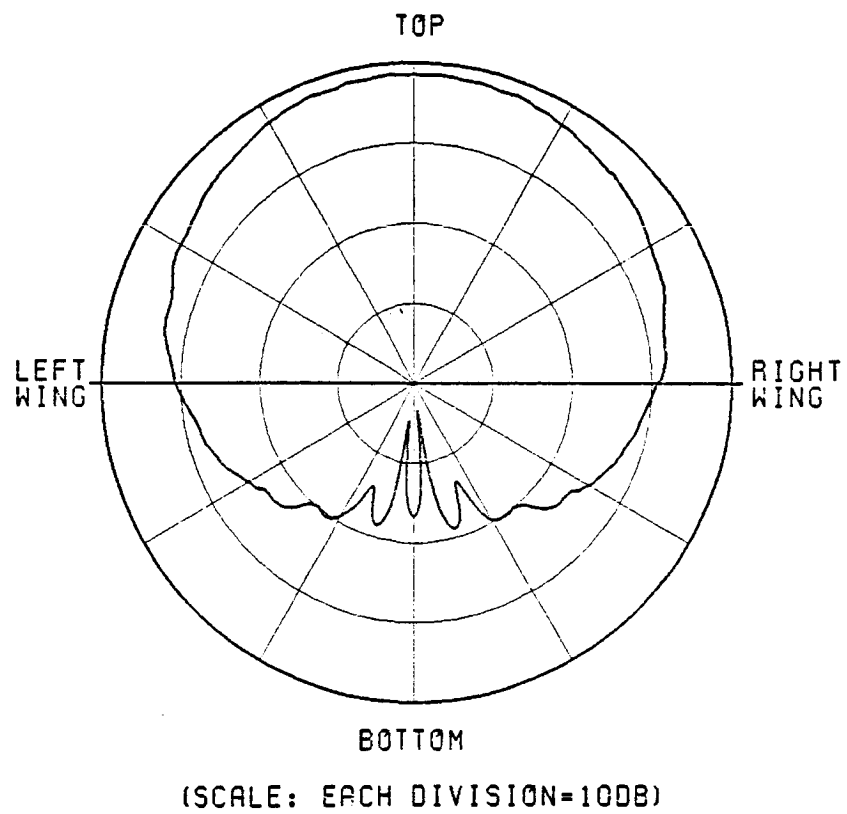
(c) E_{cp}

Figure 5.30. (Continued).

214

NOSE

CALCULATED
MEASURED

LEFT
WING

RIGHT
WING

TAIL

(SCALE: EACH DIVISION=10DB)

(a) E_ϕ

NOSE

LEFT
WING

RIGHT
WING

TAIL

(SCALE: EACH DIVISION=10DB)

(b) E_θ
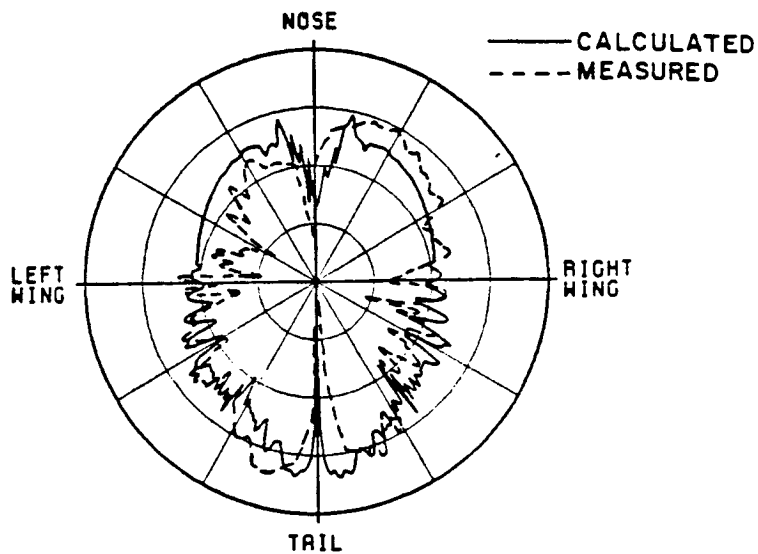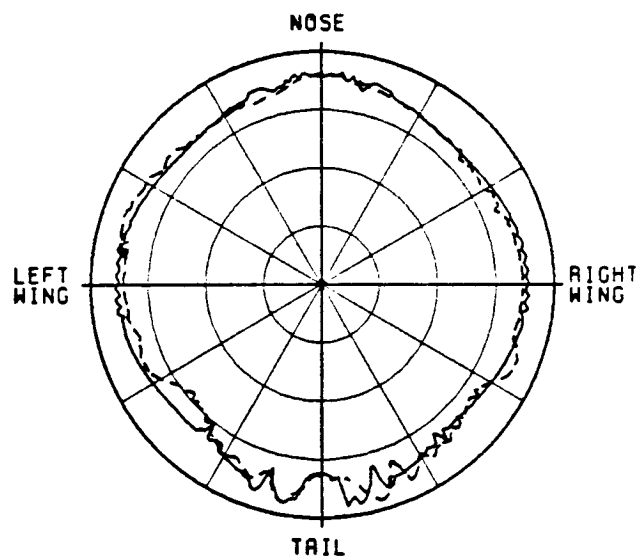
Figure 5.31. Azimuth plane pattern for a Lindberg antenna mounted on a
KC-135 aircraft.

215

NOSE

LEFT
WING

RIGHT
WING

TAIL
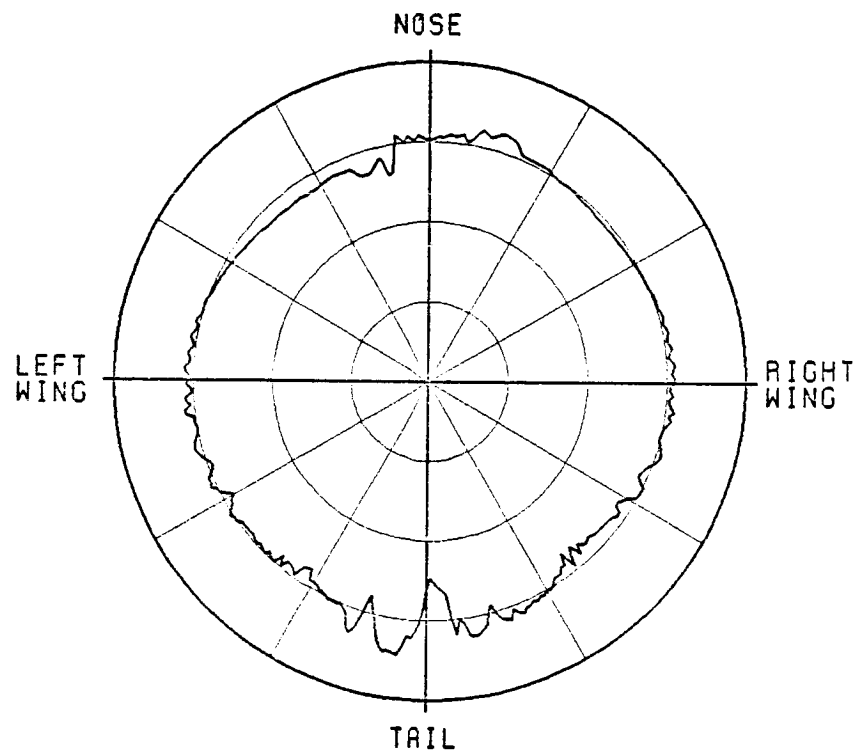
(SCALE: EACH DIVISION=10DB)

(c) E_{cp}

Figure 5.31. (Continued).

NOSE

——CALCULATED
————MEASURED

LEFT
WING

RIGHT
WING

TAIL

(SCALE: EACH DIVISION=10DB)

(a) E_ϕ

NOSE

LEFT
WING

RIGHT
WING

TAIL

(SCALE: EACH DIVISION=10DB)

(b) E_θ
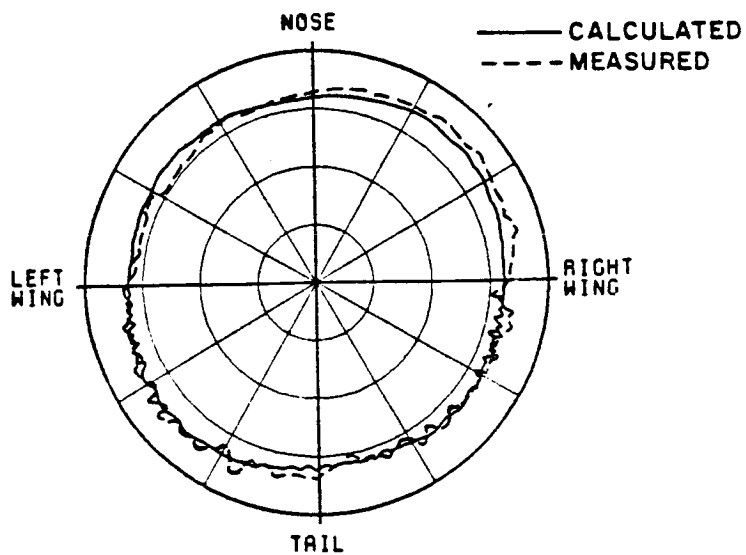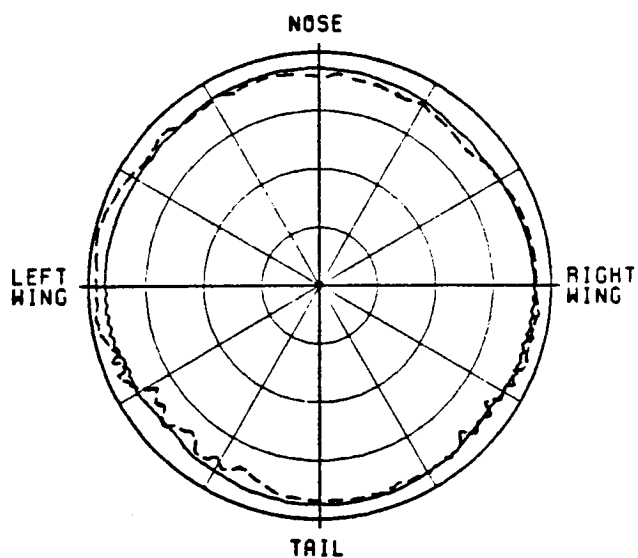
Figure 5.32. Azimuthal conical pattern (θ_p=45°) for a Lindberg antenna mounted on a KC-135 aircraft.

217

NOSE

LEFT
WING

RIGHT
WING

TAIL

(SCALE: EACH DIVISION=10DB)
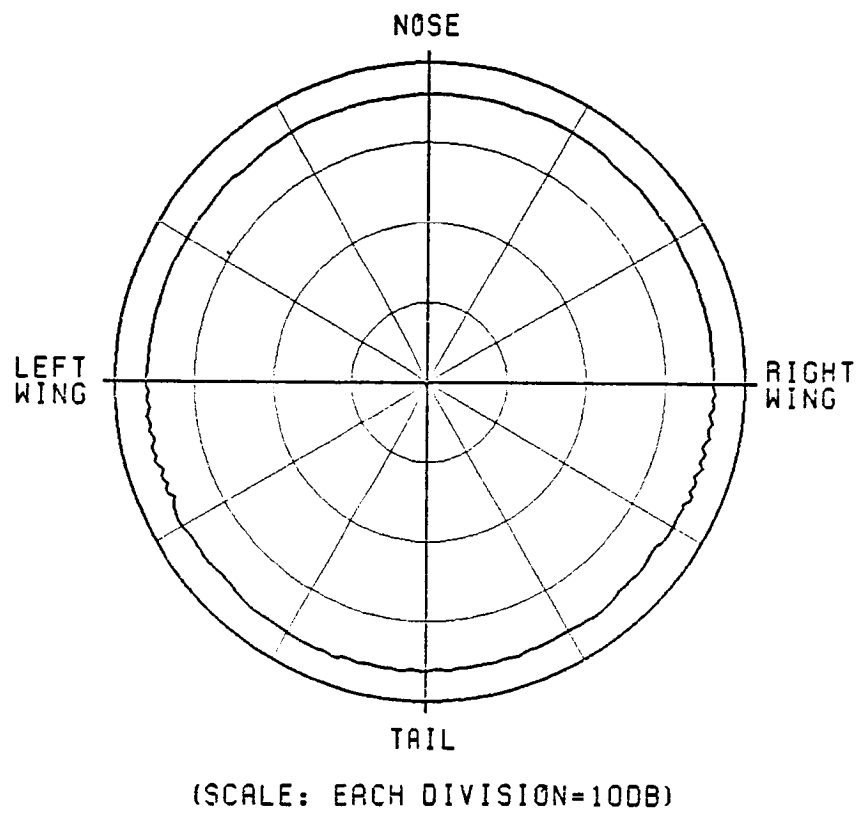
(c) E_{cp}

Figure 5.32. (Continued).

C. PRIVATE AIRCRAFT SIMULATIONS

This section presents a study of the effects on the radiation patterns associated with modeling private aircraft.

Measured roll plane patterns were provided by NASA (Hampton, Virginia) [37,38,39] and are used throughout the following discussion.

1. Cessna 402B

Let us consider the problem of modeling the Cessna 402B illustrated in Figure 5.33. Our goal now is to investigate how to model the roll plane of this aircraft using a composite ellipsoid and flat plates to best match the experimental results. Experimental results have been obtained from NASA (Hampton, Virginia), using the 1/7 scale model at a range of 50 feet; however, the model is input in full scale dimensions at a pattern range of 350 feet.

Past studies have indicated that matching the curvature of the fuselage near the antenna is more advantageous than trying to approximate the overall fuselage shape. With that in mind, the models illustrated in Figure 5.34 are considered first. Here the height and width of the ellipsoid match the corresponding dimensions of the actual fuselage top portion near the antenna, and wings are simulated as flat plates. Note that the prolate spheroid model of the old Aircraft Code [24] is also included in the figure for comparison. The resulting roll plane patterns are shown in Figure 5.35. The comparison shows that the ellipsoid model has led to a reduction in intensity of about 4 dB

ANTENNA LOCATION
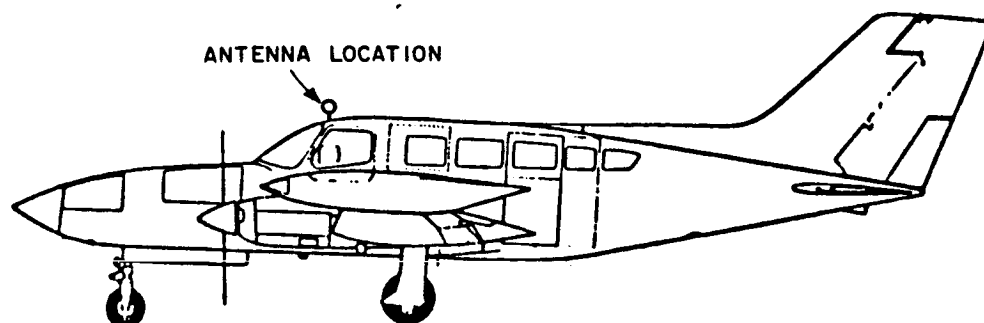
(a)   Side view.
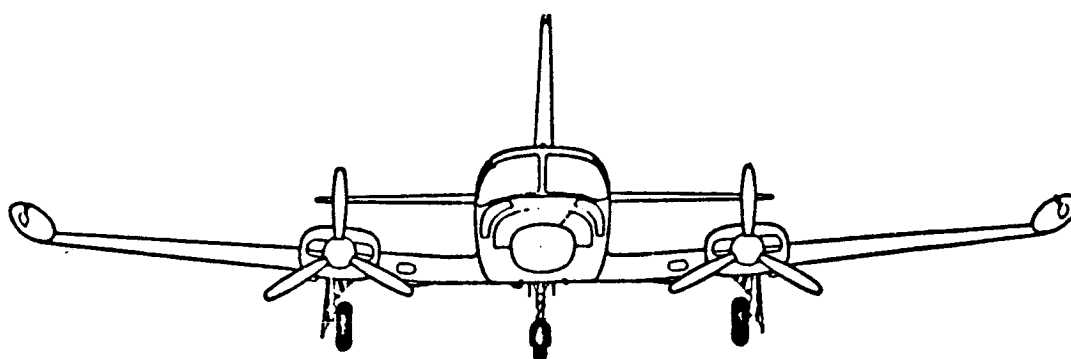
(b)   Front view.

Figure 5.33.   Cessna 402B.
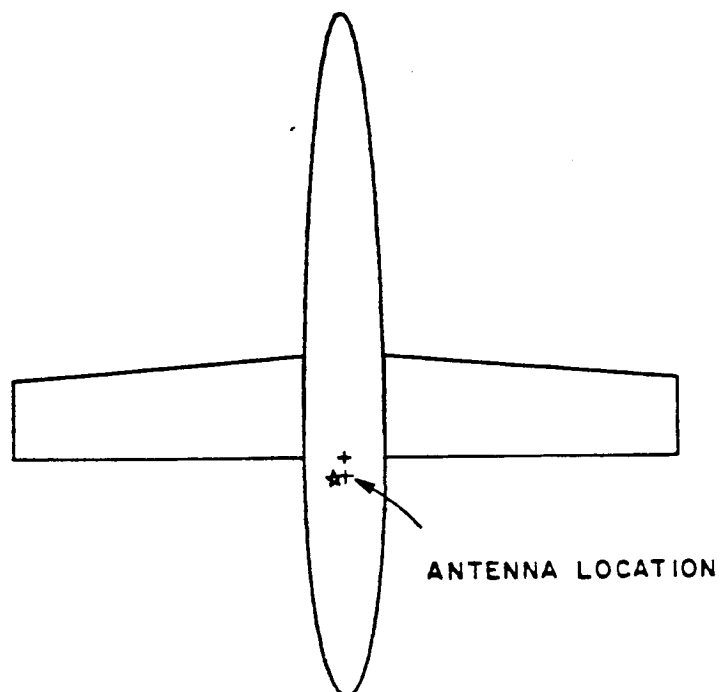
(a) TOP VIEW

(ELLIPSOID MODEL)   (PROLATE SPHEROID MODEL)

(b) FRONT VIEW

Figure 5.34. Model for Cessna 402B with wings only.

TOP

LEFT
WING

RIGHT
WING

—————CALCULATED
— — — — MEASURED

(SCALE: EACH DIVISION=10DB)

BOTTOM

(a) Pattern of Ellipsoid Model

TOP

LEFT
WING

RIGHT
WING

BOTTOM
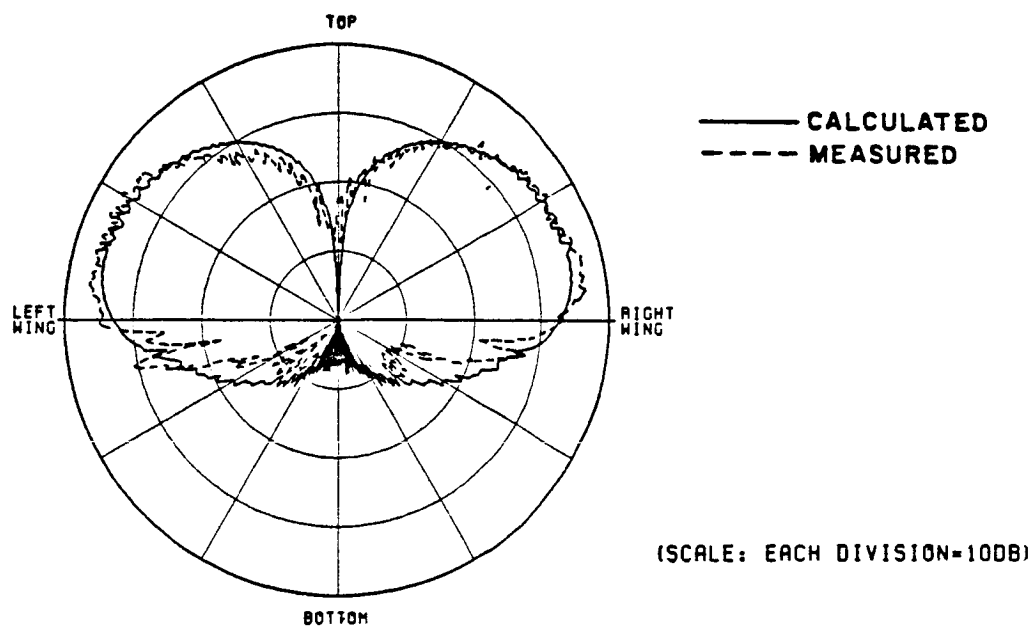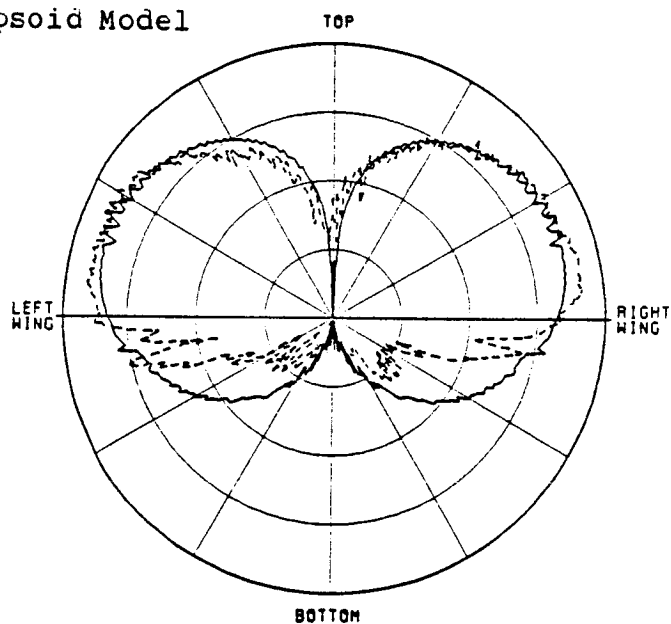
(b) Pattern of Prolate Spheroid Model

Figure 5.35. Pattern for Cessna 402B model shown in Figure 5.34.

throughout most of the lower half of the pattern, which is a definite improvement; however, the large lobes at ±105° and some ripple throughout the pattern are still missing.

A better model is obtained by consideration of the fuel tanks mounted on the wing tips. The actual shape of the tanks is curved, but of course they must be approximated by flat plates. A model with each fuel tank simulated as a single plate is shown in Figure 5.36, with the corresponding pattern shown in Figure 5.37. It is apparent that this is a major improvement in the lower half of the pattern, as the ±105° lobes are not present. A problem, however, is the excessive signal intensity in the 0° to ±20° range due to strong direct reflections off the fuel tanks.

To alleviate this problem, let us use two plates to simulate each fuel tank. This will decrease the amount of direct diffraction by better simulating the curved surface of the tank. Such a model is illustrated in Figure 5.38, with the corresponding pattern shown in Figure 5.39. A definite improvement is shown in the figure, but the intensity in the ±110° to ±140° range is still about 6 or 8 dB high. However, this pattern is within reasonable engineering agreement with the experimental result.

For greater accuracy, the effects of the engine housings can be considered. A model with engine housings and fuel tanks is shown in Figure 5.40, and the pattern resulting from this simulation model is shown in Figure 5.41. It is apparent from this result that the
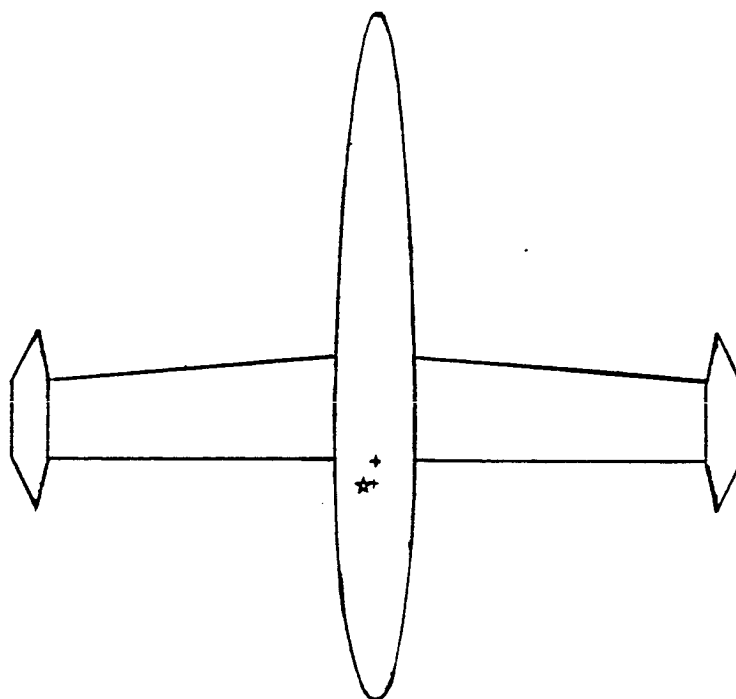
(a)   TOP VIEW

(b)   FRONT VIEW

Figure 5.36. Model for Cessna 402B with one plate simulation of fuel
              tanks.
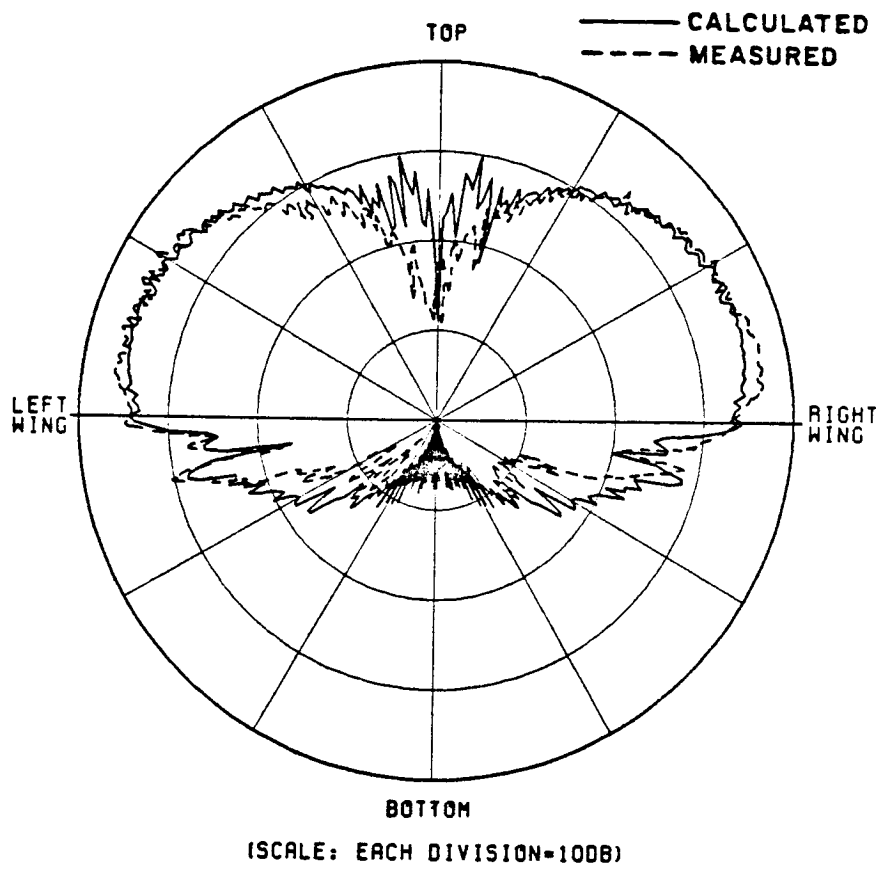
Figure 5.37. Pattern for Cessna 402B model shown in Figure 5.36.
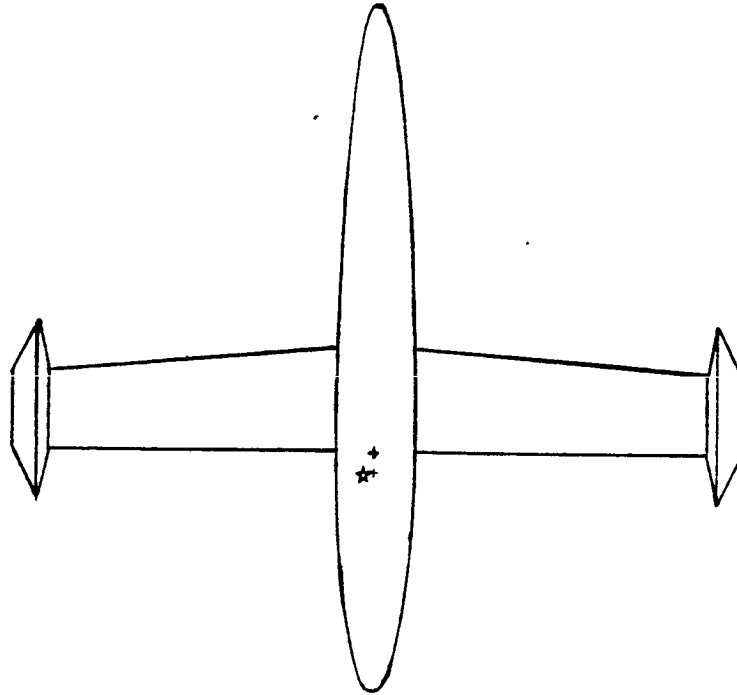
(a) TOP VIEW

(b) FRONT VIEW

Figure 5.38. Model for Cessna 402B with two plate simulation of fuel tanks.
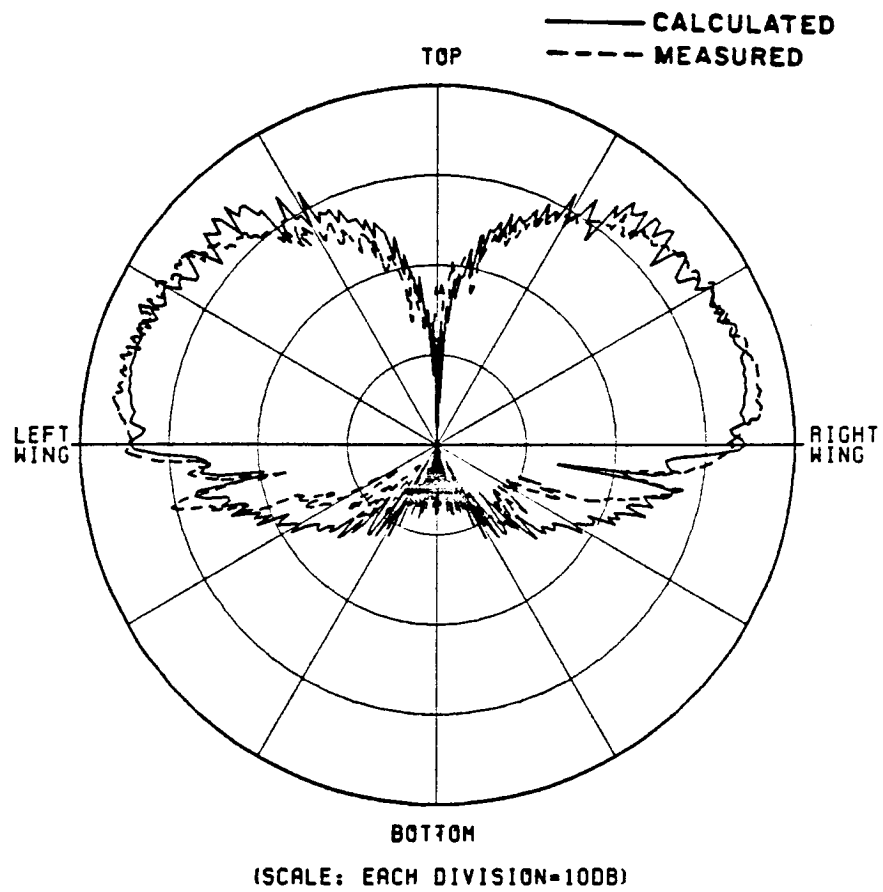
Figure 5.39. Pattern for Cessna 402B model shown in Figure 5.38.
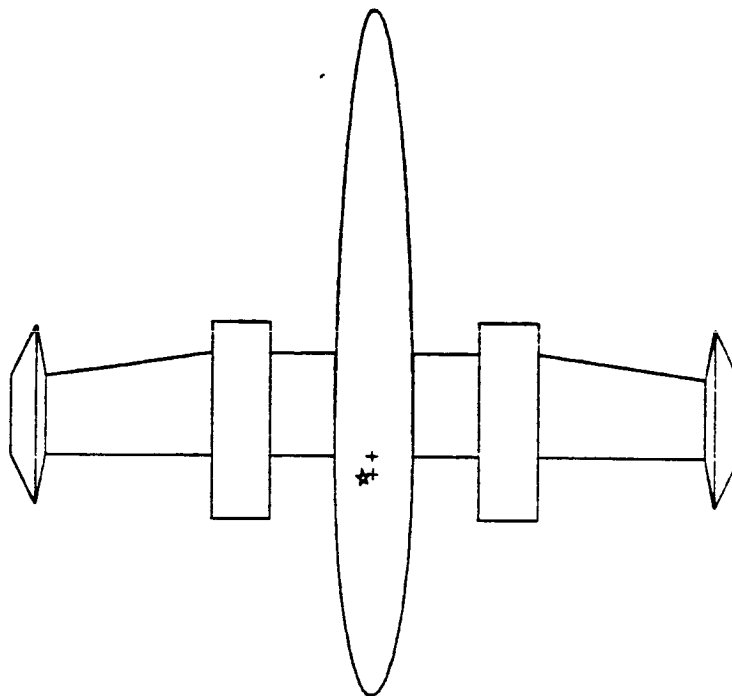
(a) TOP VIEW

(b) FRONT VIEW

Figure 5.40. Model for Cessna 402B with engines and fuel tanks.

CALCULATED

---- MEASURED

TOP

LEFT
WING

RIGHT
WING

BOTTOM

(SCALE: EACH DIVISION=10DB)
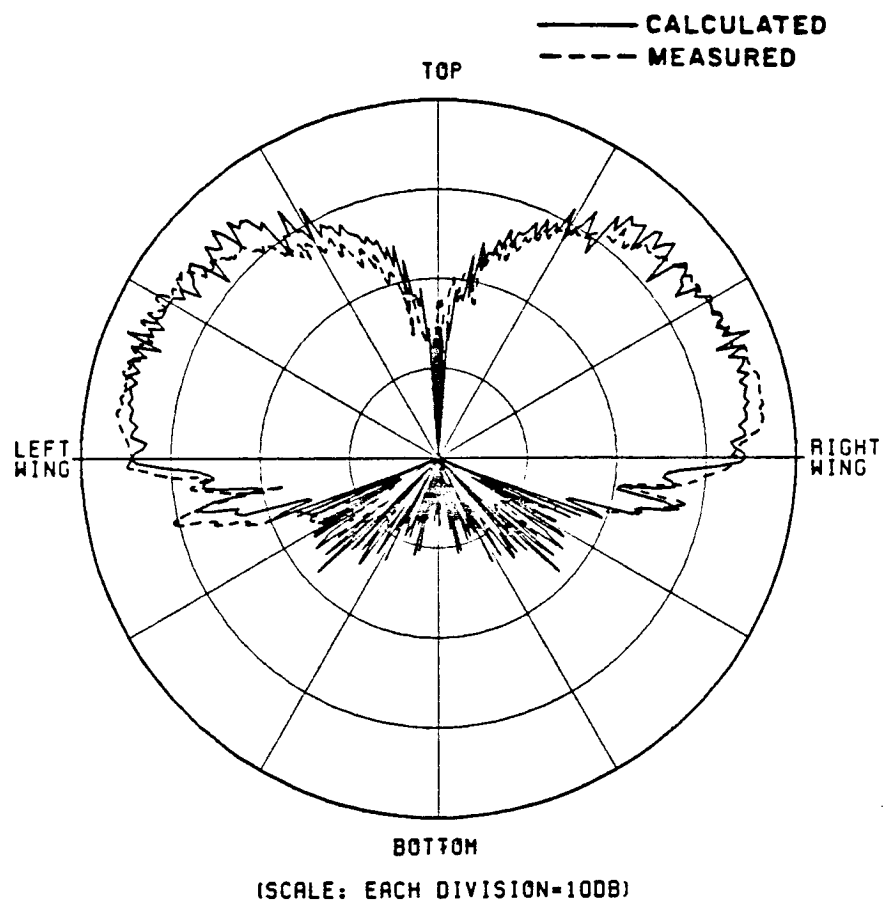
Figure 5.41. Pattern for Cessna 402B model shown in Figure 5.40.

pattern is greatly improved in the ±120° to ±180° range. Certainly

the results shown on this figure are acceptable for engineering

applications.

2. Beechcraft Baron

Another case which presents an interesting modeling challenge is

the Beechcraft Baron with the antenna mounted forward of the cockpit, as

illustrated in Figure 5.42. This model is most useful for testing our

new code in that this has wing mounted engines and propellers.

A model is desired which will yield a computed roll plane pattern

in close agreement with experimental results. An initial model

including wings and engine housings is illustrated in Figure 5.43 with

the corresponding roll plane pattern shown in Figure 5.44. One notes

that the computed result is well matched with the experimental result,

but the large ripple, especially in the lower half, is missing. Perhaps

an upgrading of the model could improve our accuracy. However, the rest

of the pattern would seem, if not perfect, at least acceptable for any

engineering applications.

Next, let us consider the effect of the rotating propellers in

front of the engines. It is necessary to check the scattering due to

the rotation of the propellers in that they are close to the antenna.

Four different positions (i.e., 0°, 45°, 90°, 135°) of the stationary

propellers are chosen to simulate the rotating motion of the propellers
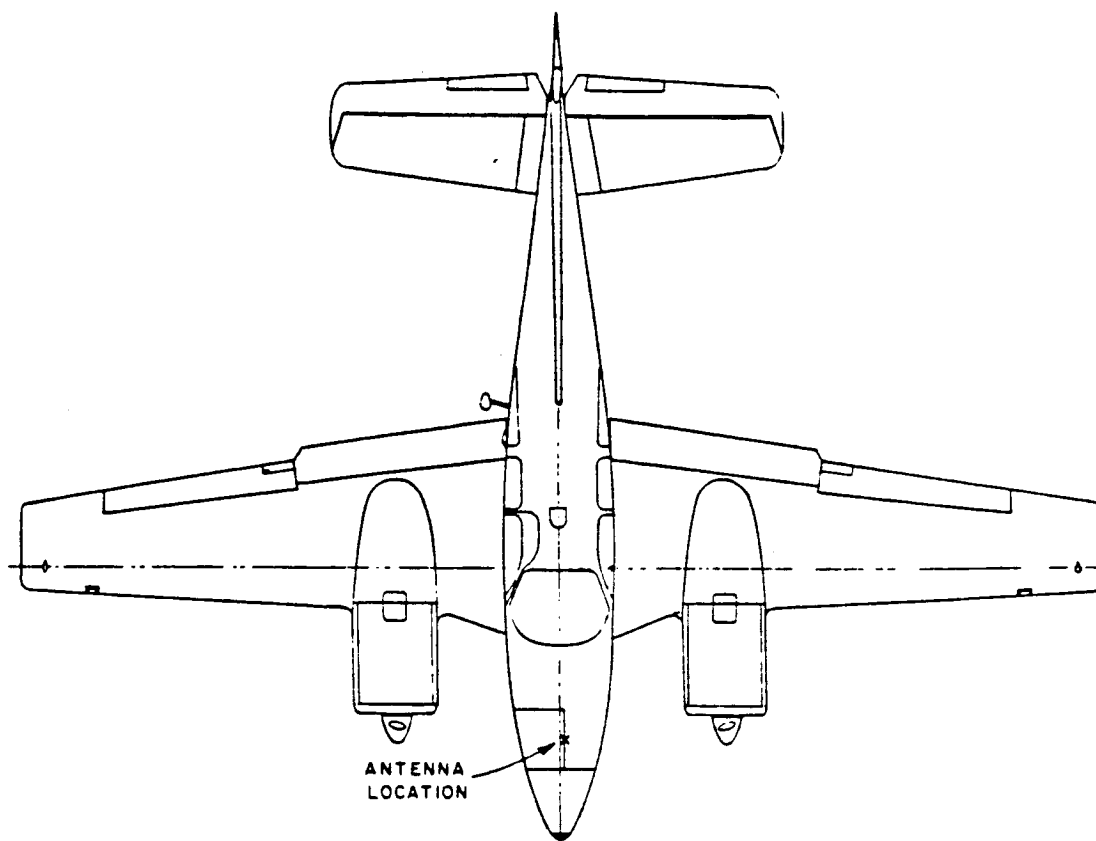
(a) TOP VIEW
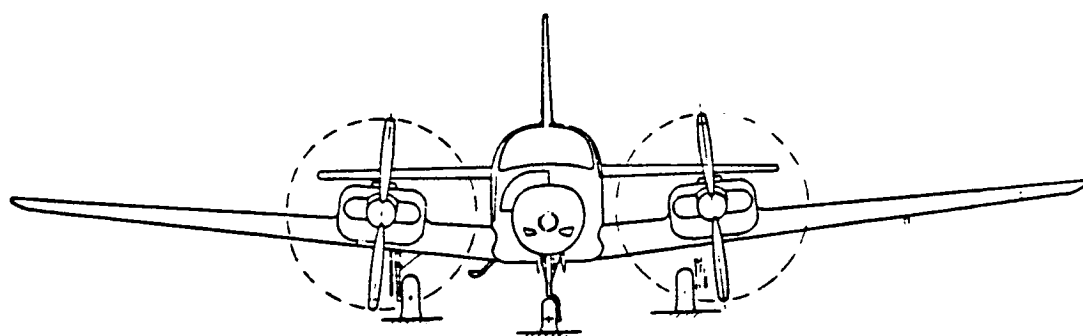
(b) FRONT VIEW

Figure 5.42. Beechcraft Baron with antenna in forward location.
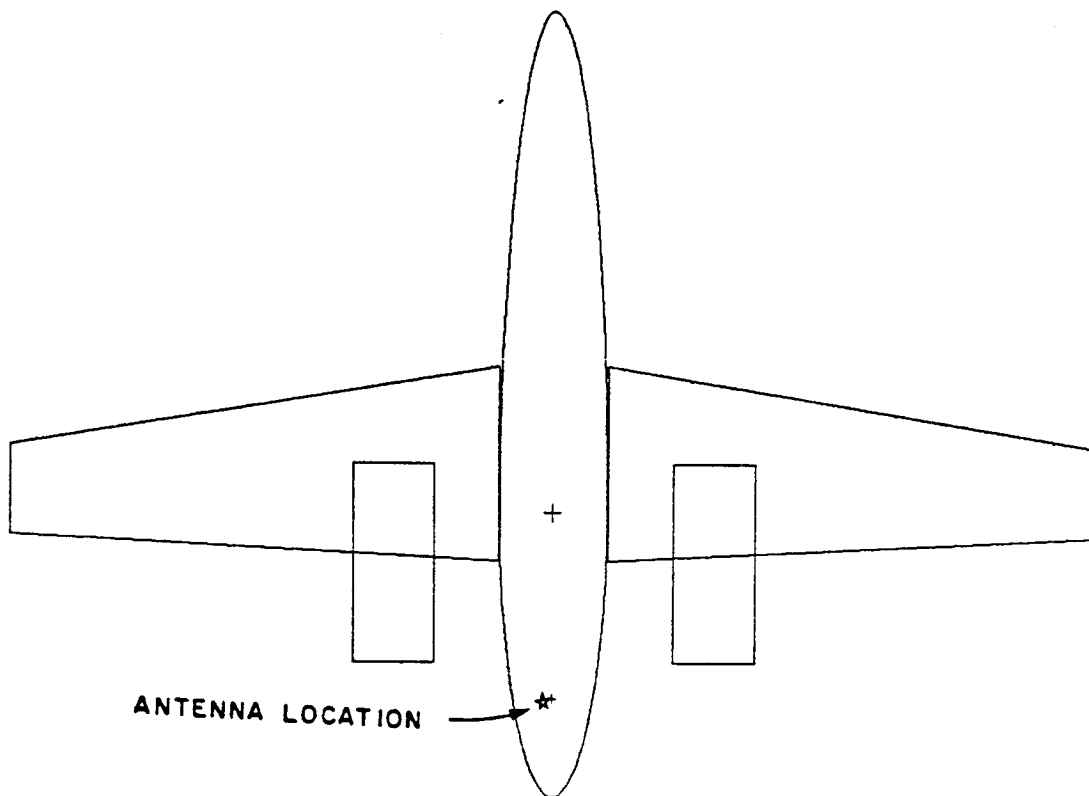
(a) TOP VIEW

(b) FRONT VIEW

Figure 5.43. Beechcraft Baron model with engine housings.
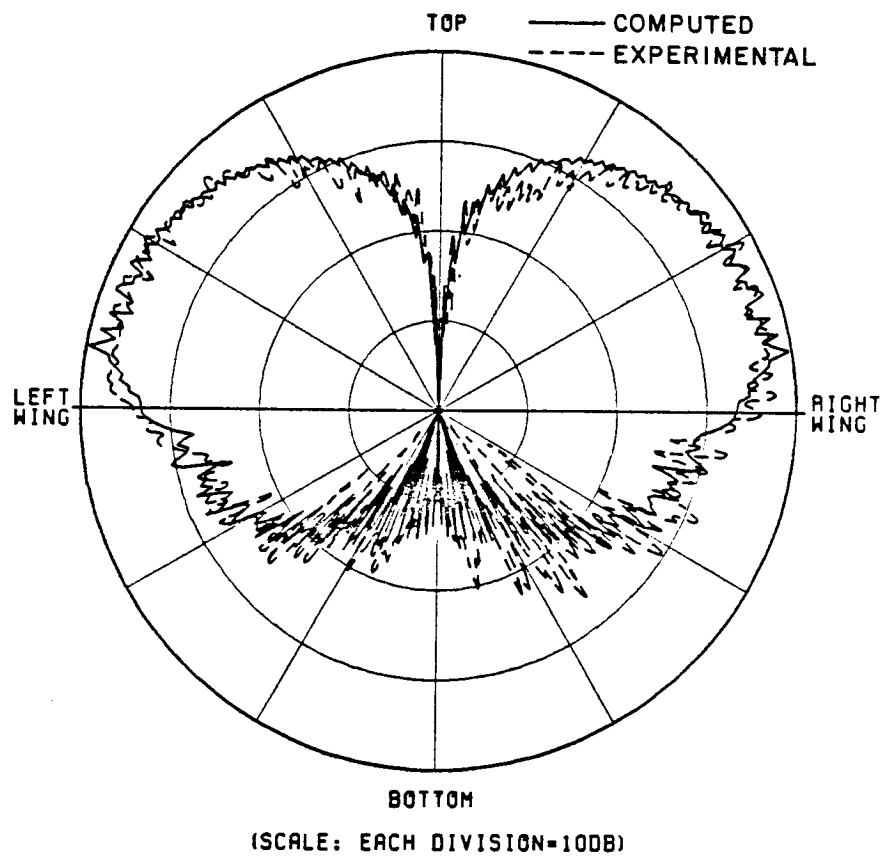
Figure 5.44. Roll conical pattern (θ_p=80°) Beechcraft Baron model shown in Figure 5.43.

233

as shown in Figure 5.45. For simplicity, only the left propeller is considered with the corresponding roll plane pattern shown in Figure 5.46. Note that width of pattern line indicates the variation of the radiation pattern due to the rotation of the propellers. One notes that the variation margin in the 200° to 300° range is about 4 or 6 dB. This example shows the extended capability of our code in the pattern analysis for the model with a rotating object.

3. Cessna 150

Another interesting modeling challenge is the Cessna 150 illustrated in Figure 5.47. Perhaps the obvious way to model the Cessna 150 would be to use the ellipsoid as a fuselage, then put in a flat plate above it to simulate the wing. However, the Aircraft Code has the requirement that the source be mounted on the ellipsoid; whereas in this case, the antenna is located on the wing. An acceptable model within the requirements of this program can be obtained as illustrated in Figure 5.48, where the ellipsoid is used lengthwise as the wing. Note that the nose and tail are modeled as flat plates. The resulting elevation plane pattern for this model is shown in Figure 5.49. Although the magnitude of ripple is not quite perfect, it is of the correct spacial frequency, and the general shape of the pattern is good.

A slight disadvantage to this particular use of the ellipsoid is due to the sharp curvature near the antenna, in that the pattern is quite sensitive to small changes in source location.
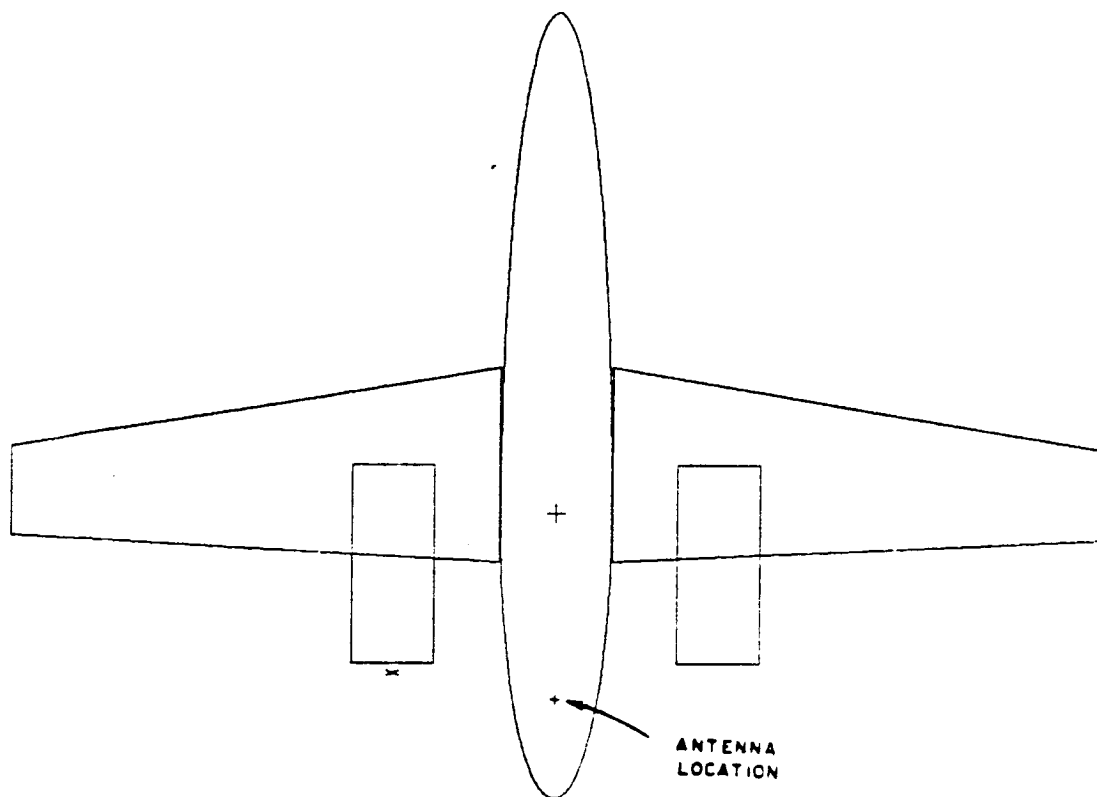
(a)   TOP VIEW
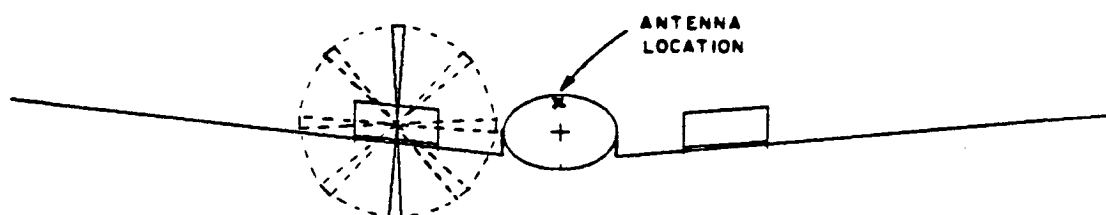
(b)   FRONT VIEW

Figure 5.45.   Beechcraft Baron model with rotating properllers on one
side.

TOP

LEFT
WING

RIGHT
WING

BOTTOM

(SCALE: EACH DIVISION=10DB)
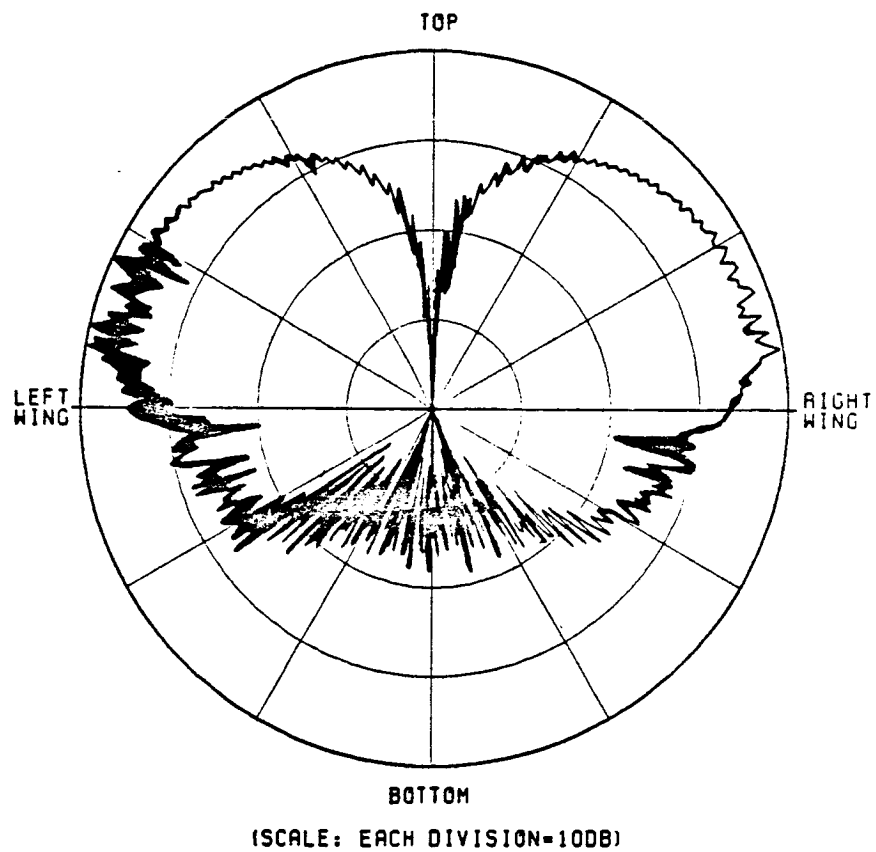
Figure 5.46. Roll plane pattern (θ_p=80°) for Beechcraft Baron model
shown in Figure 5.45.
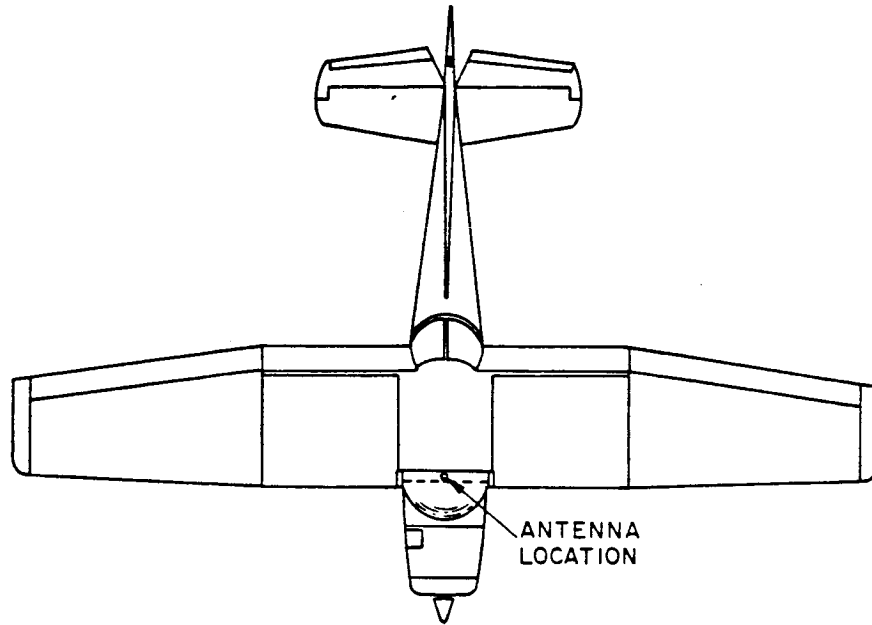
(a) Top view.
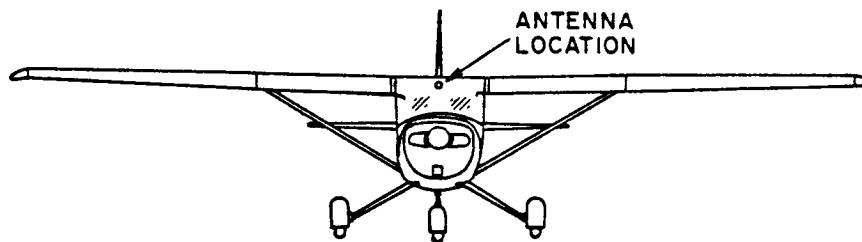
(b) Front view.

Figure 5.47. Cessna 150.

(a) Top view.

ANTENNA LOCATION
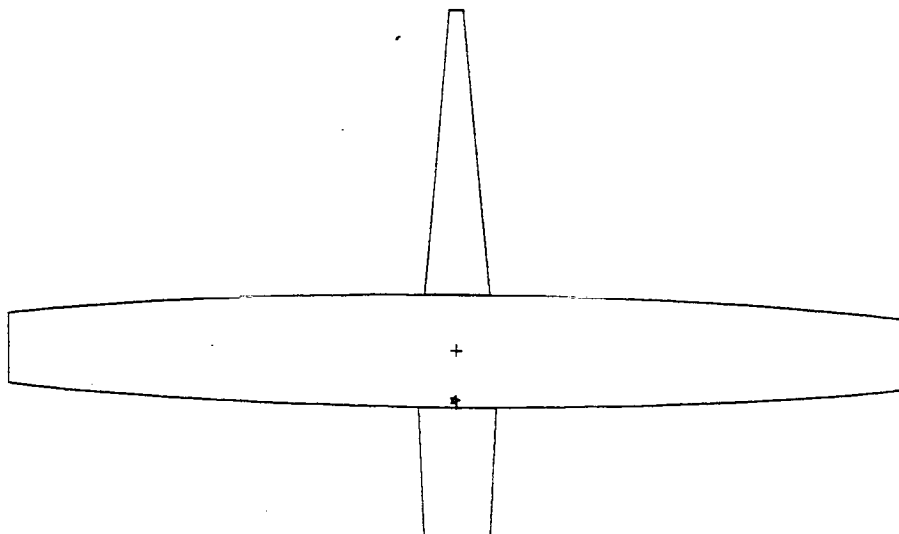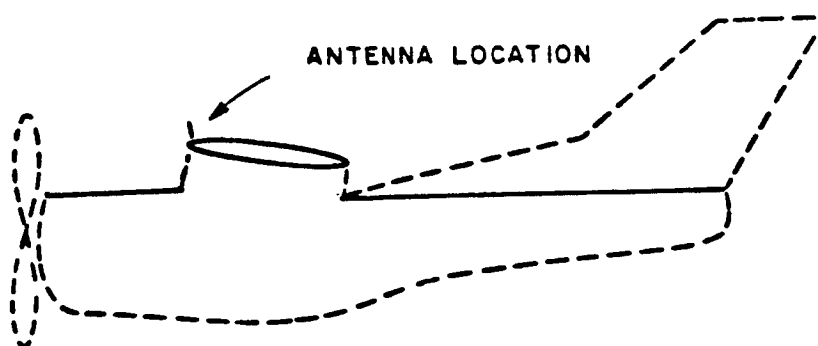
(b) Side view.

Figure 5.48. Cessna 150 model. Dashed lines are not part of the computer simulation.
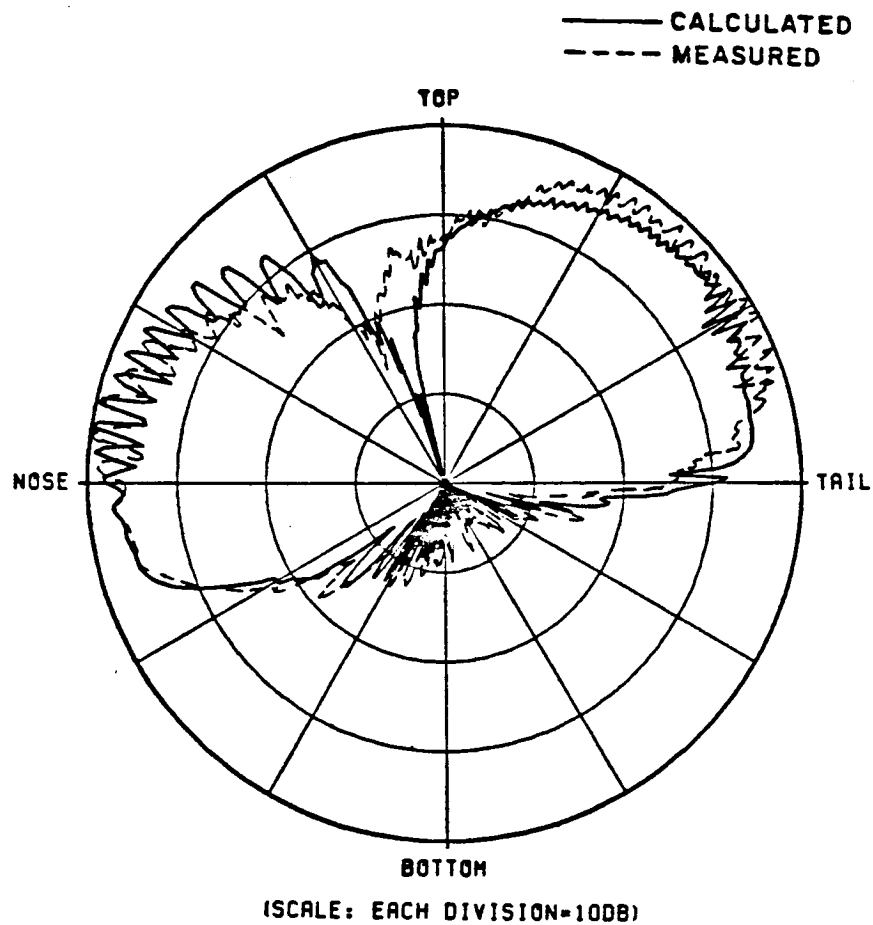
Figure 5.49. Cessna 150 elevation plane pattern for model shown in Figure 5.48.

D. MILITARY AIRCRAFT AND MISSILES

This section presents the study of the radiation patterns for the antennas mounted on the fuselage of various military aircraft (F-16, F-4, A-10 and C-141) and missiles. The ability of this solution to analyze very complex structures is verified in terms of military aircraft. Various scattering mechanisms are also studied individually using the F-16 in order to show the significance of the variouserms.

1. F-16 Fighter Aircraft

The most interesting model among military aircraft studied to date is the F-16 fighter aircraft in that extensive experimental results [47] are available. The measured data was obtained by General Dynamics using a quarter scale model of the F-16. The line drawings for a F-16 fighter aircraft are shown in Figure 5.50.

The TACAN antenna mounted on the top of the F-16 fighter fuselage as shown in Figure 5.50 is studied here and operated at a frequency of 0.96 GHz. As shown in Figure 5.51, a composite ellipsoid (21.5" x 23" x 400" x 250") is chosen to simulate the fuselage of the aircraft as accurately as possible, especially near the antenna location, and the other appendages (i.e., wings, stabilizers, tails, etc.) of the aircraft are simulated using 12 flat plates. Note that the radome of the F-16 fighter is simulated as a truncated fuselage.

TACAN ANTENNA

49.31 FT

(a)   SIDE VIEW

32.83 FT

31 FT W/O MISSILES

7.75 FT

(b)   FRONT VIEW

(c)   TOP VIEW
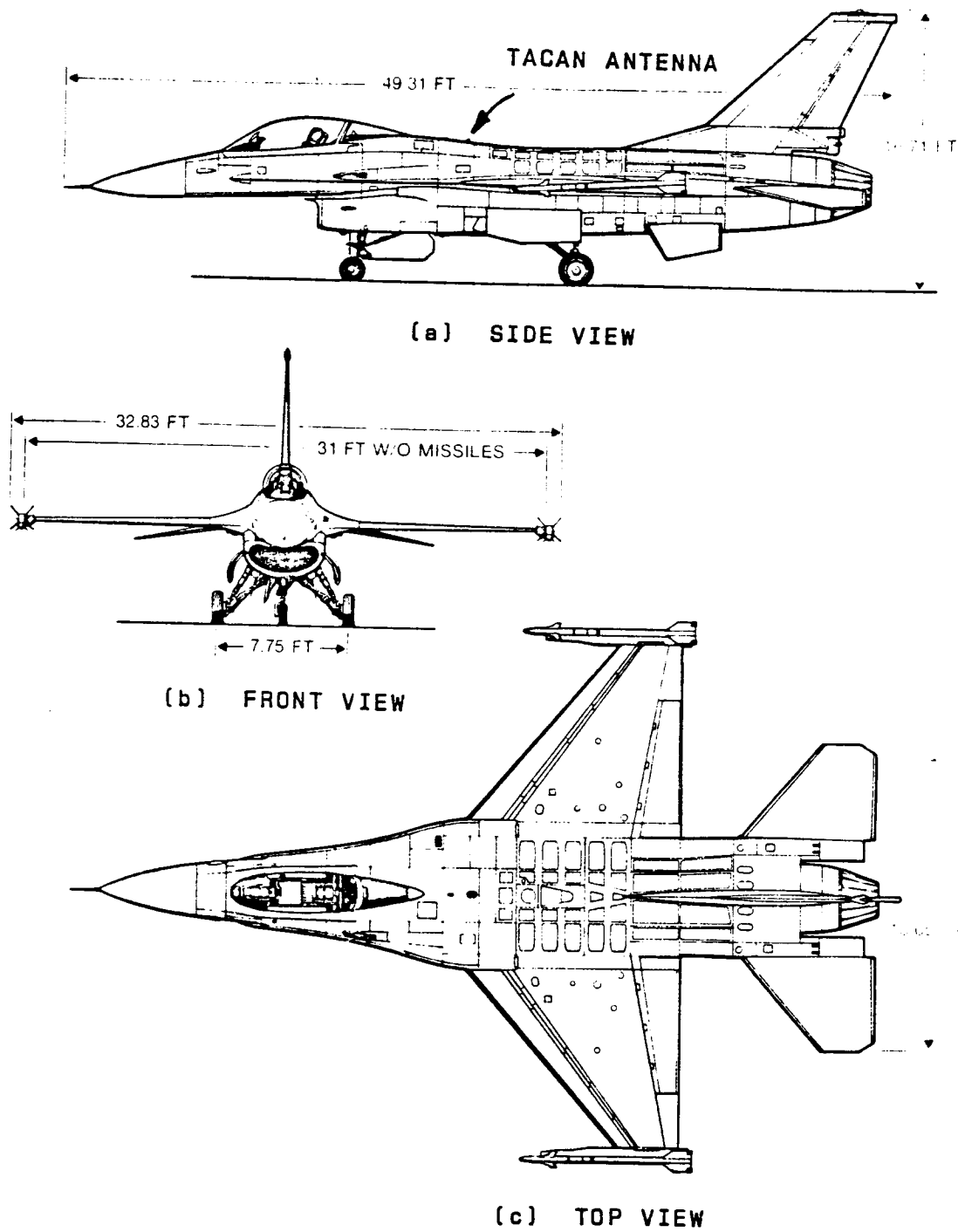
Figure 5.50.   F-16 fighter aircraft.

241

(a) SIDE VIEW

(b) FRONT VIEW

(c) TOP VIEW
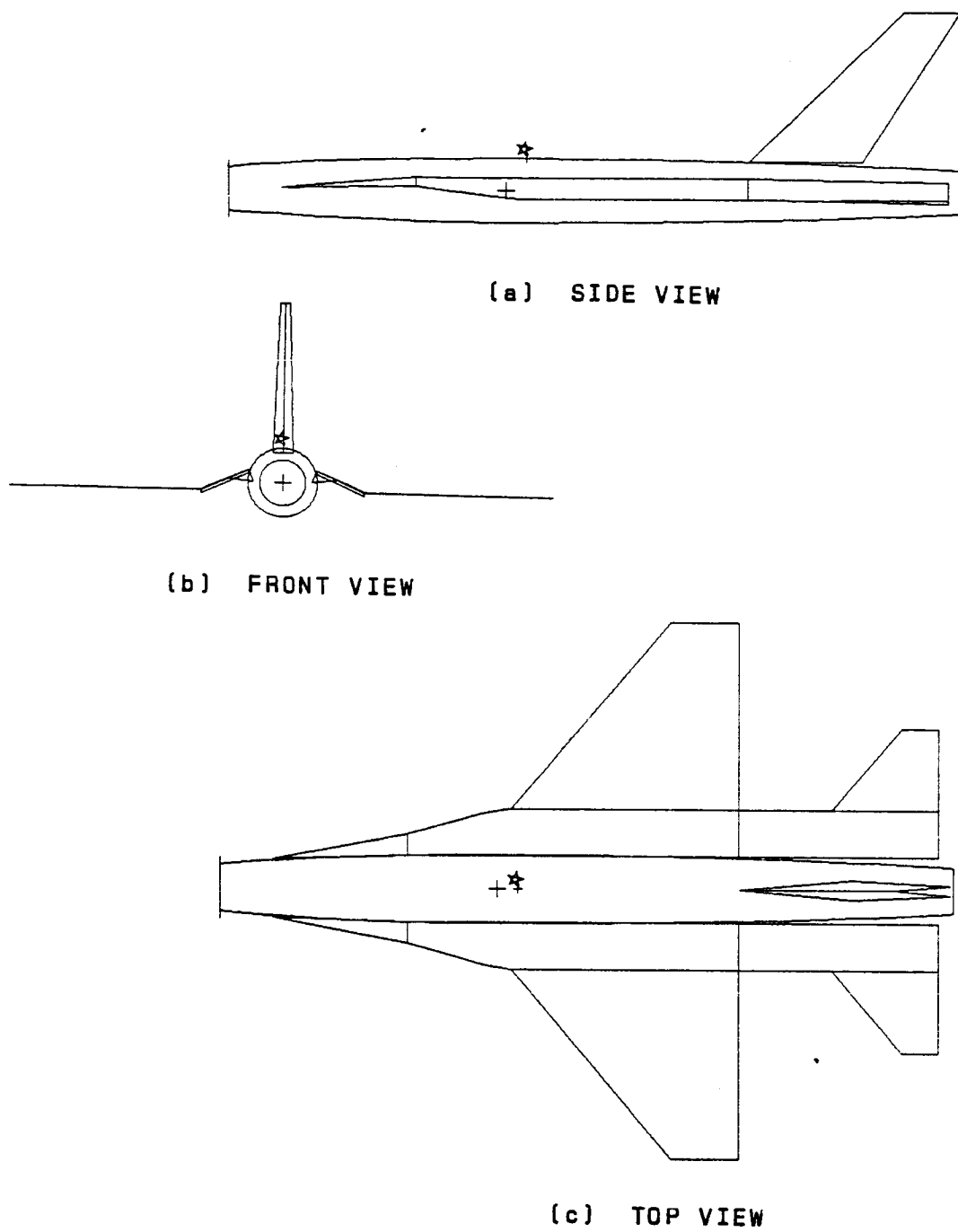
Figure 5.51. Computer simulated model of an F-16 fighter aircraft.

242

The various UTD terms are demonstrated for the roll plane radiation pattern in Figure 5.52 and the total field is compared with the experimental results in Figure 5.53. Note that the pattern of the prolate spheroid model [24] is also included in the figure to show the improvement of the new code. As can be seen from the comparison, the result of the ellipsoid model shows very good agreement with the maximum discrepancy being less than 2 dB. Note that each pattern is normalized to the same level such that one can compare the significance of each UTD term. Since the individual UTD terms can be analyzed separately using this code, one can ascertain the significant features of a complex target. The elevation plane pattern is shown in Figures 5.54 and the calculated result compares quite favorably with the measurement.

To show the complete volumetric radiation patterns, the various azimuthal conical patterns $(\theta_p = 10°, 20°, 30°, 40°, 45°, 50°, 55°, 60°, 65°, 70°, 75°, 80°, 85°, 90°, 95°, 100°, 105°, 110°, 115°, 120°,$ see Figure 5.2(c)) are calculated as shown in Figures 5.55 through 5.74. In each case, both the principal and cross polarizations are considered. The calculated results compare very favorably with the measurements in each case. It is noted that the cockpit section simulation is not complete in our model; as a result, one can not expect good agreement between the calculated and measured results in the nose region in that the cockpit would be along the direct radiation path for such radiation directions. In addition, the ripple above the aircraft in the elevation pattern is most likely created by the cockpit which is not simulated in the analysis.

243
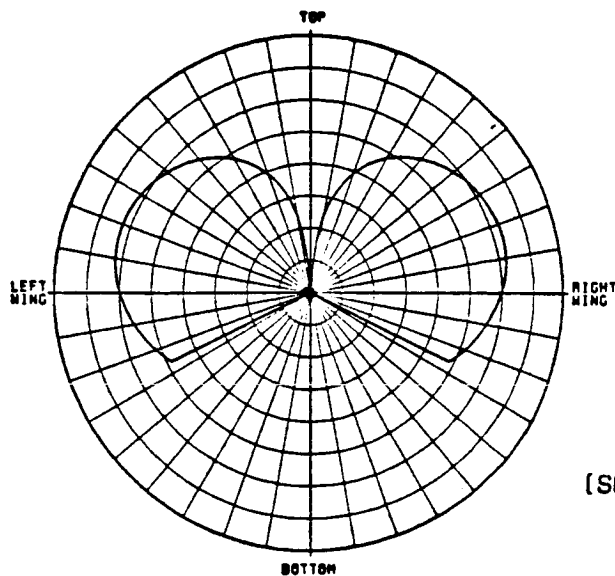
(SCALE: EACH DIVISION= 4DB)

(a) SOURCE FIELD ($\bar{E}^s$)
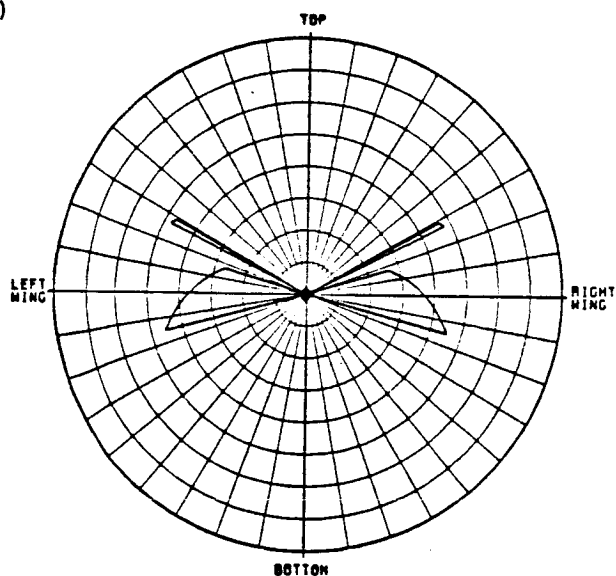
(b) REFLECTED FIELD ($\bar{E}^r$)

Figure 5.52. Various UTD terms for the roll plane pattern of a $\lambda/4$ monopole mounted on top of an F-16 fighter aircraft.

244
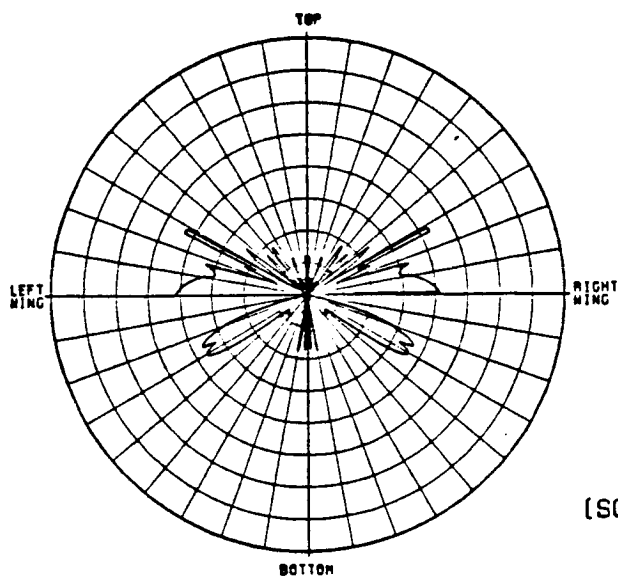
(SCALE: EACH DIVISION= 4DB)

(c) DIFFRACTED FIELD ($\bar{E}^d$)
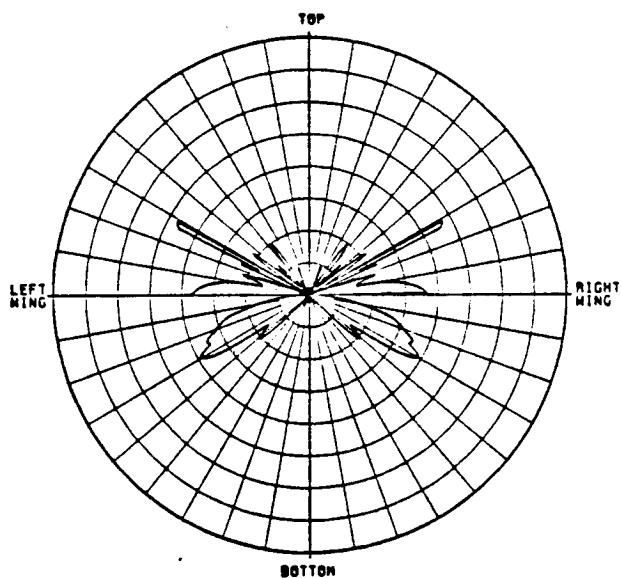
(d) DIFFRACTED AND CORNER DIFFRACTED
FIELD ($\bar{E}^d + \bar{E}^c$)

Figure 5.52. (Continued).

245
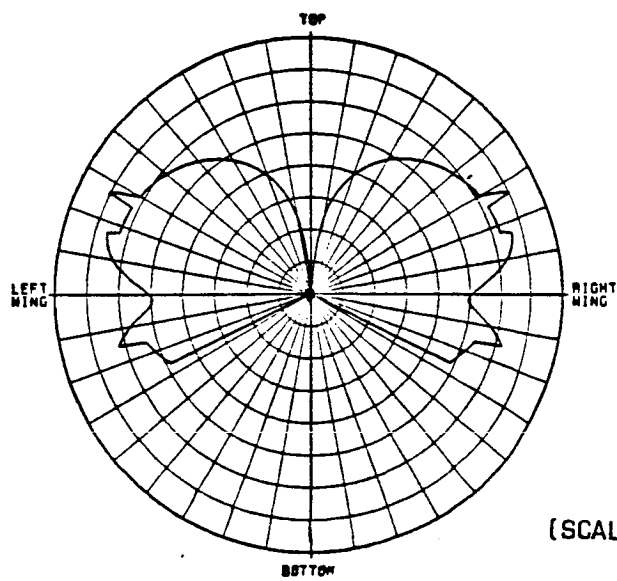
(SCALE: EACH DIVISION= 4DB)

(e) GO FIELD $(\bar{E}^S + \bar{E}^r)$
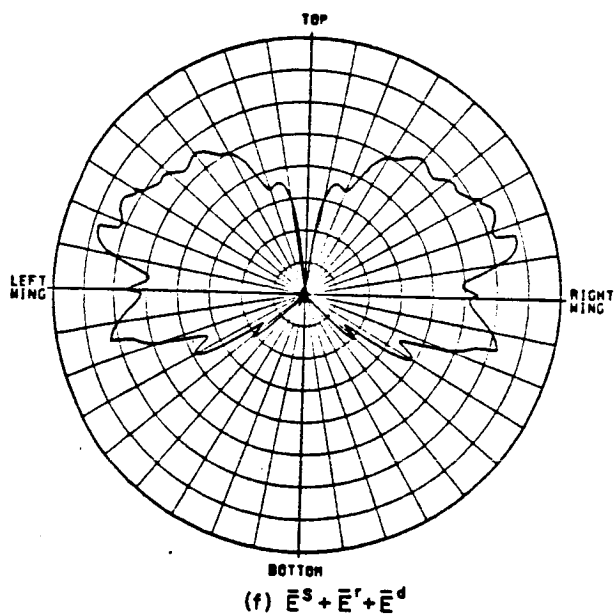
(f) $\bar{E}^S + \bar{E}^r + \bar{E}^d$

Figure 5.52. (Continued).

246

(SCALE: EACH DIVISION= 4DB)
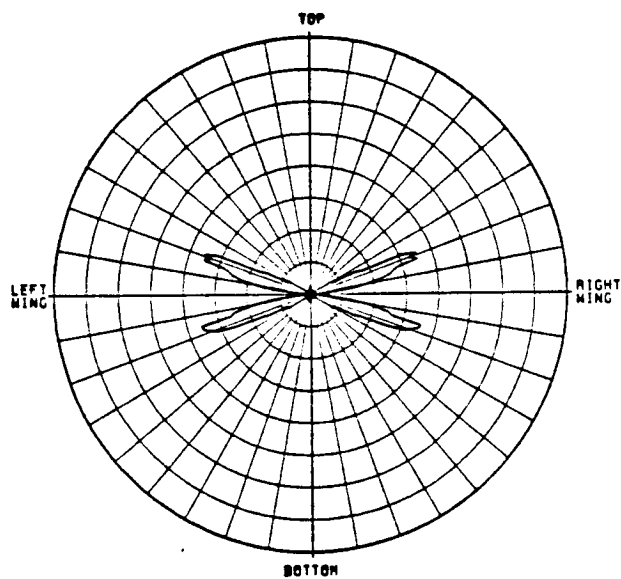
(g) HIGHER ORDER TERMS

$$(\bar{E}^{rr} + \bar{E}^{rd} + \bar{E}^{dr} + \bar{E}^{dd} + \bar{E}^{rc} + \bar{E}^{dc})$$

Figure 5.52. (Continued).

———— CALCULATED
— — — — MEASURED

(SCALE: EACH DIVISION= 4DB)

(a) Pattern of Ellipsoid Model

(b) Pattern of Prolate Spheroid Model
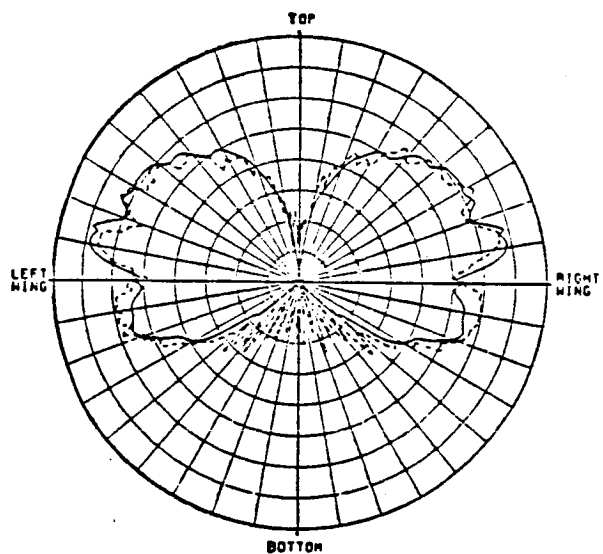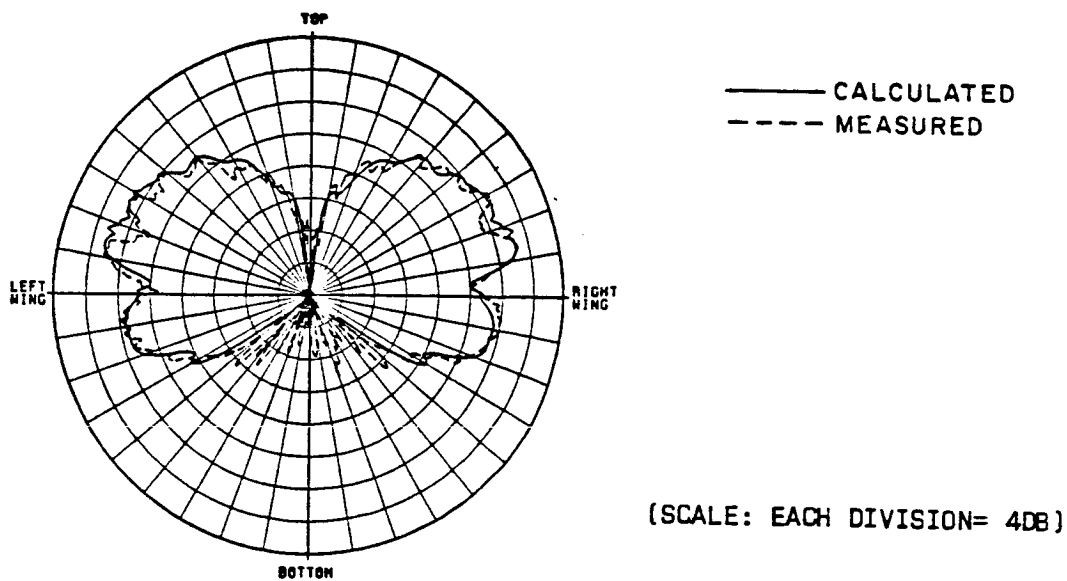
Figure 5.53. Total field for roll plane pattern of a λ/4 monopole
mounted on top of an F-16 fighter aircraft.

CALCULATED
MEASURED

TOP

TAIL

NOSE

BOTTOM

(SCALE: EACH DIVISION= 4DB)
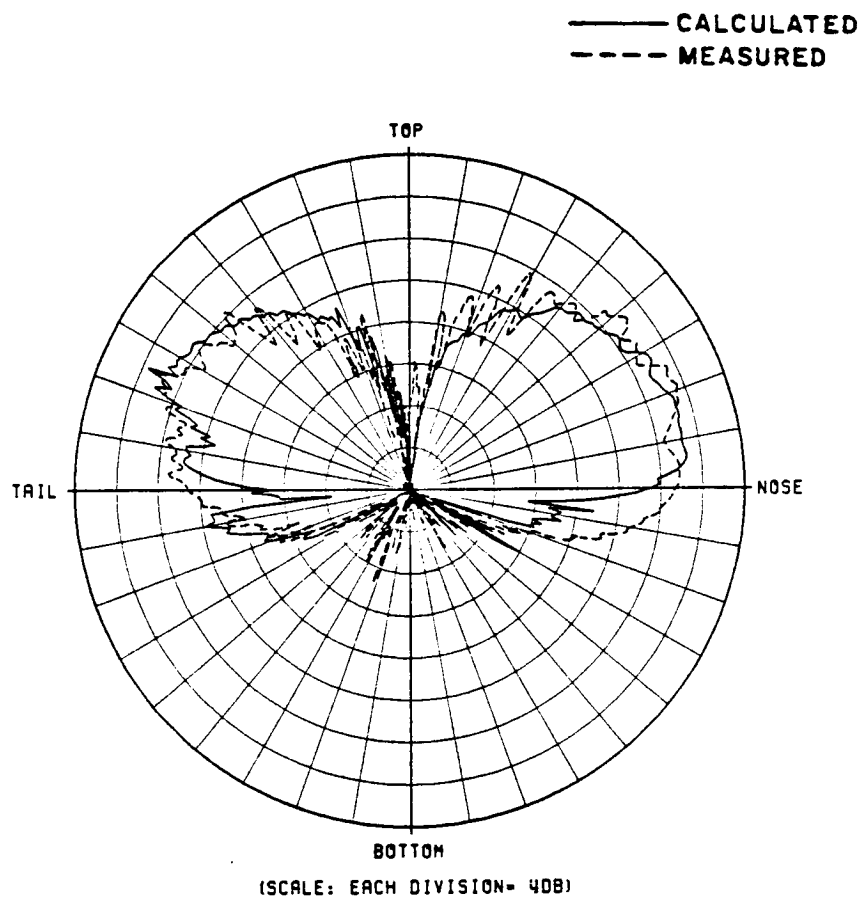
Figure 5.54. Elevation plane pattern of a λ/4 monopole
mounted on top of an F-16 fighter aircraft.

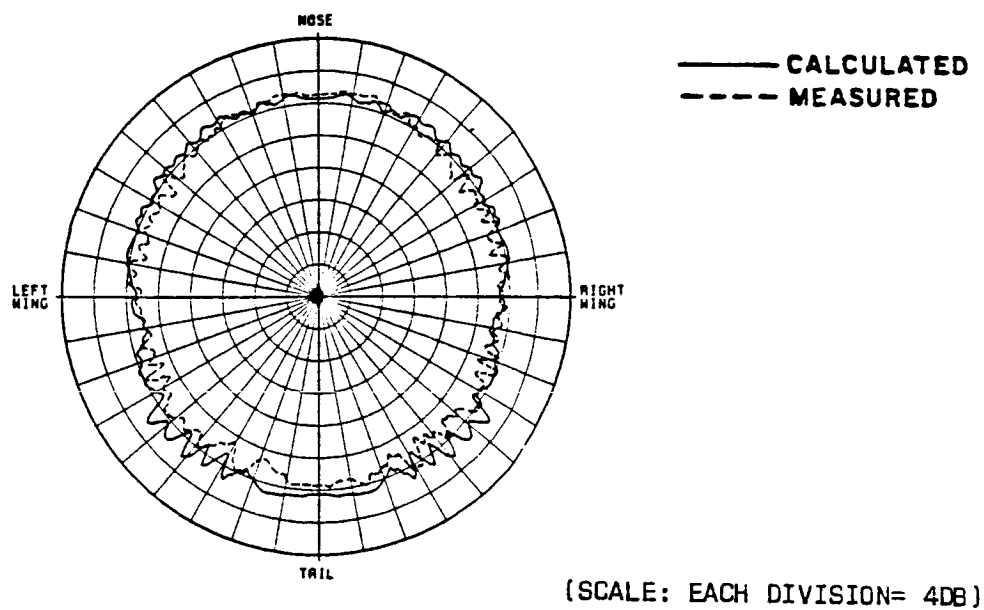249
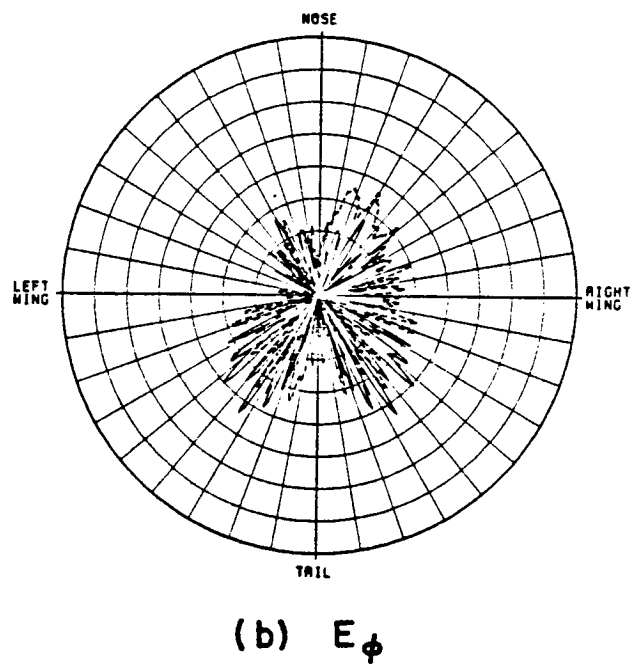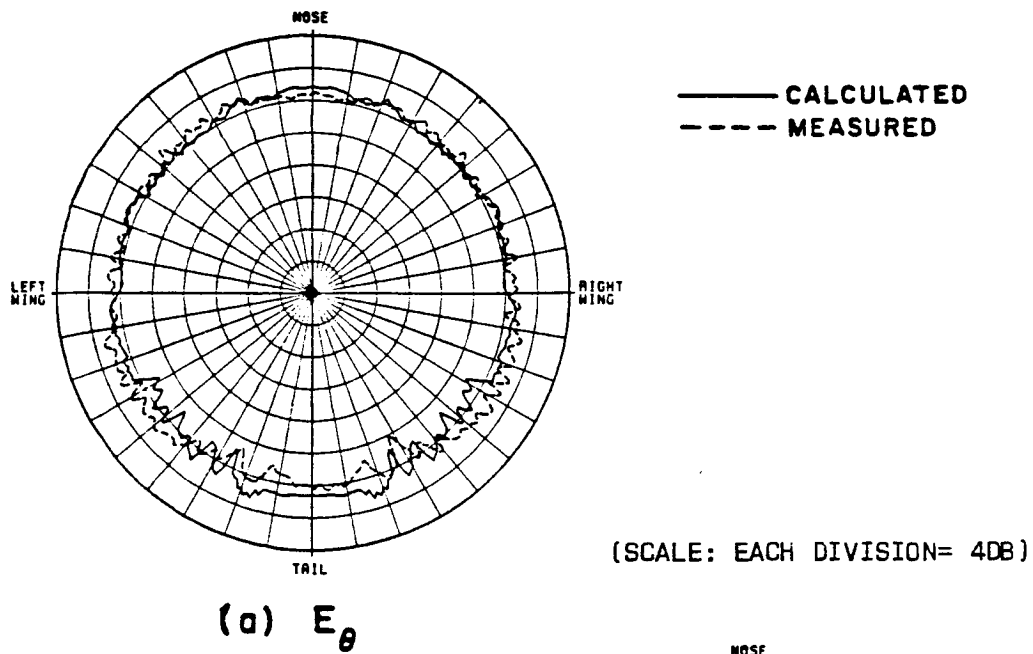
(a) E_θ

(SCALE: EACH DIVISION= 4DB)

(b) E_ϕ
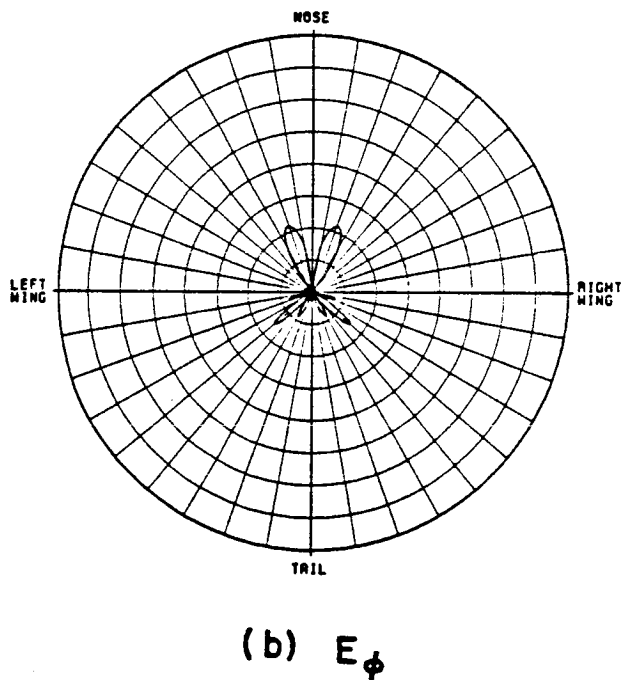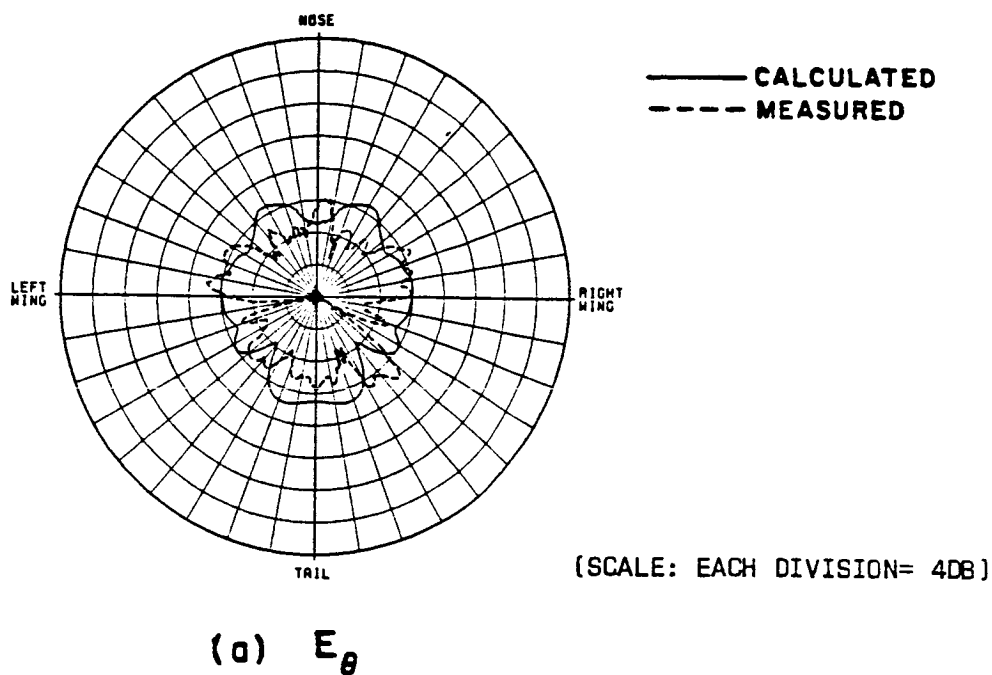
Figure 5.55. Azimuthal conical pattern ($\theta_p = 10°$) of a $\lambda/4$ monopole mounted on top of an F-16 fighter aircraft. (See Figure 5.2(c)).

250

NOSE

LEFT
WING

RIGHT
WING

———— CALCULATED
— — — — MEASURED

(SCALE: EACH DIVISION= 4DB)

TAIL

(a) E_θ

NOSE

LEFT
WING

RIGHT
WING

TAIL

(b) E_ϕ
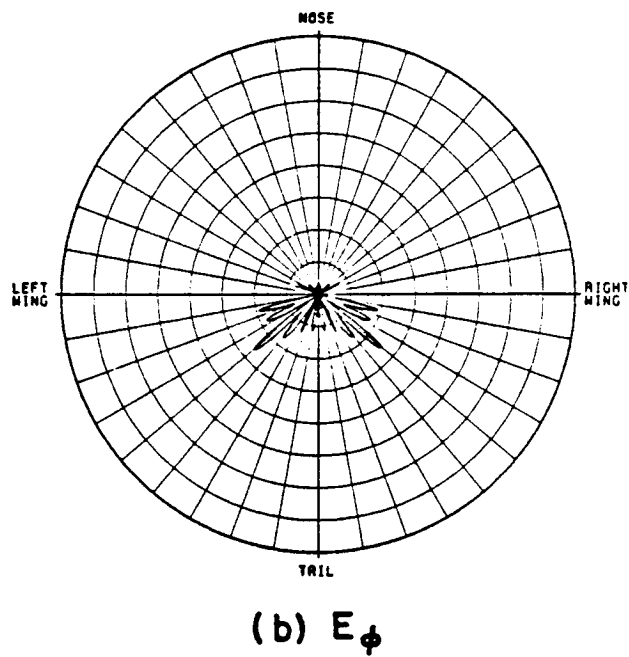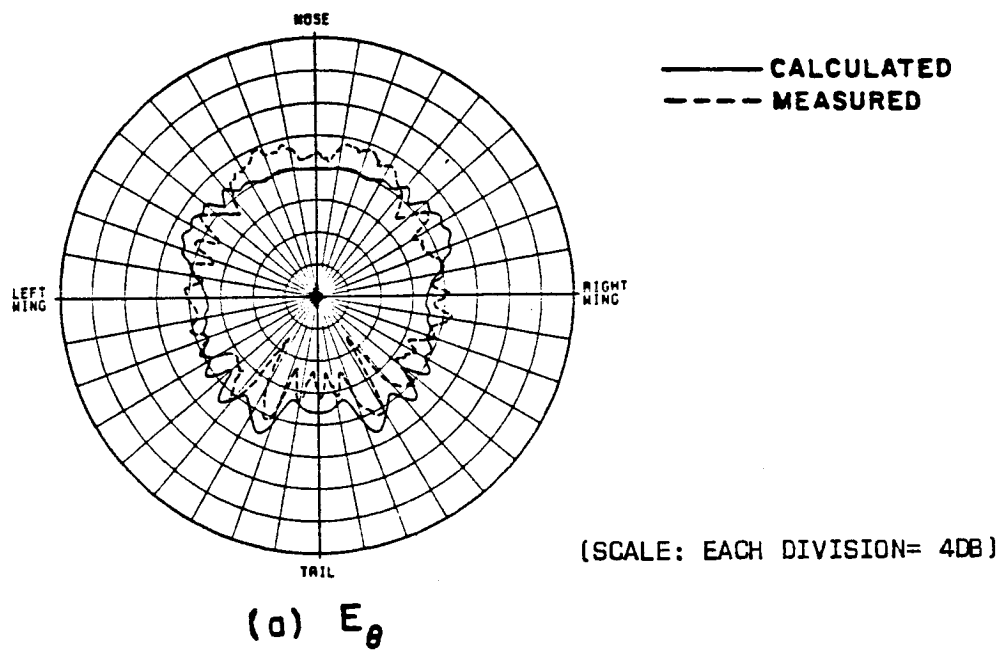
Figure 5.56. Azimuthal conical pattern ($\theta_p = 20°$) of a $\lambda/4$ monopole
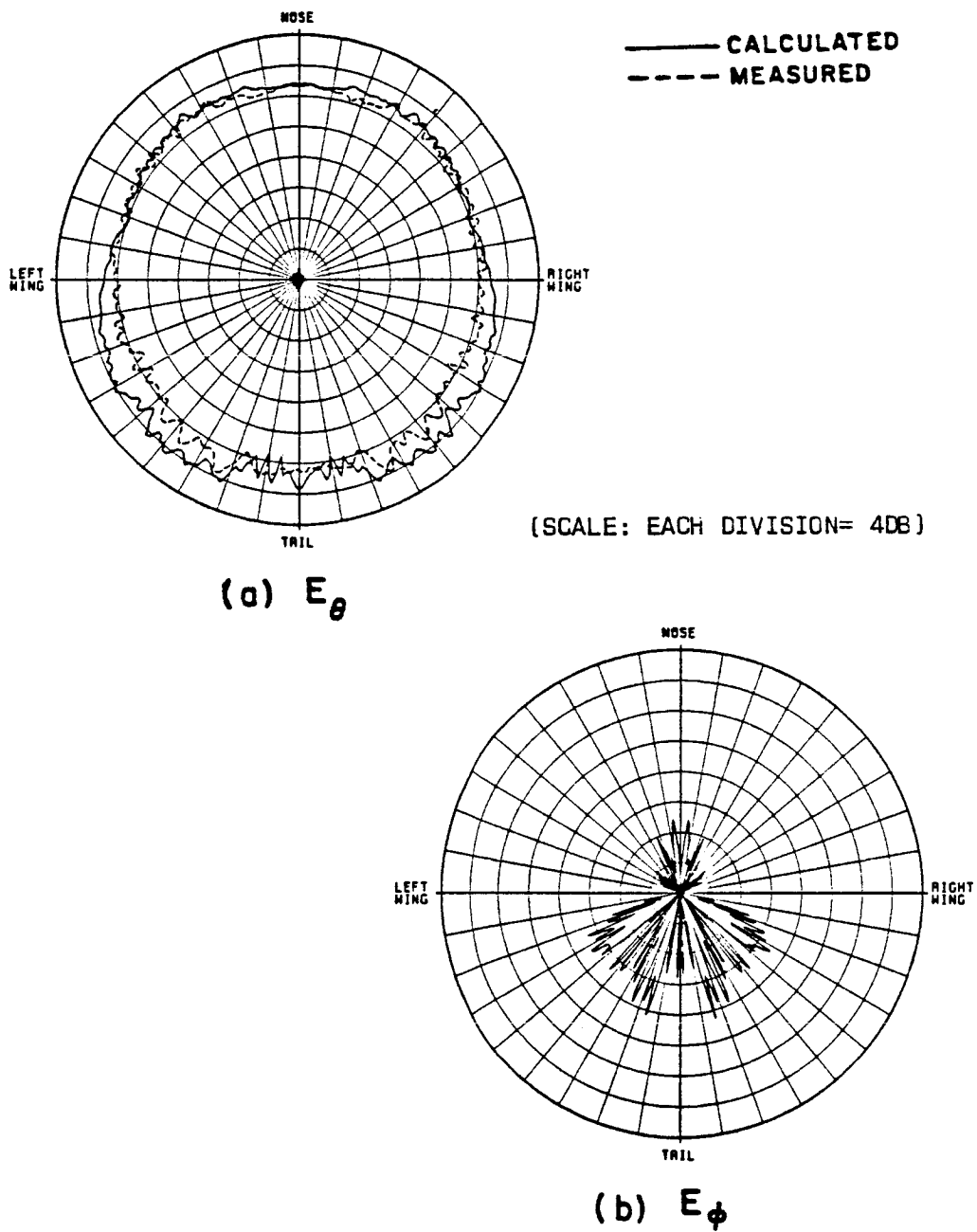mounted on top of an F-16 fighter aircraft.
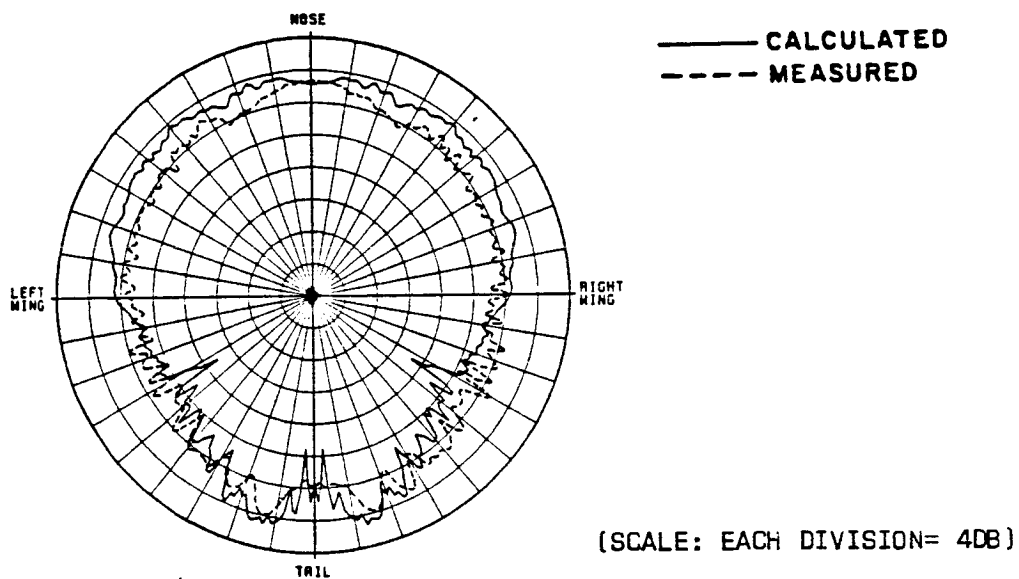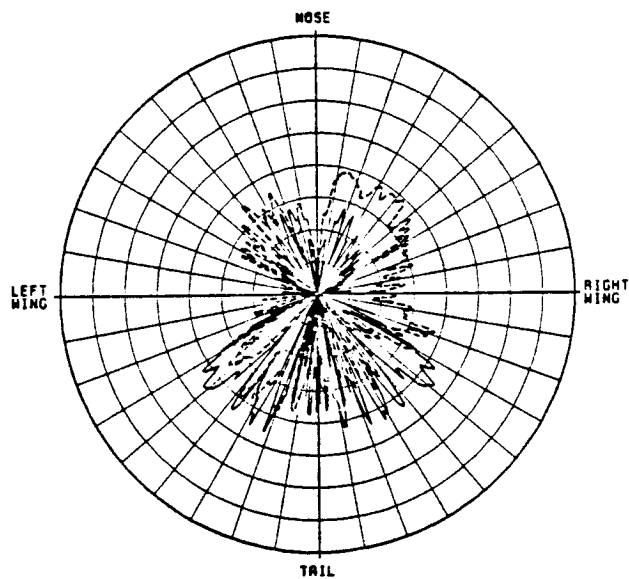
251

(a) E_θ

(SCALE: EACH DIVISION= 4DB)

(b) E_ϕ
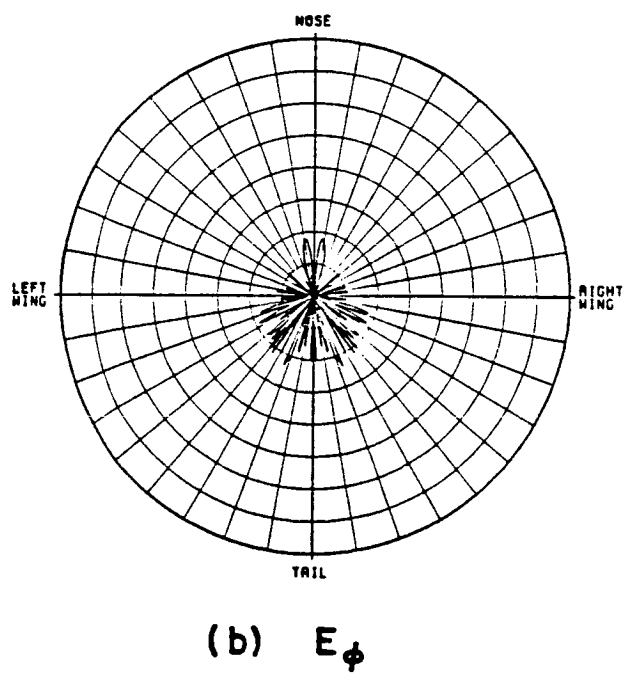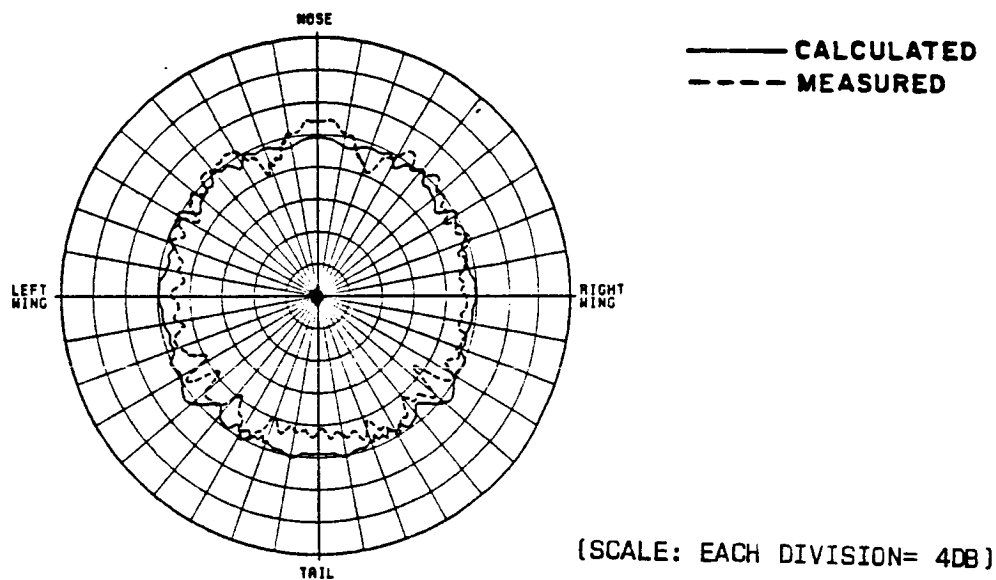
Figure 5.57. Azimuthal conical pattern ($\theta_p = 30°$) of a $\lambda/4$ monopole mounted on top of an F-16 fighter aircraft.

(a) E_θ

(SCALE: EACH DIVISION= 4DB)

(b) E_ϕ
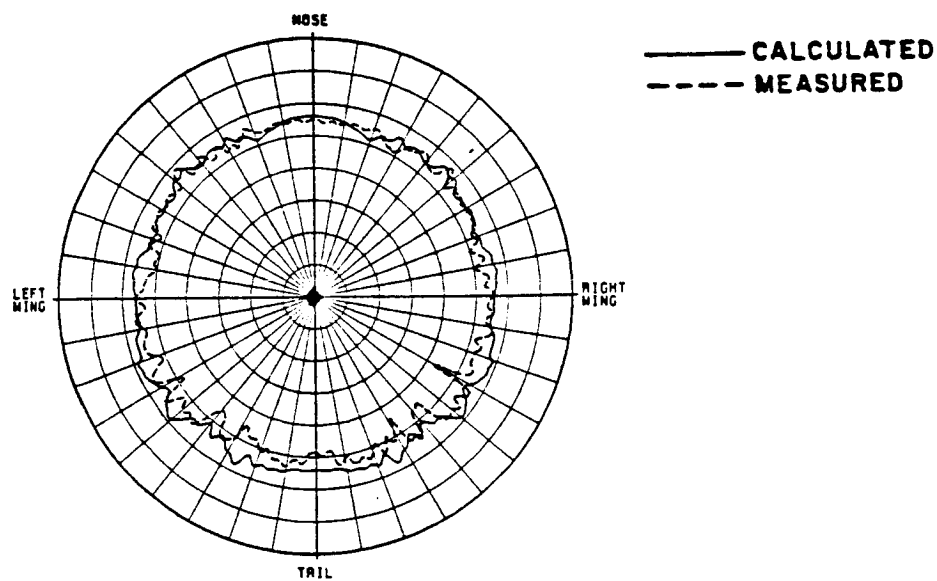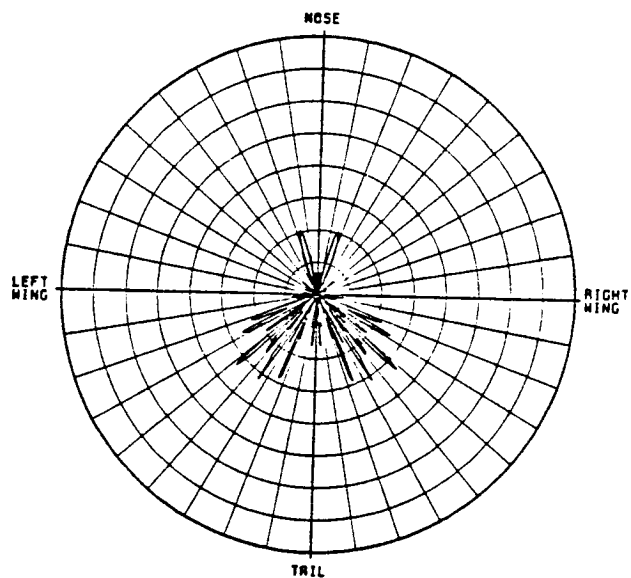
Figure 5.58. Azimuthal conical pattern ($\theta_p = 40°$) of a $\lambda/4$ monopole mounted on top of an F-16 fighter aircraft.

(a) E_θ

———— CALCULATED
– – – – MEASURED

(SCALE: EACH DIVISION= 4DB)

(b) E_ϕ
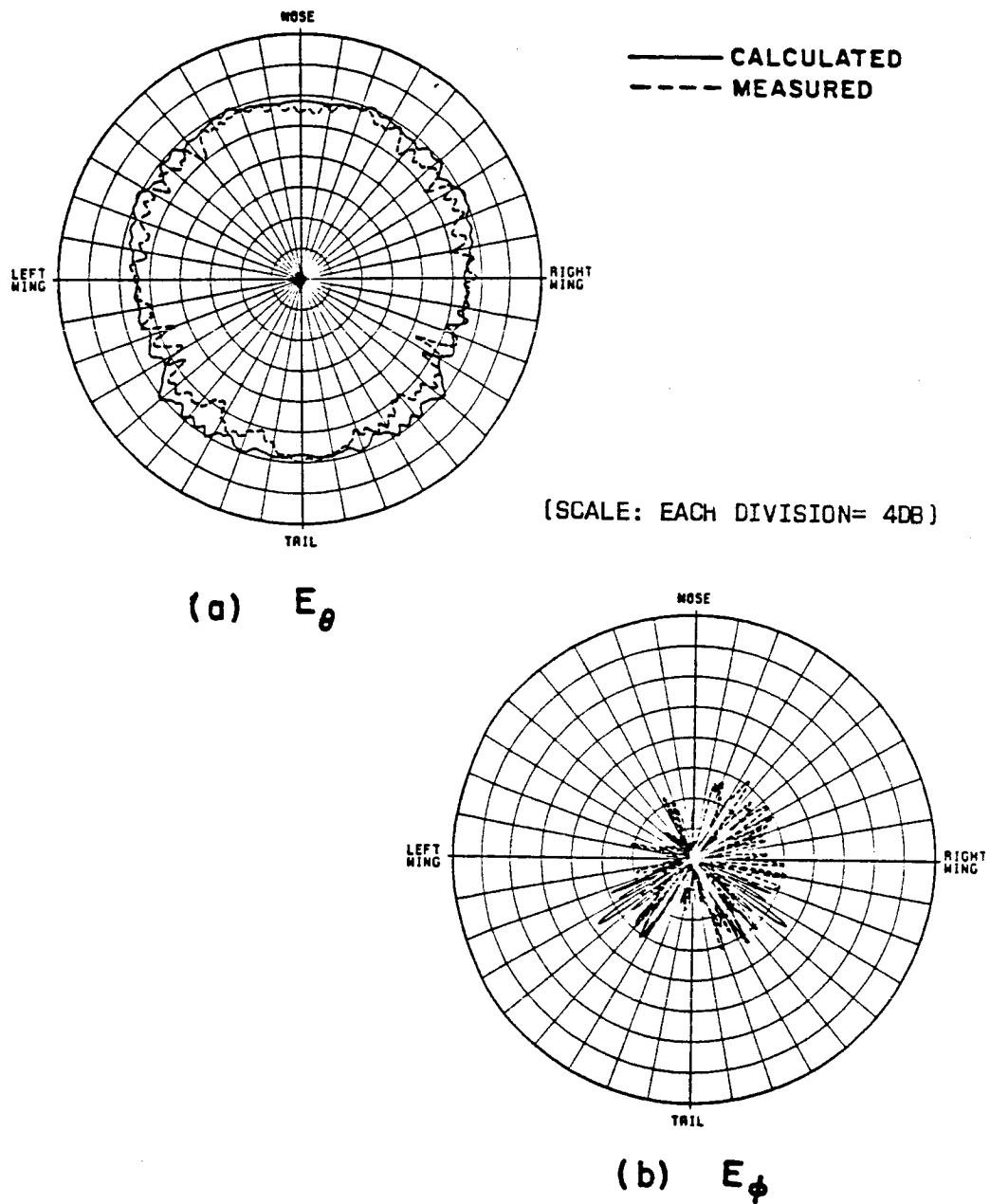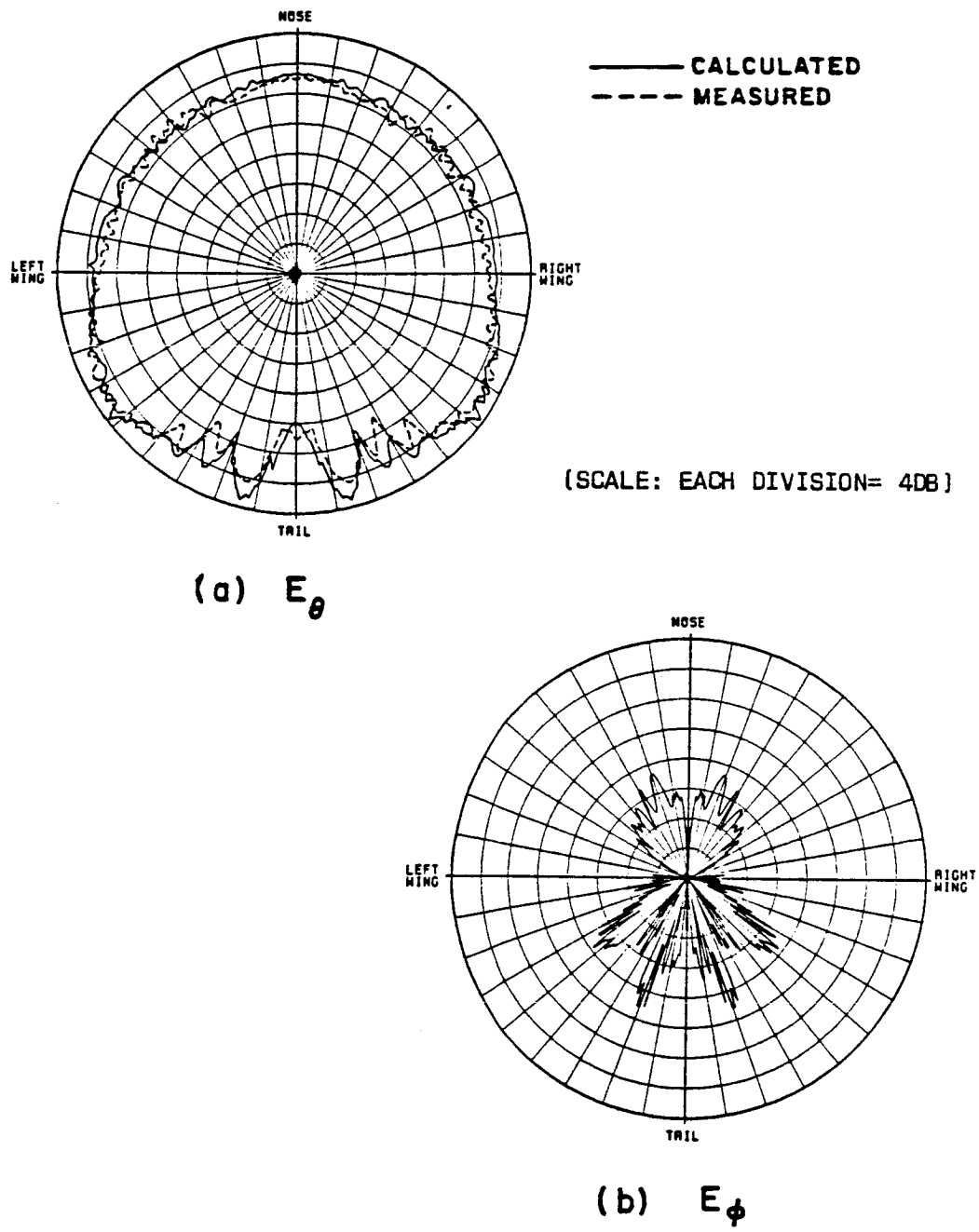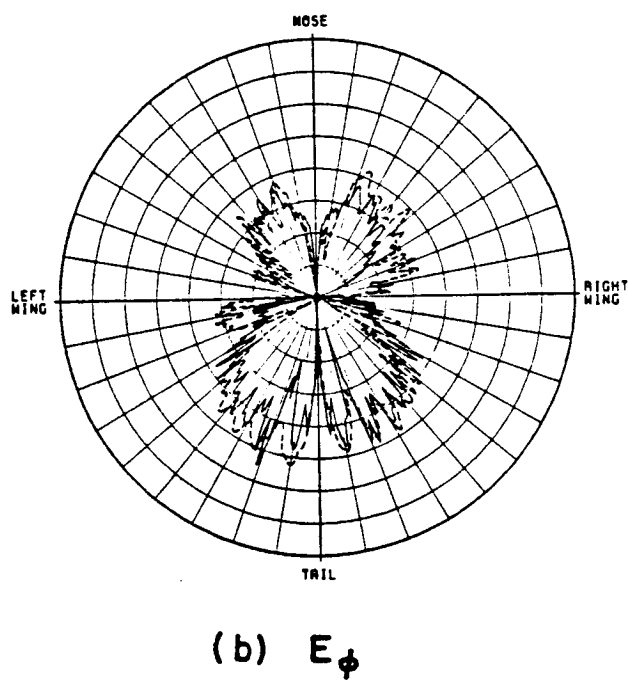
Figure 5.59. Azimuthal conical pattern (θ_p = 45°) of a $\lambda/4$ monopole mounted on top of an F-16 fighter aircraft.

254

NOSE

———— CALCULATED
— — — MEASURED

LEFT
WING

RIGHT
WING

(SCALE: EACH DIVISION= 4DB)

TAIL

(a) E_θ

NOSE

LEFT
WING

RIGHT
WING

TAIL

(b) E_ϕ
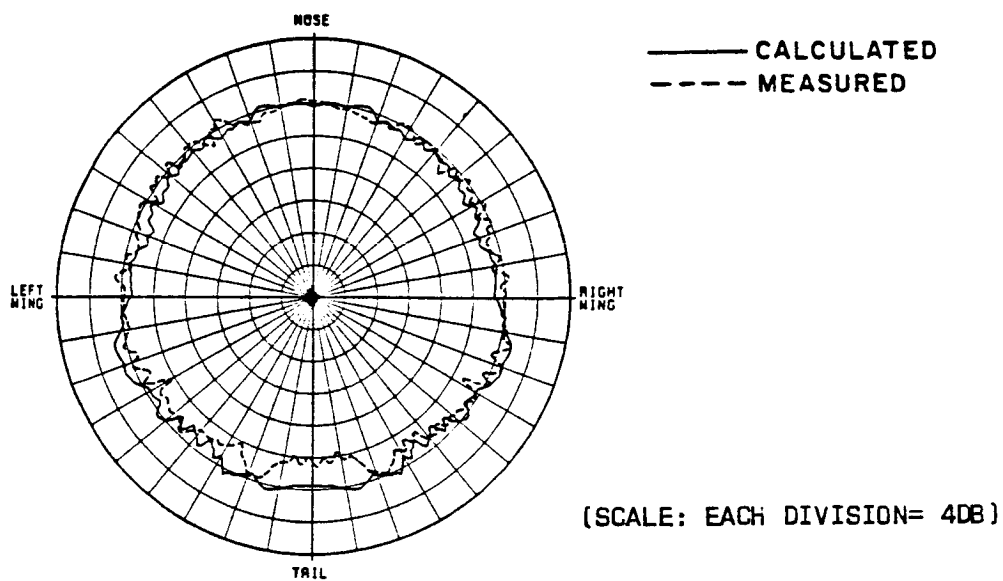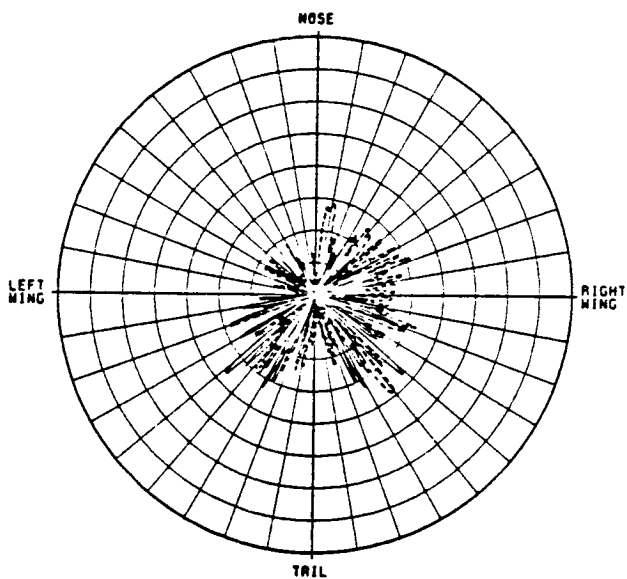
Figure 5.60. Azimuthal conical pattern (θ_p = 50°) of a $\lambda/4$ monopole mounted on top of an F-16 fighter aircraft.

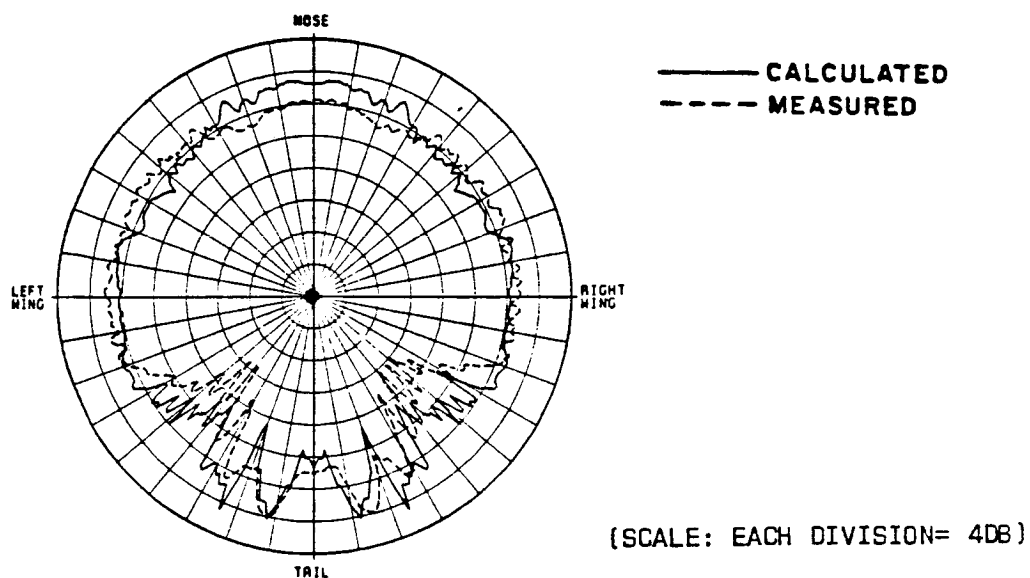255

(a) E_θ

(SCALE: EACH DIVISION= 4DB)

(b) E_ϕ
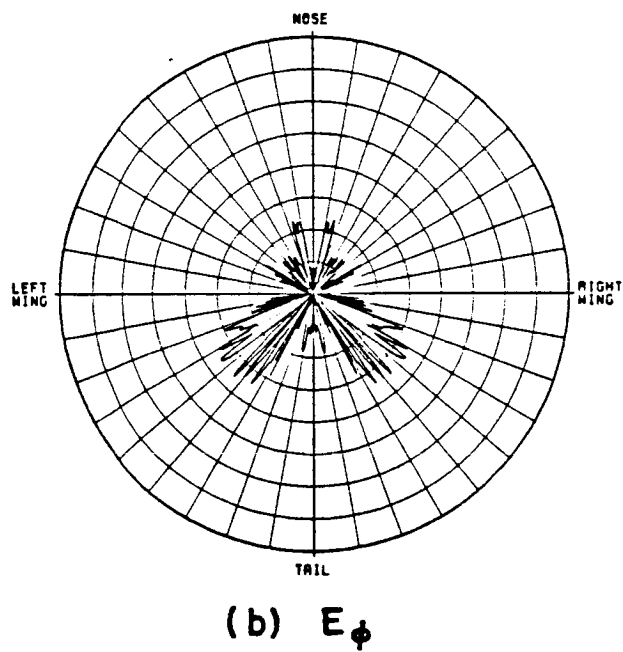
Figure 5.61. Azimuthal conical pattern ($\theta_p = 55°$) of a $\lambda/4$ monopole mounted on top of an F-16 fighter aircraft.

256

NOSE

LEFT
WING

RIGHT
WING

TAIL

——— CALCULATED
– – – – MEASURED

(SCALE: EACH DIVISION= 4DB)

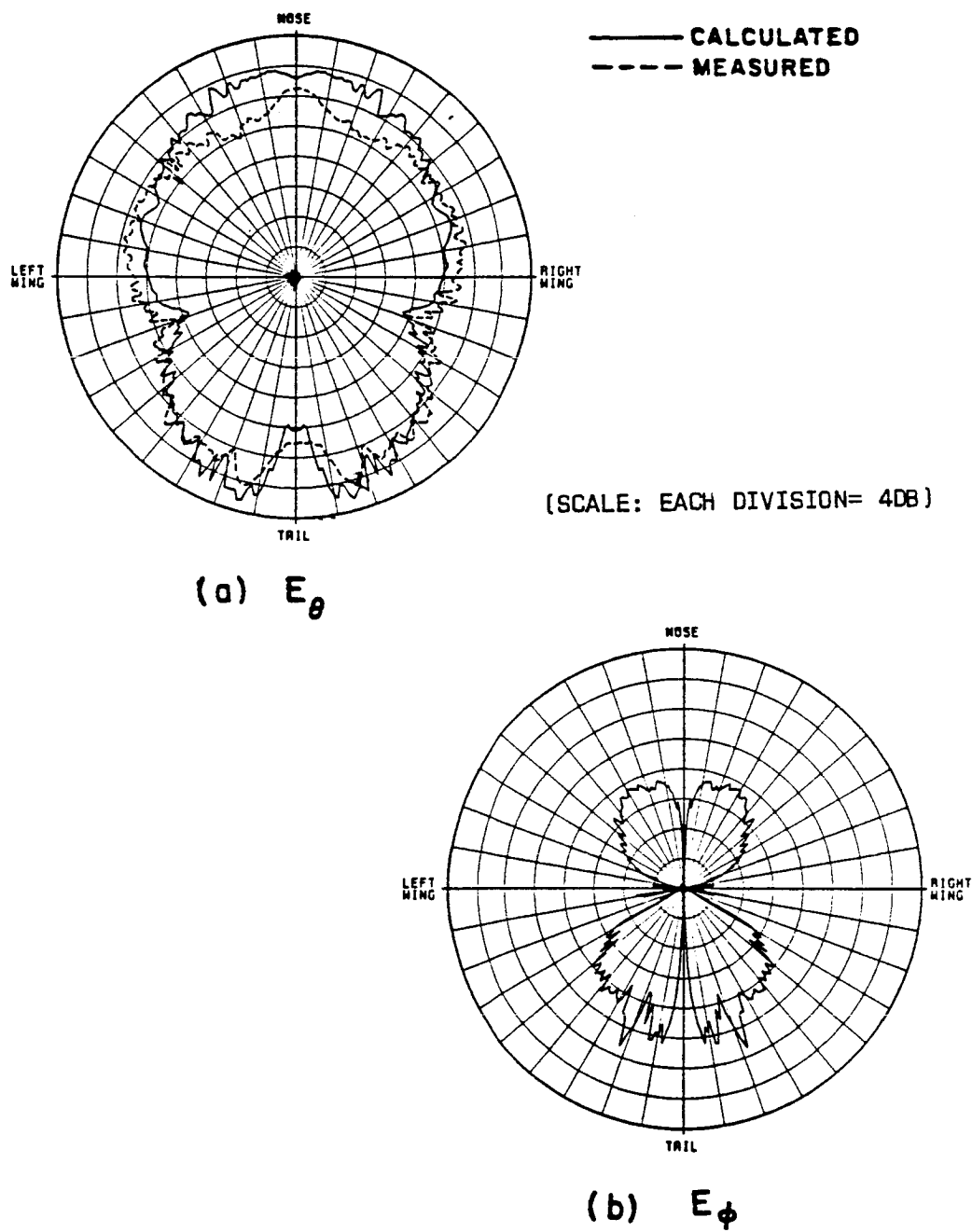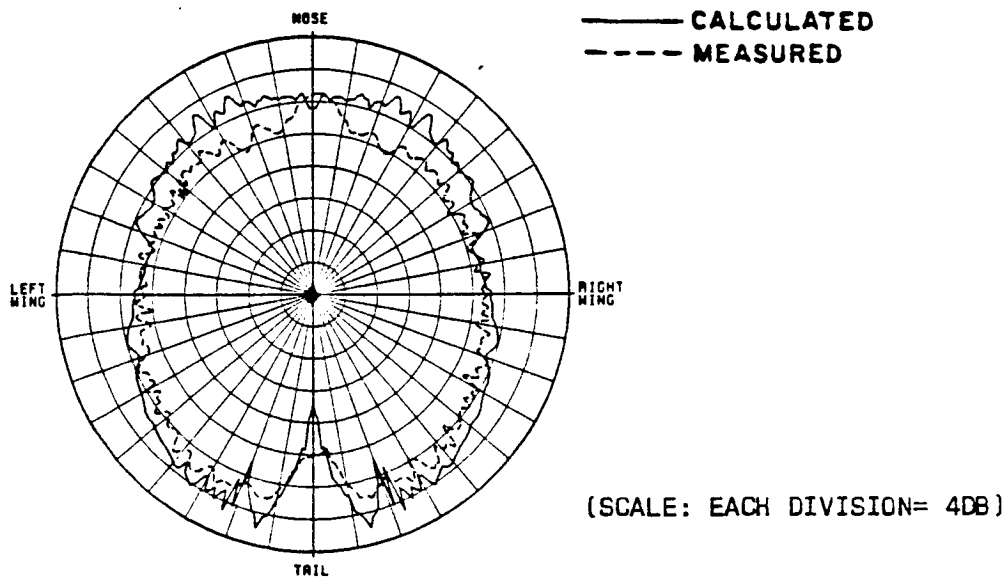(a) E_θ

NOSE

LEFT
WING

RIGHT
WING

TAIL

(b) E_ϕ

Figure 5.62. Azimuthal conical pattern ($\theta_p = 60°$) of a $\lambda/4$ monopole mounted on top of an F-16 fighter aircraft.

257

(a) E_θ

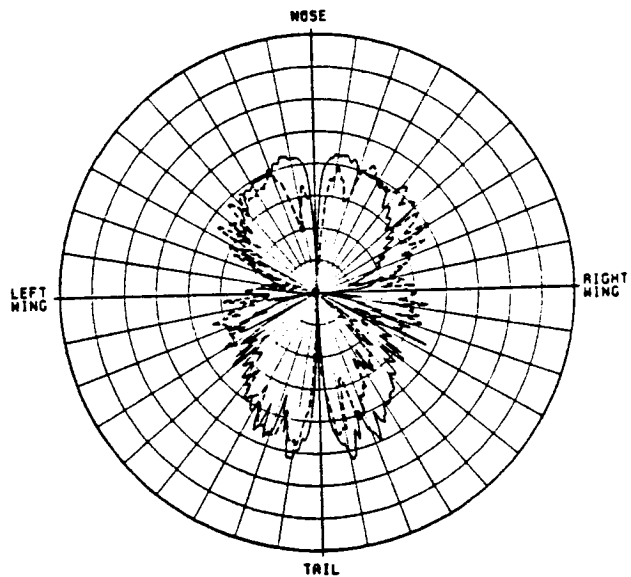————— CALCULATED

— — — MEASURED

(SCALE: EACH DIVISION= 4DB)
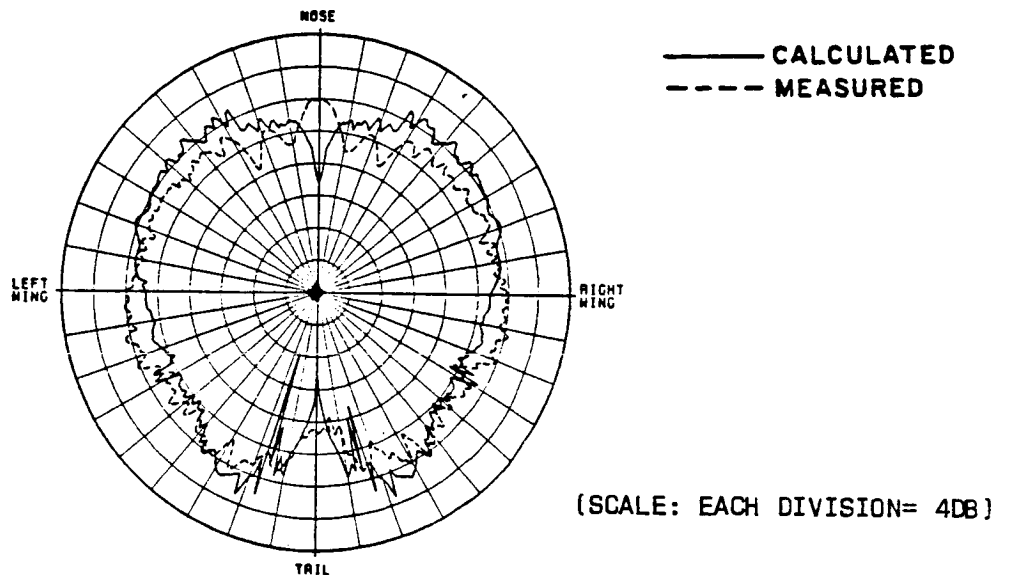

(b) E_ϕ

Figure 5.63. Azimuthal conical pattern ($\theta_p = 65°$) of a $\lambda/4$ monopole mounted on top of an F-16 fighter aircraft.

NOSE

LEFT
WING

RIGHT
WING

TAIL

(SCALE: EACH DIVISION= 4DB)

————— CALCULATED

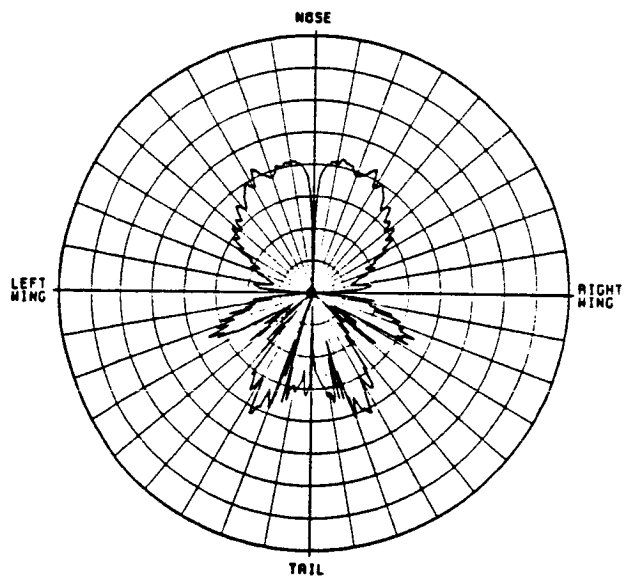————— MEASURED

(a) E_θ

NOSE

LEFT
WING

RIGHT
WING

TAIL

(b) E_ϕ

Figure 5.64. Azimuthal conical pattern (θ_p = 70°) of a $\lambda/4$ monopole mounted on top of an F-16 fighter aircraft.

259

NOSE

CALCULATED
---- MEASURED

LEFT
WING

RIGHT
WING

(SCALE: EACH DIVISION= 4DB)

TAIL

(a) E_θ

NOSE

LEFT
WING

RIGHT
WING

TAIL

(b) E_ϕ

Figure 5.65. Azimuthal conical pattern (θ_p = 75°) of a λ/4 monopole
mounted on top of an F-16 fighter aircraft.

260

NOSE

CALCULATED
MEASURED

LEFT
WING

RIGHT
WING

(SCALE: EACH DIVISION= 4DB)

TAIL

(a) E_θ

NOSE

LEFT
WING

RIGHT
WING

TAIL

(b) E_ϕ

Figure 5.66. Azimuthal conical pattern (θ_p = 80°) of a $\lambda/4$ monopole mounted on top of an F-16 fighter aircraft.
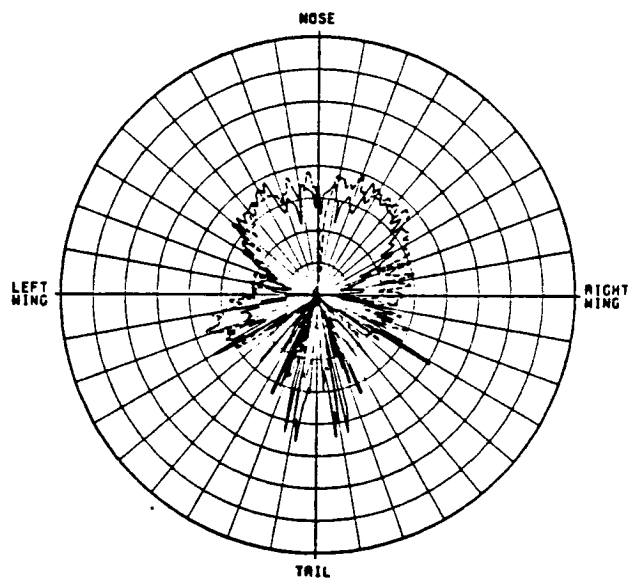
261

(a) E_θ

CALCULATED
MEASURED

(SCALE: EACH DIVISION= 4DB)

(b) E_ϕ
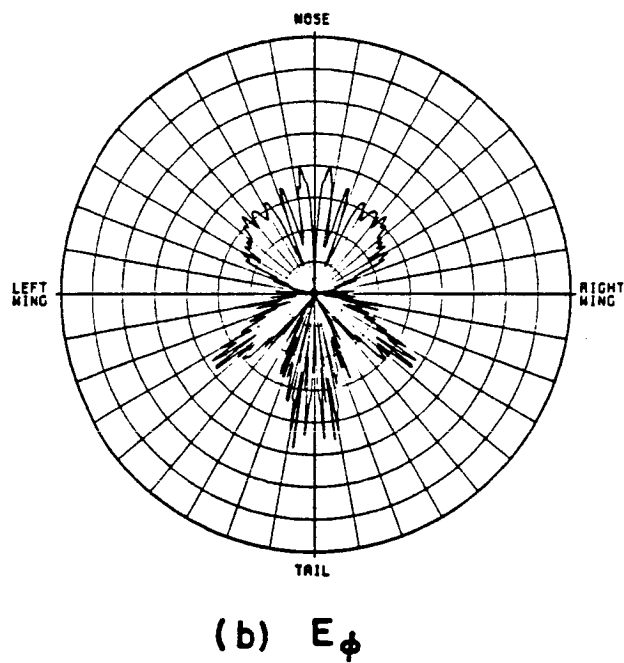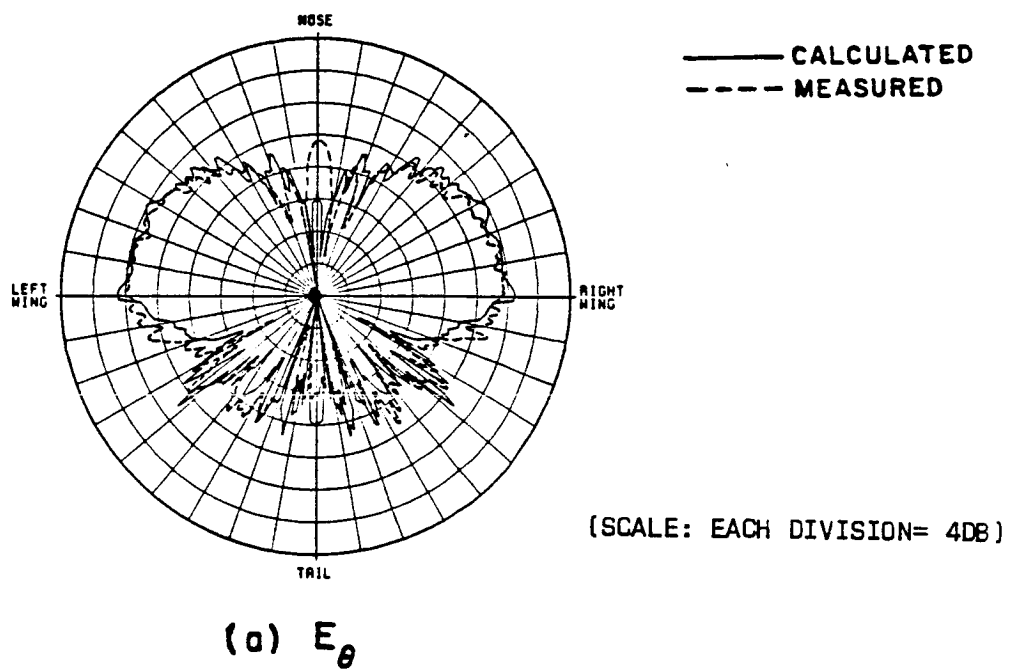
Figure 5.67. Azimuthal conical pattern (θ_p = 85°) of a $\lambda/4$ monopole mounted on top of an F-16 fighter aircraft.

CALCULATED
MEASURED

(SCALE: EACH DIVISION= 4DB)

(a) E_θ

(b) E_ϕ

Figure 5.68. Azimuthal conical pattern (θ_p = 90°) of a $\lambda/4$ monopole mounted on top of an F-16 fighter aircraft.

NOSE
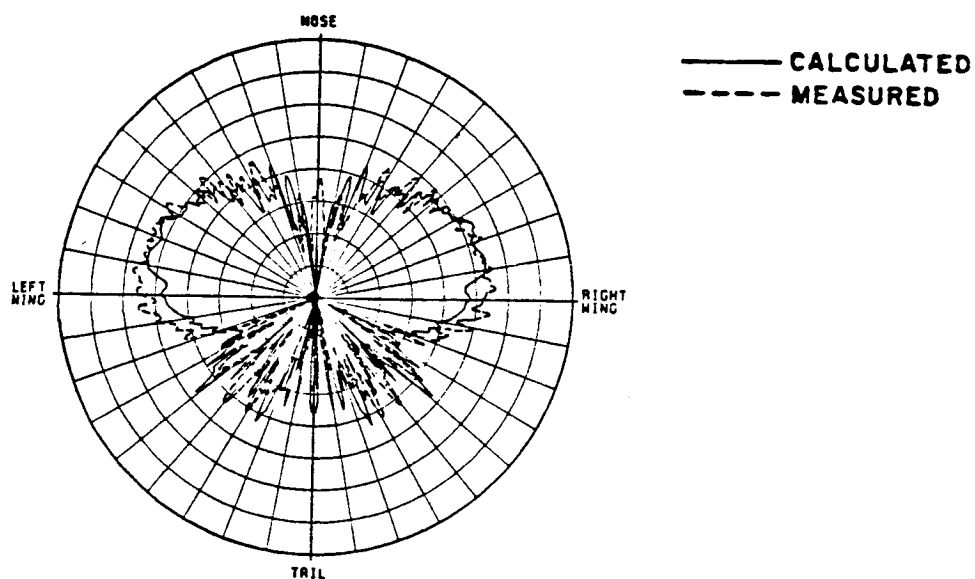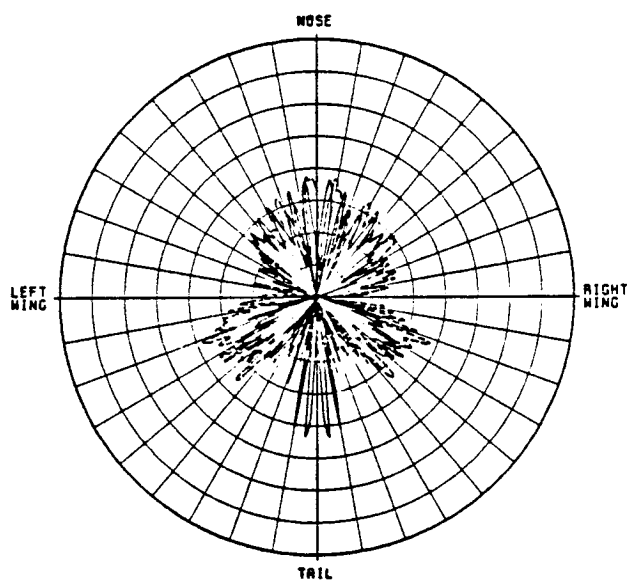
———— CALCULATED
— — — MEASURED

LEFT
WING

RIGHT
WING

(SCALE: EACH DIVISION= 4DB)

TAIL

(a) E_θ

NOSE

LEFT
WING

RIGHT
WING

TAIL

(b) E_ϕ

Figure 5.69. Azimuthal conical pattern ($\theta_p = 95°$) of a $\lambda/4$ monopole
mounted on top of an F-16 fighter aircraft.

264

(SCALE: EACH DIVISION= 4DB)

(a) E_θ

(b) E_ϕ
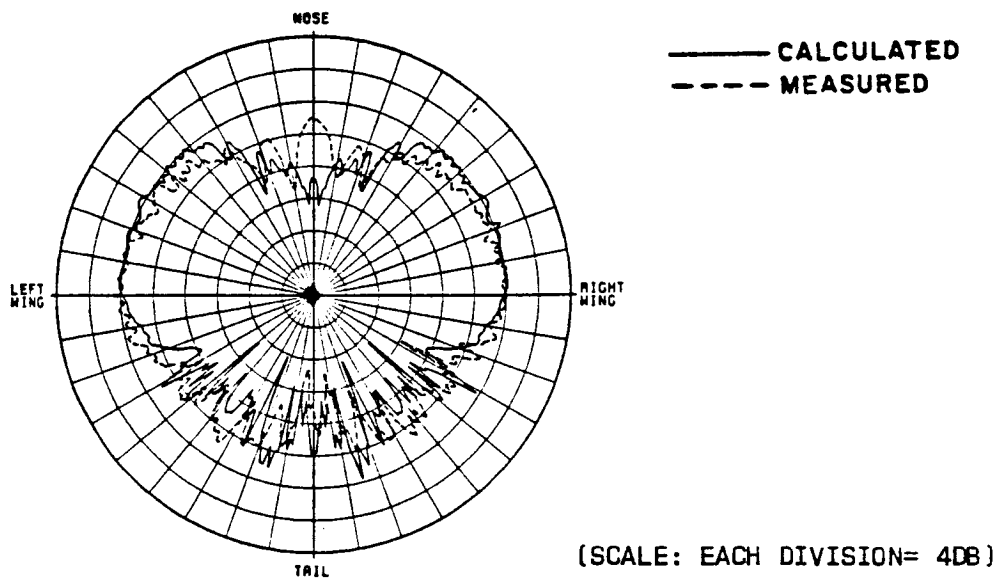
Figure 5.70. Azimuthal conical pattern (θ_p = 100°) of a $\lambda/4$ monopole mounted on top of an F-16 fighter aircraft.
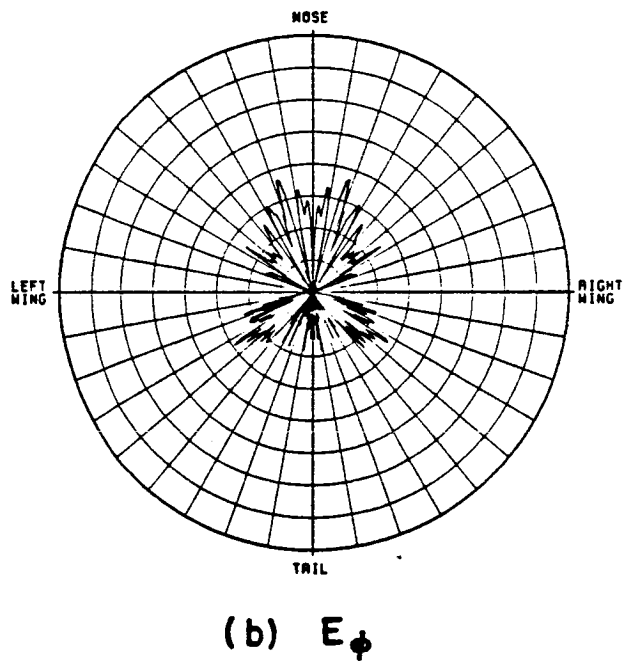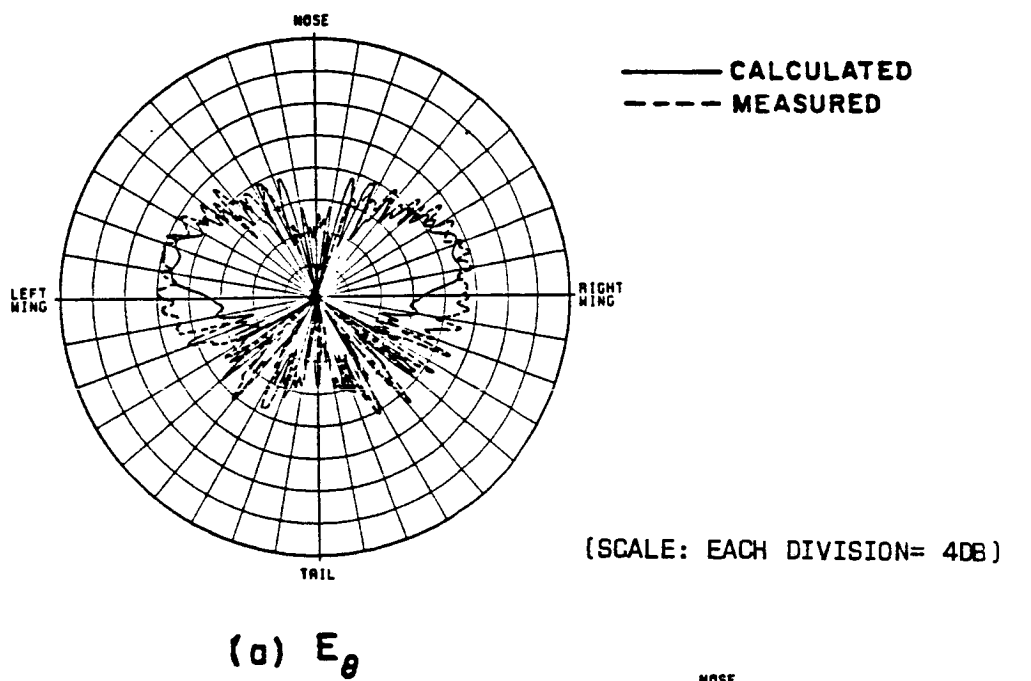
Figure 5.71. Azimuthal conical pattern ($\theta_p = 105°$) of a $\lambda/4$ monopole mounted on top of an F-16 fighter aircraft.

NOSE

——— CALCULATED
---- MEASURED

LEFT WING

RIGHT WING

TAIL

(SCALE: EACH DIVISION= 4DB)

(a) E_θ

NOSE

LEFT WING

RIGHT WING

TAIL

(b) E_ϕ

Figure 5.72. Azimuthal conical pattern ($\theta_p = 110°$) of a $\lambda/4$ monopole mounted on top of an F-16 fighter aircraft.
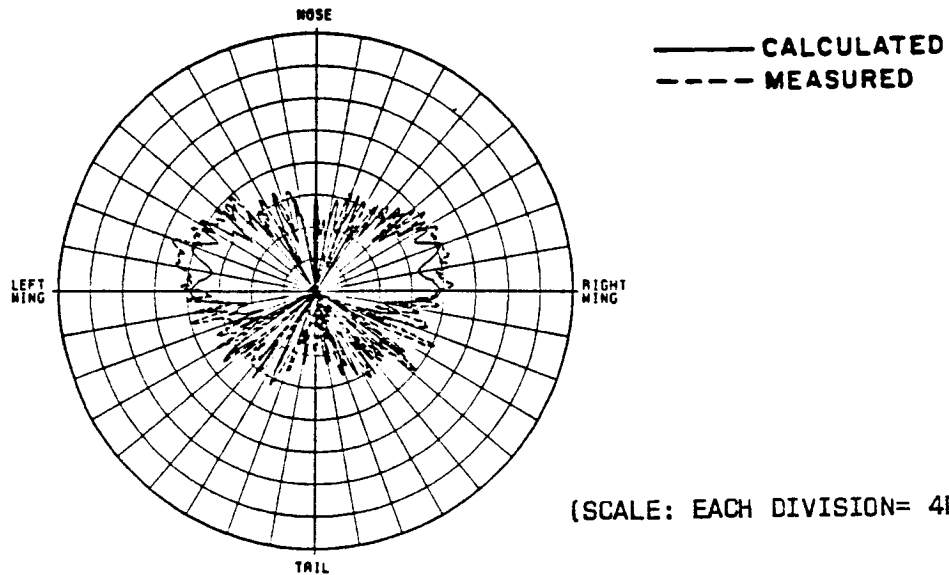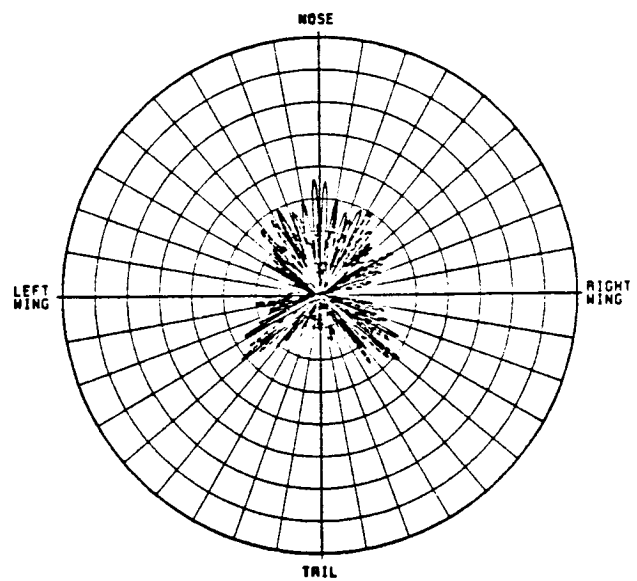
267

NOSE

CALCULATED
---- MEASURED

LEFT
WING

RIGHT
WING

TAIL

(SCALE: EACH DIVISION= 4DB)

(a) E_θ

NOSE

LEFT
WING

RIGHT
WING

TAIL

(b) E_ϕ

Figure 5.73. Azimuthal conical pattern (θ_0 = 115°) of a $\lambda/4$ monopole
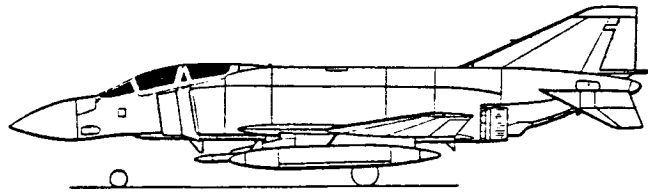mounted on top of an F-16 fighter aircraft.

268

Figure 5.74. Azimuthal conical pattern ($\theta_p = 120°$) of a $\lambda/4$ monopole mounted on top of an F-16 fighter aircraft.
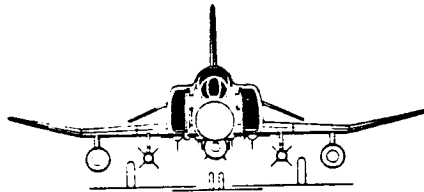
2. F-4 Fighter Aircraft

This example is illustrative in that the antenna is mounted on the belly of an F-4 aircraft which is loaded with armament. The F-4 fighter aircraft has a complex airframe with many scattering objects (i.e., fuel tanks, jet intakes, pylons, etc.) attached to the basic frame. A $\lambda/4$ monopole is used to simulate a UHF blade which is mounted on the bottom fuselage of an F-4 aircraft and operated at a frequency of 375 MHz. The measured data was obtained at the RADC Newport antenna range.

The line drawings of the F-4 fighter aircraft are shown in Figure 5.75. The computer model of the F-4 aircraft is illustrated in Figure 5.76. A composite ellipsoid (5" x 20" x 300" x 200") is chosen to simulate the bottom surface of the aircraft fuselage; whereas, the other appendages are simulated using 11 flat plates. It is noted that the actual shape of the fuel tank is curved and each fuel tank is simulated as a single plate in our model for simplicity.
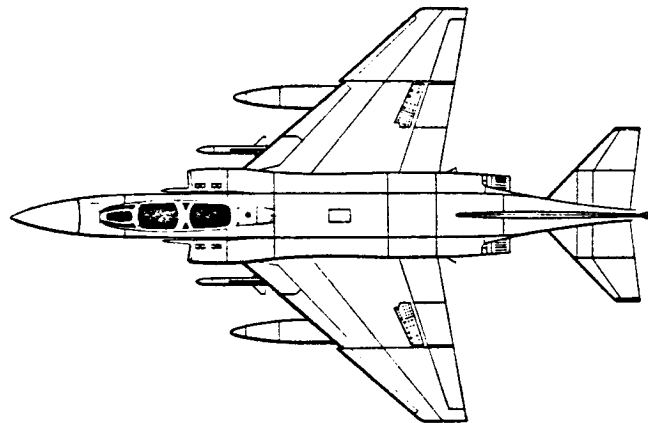
The azimuthal conical pattern (θ_p = 105°) is compared with a measurement result in Figure 5.77. Although some discrepancy does exist, the general shape of the pattern is in good agreement.
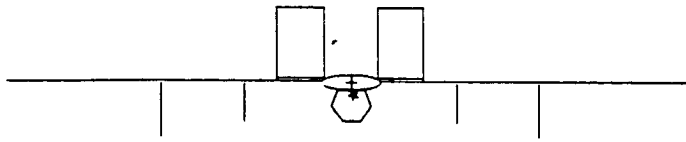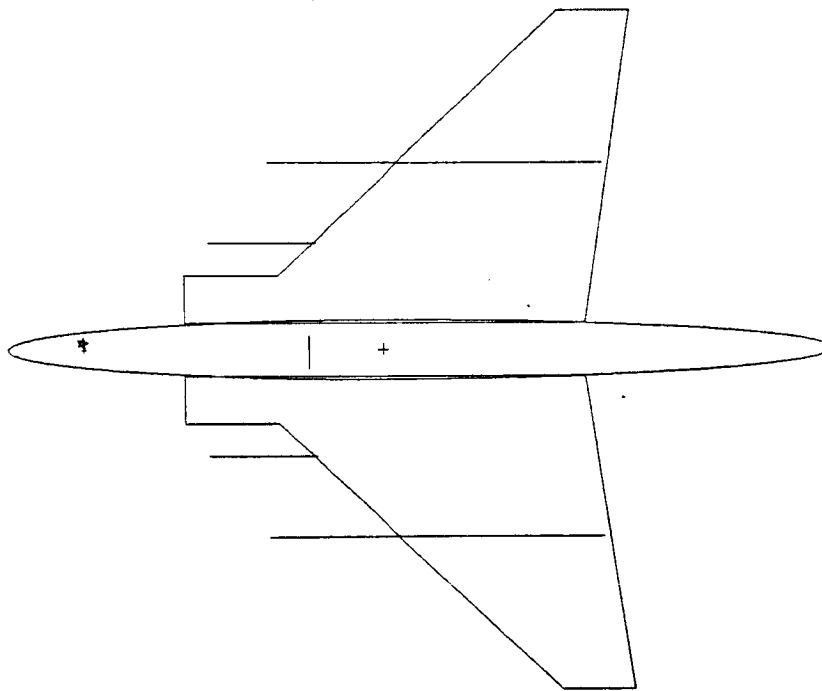
(a) SIDE VIEW

(b) FRONT VIEW

(c) TOP VIEW

Figure 5.75. F-4 (Phantom) fighter aircraft.

271

(a) FRONT VIEW

(b) BOTTOM VIEW

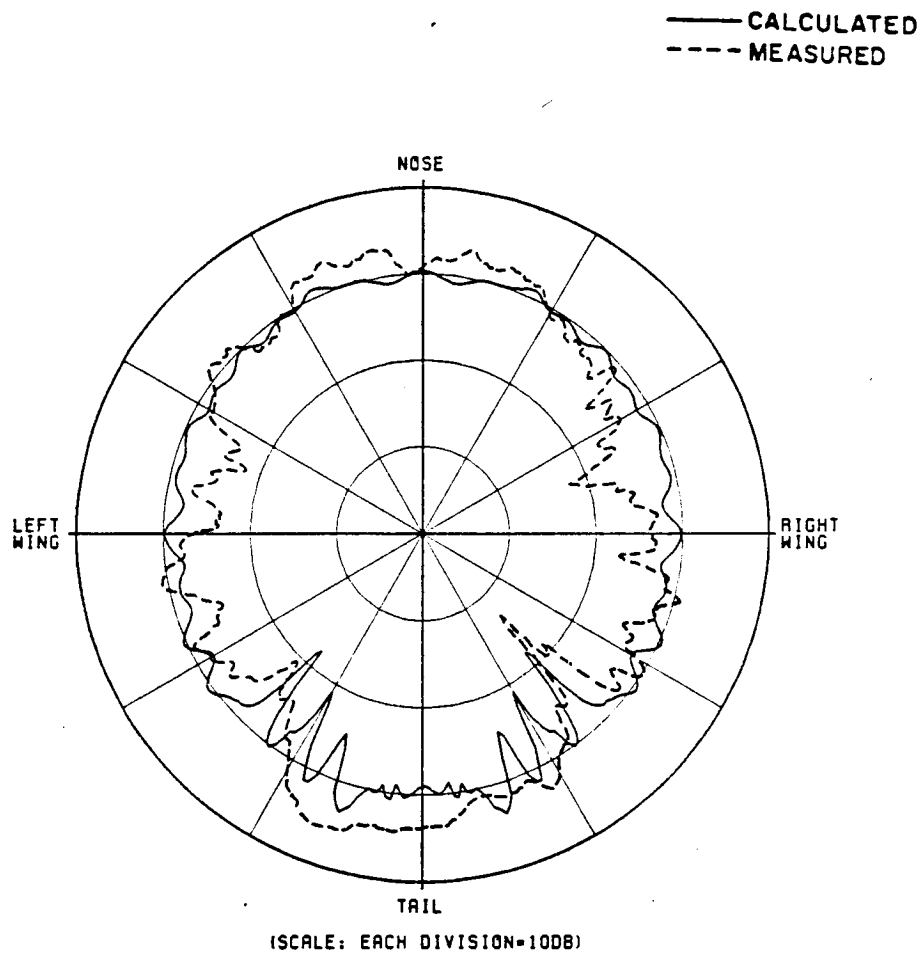Figure 5.76. Computer simulated model of an F-4 Phantom fighter aircraft.

Figure 5.77. Azimuthal conical pattern ($\theta_p = 105°$) of a $\lambda/4$ monopole mounted on the belly of an F-4 fighter aircraft.

3. A-10 Aircraft

In this case, a four monopole array is mounted on the belly of an A-10 aircraft. The line drawings are shown in Figure 5.78. The experimental data was also obtained at the RADC Newport site.

The computer simulation model is illustrated in Figure 5.79. In that the four monoples are spaced a half wavelength apart, the mutual coupling between the antennas is significant and cannot be neglected in the pattern calculations. This can be solved using a thin wire moment method code [49,50] to treat the four closely spaced loaded-dipoles (50 ohms at center of each dipole) in order to obtain the excitation of each monopole even though only one element was excited.

The azimuthal conical pattern (θ_p = 105°) is compared with measurement in Figure 5.80. The result reveals good engineering agreement.

4. C-141 Aircraft

Let us consider a monopole mounted on the top of a C-141 aircraft. The line drawings for a C-141 aircraft are shown in Figure 5.81. The experimental work [40] was performed at General Dynamics (San Diego, California) using a 1/10 scale model of a C-141 aircraft.
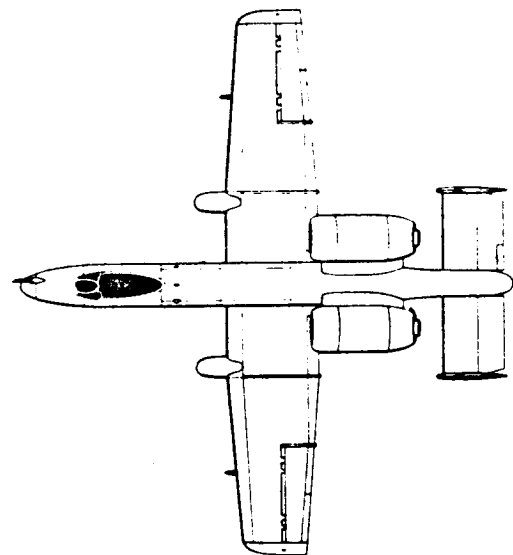
Figure 5.82 illustrates the computer model which is used to simulate a C-141 aircraft. A composite ellipsoid (7.37' x 8.37' x 90' x 46.05') is chosen to simulate the fuselage surface of the actual
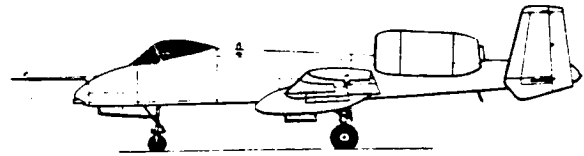
(a)   SIDE VIEW
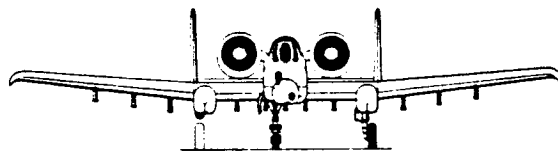
(b)   FRONT VIEW

(c)   TOP VIEW

Figure 5.78.   A-10 aircraft.
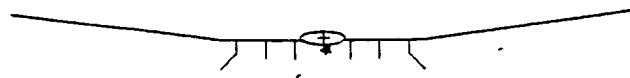
(a) FRONT VIEW
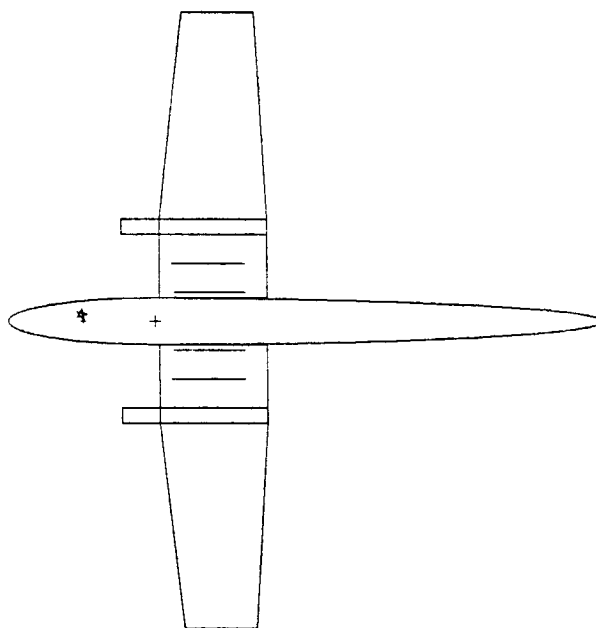
(b) BOTTOM VIEW

Figure 5.79. Computer simulated model of an A-10 aircraft.

C-3

Figure 5.80. Azimuthal conical pattern (θ_p = 105°) of four monopoles mounted on the belly of an A-10 aircraft.

277

(a) SIDE VIEW
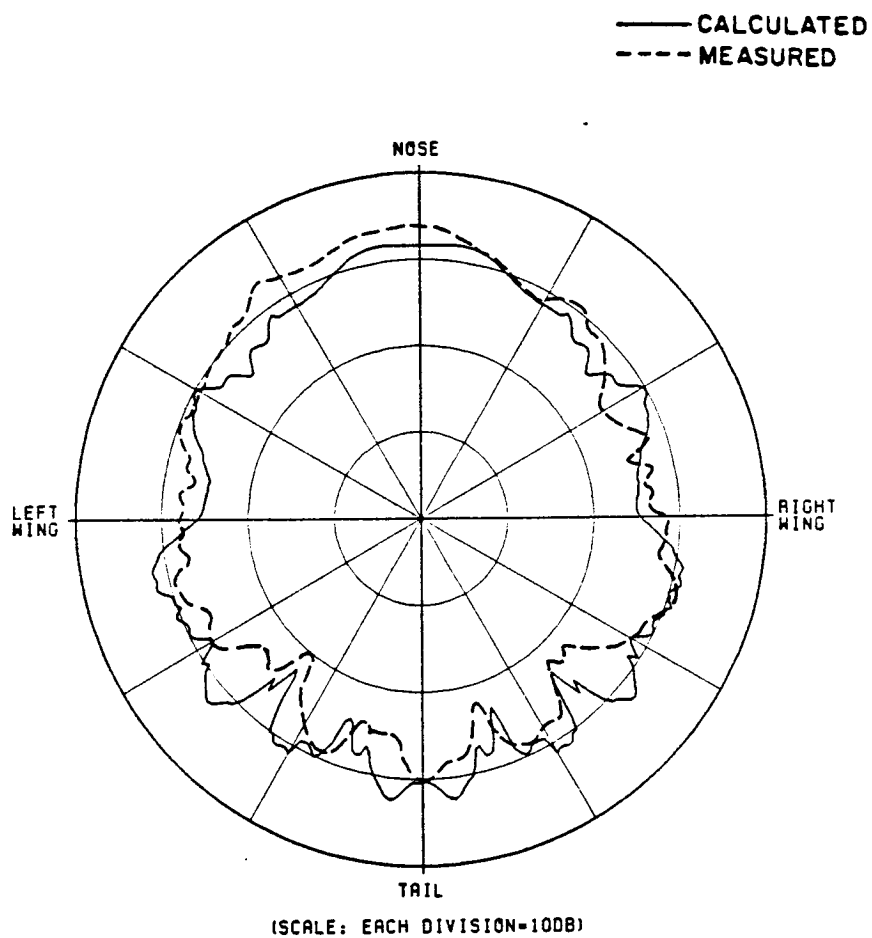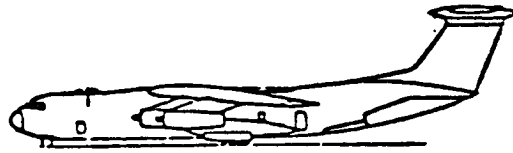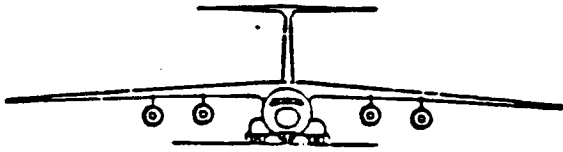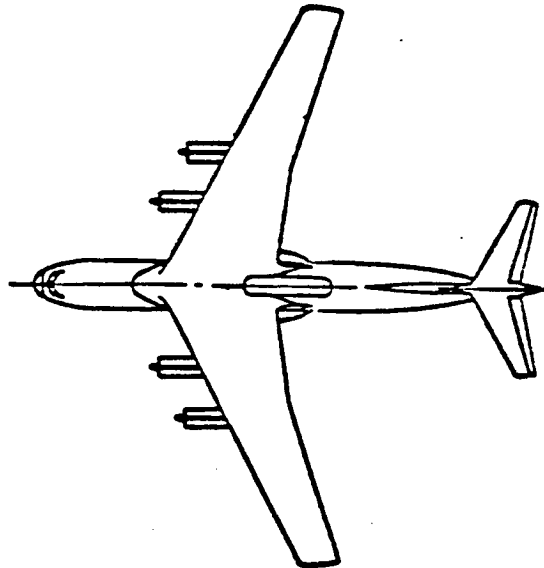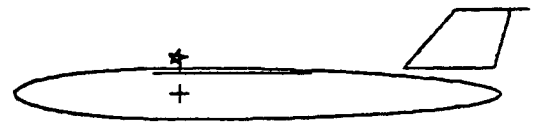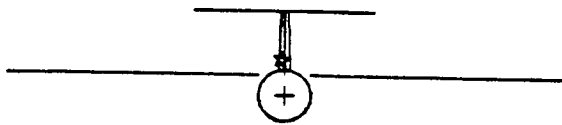
(b) FRONT VIEW

(c) TOP VIEW

Figure 5.81. C-141 aircraft.

(a) SIDE VIEW

(b) FRONT VIEW

ANTENNA
LOCATION
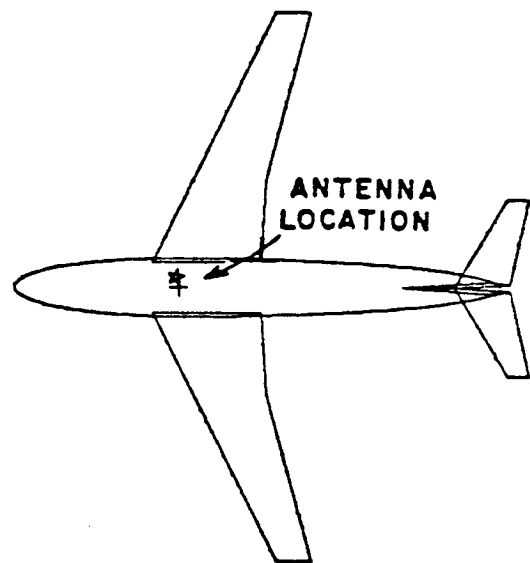
(c) TOP VIEW

Figure 5.82. Computer simulated model of a C-141 aircraft.

aircraft as accurately as possible, and finite flat plates are used to simulate the wings, vertical stabilizer and T-tail as shown in Figure 5.82.

The radiation patterns for a $\lambda/4$ monopole mounted on the fuselage of a C-141 aircraft are calculated using the model just described. In order to verify the validity of the analytic solution, various azimuthal conical patterns (10°, 20°, 30°, 40°, 50°, 60°, 70°, 80°, 90°, 100°, see Figure 5.2(c)) and the elevation plane pattern are computed and compared with measured results as shown in Figures 5.83 and 5.84, respectively. The calculated results compare very favorably with the scale model measurements.

5. Missile

The missile antenna problem considered next is interesting in that the antenna is mounted among four large ram jets which significantly impact on the antenna location problem.

The front view of the missile and the computer simulation model are shown in Figure 5.85. Note that the axial slot antenna is mounted between the ram jets. The fuselage is simulated as a composite ellipsoid and only two side walls of the intakes are simulated with two flat plates. It is noted that a fuselage blockage plate is added in the computer simulation model and is shown as a dashed line in Figure 5.85(b). This feature is added in the code to prevent the ray

CALCULATED
MEASURED

NOSE

LEFT
WING

RIGHT
WING

TAIL

(a) $\theta_p = 10°$

NOSE

LEFT
WING

RIGHT
WING

TAIL

(SCALE: EACH DIVISION=10DB)

(b) $\theta_p = 20°$
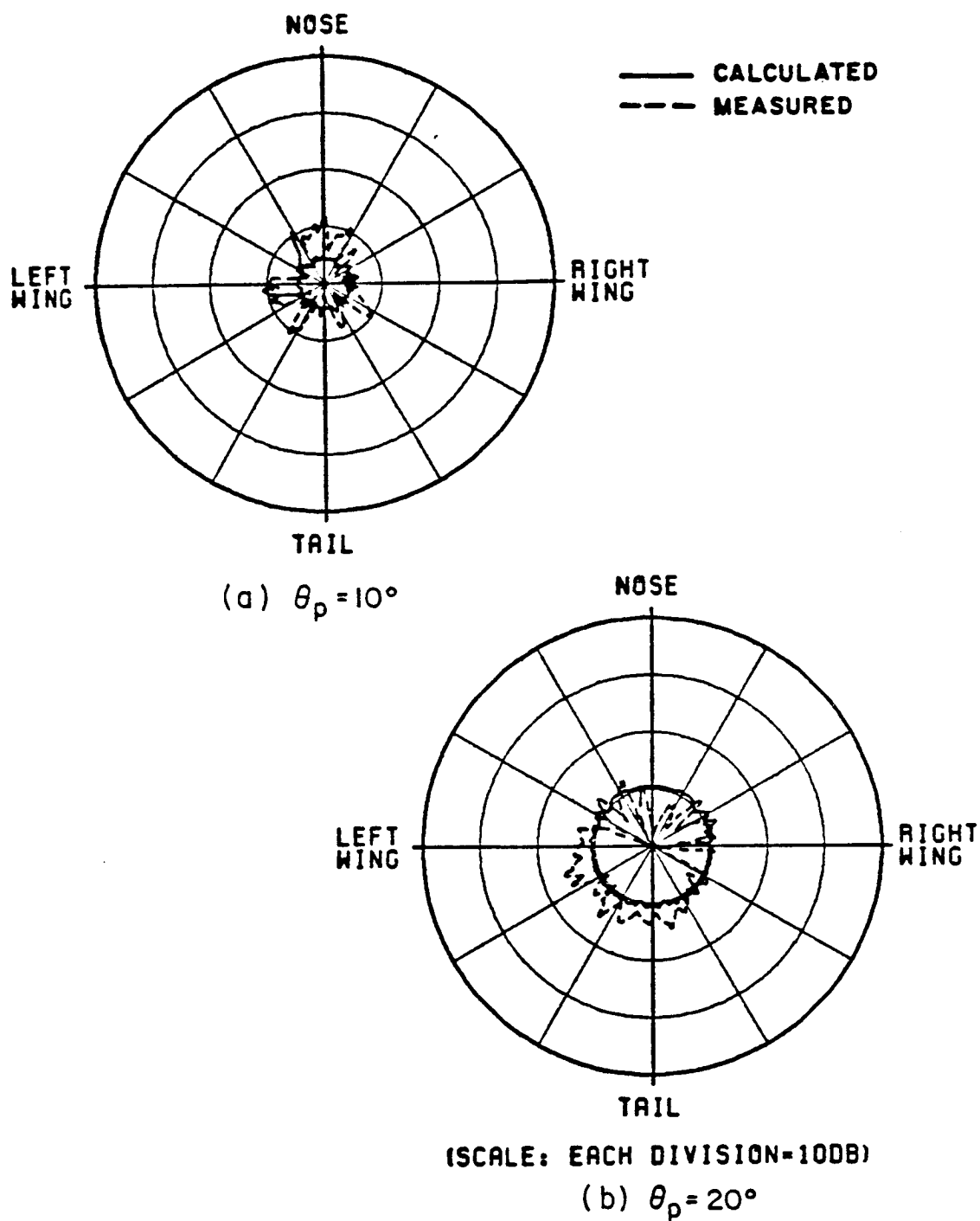
Figure 5.83. Azimuthal conical patterns of a $\lambda/4$ monopole mounted on a C-141 aircraft.

281
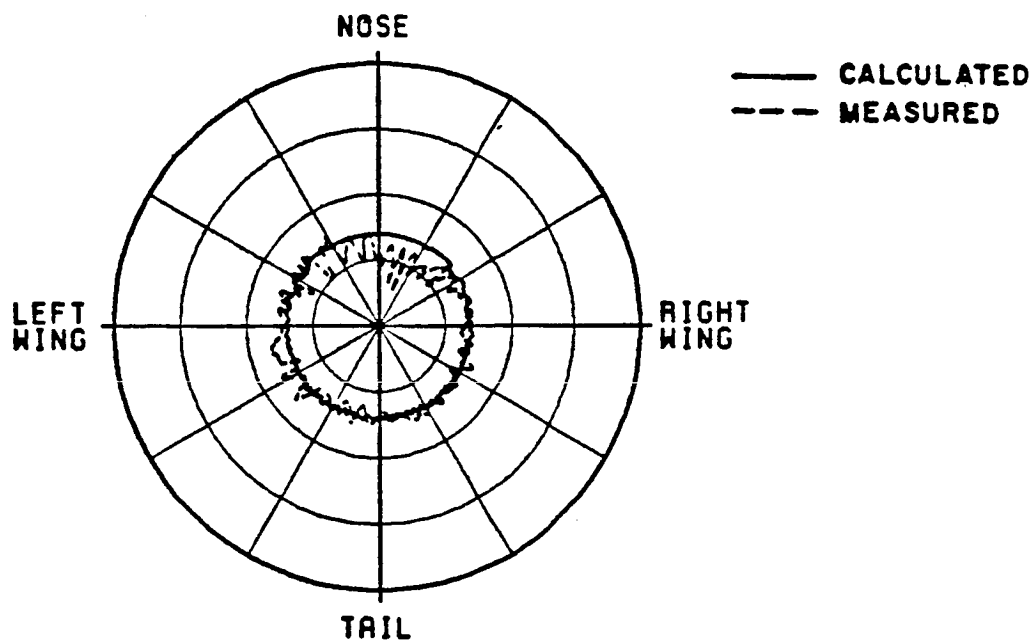
(c) $\theta_p = 30°$
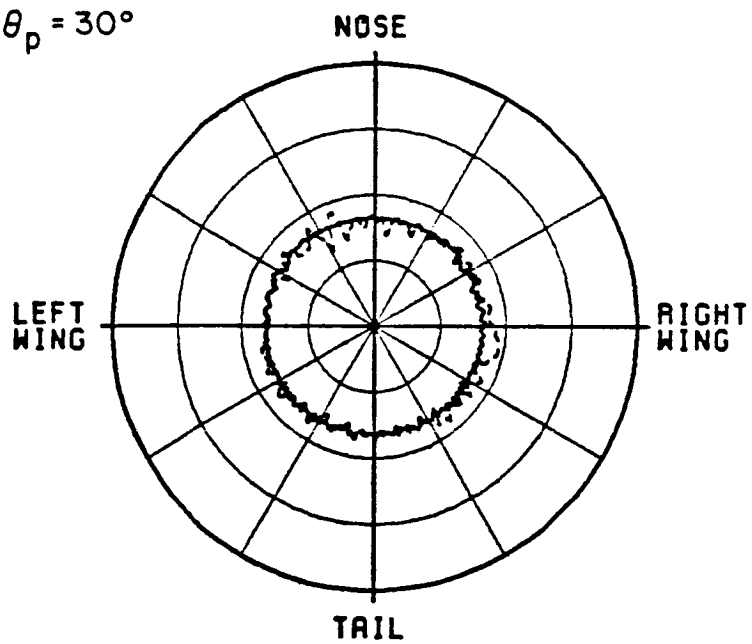
(SCALE: EACH DIVISION=10DB)

(d) $\theta_p = 40°$

Figure 5.83. (Continued).
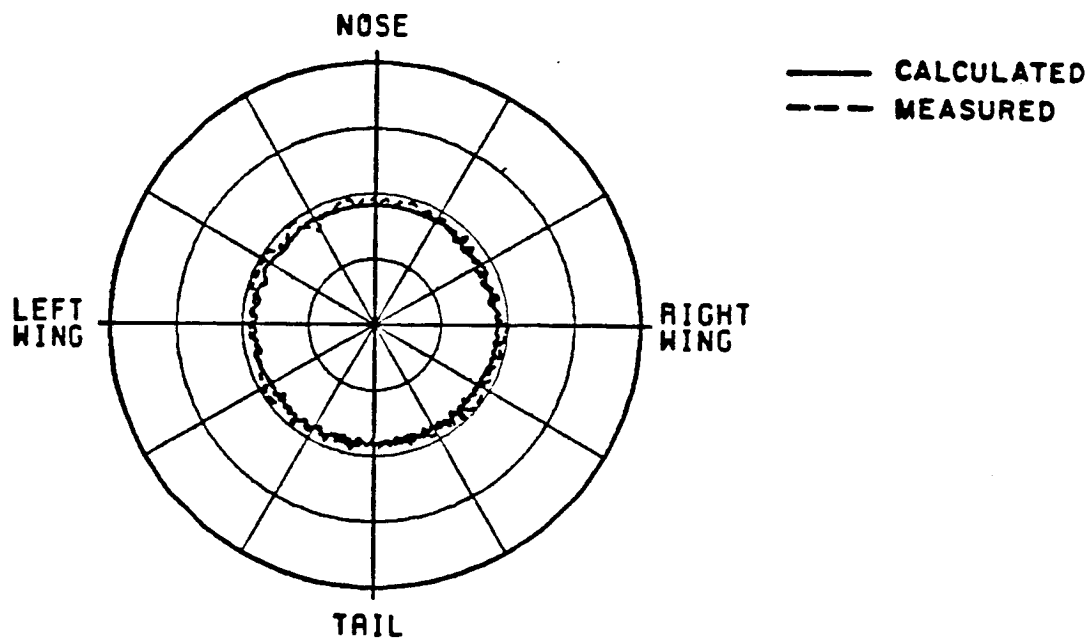
(e) $\theta_p = 50°$
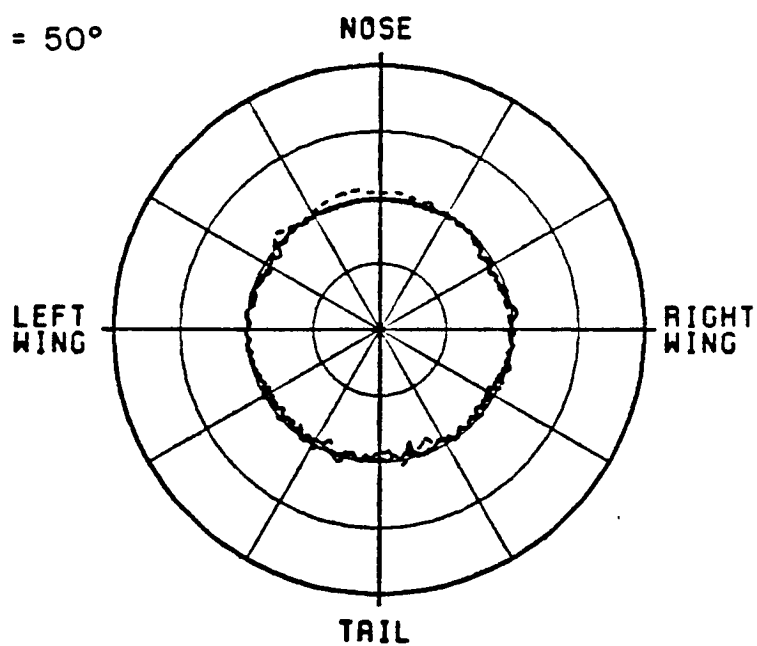
(SCALE: EACH DIVISION = 10DB)

(f) $\theta_p = 60°$

Figure 5.83. (Continued).

(g) $\theta_p = 70°$

(SCALE: EACH DIVISION=10DB)

(h) $\theta_p = 80°$

Figure 5.83. (Continued).

NOSE

TAIL

LEFT WING

RIGHT WING

CALCULATED
MEASURED

(i) $\theta_p = 90°$

NOSE

TAIL

LEFT WING

RIGHT WING

(SCALE: EACH DIVISION=10DB)

(j) $\theta_p = 100°$

Figure 5.83. (Continued).

285

TOP

TAIL

NOSE

BOTTOM

(SCALE: EACH DIVISION=10DB)
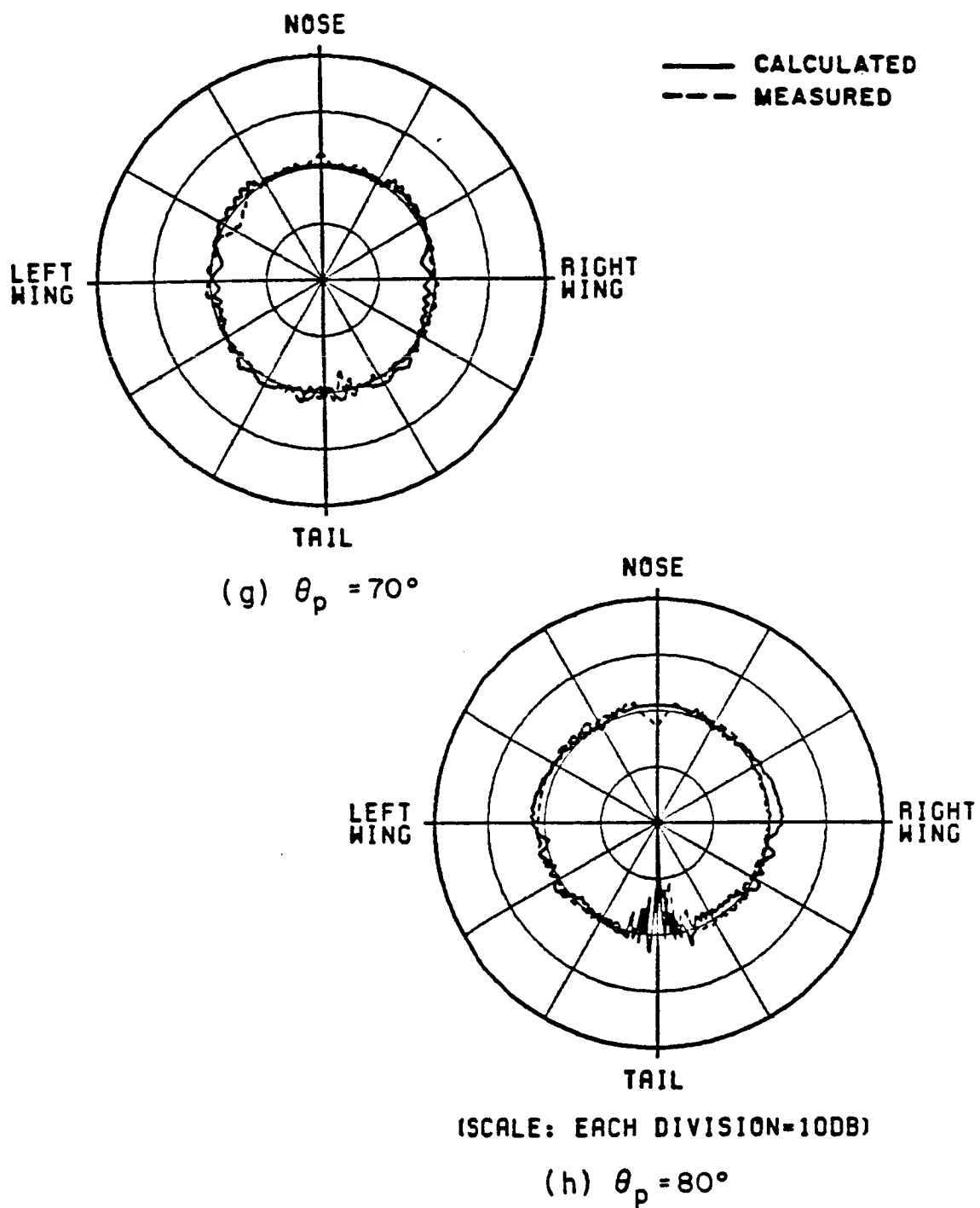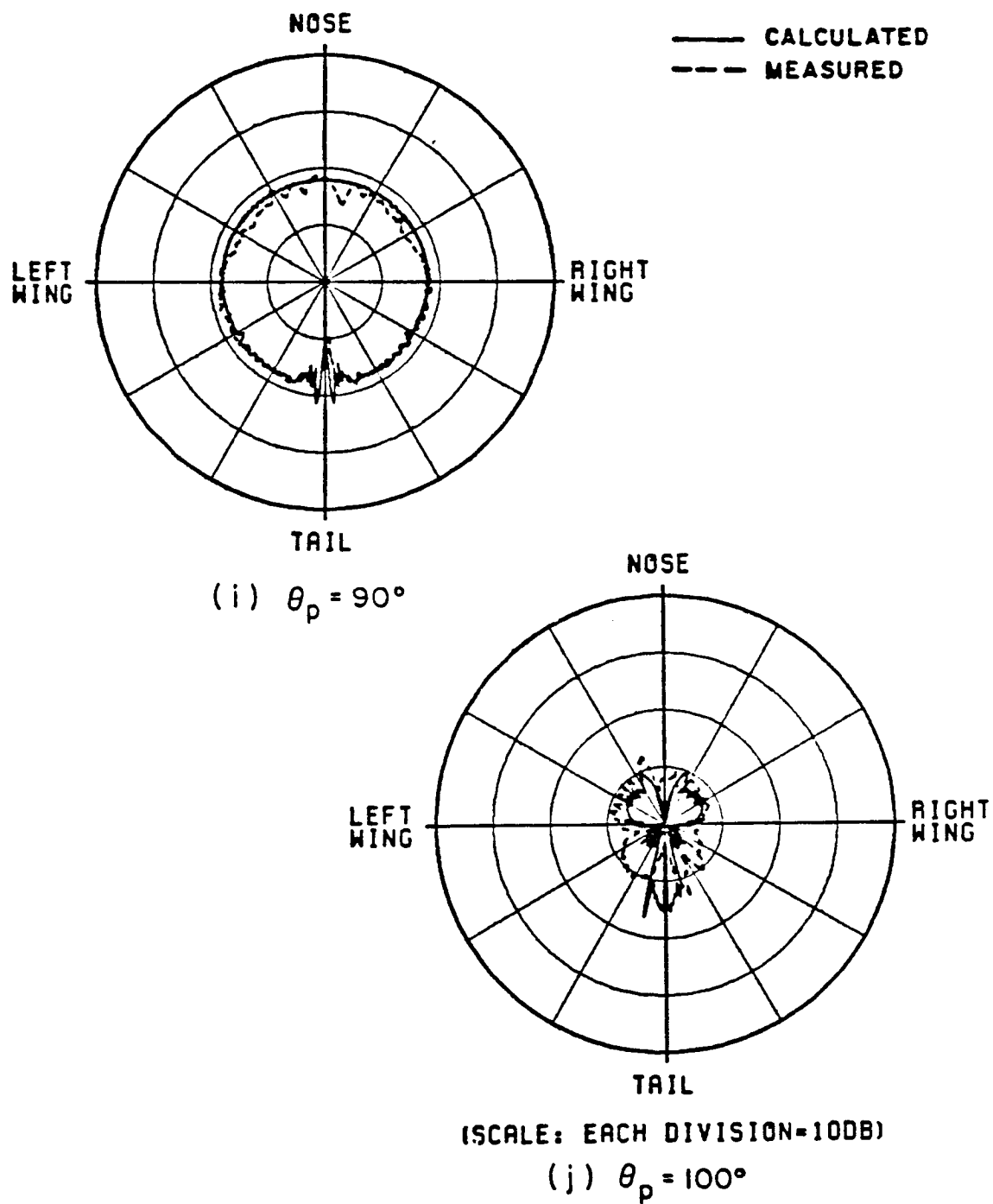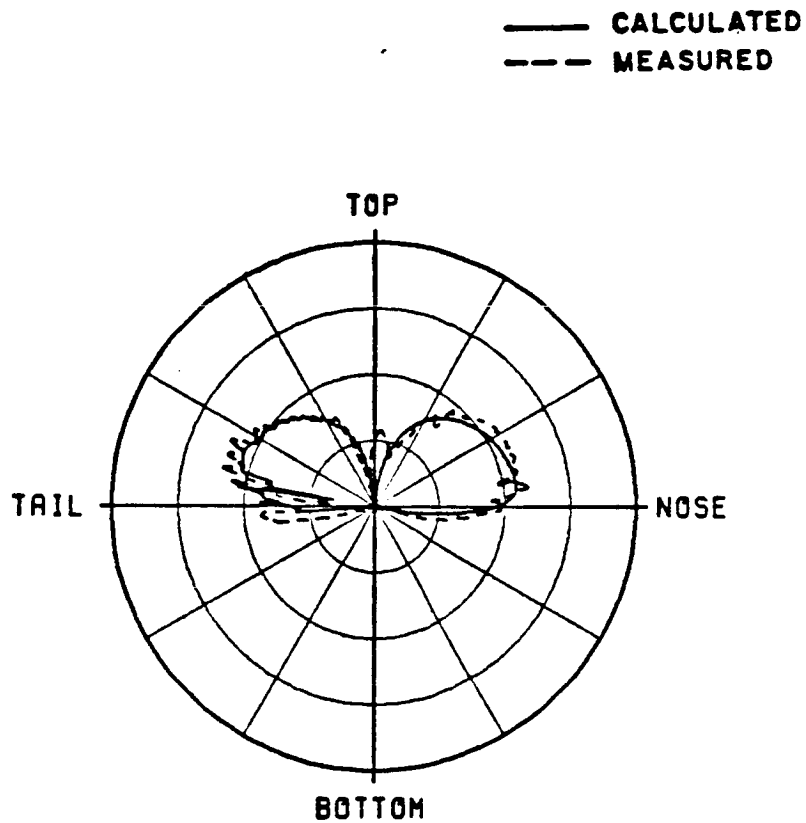
Figure 5.84. Elevation plane pattern of a λ/4 monopole mounted on top of a C-141 aircraft.
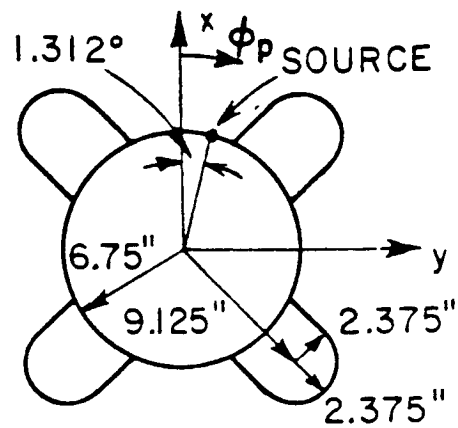
(a) MISSILE MODEL
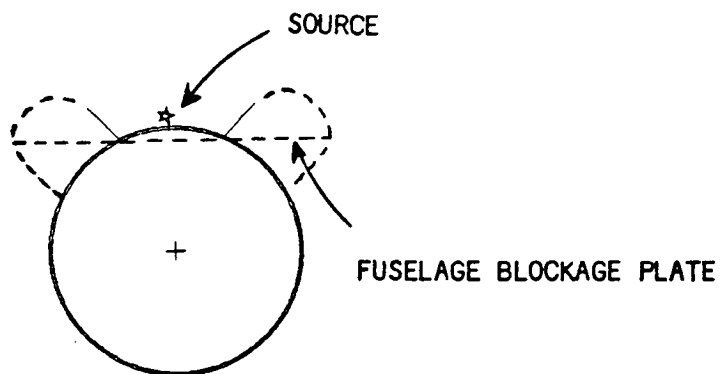
(b) COMPUTER SIMULATED MODEL

Figure 5.85. Missile model for an axial slot mounted between two
ram jets.

contribution passing through the fuselage itself in the field calculation. The roll and elevation plane patterns of this model are compared with measured results in Figures 5.86 and 5.87, respectively. The calculated results are in good agreement with the measurement.

In order to improve the pattern performance, the axial slot antenna was mounted on the ram jet instead of the fuselage as shown in Figure 5.88. In this case, the air duct is simulated as a composite ellipsoid and the other structures (including the fuselage) are simulated by multiple flat plates. The roll and elevation plane patterns are compared with measurement data in Figures 5.89 and 5.90, respectively. The results reveal very good agreement between the theoretical prediction and actual measurements.

E. SPACE SHUTTLE

In the design of antennas for spacecraft, re-entry vehicles, and high performance aircraft, the major area of difficulty is achieving near omni-directional pattern coverage with flush mounted elements. The problem is compounded by the unavailability of several prime locations on the frame, such as the top of the mid fuselage, all leading-edge surfaces, the nose, and the vertical stabilizer. These difficulties lead to the Orbiter antennas being specially developed and qualified in order to meet the performance requirements with a high degree of reliability. In addition, the radiation coverage requirements of some

Figure 5.86. Roll plane pattern for an axial slot mounted between two ram jets.

TOP

NOSE

TAIL

BOTTOM

(SCALE: EACH DIVISION=10DB)
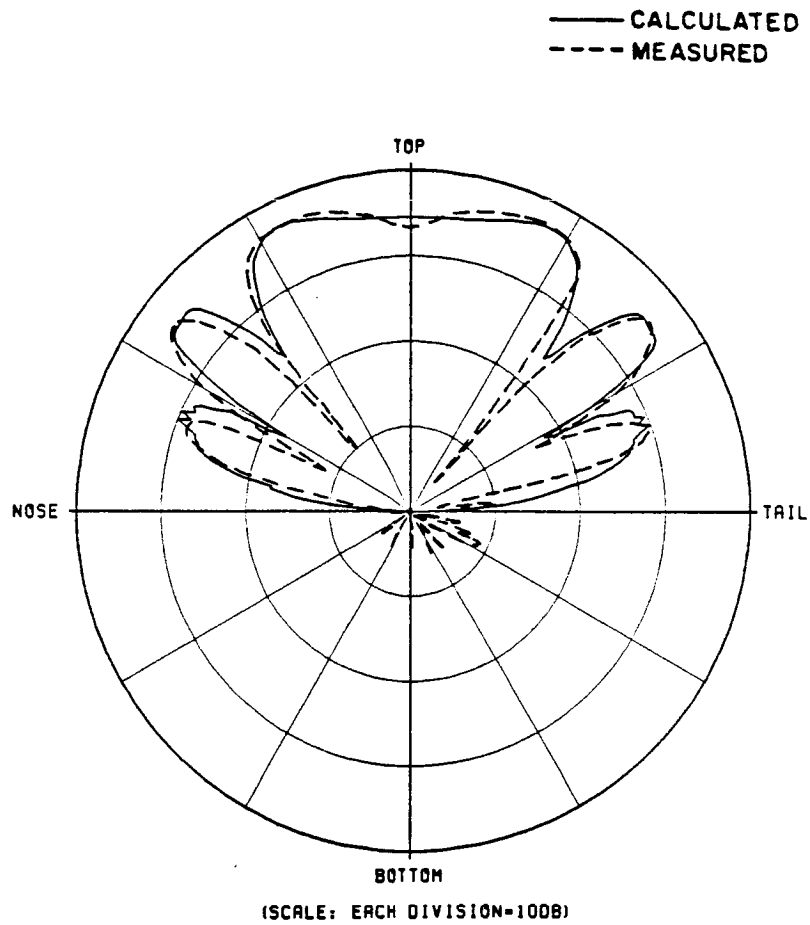
Figure 5.87. Elevation plane pattern for an axial slot mounted between two ram jets.

290
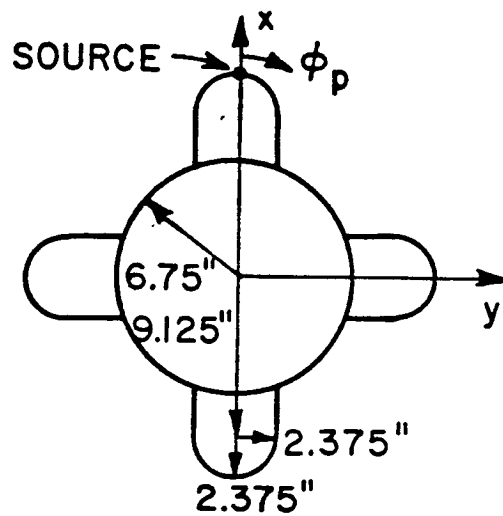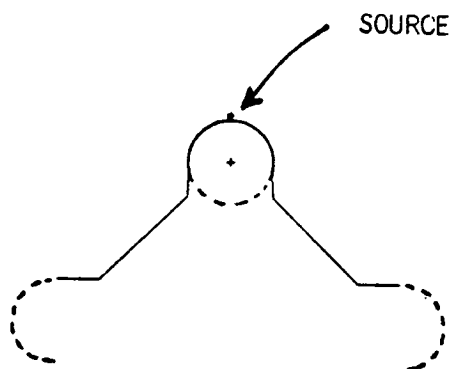
(a) MISSILE MODEL

(b) COMPUTER SIMULATED MODEL

Figure 5.88. Missile model for an axial slot mounted on a ram jet.

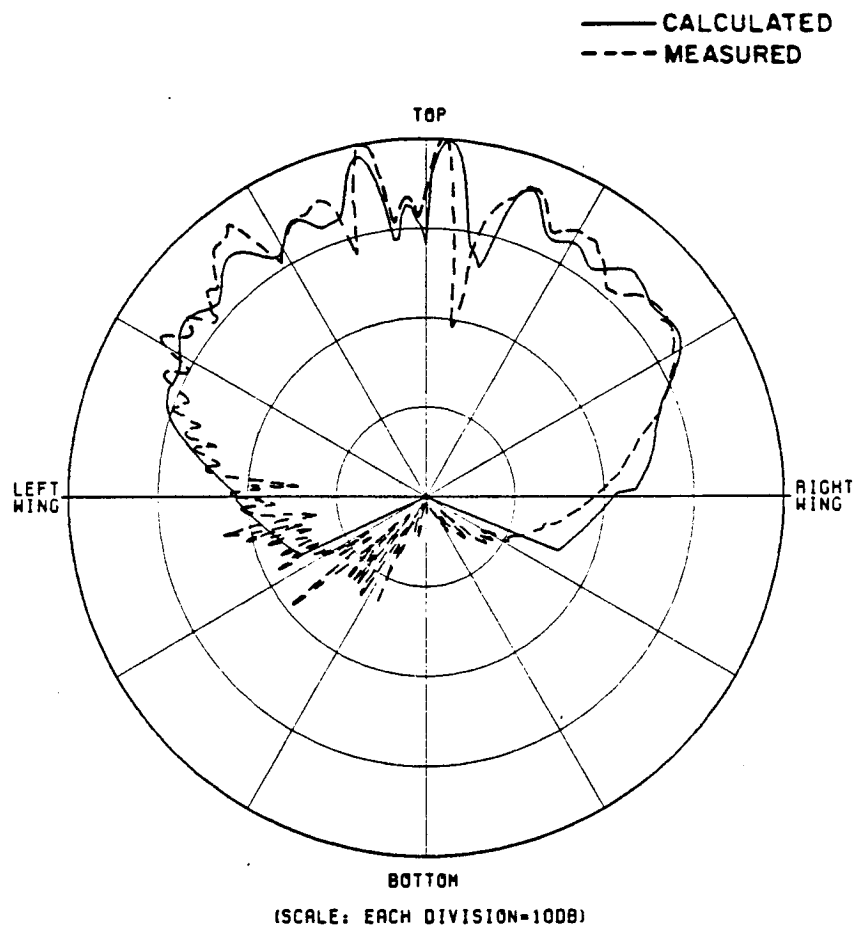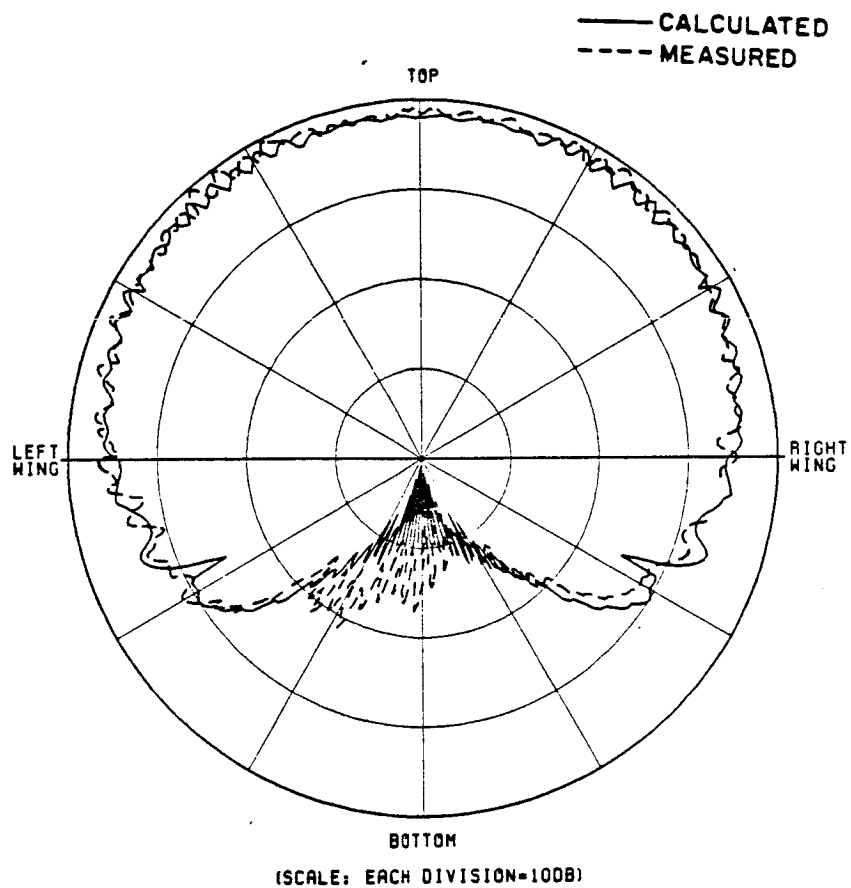Figure 5.89.   Roll plane pattern for an axial slot mounted on a ram jet.

292
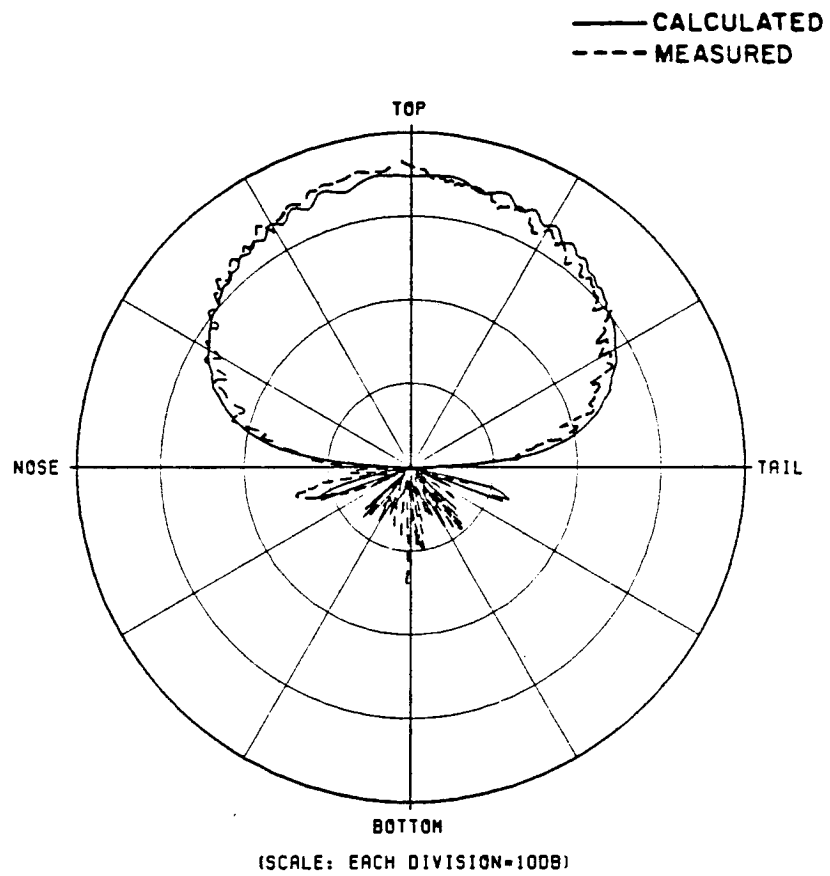
Figure 5.90. Elevation plane pattern for an axial slot mounted on a ram jet.

of the Orbiter antennas are complicated by the multiple requirements for operation during launch, from earth orbit to both ground station and relay satellites, and with the landing area during atmospheric flight.

The major factor influencing the decision as to what type of antenna design to utilize for each of the Shuttle systems is the determination of the mounting location on the Shuttle vehicle. The choice of a mounting location is influenced by such factors as available mounting structure, TPS (thermal protection system) covering material, required angular coverage, and the effects of nearby blocking structure during various phases of the Shuttle mission timeline. The task of determining antenna locations is normally accomplished utilizing a full-scale mockup of the subject vehicle on an antenna range. However, due to the large size of the Shuttle, such an approach is not feasible. Therefore, the need for an efficient analytic solution is quite apparent.

The performance of the S-Band Quad Antennas for PM communications is investigated here using this analytic solution. The basic antenna configuration [48] consists of a set of four circularly polarized antennas flush-mounted with 90° spacing around the roll axis of the Orbiter forward fuselage as shown in Figure 5.91.

The computer simulation model for the top mounted antenna is illustrated in Figure 5.92. A composite ellipsoid (75" x 104" x 1500" x 130") is chosen to simulate the top portion of the fuselage surface, and the other structures such as side walls, nose, wings and vertical

294

S-BAND QUAD ANTENNAS
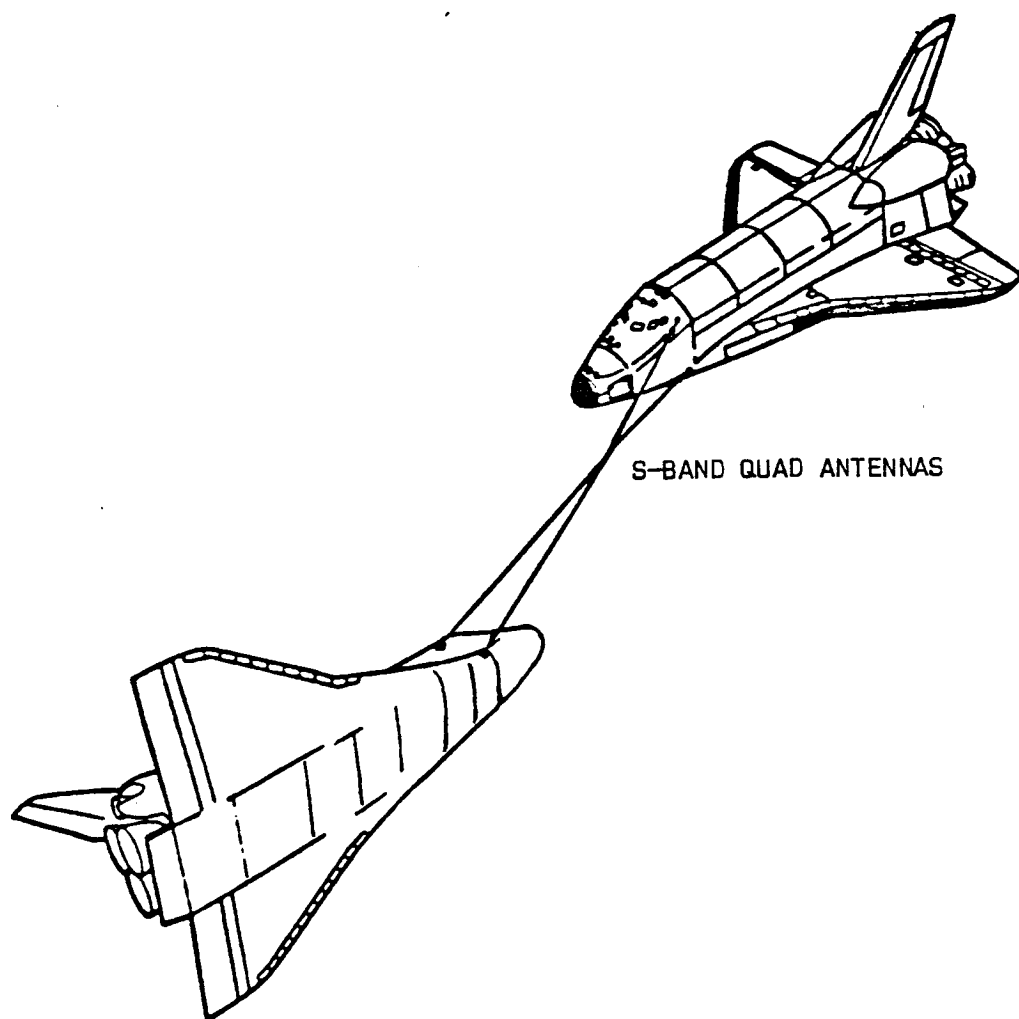
Figure 5.91. S-band quad antenna locations on a Space Shuttle.
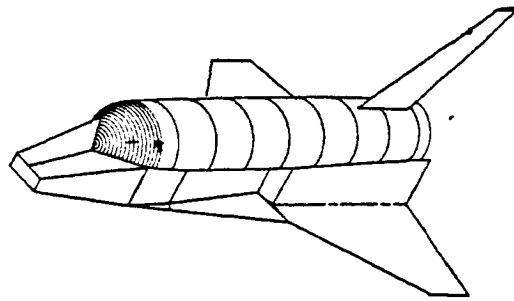
(a) 3-DIMENSIONAL VIEW
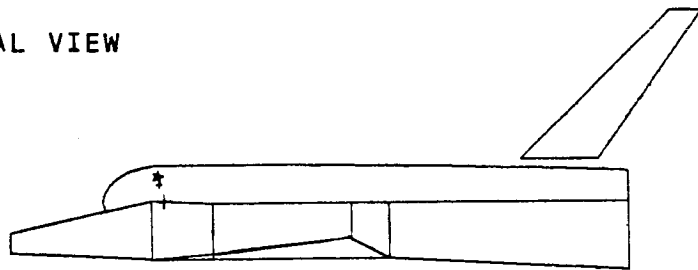
(b) SIDE VIEW
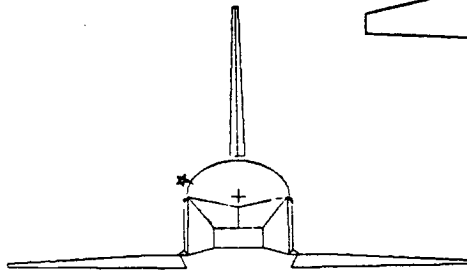
(c) FRONT VIEW
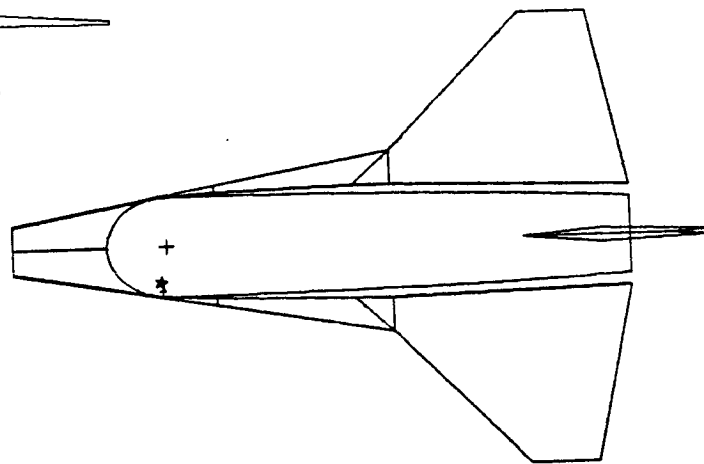
(d) TOP VIEW

Figure 5.92. Computer simulated model for a crossed-slot antenna mounted on top of a Space Shuttle Orbiter.

stabilizer are simulated by 23 flat plates as shown in Figure 5.92. The three principal plane radiation patterns for the top mounted crossed-slot antenna are computed as shown in Figures 5.93 through 5.95.

The blocking effects of the payload bay doors during various phases of the Shuttle mission timeline are analyzed by calculating the roll conical ($\theta_p=45°$) patterns with the doors open and closed. For the top mounted antenna, the heat radiators which actually cause the blocking and reflection of the incident ray are simulated as three flat plates on each side as shown in Figure 5.96. The roll conical ($\theta_p=45°$) patterns for the shuttle with payload bay doors opened are compared with those for the closed payload doors in Figures 5.97 and 5.98. Comparing these patterns, one can easily see the blocking effect of the heat radiator in the 100° to 160° range and the large disturbance (around 20 dB) in the pattern in 30° to 60° range which is the main beam region of the top mounted antenna. This is due to strong direct reflections off the heat radiator.

The computer simulation model for the bottom mounted antennas is illustrated in Figure 5.99. Note that the simulation models are turned upside down for bottom mounted antennas. For this situation, the outer covers of the payload bay doors cause the blockage and reflection, and are simulated as two flat plates on each side as shown in Figure 5.100. The roll conical patterns ($\theta_p=45°$) for the shuttle with

(SCALE: EACH DIVISION= 4DB)

(a) E_ϕ

(b) E_θ
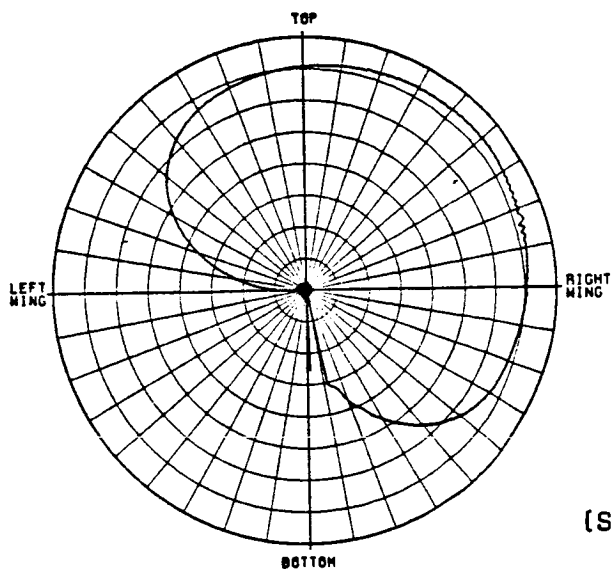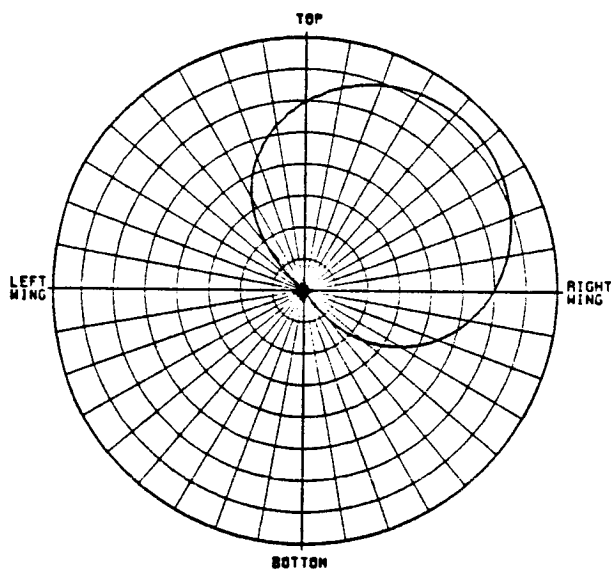
Figure 5.93.   Roll plane radiation patterns for a crossed-slot antenna
mounted on top of a Space Shuttle Orbiter.

(SCALE: EACH DIVISION= 4DB)

(a) E_ϕ

(b) E_θ
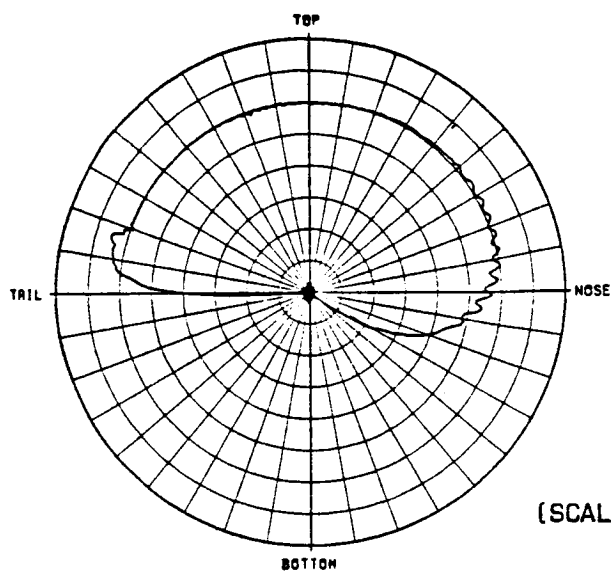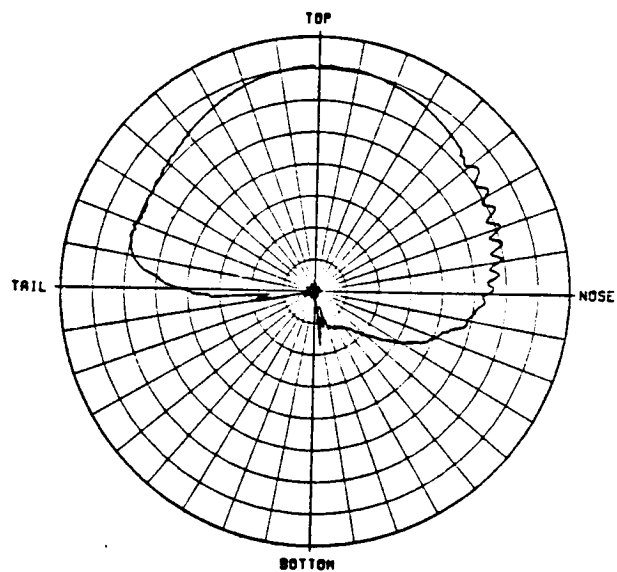
Figure 5.94. Elevation plane patterns for a crossed-slot antenna mounted on top of a Space Shuttle Orbiter.

(SCALE: EACH DIVISION= 4DB)

(a) E_ϕ

(b) E_θ
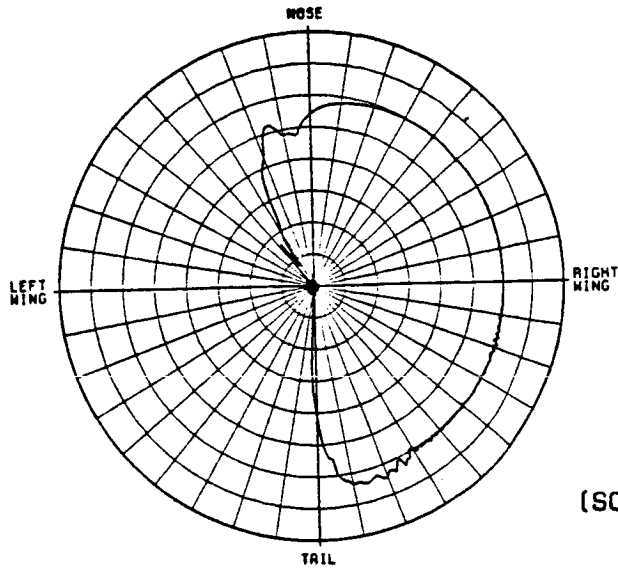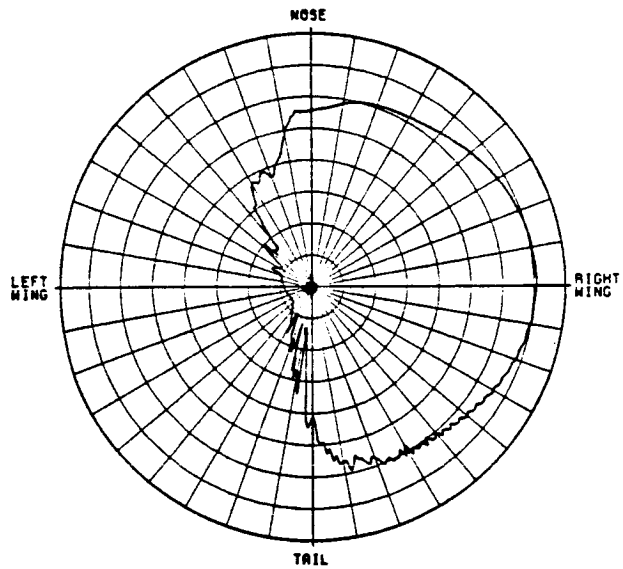
Figure 5.95. Azimuth plane patterns for a crossed-slot antenna mounted on top of a Space Shuttle Orbiter.

300
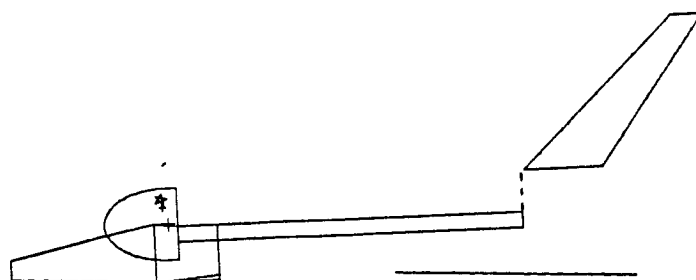
(a) SIDE VIEW

(b) FRONT VIEW

(c) TOP VIEW

Figure 5.96. Computer simulated model for a crossed-slot antenna mounted on top of a Space Shuttle Orbiter when the payload bay doors are open.

301

(SCALE: EACH DIVISION= 4DB)

(a) E_ϕ

(b) E_θ
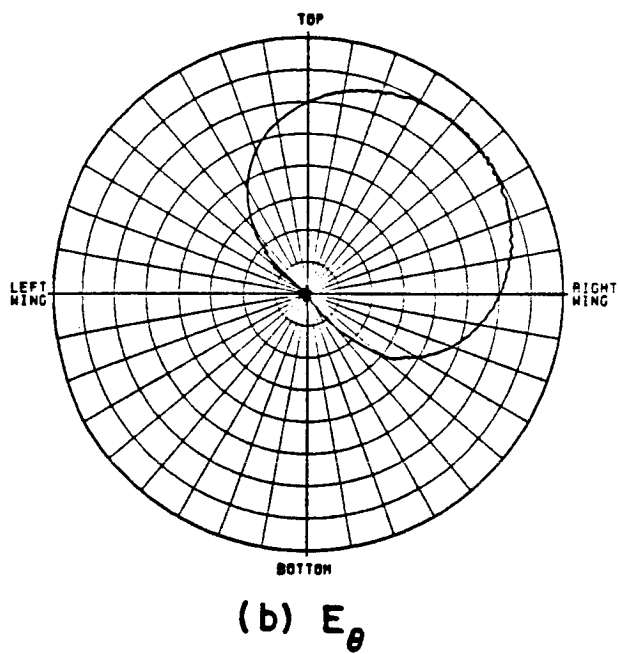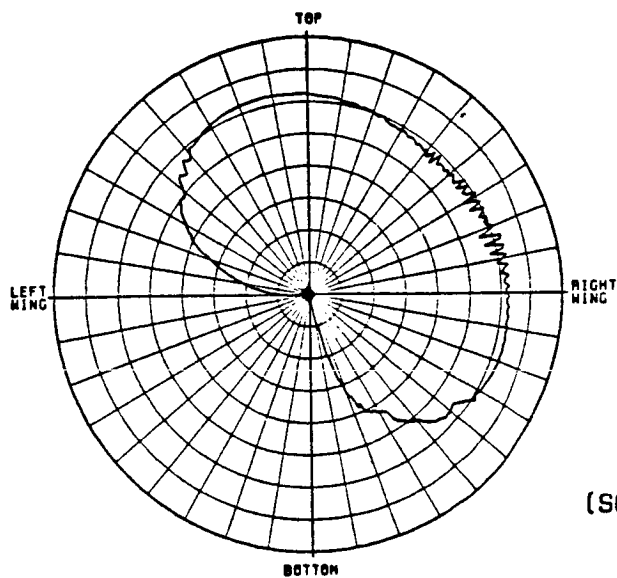
Figure 5.97. Roll conical patterns (θ_p=45°) for a crossed-slot antenna mounted on top of a Space Shuttle Orbiter when the payload bay doors are closed.

302

(SCALE: EACH DIVISION= 4DB)

(a) E_ϕ

(b) E_θ

Figure 5.98. Roll conical patterns (θ_p=45°) for a crossed-slot antenna mounted on top of a Space Shuttle Orbiter when the payload bay doors are <u>open</u>.

303

(a) SIDE VIEW

(b) FRONT VIEW

(c) BOTTOM VIEW

Figure 5.99. Computer simulated model for a crossed-slot antenna
mounted on the bottom of a Space Shuttle Orbiter.
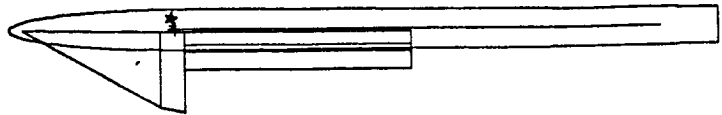
(a) SIDE VIEW
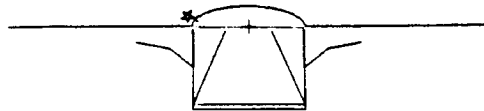
(b) FRONT VIEW
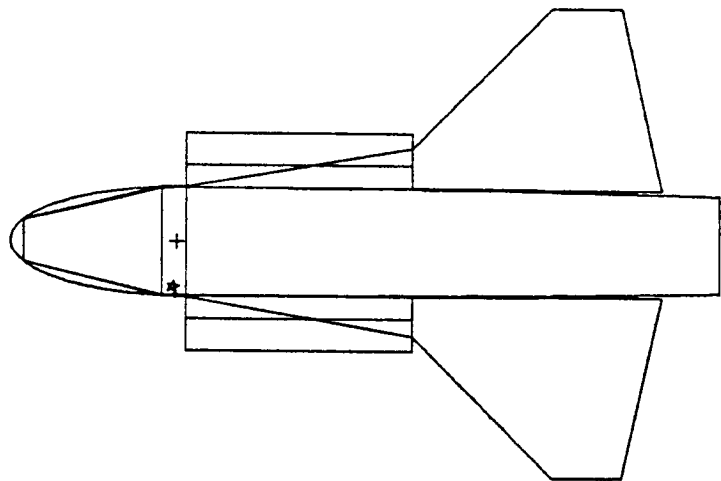
(c) BOTTOM VIEW

Figure 5.100. Computer simulated model for a crossed-slot antenna
mounted on the bottom of a Space Shuttle Orbiter when
the payload bay doors are open.

payload bay doors opened are compared with those closed in Figures 5.101 and 5.102, respectively. The results also indicate severe disturbance of the pattern due to the strong reflections off the payload bay doors.

The above results indicate why one can lose use of his communication channel during those times when the shuttle payload doors are open. This illustrates how one can quickly analyze the performance of antennas in a complex changing environment.

BOTTOM

RIGHT
WING

LEFT
WING

(SCALE: EACH DIVISION= 4DB)

TOP

(a) E_ϕ

BOTTOM

RIGHT
WING

LEFT
WING

TOP

(b) E_θ
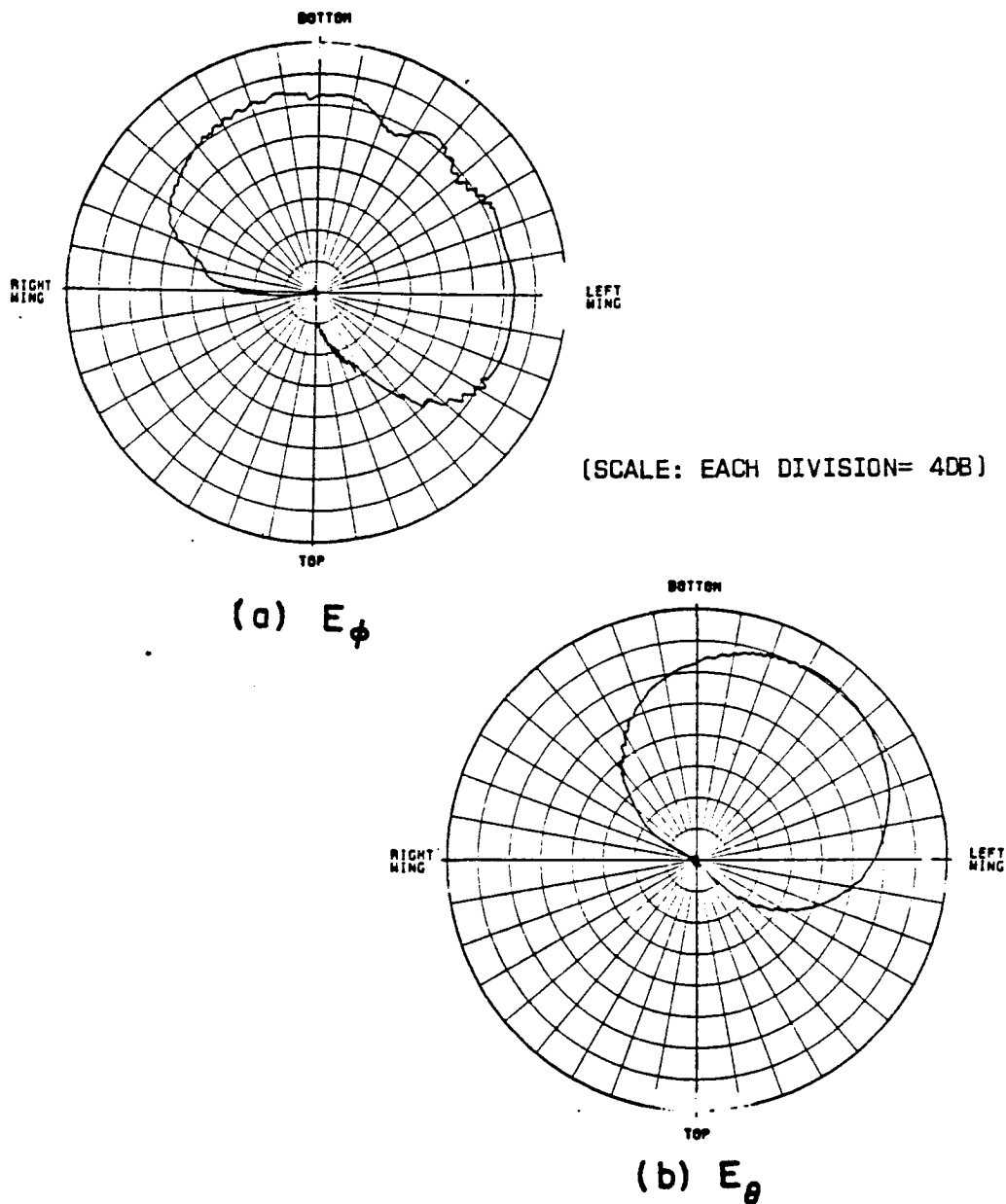
Figure 5.101. Roll conical patterns (θ_p=45°) for a crossed-slot antenna
mounted on the bottom of a Space Shuttle Orbiter when
the payload bay doors are closed.

307

(a) E_ϕ

(SCALE: EACH DIVISION= 4DB)

(b) E_θ

Figure 5.102. Roll conical platterns ($\theta_p=45°$) for a crossed-slot antenna mounted on the bottom of a Space Shuttle Orbiter when the payload bay doors are open.

CHAPTER VI

SUMMARY AND CONCLUSIONS

The object of this research has been to develop an efficient and accurate analytic solution for the high frequency radiation patterns of on-aircraft antennas mounted on the fuselage.

In most cases, scale model measurements have been used to design, and locate airborne antennas. However, this approach is both expensive and time consuming. Thus, the need for an efficient and reliable analytic solution of on-aircraft antenna patterns is quite apparent. The approach applied for this solution is the Uniform Geometrical Theory of Diffraciton (UTD). It is a high frequency technique with the only limitation being that the source and various scattering centers be separated on the order of a wavelength or more. In some cases, this requirement can be relaxed to approximately a quarter-wavelength.

The basic approach applied here is to break up the aircraft into its simplest structural form so that the study is applicable to general-type aircraft. The fuselage is modeled as a perfectly conducting composite ellipsoid; whereas, the other appendages (such as

wings, horizontal and vertical stabilizers, nose, fuel tanks and engines, etc.) are modelled as perfectly conducting flat plates that can be attached to the fuselage or to each other. The composite ellipsoid fuselage model is necessary to successfully simulate the wide variety of real world fuselage shapes. In fact, the fuselage has a dominant effect on the resulting radiation pattern in that the significant energy region is confined to the vicinity of the antenna.

An efficient numerical technique, which uses elliptic cylinder and elliptic cone perturbation methods, for the computation of the geodesic paths on an ellipsoid surface was introduced and verified by the comparisons with exact solutions in Chapter III. The results confirm that for a given radiation direction in the shadow region, the geodesic path (i.e., the actual ray path) and the final diffraction point on the ellipsoid surface can be efficiently solved using the perturbation methods. Based on the fuselage simulation techniques discussed in Chapter III, the algorithms for the actual computation of each individual UTD term such as the source field, reflected field, diffracted field, corner diffracted field, and higher order terms have been discussed in Chapter IV.

Using the fuselage simulation technique and the field calculation algorithms, this new Aircraft Code has been developed to compute and superimpose the various UTD terms for near or far field calculations. This newly developed analytic solution provides an accurate, efficient

and useful means for determination of more optimum antenna designs and locations based on their pattern performance. The capability of the new solution was demonstated for the wide variety of examples in Chapter V.

The optimum antenna locations and proper polarization have been found for the microwave landing system on a Boeing 737 aircraft. The scattering effects of the wings, tail, engine housing, fuel tanks, and rotating propellers on the radiation patterns were analyzed for the various antennas mounted on a KC-135, a Cessna 402B and a Beechcraft Baron. Note that the rotating motion of the propellers was simulated by considering 4 different stationary positions of the propellers. The program runs a pattern in approximatley 4 minutes for a commercial aircraft model on a VAX 11/780 computer.

To show the applicability of this solution for an antenna mounted on the wing of a Cessna 150 aircraft, the ellipsoid was used lengthwise as the wing, and the fuselage was modelled by flat plates.

To further demonstrate the versatility of this solution, various azimuthal radiation patterns for a monopole mounted on an F-16 fighter and C-141 aircraft were obtained. The scattering effects of complex stores mounted on military aircraft were also investigated in terms of an F-4 fighter and A-10 aircraft. Missile antennas mounted among four large ram jets were also simulated for both an antenna mounted between as well as on the ram jets.

The validity of this solution was also verified by numerous comparisons between the calculated and measured data. In most cases, the results of this solution revealed an improvement over the previous solutions [24,40] and show very good agreement between the theoretical predictions and various scale model measurements.

In a more recent example, the performance of the S-Band Quad antennas mounted on the Space Shuttle Orbiter was analyzed. The scattering and blocking effects of the open payload bay doors was analyzed by computing the roll conical patterns ($\theta_p=45°$). The results revealed large disturbances (more than 20 dB) in the pattern in the main beam regions for both the top and bottom mounted antennas. This is due to the strong reflections off the payload bay doors and heat radiators. Using this approach, one can efficiently analyze the pattern performance of antennas radiating in a complex environment such as an aircraft. With such a tool, an antenna designer can consider numerous alternatives in order to optimize his design.

APPENDIX A

EXACT GEODESIC PATHS FOR AN ELLIPSOID

A numerical method employing calculus of variations to calculate the geodesic paths on an ellipsoid [36] is presented in this appendix. This solution is used to check the validity of the perturbation solution which was introduced to efficiently calculate the geodesic paths on an ellipsoid in Section III-C.

Using rectangular coordinates, an ellipsoid can be described as

$$\frac{x^2}{a^2} + \frac{y^2}{b^2} + \frac{z^2}{c^2} = 1 \tag{A.1}$$

where, without loss of generality, it is assumed that $c > b > a > 0$. The key to the derivation of the geodesic path solution of an ellipsoid is to find a coordinate system which is orthogonal on the ellipsoidal surface.

Consider the following three equations

$$\frac{x^2}{a^2-\xi} + \frac{y^2}{b^2-\xi} + \frac{z^2}{c^2-\xi} = 1 \quad , \; a^2 > \xi \tag{A.2}$$

$$\frac{x^2}{a^2-\eta} + \frac{y^2}{b^2-\eta} + \frac{z^2}{c^2-\eta} = 1 \quad , \; b^2 > \eta > a^2 \tag{A.3}$$

$$\frac{x^2}{a^2-\tau} + \frac{y^2}{b^2-\tau} + \frac{z^2}{c^2-\tau} = 1 \quad , \; c^2 > \eta > b^2 \tag{A.4}$$

which are of an ellipsoid, a hyperboloid of one sheet, and a hyperbolid of two sheets [35], respectively, all confocal with the ellipsoid of Equation (A.2). The variables $u^1 = \xi$, $u^2 = \eta$, $u^3 = \tau$ are called ellipsoidal coordinates. The transformation to the rectangular coordinates is obtained by solving Equations (A.2), (A.3), and (A.4) simultaneously for x, y and z, such that

$$x = \pm \left[\frac{-(a^2-\xi)(a^2-\eta)(a^2-\tau)-}{(c^2-a^2)(b^2-a^2)} \right]^{1/2} \tag{A.5}$$

$$y = \pm \left[\frac{-(b^2-\xi)(b^2-\eta)(b^2-\tau)-}{(c^2-b^2)(a^2-b^2)} \right]^{1/2} \tag{A.6}$$

$$z = \pm \left[\frac{-(c^2-\xi)(c^2-\eta)(c^2-\tau)-}{(a^2-c^2)(b^2-c^2)} \right]^{1/2} \quad . \tag{A.7}$$

In terms of the ellipsoidal coordinates, the displacement vector $d\vec{r}$ can be written as

$$d\vec{r} = \frac{\partial \vec{r}}{\partial u^1} \, du^1 + \frac{\partial \vec{r}}{\partial u^2} \, du^2 + \frac{\partial \vec{r}}{\partial u^3} \, du^3 = \vec{a}_1 du^1 + \vec{a}_2 du^2 + \vec{a}_3 du^3 \; . \tag{A.8}$$

Then the length of a line element, denoted by ds, is

$$(ds)^2 = d\vec{r} \cdot d\vec{r} = \sum_{i=1}^{3} \sum_{j=1}^{3} \vec{a}_i \cdot \vec{a}_j \, du^i \, du^j$$

$$= \sum_{i=1}^{3} \sum_{j=1}^{3} g_{ij} \, du^i \, du^j \tag{A.9}$$

where

$$g_{ij} = \vec{a}_i \cdot \vec{a}_j = \frac{\partial x}{\partial u^i} \frac{\partial x}{\partial u^j} + \frac{\partial y}{\partial u^i} \frac{\partial y}{\partial u^j} + \frac{\partial z}{\partial u^i} \frac{\partial z}{\partial u^j} \; . \tag{A.10}$$

It can be shown, using Equations (A.5), (A.6) and (A.7), that

$$g_{ij} = 0, \text{ if } i \neq j \tag{A.11}$$

$$g_{11} = \frac{1}{4} \frac{(\tau-\xi)(\eta-\xi)}{(a^2-\xi)(b^2-\xi)(c^2-\xi)} \tag{A.12}$$

$$g_{22} = \frac{1}{4} \frac{(\xi-\eta)(\tau-\eta)}{(a^2-\eta)(b^2-\eta)(c^2-\eta)} \tag{A.13}$$

and

$$g_{33} = \frac{1}{4} \frac{(\eta-\tau)(\xi-\tau)}{(a^2-\tau)(b^2-\tau)(c^2-\tau)} \; . \tag{A.14}$$

By substituting Equations (A.11) through (A.14) into Equation (A.9), one

obtains

$$(ds)^2 = \frac{1}{4} \left[\frac{(\tau-\xi)(\eta-\xi)}{(a^2-\xi)(b^2-\xi)(c^2-\xi)} \; (d\xi)^2 + \frac{(\xi-\eta)(\tau-\eta)}{(a^2-\eta)(b^2-\eta)(c^2-\eta)} \; (d\eta)^2 \right.$$

$$\left. + \frac{(\eta-\tau)(\xi-\tau)}{(a^2-\tau)(b^2-\tau)(c^2-\tau)} \; (d\tau)^2 \right] \; . \tag{A.15}$$

For the ellipsoid of Equation (A.1), $\xi = d\xi = 0$. Then Equation (A.15)

becomes

$$(ds)^2 = \frac{1}{4} (\tau-\eta) \left[\frac{\eta(d\eta)^2}{(\eta-a^2)(\eta-b^2)(\eta-c^2)} - \frac{\tau(d\tau)^2}{(\tau-a^2)(\tau-b^2)(\tau-c^2)} \right] \tag{A.16}$$

or

$$S = \frac{1}{2} \int (\tau-\eta)^{1/2} \left[\frac{\eta\eta'^2}{(\eta-a^2)(\eta-b^2)(\eta-c^2)} - \frac{\tau}{(\tau-a^2)(\tau-b^2)(\tau-c^2)} \right]^{1/2} d\tau$$

$$\tag{A.17}$$

where $\eta' = d\eta/d\tau$ and $d\tau$ is assumed to be positive. Let $h(\eta,\eta',\tau)$ denote

the integrand of Equation (A.17), i.e.,

$$h = (\tau-n)^{1/2} \left[\frac{\eta n'^2}{(n-a^2)(n-b^2)(n-c^2)} - \frac{\tau}{(\tau-a^2)(\tau-b^2)(\tau-c^2)} \right]^{1/2} .$$

$$\text{(A.18)}$$

Then using the calculus of variation technique, it can be shown that the geodesic path satisfies the following Euler's equation:

$$\frac{d}{d\tau} \frac{\partial h}{\partial n'} - \frac{\partial h}{\partial n} = 0 .$$

$$\text{(A.19)}$$

The next step is to express Equation (A.19) as a complete differential. From Equation (A.18), one obtains

$$\frac{d}{d\tau} \frac{\partial h^2}{\partial n'} = \frac{\frac{d}{d\tau}\left[n'(\tau-n)\right]}{n'(\tau-n)} \frac{\partial h^2}{\partial n'} + 2 \frac{\partial h^2}{\partial n'} + \frac{2h^2}{\tau-n}$$

$$\text{(A.20)}$$

and from Equation (A.19), one obtains

$$\frac{d}{d\tau} \frac{\partial h^2}{\partial n'} = 2 \frac{dh}{d\tau} \frac{\partial h}{\partial n'} + \frac{\partial h^2}{\partial n} .$$

$$\text{(A.21)}$$

By substituting Equations (A.19) and (A.20) into Equation (A.21) and rearranging the various terms, one obtains

317

$$\frac{d[\eta'(\tau-\eta)]}{d\tau} \frac{1}{h} \frac{\partial h}{\partial \eta'} + \eta'(\tau-\eta) \frac{1}{h} \frac{d}{d\tau} \frac{\partial h}{\partial \eta'}$$

$$- \eta'(\tau-\eta) \frac{1}{h^2} \frac{dh}{d\tau} \frac{\partial h}{\partial \eta'} + \eta' = 0 \qquad\qquad (A.22)$$

which can be simplified to

$$\frac{d}{d\tau} \left[\eta'(\tau-\eta) \frac{1}{h} \frac{\partial h}{\partial \eta'} + (\eta-b^2) \right] = 0 \quad . \qquad\qquad (A.23)$$

Equation (A.19) becomes a complete differential. The derivation of the geodesic path solution is straight forward from Equation (A.23). It is obvious that

$$\eta'(\tau-\eta) \frac{1}{h} \frac{\partial h}{\partial \eta'} + \eta - b^2 = -\beta \qquad\qquad (A.24)$$

where β is a constant.

Combining Equations (A.18) and (A.24), one obtains

$$\frac{- \eta(d\eta)^2}{(\eta-a^2)(\eta-b^2)(\eta-c^2)(\eta-b^2+\beta)} = \frac{- \tau(d\tau)^2}{(\tau-a^2)(\tau-b^2)(\tau-c^2)(\tau-b^2+\beta)} \cdot \qquad (A.25)$$

Since $c^2 > \tau > b^2 > \eta > a^2$, it is obvious that $\tau-b^2+\beta > 0 > \eta-b^2+\beta$ or $b^2-\eta > \beta > b^2-\tau$. Thus, Equation (A.25) is the geodesic path solution. However, it is more convenient to make the following changes of variables.

$$\eta = a^2\sin^2\phi + b^2\cos^2\phi \quad , \tag{A.26}$$

and

$$\tau = b^2\cos^2\psi + c^2\sin^2\psi \quad . \tag{A.27}$$

In terms of ϕ and ψ, the geodesic path solution in Equation (A.25) can be rewritten as

$$\frac{[b^2 - (b^2-a^2) \sin^2 \phi] (d\phi)^2}{[(c^2-b^2) + (b^2-a^2) \sin^2 \phi] [-\beta + (b^2-a^2) \sin^2 \phi]}$$

$$= \frac{[b^2 + (c^2-b^2) \sin^2 \psi] (d\psi)^2}{[(b^2-a^2) + (c^2-b^2) \sin^2 \psi] [\beta + (c^2-b^2) \sin^2 \psi]} \quad , \tag{A.28}$$

and in integral form as

$$\int_{\phi_1}^{\phi} \left[\frac{[b^2 - (b^2-a^2) \sin^2 \phi]}{[(c^2-b^2) + (b^2-a^2) \sin^2 \phi] [-\beta + (b^2-a^2) \sin^2 \phi]} \right]^{1/2} |d\phi|$$

$$= \int_{\psi_1}^{\psi} \left[\frac{b^2 + (c^2-b^2) \sin^2 \psi}{[(b^2-a^2) + (c^2-b^2) \sin^2 \psi] [\beta + (c^2-b^2) \sin^2 \psi]} \right]^{1/2} |d\psi|$$

$$\tag{A.29}$$

where $b^2-a^2 > \beta > b^2-c^2$. Note that the absolute values of $d\phi$ and $d\psi$ are used in Equation (A.29).

319

To define the ranges of ϕ and ψ, it is necessary to go back to Equations (A.5), (A.6) and (A.7). With $\xi=0$ and in terms of ϕ and ψ, they can be rewritten as

$$x = \frac{a}{(c^2-a^2)^{1/2}} \cos\phi \, (b^2\cos^2\psi + c^2\sin^2\psi - a^2)^{1/2} \qquad (A.30)$$

$$y = b\sin\phi \, \sin\psi \qquad (A.31)$$

and

$$z = \frac{c}{(c^2-a^2)^{1/2}} \cos\psi \, (c^2-a^2\sin^2\phi - b^2\cos^2\phi)^{1/2} \, . \qquad (A.32)$$

If the goedesic path, Equation (A.29), crosses the curve $\phi=0$ or π, then $\beta<0$ and if it crosses the curve $\psi=0$ or π, then $\beta>0$. Thus to ensure the continuity of ϕ and ψ along the geodesic path, the ranges of ϕ and ψ are defined as follows:

$$0 < \psi < \pi, \; -\pi < \phi < 2\pi \qquad \text{for } \beta < 0$$

and

$$-\pi < \psi < 2\pi, \; 0 < \phi < \pi \quad \text{for } \beta > 0 \, .$$

Figure A.1 illustrates the ϕ and ψ curves as projected onto the x-z plane. Equation (A.29) is the geodesic path solution of an ellipsoid which is employed for obtaining more exact geodesic paths. When the
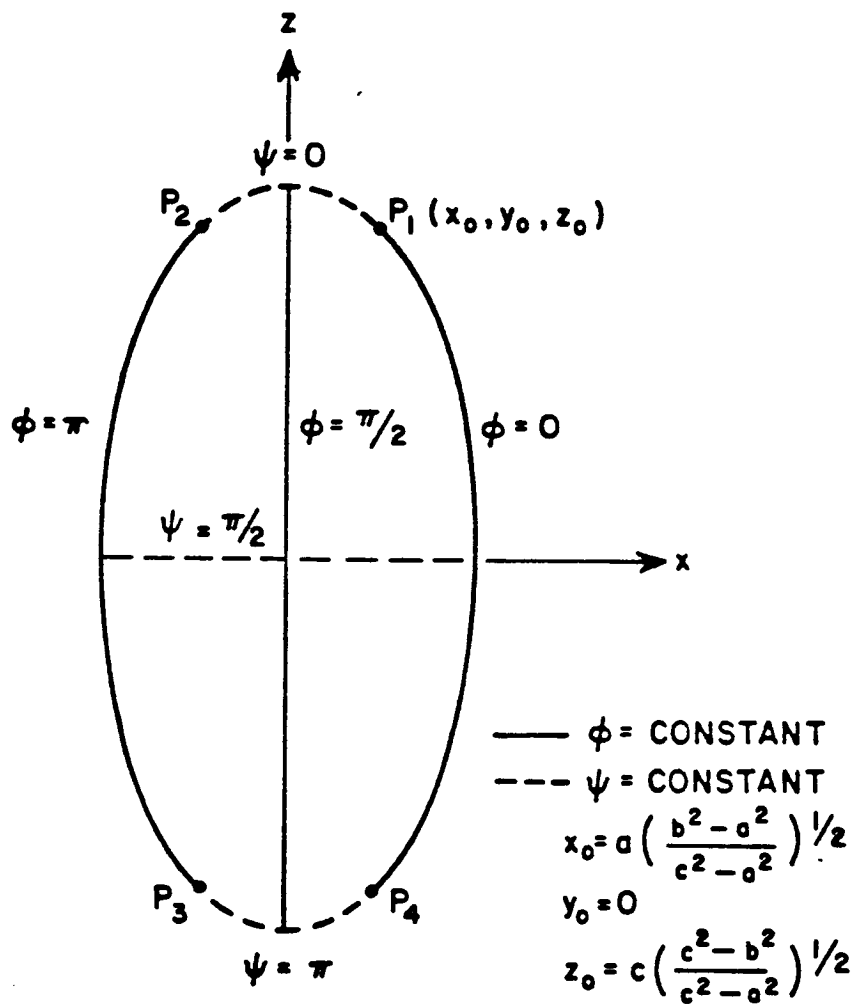
Figure A.1. Projection of ϕ- and ψ- curves onto the xz plane of an ellipsoid.

geodesic path includes one of those four points, P_1, P_2, P_3 and P_4 in the figure, then β must equal zero and the integrals in Equation (A.29) diverge at those points. Thus if $(\phi_2,\psi_2) = P_i$, $i = 1,2,3,4$, then it is necessary to replace (ϕ_2,ψ_2) by $(\phi_2+\Delta\phi, \psi_2+\Delta\psi)$ where $\Delta\phi \approx 0$ and $\Delta\psi \approx 0$. The geodesic path between the two points (ϕ_1,ψ_1) and (ϕ_2,ψ_2) can be determined from Equation (A.29) by first determining the value of β. Since there are absolute value-signs attached to the differential $d\phi$ and $d\psi$ in the geodesic path solution, it is important to know how the variables ϕ and ψ change from ϕ_1 to ϕ_2 and ψ_1 to ψ_2, respectively.

REFERENCES

[1] J.B. Keller, "Geometrical Theory of Diffraction", J. Opt. Soc. Am., Vol. 52, No. 2, pp. 116-130, 1962.

[2] P.H. Pathak, N. Wang, W.D. Burnside and R.G. Kouyoumjian, "A Uniform GTD Solution for the Radiation from Sources on a Convex Surface", IEEE Trans. on Antennas and Prop., Vol, AP-29, No. 4, pp. 609-622, July 1981.

[3] R.G. Kouyoumjian and P.H. Pathak, "A Uniform Geometrical Theory of Diffraction for an Edge in a Perfectly-Conducting Surface", Proc. IEEE, Vol. 62, November 1974, pp. 1448-1461.

[4] R.G. Kouyoumjian, P.H. Pathak and W.D. Burnside, "A Uniform GTD for the Diffraction by Edges, Vertices and Convex Surfaces", book chapter in Theoretical Methods for Determining the Interaction of Electromagnetic Waves with Structures, edited by J.K. Skwirynski, Sijthoff and Noordhoff, Netherlands, 1978.

[5] W.D. Burnside, N. Wang and E.L. Pelton, "Near-Field Pattern Analysis of Airborne Antennas", IEEE Trans. on Antennas and Prop., Vol. AP-28, pp. 318-327, May 1980.

[6] F.A. Sikta, W.D. Burnside, T.T. Chu and L. Peters, Jr., "First-Order Equivalent Current and Corner Diffraction Scattering from Flat Plate Structures", IEEE Trans. on Antennas and Prop., Vol. AP-31, No. 4, pp. 584-589, July 1983.

[7] W.D. Burnside, "Analysis of On-Aircraft Antenna Patterns", Technical Report 3390-1, August 1972, The Ohio State University ElectroScience Laboratory, Department of Electrical Engineering; prepared under Contract 62269-72-C-0354 for the Department of the Navy, Naval Air Development Center. Also a Ph.D. Dissertation, The Ohio State University, 1972.

[8] W.D. Burnside, M.C. Gilreath, R.J. Marhefka and C.L. Yu, "A Study of KC-135 Aircraft Antenna Patterns", IEEE Trans. on Antennas and Prop., Vol. AP-23, pp. 3090-316, May 1975.

[9] C.L. Yu, W.D. Burnside, and M.C. Gilreath, "Volumetric Pattern Analysis of Airborne Antennas", IEEE Trans. on Antennas and Prop., Vol. AP-26, pp. 636-641, September 1978.

[10] C.C. Huang, N. Wang, and W.D. Burnside, "The High-Frequency
     Radiation Patterns of a Spheroid-Mounted Antenna", Report
     712527-1, March 1980, The Ohio State University ElectroScience
     Laboratory, Department of Electrical Engineering; prepared under
     Contract No. N00019-80-C-0050 for the Department of the Navy,
     Naval Air Systems Command.

[11] W.D. Burnside and H.H. Chung, "Analysis of Airborne Antenna
     Pattern and Mutual Coupling and their Effects on Adaptive Array
     Performance", Technical Report 714258-5, June 1983, The Ohio State
     University ElectroScience Laboratory, Department of Electrical
     Engineering; prepared under Contract No. F30602-182-C-0009 for the
     Department of the Air Force, Rome Air Development Center. Also a
     Ph.D. dissertation, The Ohio State University, 1983.

[12] W.D. Burnside and N. Wang, "Near Field Analysis of Airborne
     Antennas", Final Report 713321-4, December 1981, The Ohio State
     University ElectroScience Laboratory, Department of Electrical
     Engineering; prepared under Contract No. N00019-80-C-0593 for the
     Department of the Navy, Naval Air Systems Command.

[13] J.J. Kim, N. Wang, and C.D. Chuang, "Geodesic Paths of an
     Ellipsoid-Mounted Antenna", Technical Report 713321-3, March 1982,
     The Ohio State University ElectroScience Laboratory, Department
     of Electrical Engineering; prepared under Contract No.
     N00019-80-PR-RJ015 for the Department of the Navy, Naval Air
     Systems Command.

[14] J.J. Kim and W.D. Burnside, "Geodesic Paths for Side-Mounted
     Antenna on an Ellipsoid Model", Technical Report 714215-1,
     October 1982, The Ohio State University ElectroScience Laboratory,
     Department of Electrical Engineering; prepared under Contract No.
     N00019-81-C-0424 for the Department of the Navy, Naval Air Systems
     Command.

[15] W.D. Burnside, J.J. Kim and B. Grandchamp, "Airborne Antenna
     Radiation Pattern Code User's Manual", Technical Report 716199-2,
     December 1984, The Ohio State University ElectroScience Laboratory,
     Department of Electrical Engineering; prepared under Grant NSG 1498
     for NASA, Langley Research Center, Hampton, Virginia.

[16] Short Course Notes on "The Modern Geometrical Theory of
     Diffraction", Vols. 1, 2 and 3, The Ohio State University
     ElectroScience Laboratory, Department of Electrical Engineering,
     1980.

[17] M.M. Lipschutz, Differential Geometry, Schaum's Outline Series,
     McGraw-Hill Book Co., New York, New York, 1969.

[18] W.D. Burnside, N. Wang, and E.L. Pelton, "Near Field Pattern Computations for Airborne Antenna", Technical Report 784685-4, June 1978, The Ohio State University ElectroScience Laboratory, Department of Electrical Engineering; prepared under Contract No. N00019-77-C-0299 for the Department of the Navy, Naval Air Systems Command.

[19] P.H. Pathak, and R.G. Kouyoumjian, "The Dyadic Diffraction Coefficient for a Perfectly Conducting Wedge", Technical Report 2183-4, June 1970, The Ohio State University ElectroScience Laboratory, Department of Electrical Engineering; prepared under Contract No. AF19(628)-5929 for the Department of the Air Force, Air Force Cambridge Research Laboratories.

[20] R.G. Kouyoumjian and P.H. Pathak, "The Dyadic Diffraction Coefficient for a Curved Edge", Technical Report 3001-3, August 1973, The Ohio State University ElectroScience Laboratory, Department of Electrical Engineering; prepared under Grant No. NGR 36-008-144 for the National Aeronautics and Space Administration.

[21] W.D. Burnside and P.H. Pathak, "A Corner Diffraction Coefficient", to appear.

[22] J.J. Kim and W.D. Burnside, "Radiation Patterns of an Antenna Mounted on the Off-Mid Section of an Ellipsoid", Technical Report 714215-3, June 1983, The Ohio State University ElectroScience Laboratory, Department of Electrical Engineering; prepared under Contract No. N00019-81-C-0424 for the Department of the Navy, Naval Air Systems Command.

[23] J.J. Kim and W.D. Burnside, "Radiation Patterns of an Antenna Mounted on the Mid Section of an Ellipsoid", Technical Report 714215-2, July 1983, The Ohio State University ElectroScience Laboratory, Department of Electrical Engineering; prepared under Contract No. N00019-81-C-0424 for the Department of the Navy, Naval Air Systems Command.

[24] H.H. Chung and W.D. Burnside, "General 3D Airborne Radiation Pattern Code User's Manual", Technical Report 711679-10, July 1982, The Ohio State University ElectroScience Laboratory, Department of Electrical Engineering; prepared under Contract No. F30602-79-C-0068 for the Department of the Air Force, Rome Air Development Center,

[25] E.L. Pelton and W.D. Burnside, "Edge Diffraction Point Analysis Used in Near-Field On-Aircraft Antenna Studies", Report 784685-2, October 1977, The Ohio State University ElectroScience Laboratory, Department of Electrical Engineering; prepared under Contract No. N00019-77-C-0299 for the Department of the Navy, Naval Air Systems Command.

[26] S.W. Lee, "Differential Geometry for GTD Application", Report No. 77-21, October 1977, University of Illinois at Urbana-Champaign, Department of Electrical Engineering, Electromagnetics Laboratory; supported by the National Science Foundation.

[27] R.G. Kouyoumjian, Numerical and Asymptotic Techniques in Electromagnetics, Topics in Applied Physics, Volume 3, edited by R. Mittra, Springer-Verlag, New York, pp. 164-215, 1975.

[28] R.G. Kouyoumjian, "Advanced Electromagnetics", The Ohio State University EE 819 Class Notes, 1981.

[29] T.T. Chu, "First Order Uniform Geometrical Theory of Diffraction Analysis of the Scattering by Smooth Structures", Ph.D. Dissertation, The Ohio State University, Department of Electrical Engineering, 1983.

[30] W.D. Burnside, "Microwave Optics (Geometrical Theory of Diffraction)", The Ohio State University EE 712 Class Notes, 1981.

[31] C.E. Ryan and L. Peters, Jr., "Evaluation of Edge-Diffracted Fields Including Equivalent Currents for the Caustic Regions", IEEE Trans. on Antennas and Prop., Vol. AP-17, pp. 292-299, May 1969; see also correction to this paper in Vol. AP-18, p. 275, March 1970.

[32] R.F. Harrington, Time Harmonic Electromagnetic Fields, McGraw-Hill Book Co., New York, 1961.

[33] C.A. Balanis, Antenna Theory Analysis and Design, Harper & Row Publishers, New York, 1982.

[34] R.C. Hansen, ed., Geometric Theory of Diffraction, IEEE Press, 1981.

[35] J.A. Stratton, Electromagnetic Theory, McGraw-Hill Book Co., New York, 1941.

[36] C.D. Chuang, "The Geodesic Path Solution of an Ellipsoid", unpublished paper.

[37] W.D. Burnside and K.W. Burgener, "Analysis of Private Aircraft Antenna Patterns', Report 710964-1, September 1978, The Ohio State University ElectroScience Laboratory, Department of Electrical Engineering; prepared under Grant NSG 1498 for National Aeronautics and Space Administration, Langley Research Center, Hampton, Virginia.

[38] K.W. Burgener and W.D. Burnside, "Analysis of Private Aircraft Antenna Patterns", Report 710964-2, January 1979, The Ohio State University ElectroScience Laboratory, Department of Electrical Engineering; prepared under Grant NSG 1498 for National Aeronautics and Space Administration, Langley Research Center, Hampton, Virginia.

[39] W.D. Burnside, "Analysis of Private Aircraft Antenna Patterns", Report 710964-7, October 1980, The Ohio State University ElectroScience Laboratory, Department of Electrical Engineering; prepared under Grant NSG 1498 for National Aeronautics and Space Administration, Langley Research Center, Hampton, Virginia.

[40] W.D. Burnside and T. Chu, "Airborne Antenna Patterns Code User's Manual", Technical Report 711588-2, March 1980, The Ohio State University ElectroScience Laboratory, Department of Electrical Engineering; prepared under Contract No. N62269-78-C-0379 for Naval Air Development Center.

[41] R.M. Janes, All the World's Aircraft, 1973-1974, McGraw-Hill Co.

[42] C.L. Yu and W.D. Burnside, "MLS Airborne Antenna Research", Semi-annual Report 2902-22, May 1975, The Ohio State University ElectroScience Laboratory, Department of Electrical Engineering; prepared under Grant NGL36-003-138 for National Aeronautics and Space Administration, Langley Research Center, Hampton, Virginia.

[43] C.L. Yu and W.D. Burnside, "Research on MLS Airborne Antenna", Semi-annual Report 2902-23, April 1976, The Ohio State University ElectroScience Laboratory, Department of Electrical Engineering; prepared under Grant NGL36-003-138 for National Aeronautics and Space Administration, Langley Research Center, Hampton, Virginia.

[44] C.L. Yu and W.D. Burnside, "Volumetric Pattern Analysis of Fuselage-Mounted Airborne Antennas", Technical Report 2902-24, April 1976, The Ohio State University ElectroScience Laboratory, Department of Electrical Engineering; prepared under Grant NGL36-003-138 for National Aeronautics and Space Administration, Langley Research Center, Hampton, Virginia.

[45] W.D. Burnside, R.J. Marhefka and E.L. Pelton, "Fuselage-Mounted Antenna Code - User's Manual", Technical Report 4583-2 (784583), July 1977, The Ohio State University ElectroScience Laboratory, Department of Electrical Engineering; prepared under Contract No. N62269-76-C-0554 for Naval Air Development Center.

[46] C.A. Lindberg, "A Shallow-Cavity UHF Crossed-Slot Antenna", IEEE Trans. AP-17, September 1969, pp. 558-563.

[47] G.F. Mason, "Radiation Pattern Measurements for F-16 Antenna Systems: Volume I - TACAN Antenna System", Report 16PR383, September 15, 1976, General Dynamics, Ft. Worth Division.

[48] H. Dean Cubley and Haynes Ellis, "Antenna Development for the Space Shuttle Orbiter Vehicle", IEEE Trans. on Communications, Vol. COM-26, No. 11, November 1978, pp. 1713-1722.

[49] J.H. Richmond, "Radiation and Scattering by Thin-wire Structures in the Complex Frequency Domain", Technical Report 2902-10, July 1973, The Ohio State University ElectroScience Laboratory, Department of Electrical Engineering; prepared under Grant NGL 36-008-138 for National Aeronautics and Space Administration, Washington, D.C.

[50] J.H. Richmond, "Computer Program for Thin-wire Structures in a Homogeneous Conducting Medium", Technical Report 2902-12, January 1974, The Ohio State University ElectroScience Laboratory, Department of Electrical Engineering; prepared under Grant NGL 36-008-138 for National Aeronautics and Space Administration, Washington, D.C.